

Advanced Computational Methods for Stability Assessment of Metal-Organic Frameworks

Citation for published version (APA):

Acuna Yeomans, E. (2025). *Advanced Computational Methods for Stability Assessment of Metal-Organic Frameworks*. [Phd Thesis 1 (Research TU/e / Graduation TU/e), Applied Physics and Science Education]. Eindhoven University of Technology.

Document status and date:

Published: 11/02/2025

Document Version:

Publisher's PDF, also known as Version of Record (includes final page, issue and volume numbers)

Please check the document version of this publication:

- A submitted manuscript is the version of the article upon submission and before peer-review. There can be important differences between the submitted version and the official published version of record. People interested in the research are advised to contact the author for the final version of the publication, or visit the DOI to the publisher's website.
- The final author version and the galley proof are versions of the publication after peer review.
- The final published version features the final layout of the paper including the volume, issue and page numbers.

[Link to publication](#)

General rights

Copyright and moral rights for the publications made accessible in the public portal are retained by the authors and/or other copyright owners and it is a condition of accessing publications that users recognise and abide by the legal requirements associated with these rights.

- Users may download and print one copy of any publication from the public portal for the purpose of private study or research.
- You may not further distribute the material or use it for any profit-making activity or commercial gain
- You may freely distribute the URL identifying the publication in the public portal.

If the publication is distributed under the terms of Article 25fa of the Dutch Copyright Act, indicated by the "Taverne" license above, please follow below link for the End User Agreement:

www.tue.nl/taverne

Take down policy

If you believe that this document breaches copyright please contact us at:

openaccess@tue.nl

providing details and we will investigate your claim.

Advanced Computational Methods for Stability Assessment of Metal-Organic Frameworks

PROEFSCHRIFT

ter verkrijging van de graad van doctor aan de Technische Universiteit Eindhoven,
op gezag van de rector magnificus prof.dr. S.K. Lenaerts, voor een commissie
aangewezen door het College voor Promoties, in het openbaar te verdedigen op
dinsdag 11 februari 2025 om 13:30 uur

door

Esteban Acuna Yeomans

geboren te Hermosillo, Mexico

Dit proefschrift is goedgekeurd door de promotoren en de samenstelling van de promotiecommissie is als volgt:

voorzitter: prof.dr. M. Creatore

1^e promotor: prof.dr. S. Calero

2^e promotor: dr. D. Dubbeldam (Universiteit van Amsterdam)

copromotor: dr. J. J. Gutierrez Sevillano (University Pablo de Olavide)

leden: prof.dr. G.H.L.A. Brocks

prof.dr. A. Lyulin

prof.dr.ir. T.J.H. Vlugt (Technische Universiteit Delft)

adviseur: dr. A. Luna Triguero

Het onderzoek of ontwerp dat in dit proefschrift wordt beschreven is uitgevoerd in overeenstemming met de TU/e Gedragscode Wetenschapsbeoefening.

Copyright ©2025 by Esteban Acuna Yeomans

ORCID iD: 0000-0002-0539-8236

The work presented in this thesis has been supported by the Eindhoven Institute for Renewable Energy Systems (EIRES). The research was conducted in the Materials Simulation & Modelling (MSM) group, Department of Applied Physics and Science Education, Eindhoven University of Technology, The Netherlands.

A catalogue record is available from the Eindhoven University of Technology Library
ISBN: 978-90-386-6289-3

CONTENTS

| | |
|---|-----------|
| List of Symbols | xi |
| 1 Introduction | 1 |
| 1.1 Metal-Organic Frameworks and Stability | 2 |
| 1.2 Zeolitic Imidazolate Frameworks | 5 |
| 1.3 Zr-based MOFs | 7 |
| 1.4 Computational modeling | 10 |
| 1.5 Outline of this thesis. | 12 |
| 2 Methodology | 15 |
| 2.1 Force fields. | 16 |
| 2.2 Energy minimization | 18 |
| 2.3 Molecular dynamics. | 20 |
| 2.4 Elastic properties of materials. | 24 |
| 2.4.1 The elastic stiffness tensor | 24 |
| 2.4.2 Direct cell-deformation technique | 26 |
| 2.4.3 Strain fluctuation at constant stress method | 30 |
| 2.4.4 Stress fluctuation at constant volume | 31 |
| 2.5 Theoretical methods to asses mechanical stability | 33 |
| 2.5.1 Born stability criteria | 34 |
| 2.5.2 Anisotropy of elastic moduli | 35 |
| 2.5.3 Iterative and Fixed-Volume Schemes for Determining Amor- phization | 37 |

| | | |
|----------|---|-----------|
| 3 | Evaluation of ZIF-8 flexible force fields | 39 |
| 3.1 | Introduction | 40 |
| 3.2 | Methodology. | 43 |
| 3.3 | Results and discussion. | 49 |
| 3.3.1 | Temperature dependence | 49 |
| 3.3.2 | Unit cell size as a function of pressure. | 50 |
| 3.3.3 | Elastic constants as a function of pressure. | 51 |
| 3.3.4 | Elastic constants using SD/CG vs. mode-following mini- mization | 54 |
| 3.4 | Conclusions | 57 |
| 4 | Linker vacancy distribution and its effect on UiO-66 stability | 59 |
| 4.1 | Introduction | 60 |
| 4.2 | Methodology. | 63 |
| 4.2.1 | Computational details. | 68 |
| 4.3 | Results and discussion. | 69 |
| 4.4 | Conclusions | 77 |
| 5 | Effect of water loading on the stability of pristine and defected UiO-66 | 79 |
| 5.1 | Introduction | 80 |
| 5.2 | Methodology. | 83 |
| 5.2.1 | Force fields and models. | 83 |
| 5.2.2 | Simulation details. | 86 |
| 5.3 | Results and discussion. | 87 |
| 5.3.1 | Effect of water loading on the pristine structures | 87 |
| 5.3.2 | Effect of water loading on defected structures. | 92 |
| 5.4 | Conclusions | 96 |
| 6 | Influence of adsorbate polarity on the structural stability of UiO-66 | 99 |
| 6.1 | Introduction | 100 |

| | | |
|----------|---|------------|
| 6.2 | Methodology | 102 |
| 6.2.1 | Force fields and models. | 102 |
| 6.2.2 | Simulation Details | 105 |
| 6.3 | Results and Discussion | 108 |
| 6.4 | Conclusions | 117 |
| 7 | Conclusions and Outlook | 121 |
| A | Appendix 1 | 129 |
| A.1 | Description of the force fields. | 129 |
| A.1.1 | Functional forms | 130 |
| A.1.2 | Parameter sets. | 133 |
| A.1.3 | Additional details | 139 |
| A.2 | Force field implementation | 141 |
| A.2.1 | Potential functions | 141 |
| A.2.2 | Simulation code congruency verification | 142 |
| A.3 | Additional results: temperature and pressure dependence of the unit cell | 144 |
| B | Appendix 2 | 147 |
| B.0.1 | Atom nomenclature and force field parameters | 147 |
| B.0.2 | Alternative reference set comparison | 149 |
| B.0.3 | Amorphization pressure with respect to number of linker vacancies | 150 |
| B.0.4 | Results data tables | 150 |
| C | Appendix 3 | 159 |
| C.1 | Framework force fields and structures | 159 |
| C.2 | Water loading on the pristine structure | 162 |
| C.3 | Water loading on the defected structures | 166 |

| | | |
|----------|--|------------|
| C.4 | Framework collapse | 172 |
| D | Appendix 4 | 173 |
| D.1 | GAFF/UFF and All UFF parametrizations | 173 |
| D.1.1 | Radial Distribution Functions | 173 |
| D.1.2 | Framework Volume Changes | 175 |
| D.1.3 | Amorphization Pressure as a Function of Fractional Loading | 180 |
| | Summary | 185 |
| | Curriculum Vitae | 187 |
| | List of Publications | 188 |
| | List of Presentations | 189 |
| | Acknowledgements | 190 |
| | Bibliography | 193 |

List of Symbols

| | |
|-------------------------|--|
| a, b, c | Lattice parameters |
| C_{ij} | Elastic constants in Voigt notation |
| $C_{\alpha\beta\mu\nu}$ | Full elastic stiffness tensor components |
| E | Young's modulus |
| $E(u)$ | Young's modulus in direction u |
| f_s | Total force of the system |
| f_i | Force acting on particle i |
| F | Deformation gradient |
| G | Shear modulus |
| G' | Tetragonal shear modulus |
| h | Transformation matrix |
| \mathcal{H}_{ij} | Hessian matrix |
| \mathcal{H}_g | Generalized Hessian matrix |
| H | Classical Hamiltonian |
| \mathcal{L} | Classical Lagrangian |
| k_B | Boltzmann constant |
| m_i | Mass of particle i |
| n_d | Number of degrees of freedom |
| N | Number of particles |
| p_i | Generalized momenta of particle i |
| p | Pressure |
| P | Isotropic pressure |
| q_i | Generalized position of particle i |
| q_i | Atomic charge of particle i |
| r_i | Cartesian position of particle i |
| S_{BET} | BET surface area |
| S_{ij} | Elastic compliance in Voigt notation |

| | |
|-----------------------------|---|
| t | Time |
| T | Temperature |
| u_{ij} | Pair interaction potential |
| U | Internal energy |
| v_i | Velocity of particle i |
| V | Unit cell volume |
| β | Inverse temperature |
| δ_{ij} | Kronecker delta |
| Δt | Time-step in MD-simulation |
| ε_i | Lagrangian strain |
| $\varepsilon_{\alpha\beta}$ | Strain tensor components |
| ε | Strain vector in Voigt notation |
| λ | Order parameter |
| λ_i | Eigenvalue of elastic tensor |
| μ | Chemical potential |
| ν | Poisson's ratio |
| \mathbf{C} | Elastic stiffness tensor |
| \mathcal{C} | Elastic stiffness tensor (0K definition) |
| ε | Strain tensor |
| σ | Stress tensor |
| $\sigma_{\alpha\beta}$ | Cauchy stress tensor components |
| \mathbf{h} | Transformation matrix for simulation cell |
| \mathbf{r}_i | Position vector of particle i |
| \mathbf{v}_i | Velocity vector of particle i |
| \mathbf{s}_i | Fractional coordinates of particle i |
| $\langle P \rangle$ | Ensemble-averaged pressure |
| P_{am} | Amorphization pressure |
| V_r | Relaxed cell volume |

| | |
|---------------------|--|
| V_t | Threshold volume for amorphization |
| ΔP | Pressure increment/decrement step in iterative simulations |
| \mathbf{u} | Directional unit vector |
| $\beta(\mathbf{u})$ | Linear compressibility modulus in direction \mathbf{u} |
| X_{VRH} | Voigt-Reuss-Hill average of modulus |
| \mathcal{H} | Generalized Hessian |
| σ_{ij} | Lennard-Jones effective size parameter |
| ε_{ij} | Lennard-Jones energy parameter |

1

INTRODUCTION

Metal-organic frameworks (MOFs), also known as porous coordination polymers, are a novel class of hybrid materials that have garnered significant attention over the past few decades. These materials possess a crystalline structure formed through the coordination of inorganic building units with organic ligands. This structure can be precisely tuned in terms of chemical composition, pore size, and the shape and type of cavities. The unique and well-defined crystalline structure of each MOF is crucial for its specific properties and applications, necessitating the preservation of its porous framework during use. Stability is a key requirement for the practical application of MOFs and is dependent on several parameters, including environmental conditions such as exposure to organic solvents, water, corrosive media, high temperature, and/or pressure, the concentration of these conditions, and the duration of exposure. Understanding and enhancing the stability of MOFs is crucial for their successful application in various fields. This chapter provides a comprehensive overview of the MOFs of study, emphasizing their properties, stability, and potential applications.

1.1 METAL-ORGANIC FRAMEWORKS AND STABILITY

Metal-organic frameworks (MOFs), also known as porous coordination polymers (PCPs), are a newer class of hybrid materials that have gained significant interest over the last few decades[1–3]. These materials have a crystalline structure formed by the coordination of inorganic building units with organic ligands. This structure can be finely tuned in terms of chemical composition (metal cations, organic linkers), pore size (micro- or mesoporous), and the shape and type of cavities (such as cages or channels in various geometries like triangular, square, or hexagonal)[4–6]. Because of their versatile and adjustable properties, MOFs are now seen as highly promising for many applications including gas storage and separation[7–10], biomedicine[11], sensing, and catalysis[12–15](Fig 1.1).

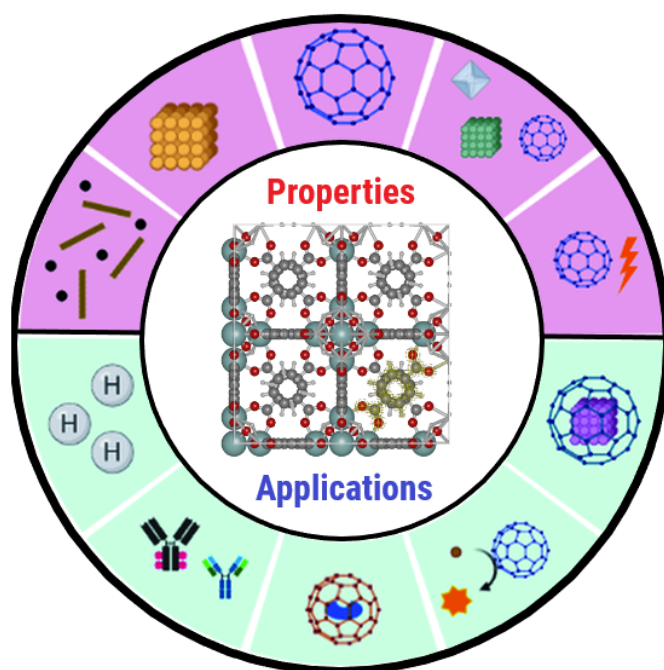


Figure 1.1: Pictorial representation of the general properties and potential applications of metal-organic frameworks. Based on Yusuf et al.[5]

The unique and well-defined crystalline structure (Fig 1.2) of each MOF is crucial

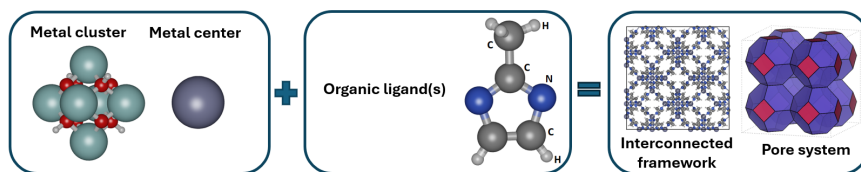


Figure 1.2: Metal-organic frameworks are composed of metal ions or clusters linked together by organic ligands. They form structured interconnected frameworks with well-defined pores and channels. Their chemical diversity can be significantly varied by altering: the type of ligands, the metal centers or clusters, and the topology.

for its specific properties and applications. Therefore, maintaining the integrity of its porous framework during use is essential. Stability is one of the key requirements for practical applications of MOFs. ‘Stability’ in the context of MOFs is not an absolute term but depends on a set of parameters related to the intended application. These parameters include the environmental conditions the MOF will be exposed to (like organic solvents, water, corrosive media, high temperature, and/or pressure), the concentration of these conditions, and the duration of exposure[16, 17]. Based on these factors, MOF stability can be categorized into three main types: (i) chemical stability, (ii) thermal stability, and (iii) mechanical stability[18]. Stability in a MOF means its resistance to structural degradation under operating conditions. Notably, thermal stability is often linked to chemical stability because heating can change the chemical structure of MOFs by triggering or speeding up chemical reactions that degrade the crystalline framework[19, 20]. This usually affects the metal cation’s coordination environment by breaking the bonds between the organic ligand and the inorganic part[21, 22] (like hydrolysis or redox reactions), or sometimes, it affects the organic linker itself[23] (like decarboxylation or alkyne oxidation).

For a given application, an MOF needs to possess one or more types of stability. For instance, chemical stability is essential for applications in aqueous environments and varying pH levels, such as molecular separation or drug delivery. Both chemical and thermal stabilities are crucial for catalytic processes under harsh conditions, like those in chemical feedstock and fuel production[19, 24]. Mechanical stability

is important when shaping MOFs into forms like pellets required for industrial processes. Initially, research on MOFs focused on creating frameworks with the highest surface area and largest pore volume. Recently, however, significant efforts have been directed towards designing highly stable structures that can be used under ambient conditions as well as in harsh and corrosive environments.

Understanding the stress responses of MOFs is critical for their successful commercialization. With reliable synthesis methods and well-characterized crystal structures for thousands of MOF materials, researchers are well-equipped to explore the structure-property relationships that govern how different MOFs react to various mechanical stresses. The compression of porous materials is an interesting subject, as the void spaces within these structures exhibit surprising behaviors under high pressure. Early research in this field focused on zeolites under such conditions. Despite the significant differences between zeolites and MOFs, these initial studies provide valuable insights into the mechanical responses of MOFs[25, 26]. However, due to the presence of organic linkers in MOFs, conclusions drawn from zeolite studies cannot be directly applied to these hybrid materials. Similarly, while advances in understanding MOF mechanics will benefit the study of other porous materials (e.g., covalent organic frameworks), each class requires dedicated investigation.

MOFs' extensive structural diversity offers an almost limitless array of species to study, but this also means it's impractical to measure every property for every framework. Thus, it's crucial to focus on structure-property relationships that allow for faster and more intuitive material evaluations. These relationships can only be established through meticulous studies that systematically vary one structural feature at a time. However, experimental data can be complicated by minor variations between MOFs due to batch-to-batch inconsistencies (such as defect density, porosity, and guest loading). Moreover, many experiments depend on sophisticated techniques like diamond anvil cell (DAC) environments and synchrotron radiation, which limit the availability of experimental data[27, 28]. Fortunately, computational simulations are powerful tools for examining MOF mechanical properties and have been extensively

used in both standalone and combined studies[29, 30]. These two complementary methods are essential for thoroughly analyzing the mechanical properties of MOFs.

1.2 ZEOLITIC IMIDAZOLATE FRAMEWORKS

Zeolitic imidazolate frameworks (ZIFs) are a unique subclass of metal-organic frameworks (MOFs) [31–34], characterized by tetrahedrally coordinated metal cations linked by imidazolate organic ligands. This distinctive architecture results in porous crystalline solids that resemble the structure of zeolites, offering high chemical and thermal stability while maintaining the tunability typical of MOFs [35, 36]. Among the various ZIFs, ZIF-8 stands out as a prototypical framework due to its ease of synthesis, low-cost starting materials, and remarkable chemical robustness [36]. ZIF-8 is composed of zinc ions coordinated to 2-methylimidazolate linkers and exhibits a sodalite (SOD) topology featuring large spherical cavities (11.5 Å in diameter) connected by 4-ring and 6-ring windows (Figure 3.1) [37–39]. These structural attributes have driven extensive research into ZIF-8 for applications such as gas storage, separation, and catalysis.

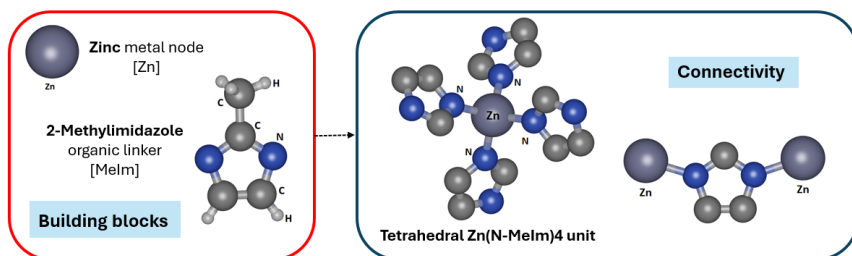


Figure 1.3: Building blocks and connectivity of the prototypical ZIF-8.

Like many other MOFs, ZIF-8 exhibits a high degree of structural flexibility. This flexibility manifests as changes in cell size, pore geometry, and framework topology in response to external stimuli, including pressure, temperature, and adsorbate loading [40–46]. One prominent example of this flexibility is the "swing effect" [47, 48], where the adsorption of gas molecules induces expansion of the pore-connecting

windows from approximately 3.4 Å to 4.2 Å [49]. This dynamic behavior enables the passage of gas molecules with kinetic diameters larger than the unperturbed window size, such as methane (CH_4), nitrogen (N_2), and propane (C_3H_8) [50–53]. However, this flexibility also makes ZIF-8 highly sensitive to compression, resulting in mechanical instability and phase transitions under high-pressure conditions commonly encountered in industrial applications [54, 55].

The remarkable structural properties of ZIFs, coupled with their responsive behavior under external stimuli, highlight the importance of understanding their mechanical and adsorption characteristics at an atomistic level. Molecular simulations have proven to be an invaluable tool for studying these properties, offering insights that are often challenging to obtain experimentally. For example, Ortiz et al. [56] investigated the mechanical response of ZIF-8 under hydrostatic pressure and demonstrated a rapid decrease in the elastic constant corresponding to the shear modulus (C_{44}) as the pressure approached 0.4 GPa, leading to framework amorphization. This phenomenon, known as shear-mode softening, was later confirmed experimentally through ball-milling studies [57, 58]. Additionally, Brillouin scattering experiments by Tan et al. [59] revealed that ZIF-8 exhibits one of the lowest shear moduli among single-crystalline extended solids under atmospheric conditions, further linking its deformation mechanism to the pliancy of the ZnN_4 tetrahedra.

Molecular simulations also facilitate the development and evaluation of force fields used to model the structural, mechanical, and adsorption properties of ZIFs. Classical flexible force fields (FFs), such as those based on the Generalized AMBER Force Field (GAFF) [60] and Universal Force Field (UFF) [61], have been extensively employed to study ZIF-8 [62–66]. These force fields have enabled predictions of properties such as gas adsorption capacities and diffusion coefficients, which are critical for practical applications. However, challenges remain in accurately describing the interactions between the framework's organic and inorganic components. For instance, early force fields often relied on *ad hoc* parameter adjustments to reproduce experimental observables, leading to variability in predictions across

different studies [67].

Recent advancements in force field development have sought to address these limitations by incorporating quantum-mechanical insights. For example, the MOF-FF framework introduced by R. Schmid and colleagues [68] captures the subtle swing effect in ZIF-8, enabling accurate predictions of both structural and dynamical properties. Despite these improvements, systematic comparisons of classical force fields for predicting mechanical properties remain sparse. Notably, Maul et al. [69] employed quantum-mechanical calculations to reveal anisotropic responses in ZIF-8's elastic constants under pressure, findings that were not replicated by earlier force fields such as those developed by Zhang [64].

1.3 ZR-BASED MOFs

Metal-organic frameworks (MOFs) have been a focal point of materials science research due to their versatile structures and extensive applications in catalysis, drug delivery, and gas storage and separation [34, 70–73]. Among these, Zr-based MOFs stand out for their remarkable chemical and thermal stability, which is largely attributed to the unique properties of hexanuclear Zr-based nodes. First introduced in 2008 by Cavka et al. [74], these Zr_6 building blocks have revolutionized MOF design, providing a robust foundation for frameworks capable of withstanding harsh conditions, such as high temperatures and moisture, which typically degrade other MOFs [75–78].

The prototypical Zr-based MOF, UiO-66, exemplifies this class of materials. Its structure consists of $Zr_6O_4(OH)_4$ clusters linked by 1,4-benzenedicarboxylic acid (BDC) ligands, forming a highly connected framework with tetrahedral and octahedral cages (Figure 1.4). The 12-fold connectivity of its Zr nodes endows UiO-66 with exceptional stability, both mechanically and chemically, distinguishing it from other MOFs such as ZIF-8 and MOF-5, which have lower coordination numbers [79]. These characteristics have made UiO-66 a benchmark material for

studying MOF behavior under various conditions.

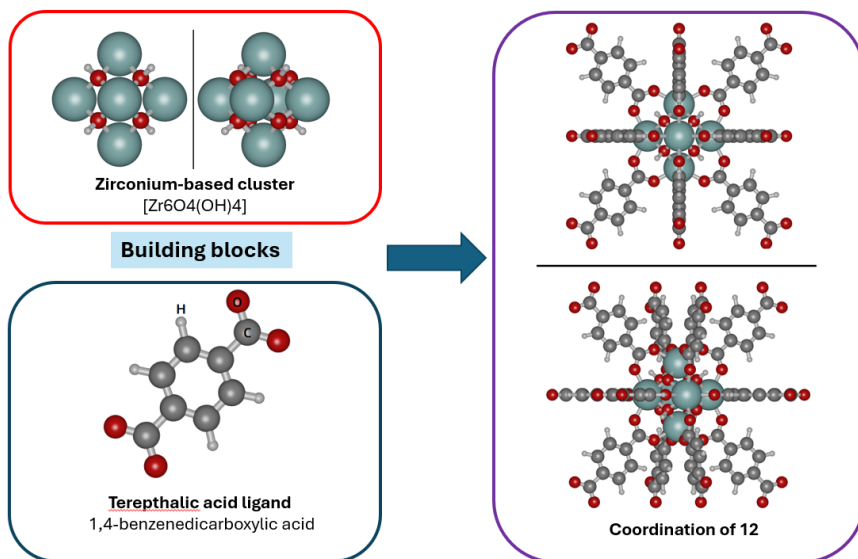


Figure 1.4: Building blocks and connectivity of the prototypical Zr-based MOF, UiO-66.

UiO-66's mechanical robustness has been extensively investigated. Early studies highlighted its resistance to deformation and pore collapse during pelletization, outperforming other MOFs in maintaining porosity under stress. Computational studies by Coudert and colleagues explored the impact of defect sites, such as missing linkers or nodes, on its structural properties. While defects enhance surface area and porosity, they also compromise the framework's mechanical stability, as reflected in reduced bulk and shear moduli [80]. These findings align with experimental observations by Dissegna et al. [81], who measured the effects of defect density on the bulk modulus of UiO-66 using precise pressure control in water-filled cells. Their results demonstrated a general decrease in bulk modulus with increasing defect density, except at very high defect concentrations, where unexpected trends suggest the need for further investigation.

In addition to defects, external stimuli such as mechanical pressure and chemical adsorption significantly influence UiO-66's stability. For example, spectroscopic

studies by Suslick et al. [82] revealed that Zr-carboxylate bonds in UiO-66 are susceptible to breakage at elevated pressures, leading to framework amorphization above 1.9 GPa. This property underscores UiO-66's potential as a mechanical shock absorber, as it stores energy upon compression. Similarly, post-synthetic modifications, such as linker substitution, have been shown to tune the framework's elastic properties. Sun et al. [83] employed atomic force microscopy to demonstrate how functionalized linkers alter UiO-66's elastic moduli, highlighting the material's adaptability for specific applications.

Molecular simulations have played a pivotal role in advancing our understanding of UiO-66's structural and adsorption properties. These simulations offer insights into the relationships between framework architecture and material performance, particularly under conditions that are challenging to replicate experimentally. For instance, computational studies have extensively examined the water and CO₂ adsorption properties of both pristine and defected UiO-66, revealing how defects influence adsorption behavior and stability [84–88]. By modeling the framework as either rigid or flexible, simulations have provided critical guidance for optimizing UiO-66 in industrial applications such as water harvesting and gas separation.

One of the most compelling features of UiO-66 is its water stability, a property rarely observed in other MOFs. The robustness of its Zr-O bonds and unique geometric arrangement minimize hydrolysis reactions, ensuring structural integrity even under moist conditions [89–91]. This stability, combined with its tunable porosity and functionalizability, makes UiO-66 an excellent candidate for water treatment applications. Functionalized derivatives further expand its utility by enabling the control of hydrophobicity and adsorption behavior, tailoring the framework to specific industrial needs [92, 93].

Despite these advantages, the presence of defects introduces a trade-off between enhanced porosity and reduced mechanical integrity. Computational techniques are invaluable in navigating this balance, enabling precise analysis of defect-induced changes at the molecular level. For example, studies using molecular dynamics and

Monte Carlo simulations have shed light on how missing linkers affect UiO-66's adsorption properties and stability, providing a framework for designing defect-engineered MOFs [94, 95].

1.4 COMPUTATIONAL MODELING

Multiscale modeling is an essential approach in the study of nanoporous systems, bridging the gap between different length and time scales to provide a comprehensive understanding of material behavior. In the context of metal-organic frameworks (MOFs) and other nanoporous materials, multiscale modeling integrates various computational techniques to simulate processes from the atomic to the macroscopic level. This holistic approach is crucial because the properties and functions of these materials are governed by phenomena occurring across multiple scales. For instance, while quantum mechanical methods can accurately describe electronic structures and bond formation at the atomic scale, molecular dynamics (MD) simulations are necessary to explore larger systems over longer timescales, capturing the dynamics and interactions of thousands to millions of atoms.

Molecular dynamics simulations offer several advantages in the study of nanoporous systems. They allow for the detailed investigation of atomic and molecular motion, which is critical for understanding diffusion, adsorption, and mechanical behavior in MOFs. MD simulations can capture the flexibility and responsiveness of frameworks to external stimuli such as pressure, temperature, and guest molecule interactions. This is particularly important for MOFs, which are known for their structural adaptability and tunable properties. The ability to simulate systems over nanoseconds to microseconds and beyond enables researchers to observe real-time phenomena that are otherwise challenging to capture experimentally. Furthermore, MD can handle systems ranging from a few nanometers to several micrometers, making it possible to study both local interactions and bulk properties.

The use of MD in multiscale modeling thus facilitates the prediction of ma-

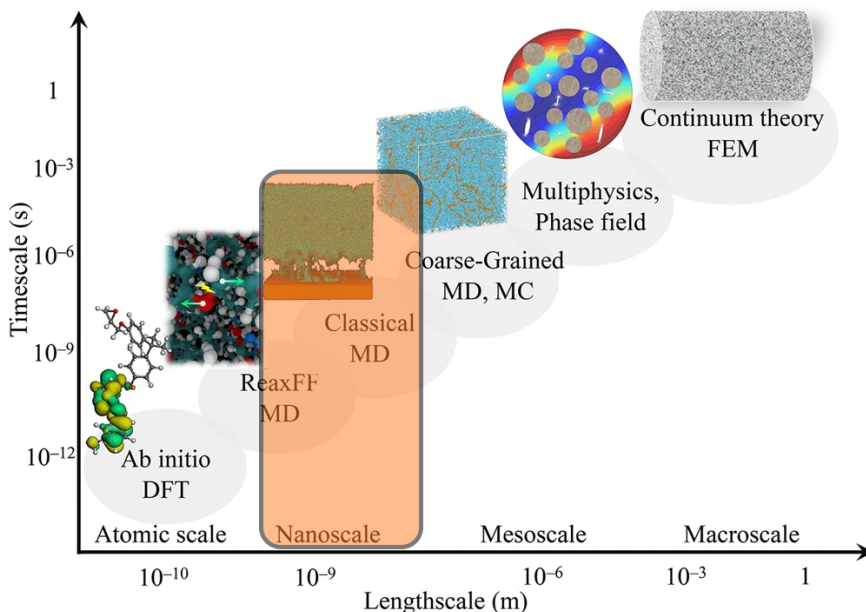


Figure 1.5: Length vs time scales in multiscale modeling. In this thesis, molecular mechanics simulations are performed to study nano-scale systems

terial behavior under various conditions, guiding the design and optimization of nanoporous materials for specific applications. For example, understanding how a MOF structure deforms under mechanical stress can inform its potential use in sensors or as a component in flexible electronics. Similarly, insights into the diffusion pathways and adsorption sites of guest molecules can enhance the efficiency of MOFs in gas storage and separation technologies. Overall, molecular dynamics serves as a powerful tool within the multiscale modeling framework, enabling the exploration and optimization of nanoporous materials with unprecedented detail and accuracy.

1.5 OUTLINE OF THIS THESIS

The primary objective of this thesis is to leverage molecular modeling tools to investigate the structural and mechanical properties and determine the limits of stability of metal-organic frameworks (MOFs), with a focus on the two most canonical Zr and Zn based MOFs, UiO-66 and ZIF-8. By employing computational methods, the research aims to enhance our understanding of how these materials behave under various conditions, including their responses to temperature changes, high pressures, and the presence of defects or adsorbates.

Chapter 3 focuses on the mechanical stability of the prototypical ZIF-8. While studies on MOF stability are limited, significant experimental work has highlighted the crucial role of elastic constants in maintaining the structural integrity of ZIF-8, with its stability closely tied to the flexibility of ZnN₄ tetrahedra. The chapter reviews various classical flexible force fields used in simulations to investigate MOF properties, comparing their ability to predict realistic structural and mechanical behaviors. The comparison of these force fields against existing density functional theory (DFT) calculations reveals that different force fields yield varying results under identical conditions, providing insights into how fundamental elastic properties are influenced by force field parametrization.

Chapter 4 explores the impact of linker vacancy distribution on the stability of defected UiO-66 structures. To enable the analysis of a large number of configurations, we made a deliberate tradeoff by not fully modeling the framework's electrostatic interactions in the energy equation. While this approach limits the quantitative accuracy of the results, it provides a meaningful way to assess the relative instability associated with different defect distributions. We find that higher numbers of vacancies generally lead to reduced stability, although the distribution and orientation of these vacancies significantly influence amorphization. Structures with more uniformly distributed vacancies show a positive correlation between amorphization pressure and bulk modulus, while those with clustered vacancies or

large intact portions of the framework exhibit anomalous behavior. Elastic moduli anisotropies are analyzed to examine how the distribution of linker vacancies affects the directional instability of the structures.

Chapter 5 investigates the effects of water loading on the structural and mechanical properties of the pristine and a limited number of defected UiO-66 frameworks. The study compares two methods for modeling non-bonded interactions between the framework and water: direct Lorentz-Berthelot mixing and hybrid mixing. Through molecular dynamics simulations, the research assesses water molecule arrangement, interaction with framework sites, and their impact under various conditions, such as high hydrostatic pressure, and increase water loading.

Chapter 6 expands on the previous chapter by studying the influence of diverse adsorbates, including methane, methanol, water, dimethylformamide (DMF), and chloroform, on the structural stability of UiO-66. Through molecular dynamics simulations, the study evaluates the interplay of adsorbate properties—such as polarity, molecular size, and hydrogen-bonding capacity—and their impact on framework amorphization pressure and atmospheric structural changes.

2

METHODOLOGY

This chapter outlines the methodology for studying flexible atomistic frameworks, focusing on force fields, energy minimization, molecular dynamics, and the calculation of elastic properties of crystals via molecular simulations. It begins with an overview of molecular mechanics (MM) methods. It then discusses energy minimization techniques and molecular dynamics simulations, detailing methods for optimizing system configurations and simulating particle dynamics. Additionally, the chapter covers approaches for calculating elastic properties, including methods for determining the stiffness tensor using molecular modeling. It concludes with a discussion on assessing the mechanical stability of Metal-Organic Frameworks (MOFs), highlighting theoretical methods for evaluating material stability and flexibility. This methodology provides a foundation for analyzing and characterizing the stability and mechanical properties of MOFs in the following chapters.

In theory, all molecular structures and interactions can be predicted from first principles using quantum mechanics. However, the computational demands of quantum mechanical calculations make it impractical for many systems. Consequently, simplifications are necessary for studying the structure and dynamics of molecular systems[96]. Molecular mechanics (MM) methods simplify calculations by ignoring the electronic degrees of freedom and focusing solely on the motions of the nuclei[96, 97]. The fundamental assumption behind all MM methods is the Born-Oppenheimer approximation, which separates nuclear and electronic motions (occurring on different time scales) and allows the system's energy to be expressed as a function of nuclear coordinates alone[98–102]. Additionally, MM force fields rely on two key assumptions: additivity and transferability. Additivity implies that the total potential energy of the system can be expressed as a sum of different potential energy terms, each with a clear physical meaning (such as bond deformations, electrostatic interactions, and dispersion forces). Transferability suggests that potential energy functions developed for a small set of molecules can be applied to a broader range of molecules with similar chemical groups[97, 103, 104]. The accuracy of MM force fields depends on the validity of these assumptions.

2.1 FORCE FIELDS

Classical force fields typically include five primary terms with straightforward physical interpretations: bond stretching/compression, angle bending, dihedral (torsional) interactions, electrostatic interactions, and van der Waals interactions. More sophisticated force fields may include additional terms to account for atomic polarizability and complex coupling terms, such as cross-coupling between bonds and angles[105, 106].

A force field is defined by the equations used to model the potential energy and their associated parameters[105]. The Potential Energy Surface (PES) describes the energy of a molecular system as a function of atomic positions[26, 107]. The

classical molecular energy is often represented as a Taylor expansion in chemical entities like bonds, bends, and torsions[108, 109]:

$$U^{\text{total}} = U^{\text{intra}} + U^{\text{inter}} \quad (2.1)$$

The intra-molecular energy U^{intra} is given by:

$$\begin{aligned} U^{\text{intra}} = & \sum_{\text{bonds}} U_b(r) + \sum_{\text{bends}} U_\theta(\theta) + \sum_{\text{torsions}} U_\phi(\phi) + \sum_{\text{out-of-plane bends}} U_\chi(\chi) \\ & + \sum_{\text{bond-bond}} U_{bb'}(r, r') + \sum_{\text{bond-bend}} U_{b\theta'}(r, \theta) + \sum_{\text{bend-bend}} U_{\theta\theta'}(\theta, \theta') \\ & + \sum_{\text{bond-torsion}} U_{r\phi}(r, \phi, r') + \sum_{\text{bend-torsion}} U_{\theta\phi}(\theta, \phi, \theta') + \dots \end{aligned} \quad (2.2)$$

The inter-molecular energy U^{inter} is expressed as:

$$U^{\text{inter}} = \sum_{\text{non-bonded}} U_{nb}(r) \quad (2.3)$$

The non-bonded terms are most commonly represented using a combination of Lennard-Jones (LJ) and Coulombic pair potentials[105, 106, 110]:

$$U_{nb} = \sum_{i < j} 4\epsilon \left[\left(\frac{\sigma}{r} \right)^{12} - \left(\frac{\sigma}{r} \right)^6 \right] + \sum_{i < j} \frac{1}{4\pi\epsilon_0} \frac{q_i q_j}{r} \quad (2.4)$$

where the summation runs over pairs of atoms i and j , with charges q_i and q_j and inter-atomic distance r . The terms ϵ and σ are the Lennard-Jones strength and size parameters, respectively, and ϵ_0 is the permittivity of free space[111, 112].

It is crucial to acknowledge that molecular mechanics force fields are empirical. The decomposition of potential energy into terms with simple physical interpretations is an approximation, as there is no unique way to translate quantum mechanical effects into classical mechanics equations[102, 104, 105]. Consequently, there is no

single optimal set of functions and parameters. Different force fields may reproduce the same PES by summing contributions that vary significantly.

2

2.2 ENERGY MINIMIZATION

In energy minimization, the focus is on finding the ground state energy, which is the potential energy of the system at 0 K, ignoring kinetic energy. For a molecular system, its potential energy $U(R^N)$ depends on the position vectors R^N of its N atoms[113]. A common approach to finding the minimum of a function is through its derivatives[114].

For a single-variable function $f(x)$, the minimum value is found where $f'(x) = 0$ and $f''(x) > 0$. For a multi-variable function $f(x_1, x_2, \dots, x_n)$, this is similarly expressed as:

$$\frac{\partial f}{\partial x_i} = 0 \quad \text{and} \quad \frac{\partial^2 f}{\partial x_i^2} > 0, \quad i = 1, 2, \dots, n. \quad (2.5)$$

Thus, minimizing the energy of a system with N atoms involves finding a set of position vectors $R_{\min}^N = \{r_1^{\min}, r_2^{\min}, r_3^{\min}, \dots, r_N^{\min}\}$ that satisfy[113, 114]:

$$\left. \frac{\partial U(R^N)}{\partial r_{i,\alpha}} \right|_{R^N=R_{\min}^N} = 0, \quad \left. \frac{\partial^2 U(R^N)}{\partial r_{i,\alpha}^2} \right|_{R^N=R_{\min}^N} > 0 \quad (2.6)$$

$$i = 1, 2, 3, \dots, N; \quad \alpha = x, y, z.$$

where, $r_{i,\alpha}$ represents the component of r_i in the α -direction.

The derivatives can be calculated analytically or numerically, however analytical methods provide exact expressions but can be cumbersome for multi-variable functions[115, 116]. Therefore, numerical methods, such as the finite difference approach, are often used[105, 106, 117]. Two popular methods for energy minimization are the steepest descent method and the conjugate gradient method, both

utilizing the first-order derivative of $U(R^N)$. The general idea is to compute the initial potential energy $U(R^N)$, then iteratively adjust the atomic positions to reduce the energy. The steepest descent method moves atoms in the direction of the steepest energy decrease, while the conjugate gradient method optimizes the direction of movement to converge more quickly[118, 119].

After k iterations, the positions of the atoms are $R_{(k)}^N = \{r_1^{(k)}, r_2^{(k)}, \dots, r_N^{(k)}\}$. For the $(k+1)$ -th step, the potential energy $U(R^N + \Delta R^N)$ is expanded using the Taylor series:

$$U(R_{(k)}^N + \Delta R^N) = U(R_{(k)}^N) + \Delta R^N \cdot U'(R_{(k)}^N) + \frac{1}{2} \Delta R^N \cdot U''(R_{(k)}^N) \cdot (\Delta R^N)^T + \dots, \quad (2.7)$$

$$U'(R_{(k)}^N) = \left(\frac{\partial U(R^N)}{\partial r_1}, \frac{\partial U(R^N)}{\partial r_2}, \dots, \frac{\partial U(R^N)}{\partial r_N} \right) \Bigg|_{R^N=R_{(k)}^N}, \quad (2.8)$$

$$U''(R_{(k)}^N) = \begin{bmatrix} \frac{\partial^2 U(R^N)}{\partial r_1^2} & \frac{\partial^2 U(R^N)}{\partial r_1 \partial r_2} & \dots & \frac{\partial^2 U(R^N)}{\partial r_1 \partial r_N} \\ \frac{\partial^2 U(R^N)}{\partial r_2 \partial r_1} & \frac{\partial^2 U(R^N)}{\partial r_2^2} & \dots & \frac{\partial^2 U(R^N)}{\partial r_2 \partial r_N} \\ \dots & \dots & \dots & \dots \\ \frac{\partial^2 U(R^N)}{\partial r_N \partial r_1} & \frac{\partial^2 U(R^N)}{\partial r_N \partial r_2} & \dots & \frac{\partial^2 U(R^N)}{\partial r_N^2} \end{bmatrix} \Bigg|_{R^N=R_{(k)}^N} \quad (2.9)$$

Here, $U'(R_{(k)}^N)$ is the gradient (denoted as $g_{(k)}$) and $U''(R_{(k)}^N)$ is the Hessian matrix (denoted as $H_{(k)}$) of $U(R^N)$ at $R_{(k)}^N$. The term $(\Delta R^N)^T$ is the transpose of the displacement vector ΔR^N [113, 116, 117].

Various advanced optimization methods utilize the energy, first derivative, and second derivative of the Taylor-expanded potential function. Among these, the Newton-Raphson method incorporates both the first derivative and the Hessian matrix. Although this approach demands more memory and computational resources, it enhances reliability and accelerates convergence, reducing the number of steps required. Methods involving second derivatives also allow the first derivatives to

be minimized arbitrarily close to zero. The Newton-Raphson algorithm generally locates stationary points with a curvature matching the Hessian at the initial point, determined by the number of negative eigenvalues.

2

Eigenmode-following addresses the Newton-Raphson method's limitation by altering some eigenvalues' signs to achieve the desired curvature, ensuring the identification of the correct stationary points. Notably, eigenmode-following is the only method that guarantees finding a true (local) minimum. Other techniques necessitate verification to confirm whether the stationary point is indeed a minimum. For any system, Cartesian coordinates can be employed, and the energy potential, gradients, and Hessians are typically computed directly in these coordinates. Alternatively, (non)-redundant internal coordinates can be used. The second derivative matrix encompasses derivatives concerning the center of mass position, rotation elements, and strain. Analytical derivatives are preferred due to their accuracy and rapid computation.

2.3 MOLECULAR DYNAMICS

Molecular Dynamics (MD) simulations form the basis of computational approaches to studying the dynamic and thermodynamic properties of complex materials by numerically solving Newton's equations of motion for each particle in a system[96, 105, 106, 120, 121]. In MD, the forces f_i acting on each particle i are derived from the negative gradient of a pre-defined potential energy surface U , which captures the interactions between particles within the system. This is mathematically expressed as:

$$f_i = -\frac{\partial U}{\partial r_i} \quad (2.10)$$

where r_i denotes the Cartesian coordinates of the particle i . By calculating these forces, the MD simulation iteratively integrates the equations of motion, updating particle positions and velocities to generate a trajectory that reflects the system's

evolution over time. A widely used integration scheme for is the Verlet algorithm, known for its high accuracy and stability. This method computes positions and velocities using the following equations[105, 121, 122]:

$$r_i(t + \Delta t) = 2r_i(t) - r_i(t - \Delta t) + \frac{f_i(t)}{m_i} \Delta t^2, \quad (2.11)$$

$$v_i(t) = \frac{r_i(t + \Delta t) - r_i(t - \Delta t)}{2\Delta t}, \quad (2.12)$$

where t represents the time, Δt is the time step, r_i is the position of particle i , v_i is its velocity, and f_i is the force acting on it.

Choosing an appropriate time step Δt is crucial. The step must be small enough to accurately capture high-frequency motions, such as those in systems with stiff molecular bonds, while remaining large enough to ensure computational efficiency. Systems with stiff bonds typically require a smaller Δt to resolve rapid oscillations, whereas larger Δt values are more practical for simulations of rigid or semi-rigid molecules, striking a balance between precision and performance[106, 122, 123]. Maintaining stable long-term conservation of energy, momentum, and other conserved quantities is essential for the physical accuracy of simulations, especially when modeling systems over extended timescales.

MD simulations inherently simulate the NVE ensemble, conserving the number of particles N , volume V , and energy E throughout the simulation[105, 106]. This ensemble is particularly relevant for studying isolated systems where energy conservation is essential. However, MD simulations can be extended to simulate other thermodynamic ensembles by introducing thermostats and barostats, which regulate temperature and pressure, respectively[124, 125]. A thermostat maintains temperature to enable NVT (constant number of particles, volume, and temperature) ensemble simulations, while a barostat allows pressure control for the NPT ensemble (constant number of particles, pressure, and temperature). These en-

hancements provide versatile tools for simulating systems under a range of physical conditions, thereby expanding the applicability of MD across diverse material environments[126].

2

One key advantage of MD simulations over quantum mechanical (QM) methods lies in their ability to simulate larger systems and longer timescales. QM methods, while providing insights into electronic structure, are computationally intensive and typically restricted to small systems over short timescales. MD, in contrast, can handle systems with millions of particles, allowing for simulation times that reach into the nanosecond or microsecond range. MD also complements Monte Carlo (MC) simulations, which are commonly used to sample configurations within thermodynamic ensembles. While MC excels in equilibrium sampling, MD provides time-dependent trajectories of particles, making it uniquely valuable for calculating dynamic properties such as diffusion coefficients, viscosities, and other transport-related metrics. These dynamic properties, derivable from time correlation functions, are crucial for understanding molecular-level processes and material behavior under non-equilibrium conditions[105, 106, 121].

For crystalline solids, MD simulations typically employ a periodic simulation cell h , defined by three basis vectors a, b, c . The volume V of this simulation cell is given by the determinant of the matrix h :

$$V = \det[h] \quad (2.13)$$

The position r_i of a particle can be expressed in terms of fractional coordinates s_i , which allows representation within the periodic cell as[106]:

$$r_i = h \cdot \mathbf{s}_i = \begin{pmatrix} a_x & b_x & c_x \\ a_y & b_y & c_y \\ a_z & b_z & c_z \end{pmatrix} \cdot \mathbf{s}_i \quad (2.14)$$

where $0 \leq s_i \leq 1$.

To simulate systems under constant pressure while allowing for changes in both the size and shape of the simulation cell, the Parrinello-Rahman method extends traditional Molecular Dynamics by treating the simulation cell as a dynamic variable[124, 125, 127]. This approach is essential for studying phenomena like structural phase transitions, mechanical deformation, and material responses to stress.

In this method, the simulation cell is represented by the matrix h , which evolves dynamically alongside the atomic positions r_i [127, 128]. The system's behavior is governed by a Lagrangian that incorporates the kinetic energy of the particles, the cell's degrees of freedom, and the potential energy. The Lagrangian is written as:

$$\mathcal{L} = \sum_i \frac{1}{2} m_i \left(\frac{dr_i}{dt} \right)^2 + \frac{1}{2} W \sum_{\alpha, \beta} \left(\frac{\partial h_{\alpha\beta}}{\partial t} \right)^2 - U(\{r_i\}, h) \quad (2.15)$$

where m_i is the particle mass, W is a fictitious mass parameter controlling the cell's dynamics, and U is the potential energy, which depends on both particle positions and cell geometry. Here, $\frac{\partial h_{\alpha\beta}}{\partial t}$ represents the components of the time derivative of the simulation cell matrix. From this Lagrangian, equations of motion are derived for both the particles and the simulation cell[120, 129, 130]. The particles move according to:

$$m_i \frac{d^2 r_i}{dt^2} = - \frac{\partial U}{\partial r_i} \quad (2.16)$$

while the simulation cell evolves dynamically under the influence of internal and external stresses:

$$W \frac{\partial^2 h_{\alpha\beta}}{\partial t^2} = \sigma_{\alpha\beta} - P_{\text{ext}} \cdot V \cdot (h^{-1})_{\alpha\beta} \quad (2.17)$$

where $\sigma_{\alpha\beta}$ is the internal stress tensor, P_{ext} is the external pressure, and V is the cell volume[124, 128, 130].

The internal stress tensor σ includes contributions from interatomic forces and particle velocities[125, 130] and is calculated using the virial expression:

$$\sigma_{\alpha\beta} = \frac{1}{V} \left(\sum_i m_i v_{i,\alpha} v_{i,\beta} - \sum_{i<j} r_{ij,\alpha} f_{ij,\beta} \right) \quad (2.18)$$

where $v_{i,\alpha}$ is the α -component of the velocity of particle i , $r_{ij,\alpha}$ is the α -component of the vector between particles i and j , and $f_{ij,\beta}$ is the β -component of the force acting between them.

The Parrinello-Rahman method enables *NPT* ensemble simulations by dynamically adjusting the simulation cell to maintain constant pressure. This flexibility allows for the exploration of a wide range of material behaviors, including phase transitions (such as structure amorphization), stress-strain relationships, and thermal expansion under realistic conditions[105, 121, 126].

2.4 ELASTIC PROPERTIES OF MATERIALS

2.4.1 THE ELASTIC STIFFNESS TENSOR

The elastic stiffness tensor is defined in the regime of small deformations, where the relationship between deformation and stress is linear, as described by the generalized Hooke's law[106, 131, 132]:

$$\sigma_{\alpha\beta} = C_{\alpha\beta\mu\nu} \varepsilon_{\mu\nu} \quad (2.19)$$

where the implicit Einstein's summation convention is used, and α, β, μ, ν denote the Cartesian coordinates x, y and z . The strain tensor ε , the stress tensor σ , and the stiffness tensor \mathcal{C} , which is a fourth-rank tensor, are related[131–133]. The elements of the strain tensor indicate the change in length of an element when the body is deformed. For small deformations, the strain tensor elements are given by:

$$\varepsilon_{\alpha\beta} = \frac{1}{2} \left(\frac{\partial d_\alpha}{\partial r_\beta^0} + \frac{\partial d_\beta}{\partial r_\alpha^0} \right) \quad (2.20)$$

where $\mathbf{d} = \mathbf{r} - \mathbf{r}^0$ represents the displacement of point \mathbf{r} from its reference state \mathbf{r}^0 .

From the thermodynamics of deformation, the components of the stress tensor $\sigma_{\alpha\beta}$ are derived by differentiating the free energy with respect to the strain tensor components at constant temperature. In molecular simulations, the instantaneous stress tensor is typically computed using the virial theorem as the negative of the pressure tensor. The stress tensor is then taken as the ensemble average of this quantity[121, 121, 134].

It is established that ε and σ are symmetric tensors. The Voigt notation is often employed to represent symmetric tensors by reducing their order and simplifying notation. Pairs of indices $\alpha\beta$ are represented as single indices, with $xx = 1, yy = 2, zz = 3, yz = 4, xz = 5$, and $xy = 6$. Using this notation, ε and σ can be expressed as vectors with six components, and \mathcal{C} as a 6 by 6 matrix. The generalized Hooke's law is then written as[131, 135, 137]:

$$\sigma_i = C_{ij} \varepsilon_j \quad (2.21)$$

using the implicit sum convention with $j = 1$ to 6 and $\varepsilon_4 = 2\varepsilon_{yz}$, $\varepsilon_5 = 2\varepsilon_{xz}$, and $\varepsilon_6 = 2\varepsilon_{xy}$.

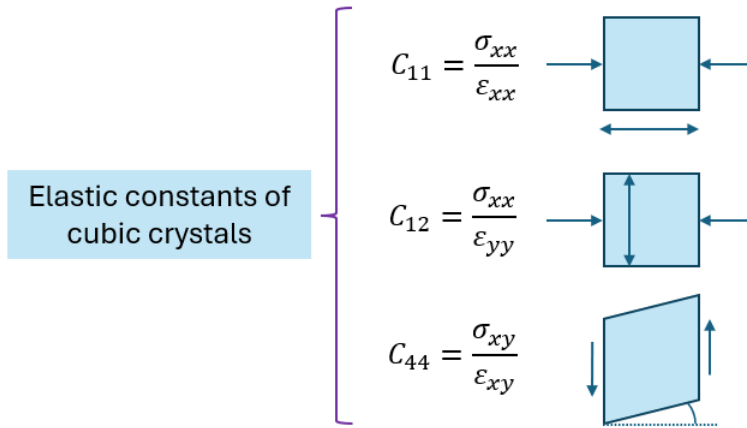


Figure 2.1: The elastic constants are the elements of the elastic stiffness tensor, which relates the stress applied to a system to the strain. The elastic stiffness tensor is a fourth-order tensor and for cubic crystals it simplifies due to symmetry considerations. C_{11} represents the response of a crystal to normal stress applied along one of its principal axes. C_{12} quantifies how stress applied in one direction affects the strain in a perpendicular direction. C_{44} pertains to the material's response to shear stress[135, 136].

2.4.2 DIRECT CELL-DEFORMATION TECHNIQUE

The calculation of elastic constants for a crystal using the cell deformation method is a process that relies on the relationship between stress, strain, and the resulting changes in energy. This method involves applying small deformations to the crystal lattice and calculating the energy variations that occur [134–136]. Initially, the equilibrium lattice parameters (\mathbf{a}_0 , \mathbf{b}_0 , \mathbf{c}_0) and atomic positions of the orthorhombic crystal are obtained through an initial energy minimization / cell relaxation run. From these parameters, the initial volume ($V_0 = [\mathbf{a}_0 \times \mathbf{b}_0] \cdot \mathbf{c}_0$) of the simulation cell is calculated.

The 3×3 symmetric strain tensor $\boldsymbol{\epsilon}$ is defined to represent the deformation of the crystal. For small strains, it can be expressed as[136, 137]:

$$\boldsymbol{\varepsilon} = \begin{pmatrix} \varepsilon_{xx} & \varepsilon_{xy} & \varepsilon_{xz} \\ \varepsilon_{xy} & \varepsilon_{yy} & \varepsilon_{yz} \\ \varepsilon_{xz} & \varepsilon_{yz} & \varepsilon_{zz} \end{pmatrix} \quad (2.22)$$

Deformations are applied to the unit cell by modifying the lattice vectors accordingly. For an orthorhombic crystal, these lattice vectors (\mathbf{a} , \mathbf{b} , \mathbf{c}) are orthogonal, and the deformation is applied by adjusting these vectors in line with the strain tensor [135, 136]. For each deformation, the system energy is recalculated. The energy of the deformed cell, $E(\boldsymbol{\varepsilon})$, is calculated for positive and negative strain. The elastic energy change (ΔE) due to strain is then determined as:

$$\Delta E(\boldsymbol{\varepsilon}) = E(\boldsymbol{\varepsilon}) - E_0 \quad (2.23)$$

where E_0 is the energy of the undeformed cell. For small deformations, $\Delta E(\boldsymbol{\varepsilon})$ can be expanded in a Taylor series, allowing the elastic energy per unit volume to be expressed as:

$$\frac{\Delta E(\boldsymbol{\varepsilon})}{V_0} = \frac{1}{2} \sum_{i,j} C_{ij} \varepsilon_i \varepsilon_j \quad (2.24)$$

where C_{ij} are the elastic constants.

Given the symmetry of an orthorhombic crystal, there are nine independent elastic constants: $C_{11}, C_{22}, C_{33}, C_{44}, C_{55}, C_{66}, C_{12}, C_{13}, C_{23}$ [105, 131, 138]. Specific strains are applied to isolate each constant. For instance, to determine C_{11} , a strain ε_{xx} is applied with all other strain components set to zero. Similarly, other appropriate strains are applied to find C_{22}, C_{33} , and so forth. For each applied strain, the calculated energy changes are fitted to the quadratic form of the elastic energy

expression to determine the corresponding elastic constants. For example, to extract C_{11} :

$$E(\epsilon_{xx}) \approx E_0 + \frac{1}{2}C_{11}\epsilon_{xx}^2 \quad (2.25)$$

The explicit deformation method utilizes the generalized Hooke's law and is applicable only in the elastic (linear) regime. This approach has been employed in the molecular simulation community for several decades and continues to be widely used[105, 120, 121, 123]. Essentially, various types of deformations are applied to the simulation box. After equilibration, a prolonged simulation is performed to obtain the equilibrium stress tensor under a small deformation. The complete set of C_{ij} elements can be derived from multiple deformations.

In this work, when employing this method, we used six different deformation types, referred to as elementary deformations because all elements of the strain tensor are zero except one[139]. This allows C_{ij} to be directly the proportionality coefficient between the stress element σ_i and the strain element ϵ_j . For each deformation type, we apply different magnitudes of deformation and determine C_{ij} from the slope of the corresponding stress-strain plot[131, 135, 136].

In the first deformation type, the box is elongated (or compressed) in the x direction by a relative amount ξ . This deformation results in a volume change. During this elongation, each point in the periodic cell is transformed as follows[131, 136]:

$$\begin{pmatrix} x \\ y \\ z \end{pmatrix} \rightarrow \begin{pmatrix} x(1 + \xi) \\ y \\ z \end{pmatrix} \quad (2.26)$$

where the strain component ϵ_1 is then given by[139]:

$$\varepsilon_1 = \varepsilon_{xx} = \frac{\partial}{\partial x}(x\xi) = \xi \quad (2.27)$$

and the strain tensor is $\varepsilon = (\varepsilon_1, 0, 0, 0, 0, 0)$. The second and third deformation types are elongations identical to the first one, but in the y and z directions, respectively.

The fourth deformation type is a shear strain. The orthorhombic box is deformed, at constant volume, into a monoclinic box by changing the angle α between the b and c box vectors by a relative quantity ξ , such that α becomes $\alpha(1 - \xi)$. During this shear, each point of the periodic cell is transformed as:

$$\begin{pmatrix} x \\ y \\ z \end{pmatrix} \rightarrow \begin{pmatrix} x \\ y + z \tan(\alpha\xi) \\ z \end{pmatrix} \quad (2.28)$$

where the strain component ε_4 is given by:

$$\varepsilon_4 = 2\varepsilon_{yz} = \frac{\partial}{\partial z}(z \tan(\alpha\xi)) = \tan(\alpha\xi) \quad (2.29)$$

and the strain tensor is $\varepsilon = (0, 0, 0, \varepsilon_4, 0, 0)$. The fifth and sixth deformation types are similar to the fourth one, but applied to the angles β and γ , respectively.

Finally, the expression used to compute the stress tensor in MD simulations is given by[134]:

$$\sigma_{\alpha\beta} = -\frac{1}{V} \left[\sum_{i=1}^N m_i v_{i,\alpha} v_{i,\beta} + \sum_{i=1}^N \sum_{j>i}^N \left(-\frac{\partial U(r)}{\partial r} \right)_{r=r_j} \frac{r_{\alpha,ij} r_{\beta,ij}}{r_{ij}} \right] \quad (2.30)$$

where N is the total number of particles in the system, V is the volume of the

simulation box, and $U(r)$ is the pair potential. m_i , \mathbf{r}_i , and \mathbf{v}_i represent the mass, position, and velocity of particle i , respectively. The vector \mathbf{r}_{ij} is defined as $\mathbf{r}_i - \mathbf{r}_j$.

2

2.4.3 STRAIN FLUCTUATION AT CONSTANT STRESS METHOD

In 1981, Parrinello and Rahman introduced an MD algorithm to sample the isostress-isoenthalpic ($N\sigma H$) ensemble[124]. They later demonstrated in 1982 that strain fluctuations in this ensemble can be linked to the adiabatic elastic stiffness tensor[128]. In 1985, Ray and Rahman provided an expression for the isothermal elastic stiffness tensor, which is applicable in the isothermal-isostress ($N\sigma'T$) or isothermal-isobaric (NpT) ensemble[140]:

$$C_{\alpha\beta\mu\nu} = \frac{k_B T}{\langle V \rangle} [\langle \epsilon_{\alpha\beta} \epsilon_{\mu\nu} \rangle - \langle \epsilon_{\alpha\beta} \rangle \langle \epsilon_{\mu\nu} \rangle]^{-1} \quad (2.31)$$

where T represents the temperature, and $\langle V \rangle$ is the average volume of the simulation box. This equation can be used in both MC and MD simulations. During MD simulations, specific equations of motion are necessary to maintain constant temperature and stress tensor values[141].

To calculate the strain tensor, we define the scaling matrix $\mathbf{h} = \{\mathbf{a}, \mathbf{b}, \mathcal{C}\}$, where $\mathbf{a}, \mathbf{b}, \mathcal{C}$ are the vectors that define the molecular simulation cell. The matrix \mathbf{h} describes the instantaneous size and shape of the simulation box, and the box volume is given by $V = \det(\mathbf{h})$. The strain tensor is computed as follows[131, 140]:

$$\epsilon = \frac{1}{2} [(\mathbf{h})^{-1, T} \mathbf{h}^T (\mathbf{h})^{-1} - \mathbf{I}] \quad (2.32)$$

where \mathbf{h} is the ensemble average of h (or equivalently the reference box), \mathbf{I} is the identity matrix, the superscript T denotes the transpose, and the superscript -1 denotes the inverse. During simulations, the norms of vectors \mathbf{a}, \mathbf{b} , and \mathcal{C} , along

with the three angles α (between \mathbf{b} and \mathcal{C}), β (between \mathbf{a} and \mathcal{C}), and γ (between \mathbf{a} and \mathbf{b}), are recorded to compute the strain tensor from the previous equation. The instantaneous scaling matrix is given by[140]:

$$\mathbf{h} = \begin{pmatrix} \|\mathbf{a}\| & \|\mathbf{b}\| \cos \gamma & \|\mathcal{C}\| \cos \beta \\ 0 & \|\mathbf{b}\| \sin \gamma & \frac{\mathbf{b} \cdot \mathcal{C} - b_x c_x}{b_y} \\ 0 & 0 & (\|\mathcal{C}\|^2 - c_x^2 - c_y^2)^{1/2} \end{pmatrix} \quad (2.33)$$

assuming \mathbf{a} lies along the positive x axis, \mathbf{b} lies in the xy plane with a strictly positive y component, and \mathcal{C} can have any orientation with a strictly positive z component.

2.4.4 STRESS FLUCTUATION AT CONSTANT VOLUME

Squire et al. derived a method for computing the isothermal elastic stiffness tensor in the canonical ensemble. The expression for the stress is given by[142]:

$$\sigma_{\alpha\beta} = \langle \sigma_{\alpha\beta}^B \rangle - \rho k_B T \delta_{\alpha\beta} \quad (2.34)$$

and the elastic stiffness tensor is given by:

$$C_{\alpha\beta\mu\nu} = \langle C_{\alpha\beta\mu\nu}^B \rangle - \frac{V}{k_B T} \left[\langle \sigma_{\alpha\beta}^B \sigma_{\mu\nu}^B \rangle - \langle \sigma_{\alpha\beta}^B \rangle \langle \sigma_{\mu\nu}^B \rangle \right] + \frac{N k_B T}{V} (\delta_{\alpha\mu} \delta_{\beta\nu} + \delta_{\alpha\nu} \delta_{\beta\mu}) \quad (2.35)$$

Here, $\sigma_{\alpha\beta}^B$ represents the Born contribution to the stress tensor:

$$\sigma_{\alpha\beta}^B = \frac{1}{V} \frac{\partial U}{\partial \varepsilon_{\alpha\beta}} \quad (2.36)$$

and $C_{\alpha\beta\mu\nu}^B$ denotes the Born contribution to the elastic stiffness tensor:

$$C_{\alpha\beta\mu\nu}^B = \frac{1}{V} \frac{\partial^2 U}{\partial \varepsilon_{\alpha\beta} \partial \varepsilon_{\mu\nu}} \quad (2.37)$$

In these equations, U is the potential energy of the system, T represents temperature, V is volume, N denotes the number of particles, k_B is the Boltzmann constant, and $\delta_{\alpha\beta}$ is the Kronecker delta. This method is known as the stress-fluctuation method due to the inclusion of the stress fluctuation term in the elastic stiffness tensor equation[143]. The Born stress tensor in Eq. 2.34 corresponds to the virial contribution to the microscopic stress tensor commonly utilized in molecular simulations[142]. The kinetic part of the microscopic stress tensor averages to the second term on the right-hand side of Eq. 2.34.

Since the Born stress term is typically calculated in most molecular simulation codes, the second term on the right-hand side of Eq. 2.36 can be efficiently computed during post-processing. However, the Born matrix is more challenging to determine and cannot be expressed using standard quantities[134, 141]. Various methods have been developed to compute the Born matrix, including the analytical derivative method and the numerical derivative method[134, 136].

The derivatives of the potential energy, used in the calculation, are determined during the simulation with the following formulas:

$$\frac{\partial U}{\partial \varepsilon_{\alpha\beta}} = \sum_{i=1}^N \sum_{j>i} \left(\frac{\partial u(r)}{\partial r} \right)_{r=r_{ij}} \frac{r_{ij,\alpha} r_{ij,\beta}}{\|r_{ij}\|} \quad (2.38)$$

$$\frac{\partial^2 U}{\partial \varepsilon_{\alpha\beta} \partial \varepsilon_{\mu\nu}} = \sum_{i=1}^N \sum_{j>i} \left(\frac{\partial^2 u(r)}{\partial r^2} \right)_{r=r_{ij}} \frac{r_{ij,\alpha} r_{ij,\beta} r_{ij,\mu} r_{ij,\nu}}{\|\mathbf{r}_{ij}\|^2} - \left(\frac{\partial u(r)}{\partial r} \right)_{r=r_{ij}} \frac{r_{ij,\alpha} r_{ij,\beta} r_{ij,\mu} r_{ij,\nu}}{\|\mathbf{r}_{ij}\|^3} \quad (2.39)$$

where $u(r)$ is the pair potential used in the simulation. The Born contributions $\sigma_{\alpha\beta}^B$ and $C_{\alpha\beta\mu\nu}^B$ are recorded throughout the simulation, allowing for the elastic stiffness tensor to be computed post-simulation.

2.5 THEORETICAL METHODS TO ASSES MECHANICAL STABILITY

The first approach in the theoretical investigation of MOF stability focuses on analyzing the effects of small-amplitude deformations on the crystalline phase stability, via comparison with the relaxed structure and guided by the foundational Born stability criteria[144], which provide a comprehensive set of necessary and sufficient conditions for mechanical stability. The second method aims to link the flexibility of a MOF to directional variations in its mechanical moduli. By examining the directional dependence of these moduli, it becomes possible to distinguish the degree of structural rigidity of a crystal at given conditions. For instance, highly flexible MOFs exhibit an anisotropy factors greater than 100, indicative of pronounced directional dependence, where the material's mechanical properties vary significantly along different axes. The third technique involves constructing a comprehensive pressure-versus-volume equation of state for the MOF of study via subsequent flexibleNPT simulations. The EOS provides essential information on mechanical stability by identifying volume points at which phase stability is lost, marking potential phase transitions.

2.5.1 BORN STABILITY CRITERIA

First stated by Born in his 1940 paper[144], the Born stability criteria form a set of necessary and sufficient criteria that determine whether a given unstressed material is stable. These stability criteria are obtained by requiring that the energy of the lattice increases for any infinitesimal strain $\boldsymbol{\varepsilon}$ imposed on the unit cell in its equilibrium volume V_0 . To second order, this energy is given by

$$E(\boldsymbol{\varepsilon}) = \frac{V_0}{2} \boldsymbol{\varepsilon}^T \mathcal{C} \boldsymbol{\varepsilon} + O(\boldsymbol{\varepsilon}^3) \quad (2.40)$$

These criteria therefore require the second-order elastic stiffness tensor \mathcal{C} to be positive-definite in equilibrium. In Voigt notation, this tensor is defined as:

$$C_{ij} = \frac{1}{V_0} \left. \frac{\partial^2 E}{\partial \varepsilon_i \partial \varepsilon_j} \right|_{V_0} \quad (2.41)$$

These thermodynamic criteria were later generalized to account for systems subject to an arbitrary external Cauchy stress $\boldsymbol{\sigma} = P\mathbf{1} + \boldsymbol{\sigma}_2$, where P is the isotropic pressure and $\boldsymbol{\sigma}_2$ is the deviatoric stress[136]. For a purely isotropic loading $\boldsymbol{\sigma} = P\mathbf{1}$, the unstressed second-order elastic stiffness tensor \mathcal{C} is replaced by its stressed analogue \mathbf{B} , given by:

$$B_{a\beta\gamma x} = C_{a\beta px} - P(\delta_{a\gamma}\delta_{\beta x} + \delta_{ax}\delta_{\beta\gamma} - \delta_{a\rho}\delta_{\gamma x}) \quad (2.42)$$

To confirm the stability of a material at a given temperature T and subject to a given pressure P , the positive-definiteness of the second-order stiffness tensor \mathbf{B} needs to be confirmed, for instance by verifying that all of its eigenvalues are positive or that all of its leading principal minors are positive (Sylvester's criterion)[136–138]. This procedure has to be repeated for a set of temperatures and/or pressures to determine the conditions for which one of the Born stability criteria is first violated.

For a general crystal system, the second-order elastic stiffness tensor \mathcal{C} consists of 21 independent elastic constants[145]. For more symmetric systems, \mathcal{C} becomes sparser, leading to a more comprehensive set of Born stability criteria. For instance, for the cubic crystal system, only three independent elastic constants exist, such that the stability under tensile and shear deformations can be separated. The positive-definiteness of \mathbf{B} under a hydrostatic pressure P leads to the following three Born stability criteria[145, 146]

$$\begin{aligned} C_{11} + 2C_{12} + P &> 0, \\ C_{11} - C_{12} - 2P &> 0, \\ C_{44} - P &> 0 \end{aligned} \tag{2.43}$$

These three criteria encompass an isotropic tensile deformation, a twofold-degenerate axial tensile deformation, and a threefold-degenerate shear deformation.

2.5.2 ANISOTROPY OF ELASTIC MODULI

A second approach for evaluating the mechanical stability of crystals was proposed in 2012 by the Coudert group, focusing on the anisotropy of the mechanical moduli of the material's structure. This method leverages the directional response of the crystal to external stresses, specifically examining the variation in stiffness and compressibility across different orientations within the material. The uniaxial stiffness of the crystal along any given direction u is described by Young's modulus $E(u)$, which quantifies the resistance to uniaxial deformation in that direction. Conversely, the deformation response to uniform, isostatic compression in the same direction is captured by the linear compressibility modulus $\beta(u)$, which indicates how much the material contracts or expands.

To determine the directional dependence of these mechanical moduli, the approach utilizes the fourth-order elastic stiffness tensor \mathcal{C} , also known as the compli-

ance tensor, which encapsulates the material's full elastic response. By applying a rotation that maps the x-axis onto the direction of the unit vector u , the directional properties of the moduli can be obtained from the inverse of \mathcal{C} . Specifically, Einstein notation is employed in the following expressions to calculate Young's modulus $E(u)$ and the linear compressibility modulus $\beta(u)$ along any arbitrary direction u :

$$E(u) = \frac{1}{u_p u_q u_r u_s [\mathcal{C}^{-1}]_{pqrs}}, \quad (2.44)$$

$$\beta(u) = u_p u_q [\mathcal{C}^{-1}]_{pqrr} \quad (2.45)$$

where the components u_x represent elements of the rotation matrix that align the original coordinate system with the direction u . These formulations allow for a comprehensive assessment of the directional mechanical behavior of the material by yielding values for $E(u)$ and $\beta(u)$ as functions of orientation.

The anisotropy in each property—stiffness and compressibility—can then be quantified by calculating the ratio of the maximum to minimum values of each modulus over all directions. These anisotropy factors provide insights into the material's flexibility or rigidity. Values of the anisotropy factor closer to unity indicate an isotropic, rigid material with similar properties in all directions, typical of highly structured frameworks. In contrast, large anisotropy factors indicate pronounced directional dependence, often seen in softer or more flexible materials, such as certain metal-organic frameworks (MOFs) or layered crystals, which can readily deform in specific orientations.

While these anisotropy values offer valuable insight into the structural flexibility of the crystal, they are generally only computed at a single set of thermodynamic conditions, such as a specific temperature and pressure. Consequently, this approach does not provide quantitative data on how stability and flexibility might vary with changing temperature or pressure, limiting its utility in predicting instability

thresholds under different environmental conditions.

2.5.3 ITERATIVE AND FIXED-VOLUME SCHEMES FOR DETERMINING AMORPHIZATION

Amorphization in flexible metal-organic frameworks (MOFs) occurs when an initially crystalline structure transforms into a disordered, amorphous state under external stress. This transition leads to the loss of long-range periodicity and critical material properties like porosity and mechanical integrity.

To estimate the pressure at which framework amorphization occurs (P_{am}), iterative molecular dynamics (MD) simulations in the flexible NPT ensemble ($N, P, \sigma_{\alpha} = 0, T$) can be employed. In this approach, the number of particles (N) is fixed, while internal pressure (P_i), deviatoric stress ($\sigma_{\alpha,i}$), and temperature (T_i) are dynamically controlled. The simulation cell is allowed to adjust its volume (V) and shape (h_0) in response to the external pressure pressure. The method involves running flexible NPT simulations at high pressure, monitoring the instantaneous volume (V_i) of the framework. A predefined volume threshold (V_t , significantly smaller than the initial framework volume) is set, below which the structure is considered to have collapsed. If V_i remains below V_t for a sustained period, amorphization is deemed to have occurred, and the next simulation is run at a lower pressure by reducing the pressure by ΔP . Conversely, if the structure does not collapse, the pressure is increased by ΔP . This iterative process continues until the structure no longer collapses, marking the approximate pressure at which the force field predicts amorphization (P_{am}).

However, the flexible NPT ensemble is prone to large fluctuations in instantaneous pressure, potentially inducing phase transitions at artificially low pressures, particularly for highly flexible MOFs. To mitigate this issue, larger simulation cells can be used or alternative methods must be applied.

An alternative approach proposed by the Van Speybroeck group[94, 147] employs the $N, V, \sigma_{\alpha} = 0, T$ ensemble, where the volume (V) is fixed, and the simulation cell shape fluctuates to maintain zero deviatoric stress ($\langle \sigma_{\alpha} \rangle = 0$)[147]. This en-

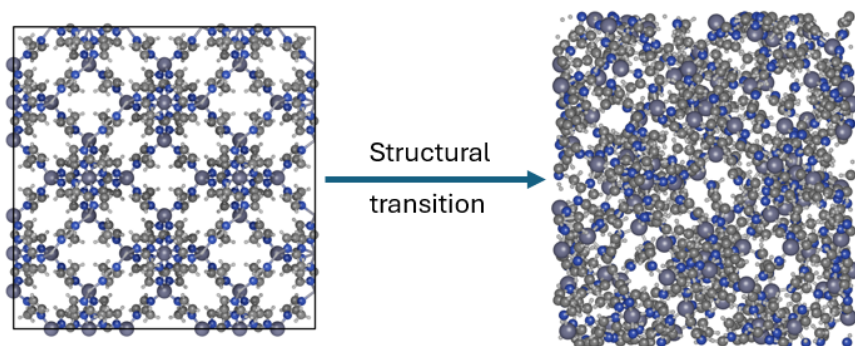


Figure 2.2: Pictorial representation of ZIF-8 simulation cell before and after amorphization due to external stress.

semble reduces internal pressure fluctuations, improving convergence and avoiding premature phase transitions. Molecular dynamics simulations are conducted at discrete volumes, allowing the construction of a pressure-volume equation of state ($P(V)$). The $P(V)$ profile provides macroscopic insights into the material's response under pressure and points where $\partial P/\partial V < 0$ indicate thermodynamically stable states, while local minima and maxima correspond to critical pressures beyond which metastable phases cease to exist. These transition pressures delineate stability limits and the conditions for phase transitions, offering a robust method to predict amorphization behavior and mechanical stability across a wide range of pressures.

3

3

EVALUATION OF ZIF-8 FLEXIBLE FORCE FIELDS

Metal-Organic Frameworks (MOFs) offer considerable potential for applications in adsorption due to their large pore volumes and surface areas. Studies on mechanical stability of MOFs are scarce. Seminal experimental work has shed a new light on the role that elastic constants play in establishing the structural stability of the prototypical ZIF-8 MOF, with its elastic deformation mechanism being linked to the pliant ZnN_4 tetrahedra[59]. Over the past decade, several classical flexible force fields have been proposed to study the physical properties of the system using simulations[62–66, 68, 149]. In this work, we evaluated the majority of them for reproducing structural and mechanical properties (unit cell sizes as a function of temperature and pressure, and elastic constants as a function of pressure), compared them to existing DFT calculations[59, 69] and found that they provide different results under the same testing conditions. The obtained results provide insight

Based on  E. Acuna-Yeomans, J.J. Gutierrez-Sevillano, S. Calero and D. Dubbeldam, *Evaluation of ZIF-8 flexible force fields for structural and mechanical properties*, *Microporous and Mesoporous Materials*, **2022**, 348, 1387-1811 [148].

into the relationship between fundamental elastic properties and the chosen force field parametrization, allowing us to characterize the applicability of each of the force fields. Furthermore, the employed two-code approach allowed us to find significant discrepancies in elastic constant values for the same force field between methodologies that employ different energy minimization algorithms, suggesting that eigenmode-following approaches might be needed to guarantee true minimum energy configurations for ZIFs.

3

3.1 INTRODUCTION

Zeolitic imidazolate frameworks (ZIFs) are a family of metal-organic frameworks (MOFs) [31–34] structurally characterized by tetrahedrally-coordinated metal cations connected via imidazolate organic linkers which assemble to form porous crystalline solids [35, 36]. ZIF-8, composed of Zn ions and 2-Methylimidazolate linkers [37], exhibits an SOD topology featuring large spherical cavities (~ 11.5 Å in diameter) connected by 4-ring and 6-ring windows [38, 39] (see Figure 3.1). ZIF-8 is one of the most studied MOFs owing to its ease of synthesis, low-cost raw starting materials, and remarkably high chemical and thermal stability [36]. Not unlike other MOFs, ZIF-8 is not rigid and presents different types of flexibility, that is, a modification of its cell size and shape and hence, the pore size and geometry of the framework, upon external stimuli such as mechanical pressure, molecule adsorption or temperature [40–46]. A prominent example of the impact of framework flexibility in ZIF-8 is the so-called “swing effect” [47, 48], in which the adsorption of molecules induces the expansion of the pore-connecting windows (from ~ 3.4 Å to ~ 4.2 Å) [49], allowing for movement of gas molecules that have larger kinetic diameters, such as CH_4 , N_2 , C_2H_6 and C_3H_8 [50–53]. The system has also been found to be highly sensible to compression, resulting in mechanical instability and subsequent phase changes [54, 55] at industrially available pressures.

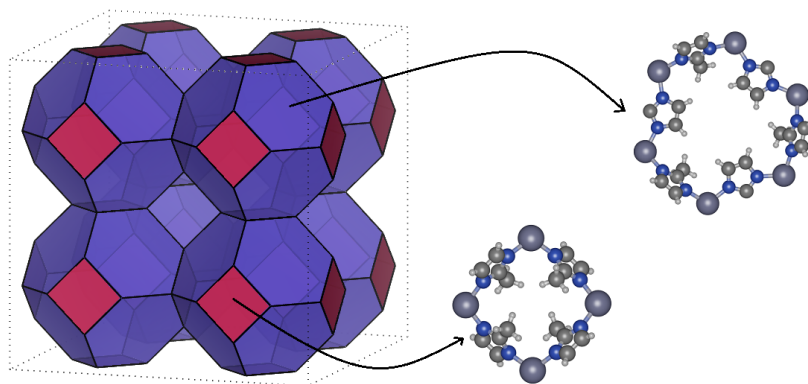


Figure 3.1: ZIF-8 SOD topology and pore-connecting windows.

In a previously published computational study, Ortiz et al.[56] monitored the mechanical properties of ZIF-8 as a function of hydrostatic pressure and found that the elastic constant corresponding to the shear modulus (C_{44}) rapidly drops as the pressure approaches ~ 0.4 GPa, resulting in the amorphization of the framework. The weak resistance against shear deformation (shear-mode softening) was later experimentally verified during ball-milling[57, 58]. Interestingly, ZIF-8 is one of the few MOFs for which the elastic constants have been experimentally measured, via Brillouin scattering[59]. It was found that the shear modulus of the crystal is remarkably low under atmospheric conditions (≤ 1 GPa), which is the lowest yet reported for a single-crystalline extended solid. Moreover, its elastic deformation mechanism was linked to the pliant ZnN_4 tetrahedra.

To properly exploit ZIF-8 for its proposed technical applications, it is essential to gain an atomistic understanding of the underlying mechanisms that control its flexible behaviour. For this, molecular simulations are a valuable tool. For computing structural, gas adsorption and gas diffusion properties, classical flexible force fields (FFs) have been developed to provide sufficiently good predictions[67]. However, the accurate description of the interactions between the organic and inorganic parts of the framework remains a challenge. Over the past decade a number of flexible force fields have been proposed for ZIF-8, the earliest of which [62–66]

make use the functional baseline provided by the generic GAFF[60] force field and combine UFF[61] and AMBER[60] parameters, modified in an *ad-hoc* manner, to reproduce experimental observables. In terms of results, these FFs mostly focus on the prediction of gas adsorption and diffusion properties and were initially validated by comparing structural properties, such as the lattice parameter of the unit cell at atmospheric conditions, with crystallographic data. In recent years, more sophisticated and complex *ab-initio* derived force fields have been proposed. In 2019, R. Schmid and colleagues[68] extended the MOF-FF methodology[150], which focuses on accuracy instead of transferability, and proposed a force field capable of reproducing the subtle swing-effect behaviour, as well as certain structural and dynamical properties of ZIF-8. In contrast, the one proposed by Weng and Schmidt [149] trades accuracy for transferability and is able to describe several of the ZIF-8 polymorphs. Systematic comparisons and evaluations of these force fields for the prediction of mechanical properties are lacking.

In a recent study, Maul et al.[69] investigated the mechanical response of ZIF-8 using quantum-mechanical calculations over a range of pressures and found that at $P > 0.2$ GPa an anisotropic response along $\langle 111 \rangle$ and $\langle 100 \rangle$ is observed, characterized by nonlinear behaviour of the C_{11} and C_{12} elastic constants. These results were contrasted to classical simulation data obtained by Ortiz et al.[56] using the Zhang[64] force field, which was unable to describe said behaviour. In general, we found that systematic comparisons and evaluations of classical force fields for the prediction of mechanical properties are lacking.

In this work, five published flexible force fields for ZIF-8 were implemented and validated in both the RASPA[151] and LAMMPS[152] simulation packages. Molecular dynamics simulations in the isothermal-isobaric ensemble were conducted to determine the temperature and pressure dependence of the framework lattice parameters, and the 0K elastic constants at different values of pressure were calculated using the eigenmode-following technique[153, 154], which are compared with existing experimental measurements and quantum-mechanical calculations.

The obtained results provide insight into the relationship between structural and elastic properties and the chosen parametrization, and suggest further adoption of “top-down” philosophies to the construction of future classical force fields would be beneficial to their accuracy in this respect. Our two-code approach led us to identify that the calculation of OK elastic constants is highly dependent on finding true (global) energy minimum configurations, and therefore the chosen minimization procedure is essential. We found that eigenmode-following fared best in this respect when compared to methodologies that rely on other minimization procedures, such as conjugate gradient and steepest descent.

3.2 METHODOLOGY

The term “force field” refers to the functional form and parameter sets of the energy equation. A force field consists of two parts:

1. An analytical expression for the inter-atomic potential energy $U(\mathbf{r})$ as a function of the atomic coordinates \mathbf{r} .
2. Definitions and parameters for “atom types”, classified based on bonding and environment. Parameters are assigned based on the atom types involved.

The Generalized AMBER Force Field (GAFF) energy equation is defined as [155]:

$$U = U_{\text{bonded}} + U_{\text{non-bonded}} \quad (3.1)$$

where

$$U_{\text{bonded}} = \sum_{\text{bonds}} \frac{1}{2} K_r (r - r_0)^2 + \sum_{\text{angles}} \frac{1}{2} K_\theta (\theta - \theta_0)^2 \quad (3.2)$$

$$+ \sum_{\text{dihedrals}} K_\phi [1 + \cos(m\phi - \phi_0)] + \sum_{\text{improper}} K_\xi [1 + \cos(m\xi - \xi_0)]$$

$$U_{\text{non-bonded}} = \sum_{i < j} 4\epsilon_{ij} \left[\left(\frac{\sigma_{ij}}{r_{ij}} \right)^{12} - \left(\frac{\sigma_{ij}}{r_{ij}} \right)^6 \right] + \sum_{i < j} \frac{q_i q_j}{4\pi\epsilon_0 r_{ij}} \quad (3.3)$$

The three main categories of classical simulation methodologies are Molecular Dynamics (MD), and Monte Carlo (MC), and Molecular Mechanics (MM). In a Molecular Dynamics (MD) simulation, all atoms move according to Newton's equations of motion and the forces computed on the atoms. The forces are given by the gradients of the potential energy with respect to the internal coordinates of the molecule.

The potential energy surface U of a periodic system can be Taylor-expanded around a configuration \mathbf{x} of the system

$$U(\mathbf{x} + \delta\mathbf{x}) = U(\mathbf{x}) + \mathbf{h}^T \delta\mathbf{x} + \frac{1}{2} \delta\mathbf{x}^T \mathcal{H} \delta\mathbf{x} + \dots \quad (3.4)$$

where $\mathbf{h} = \left(\frac{\partial U}{\partial x_i^\alpha} \right)$ is the gradient and $\mathcal{H} = \frac{\partial^2 U}{\partial x_i^\alpha \partial x_j^\beta}$ is usually referred to as the Hessian matrix. The superscript T denotes the transpose of a vector or matrix. The generalized Hessian, having dimensions $(3N + 6) \times (3N + 6)$ with N being the number of atoms, is given as

$$\mathcal{H} = \begin{pmatrix} \mathcal{H}_{ij} = \frac{\partial^2 U}{\partial r_i \partial r_j} & \mathcal{H}_{i\epsilon} = \frac{\partial^2 U}{\partial r_i \partial \epsilon} \\ \mathcal{H}_{\epsilon i} = \frac{\partial^2 U}{\partial \epsilon \partial r_i} & \mathcal{H}_{\epsilon\epsilon} = \frac{\partial^2 U}{\partial \epsilon \partial \epsilon} \end{pmatrix} \quad (3.5)$$

with the force constant matrix \mathcal{H}_{ij} ($3N \times 3N$) and the Born term $\mathcal{H}_{\epsilon\epsilon}$ (6×6) being the second order derivative of the internal energy with respect to position and strain ϵ , respectively. The strain (and also stress tensor) is symmetric and can be simplified to a 6-dimensional vector using Voigt notation: $\epsilon = (\epsilon_{xx}, \epsilon_{yy}, \epsilon_{zz}, \epsilon_{yz}, \epsilon_{xz}, \epsilon_{xy}) = (\epsilon_1, \epsilon_2, \epsilon_3, \epsilon_4, \epsilon_5, \epsilon_6)$. The Born term accounts for distortions of the lattice, $\mathcal{H}_{i\epsilon}$ and $\mathcal{H}_{\epsilon i}$ are cross-terms. The 0 K elastic tensor is defined as the derivative of the stress with respect to the strain [156, 157] at zero gradient $\mathbf{h} = 0$ and can be expressed in

terms of the generalized Hessian [158]

$$\begin{aligned}
 \mathcal{C}_{\alpha\beta\mu\nu} &= -\frac{1}{V} \left. \frac{\partial \sigma_{\alpha\beta}}{\partial \varepsilon_{\mu\nu}} \right|_{\mathbf{h}=0} = \frac{1}{V} \left. \frac{\partial^2 U}{\partial \varepsilon_{\alpha\beta} \partial \varepsilon_{\mu\nu}} \right|_{\mathbf{h}=0} \\
 &= \frac{1}{V} \left[\underbrace{\frac{\partial^2 U}{\partial \varepsilon_{\alpha\beta} \partial \varepsilon_{\mu\nu}}}_{\text{Born term}} - \underbrace{\frac{\partial^2 U}{\partial \varepsilon_{\alpha\beta} \partial r_{i\lambda}} \left(\mathcal{H}^{-1} \right)_{i\lambda, j\xi} \frac{\partial^2 U}{\partial \varepsilon_{\mu\nu} \partial r_{j\xi}}}_{\text{Relaxation term}} \right] \\
 &= \frac{1}{V} \left[\mathcal{H}_{\varepsilon\varepsilon} - \mathcal{H}_{\varepsilon i} \left(\mathcal{H}_{ij} \right)^{-1} \mathcal{H}_{i\varepsilon} \right]
 \end{aligned} \tag{3.6}$$

The relaxation term arises when more than one particle is present in the unit cell [158]. When the system is strained the atoms need to relax relative to one another, because before and after the strain applied the system must be in a state of zero net force. The state at which elastic constant are computed must a true (global) energy minimum: all forces (also on the cell) must be zero and all eigenvalues of the generalized Hessian matrix *must* be positive.

The systematic study of the lattice stability was done by Born and Huang [159], who formulated the stability criteria in terms of the elastic constants C_{ij} , by expanding the internal crystal energy in a power series in the strain and imposing the convexity of the energy. This criterion expresses the fact that any mechanical strain must increase the total mechanical energy of a system at equilibrium (resulting from the requirement that the eigenvalues of the elastic stiffness matrix \mathcal{C} must be positively defined). The eigenvectors are the deformation modes. The Born elastic stability criteria restrict what values various moduli may have if the crystal is to be stable. In the case of external pressure the relevant free energy is G and the relevant moduli are B_{ij} . In the cubic crystal system the stability criteria are (Voigt notation)

[160]

$$C_{11} + 2C_{12} > 0 \quad (3.7)$$

$$C_{44} > 0 \quad (3.8)$$

$$C_{11} - C_{12} > 0 \quad (3.9)$$

3

which are related with the bulk ($K_V = C_{11} - 2C_{12})/3$), trigonal shear ($G = C_{44}$) and tetragonal shear ($G' = (C_{11} - C_{12})/2$) moduli, respectively, and are known as spinodal, shear and Born criteria. The criteria which is violated first is related to the elastic instability associated to the structural transformation. For a cubic crystal under hydrostatic pressure the generalized stability criteria and deformation modes in analogy with the conventional zero-stress criteria are [156, 161]

$$C_{11} + 2C_{12} + P > 0 \quad (3.10)$$

$$C_{11} - C_{12} - 2P > 0 \quad (3.11)$$

$$C_{44} - P > 0 \quad (3.12)$$

The flexible force fields considered in this work are the following:

- **FF1** : B. Zheng et al. (2012) [62]
- **FF2** : J. Jiang et al. (2012) [63]
- **FF3** : L. Zhang et al. (2013) [64]
- **FF4** : X. Wu et al. (2014) [65]
- **FF5** : T. Weng and J. R. Schmidt (2019) [149]

They were implemented in both the LAMMPS [152] and RASPA [151] simulation packages and subsequently validated. This was done via comparison of the average lattice parameters at atmospheric conditions, which are sensitive to the

parameters and the details of the implementations. The sets of functional forms, corresponding parameters and additional implementation details for all force fields are included in Appendix A.1. Other existing force fields such as the ones proposed by Krokidas et al.[66] and Schmid et al.[68] were left out of the scope of this study, the former because of multiple ambiguities in the definitions of the potential energy terms in the original paper and the latter because of the inability to properly implement the specified non-bonded potentials in RASPA.

The average lattice parameters of the ZIF-8 crystal structure at different fixed values of temperature and pressure were calculated using Molecular Dynamics (MD) in the isothermal-isobaric ensemble (NPT) with LAMMPS. The simulations were performed in a supercell of ZIF-8 consisting of $2 \times 2 \times 2$ unit cells. Periodic boundary conditions were applied in all three dimensions. Long-range electrostatic interactions were treated via the Ewald method. The simulation timestep used for the integrator was 1 fs. For each framework atom, a “scaled 1-4” policy was taken into account; that is, both non-bonded interactions (VdW and electrostatic) between couples of bonded atoms (1-2) or between atoms bonded to a common atom (1-3) were excluded, while the interaction between atoms separated by two others (1-4) were scaled according to the information provided by each force field.

In order to employ the two-code approach for the analysis and comparison of structural and mechanical properties, it is necessary to first verify that the FF implementations provide congruent results between the codes. For this, the term-by-term contributions to the energy were calculated with both codes, for the same atomic configuration. The results for LAMMPS and RASPA for a chosen initial configuration per energy contribution were calculated and are included in Table A.9. For all implemented force fields, the energy terms of each contribution match up to at least the fourth decimal in the case of bonded and VdW interactions and up to the second decimal in the case of electrostatic interactions. The differences in the latter might be due to either different implementations of the Ewald summation in the codes or the finite precision of the specified atom positions. We found that often the

literature force field descriptions are defined unclear and/or ambiguously. Significant reverse-engineering and trial and error was required to resolve all ambiguities.

3.3 RESULTS AND DISCUSSION

3.3.1 TEMPERATURE DEPENDENCE

To examine the effect of temperature on the size and shape of the ZIF-8 unit cell, a series of MD simulations were performed at a pressure of 1 atm between the ranges of 100-900 K for all implemented force fields. As can be seen in Figure 3.2 for FF1, and in Figure A.3 for all evaluated force fields, it was found that the lattice parameter depends only weakly on temperature, confirming their high thermal stability as experimentally observed. Also in agreement with experiments, is that the unit cell becomes larger with increasing temperature (positive thermal expansion)[162]. FF1 qualitatively matches the data of Zhou et al.[162] quite well, albeit lower in value. As can be seen in Figure A.3, all other evaluated force fields do better in this respect, providing closer estimates.

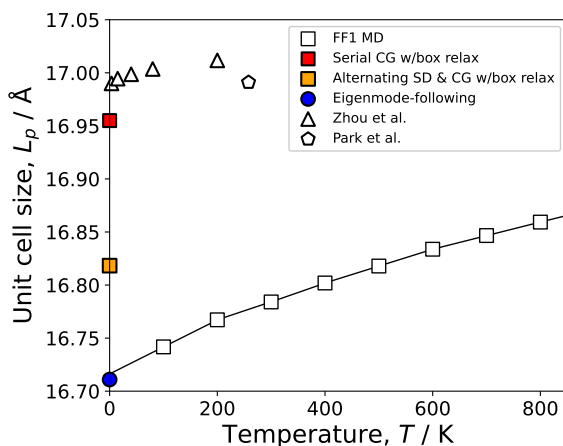


Figure 3.2: Size of the unit cell of ZIF-8 predicted by the model proposed by Zheng et al. (FF1). MD data obtained at a pressure of 1atm. Experimental measurements from Park et al.[36] (XRD) and Zhou et al.[162] (neutron HRPD) represented with stars and triangles, respectively. Minimization routines that make use of the conjugate gradient (CG) and steepest descent (SD) algorithms (along with simulation box relaxation) overestimate the cell size. After fitting a spline through the data, the extrapolated value is 16.717 Å at 0 K. Using the eigenmode-following minimization technique, a very close value of 16.711 Å is obtained.

In Figure 3.2 we also compared the Conjugate Gradient[163] (CG) method, with

a combination of Steepest Descent[164] (SD) and CG methods, and with the more advanced (but also more expensive) eigenmode following[153, 154] method. A crucial requirement is that the MD results for low temperatures must converge to the 0K result obtained with energy minimization. Eigenmode following minimization consistently displays this behavior (Fig. A.3), while the SD and CG methods gave erroneous results. We confirmed that these structures do have zero forces, but do not pass the requirement of having all positive eigenvalues of the generalized Hessian matrix. That is, the CG and SD/CG methods were not able to find *true* minimum energy structures. This has important implications for the reliability and accuracy of elastic constants.

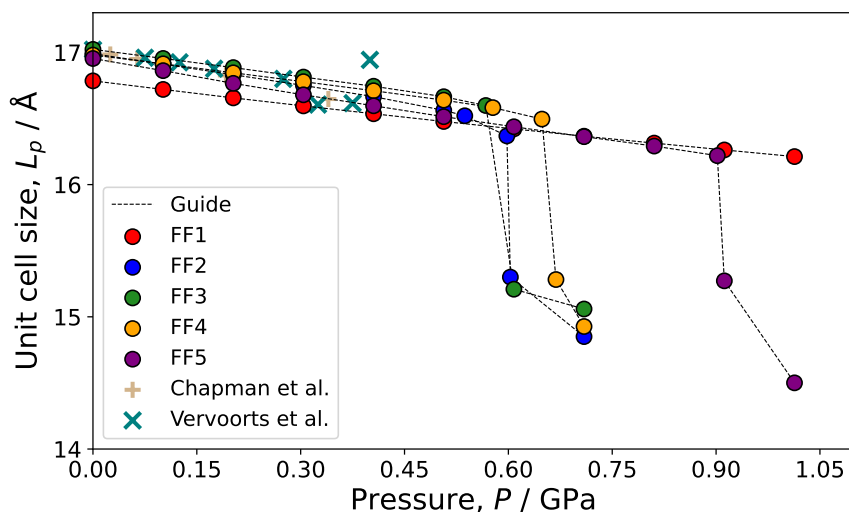


Figure 3.3: Lattice parameter of the unit cell predicted by the implemented force fields. MD data obtained at a temperature of 300 K. Available experimental data at $P < 0.4$ GPa (before framework amorphization) represented by crosses.[54, 165]

3.3.2 UNIT CELL SIZE AS A FUNCTION OF PRESSURE

Next, we examine the effect of pressure on the ZIF-8 unit cell lattice parameter. A series of MD simulations were performed at a temperature of 300 K over a wide range of pressures using all implemented force fields (Fig. 3.3 and Fig. A.4). It was

found that force fields 2 through 5 were able to accurately reproduce the experimental geometric properties of the ZIF-8 unit cell at low values of pressure ($P < 0.4$ GPa). These force fields qualitatively reproduce the experimental amorphization of the system that occurs at higher values of pressure. FF1 both underestimates the lattice parameter at lower values of pressure and fails to reproduce the pressure-induced phase change.

3.3.3 ELASTIC CONSTANTS AS A FUNCTION OF PRESSURE

Evaluating the elastic constant dependency on pressure allows us to shed more light on the amorphization mechanism. Figure 3.4 shows the computed elastic constants as a function of pressure at 0 K for all implemented force fields. When compared to each other, the force fields provide not only different quantitative results, but more importantly different qualitative results as well.

At zero pressure, the agreement between M06-2X DFT and experimental values from ambient temperature and pressure measurements is good, except for a slight overestimation of C_{12} . Force fields 3 and 4 compare reasonably well with experimental and DFT values, while FF1, FF2 and FF5 differ significantly in one or more elastic constant value. We can observe that while all the studied force fields present a negative linear dependency of C_{44} throughout the pressure range; with FF5 providing exceptional quantitative estimations, none of them are able to properly describe the non-linear behaviour of C_{11} and C_{12} at $P > 0.2$ predicted by DFT calculations.

FF3 and FF4, while underestimating the amorphization pressure, provide qualitatively similar results and come closest to predict the EC trends described by the DFT results. FF1 provides a consistent overestimation C_{44} over the pressure range, leading to a predicted amorphization pressure that is too high (i.e. FF1 is stable up to and over 1 GPa), which is congruent with results shown in Figure 3.3. These three force fields correctly suggest that the negative pressure dependence of C_{44} is the clear direct route to instability, that is, via the breaking of the third Born criteria (Eq. 3.12) or shear mode softening, in agreement with the experimental finding. In

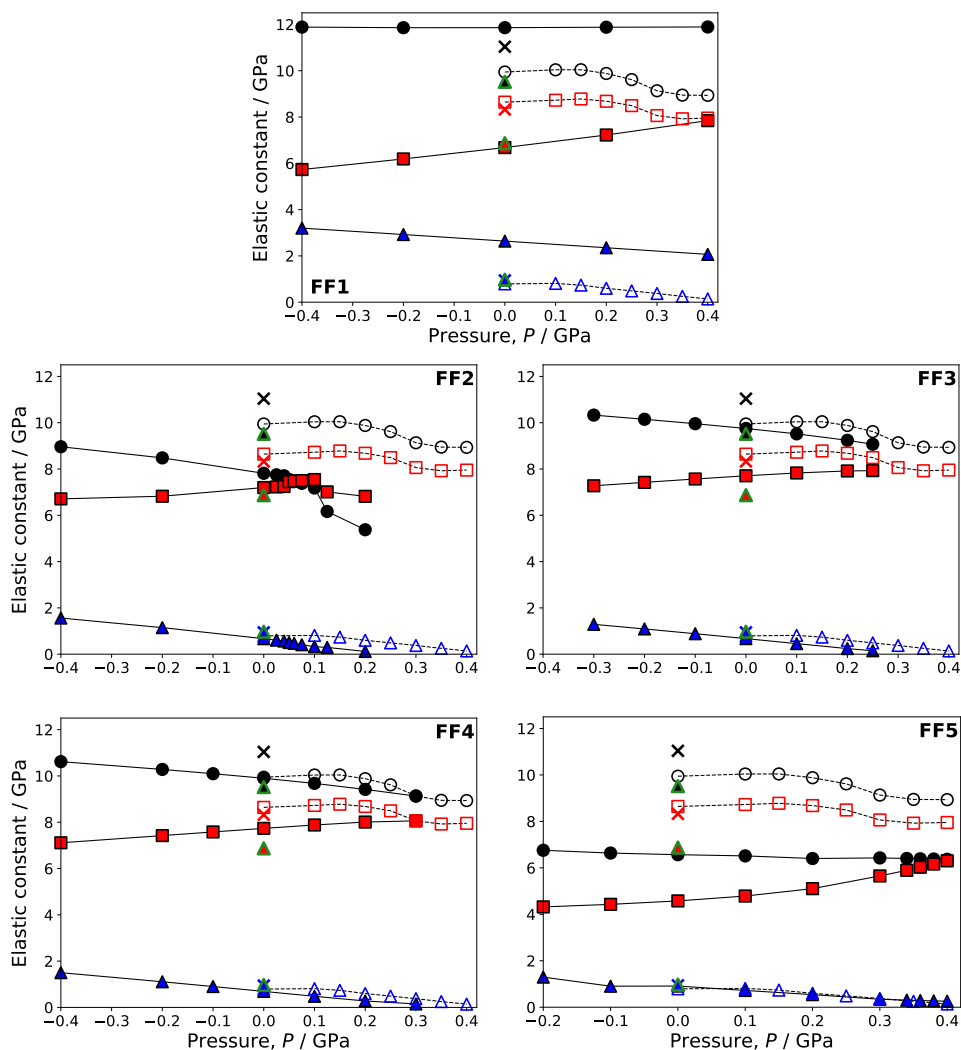


Figure 3.4: 0 K elastic constants obtained using the mode-following technique over a range of pressures. Black data points indicate the C_{11} elastic constants, red the C_{12} elastic constants and blue the C_{44} elastic constants. The simulated values are compared to the Brillouin scattering measurements (filled symbols with green borders)[59] conducted at 295K as well as B3LYP DFT (crosses)[59] and M06-2X DFT (open symbols)[69] results.

contrast, both FF2 and FF5 qualitatively show another amorphization mechanism, namely Eq. 3.11, where C_{11} becomes larger than $C_{12} + 2P$, which for the former FF occurs at pressures lower than 0.1 GPa. Owing to the sharp increase of the C_{12}

elastic constant at $P > 0.2$, FF5 presents ambiguity regarding which stability criteria is violated first and therefore the amorphization mechanism related to the structural transformation of the framework.

Table 3.1: Comparison of Elastic Constants (C_{ij}), Shear Modulus (G), Young's modulus (E) and Bulk modulus (K) found in the literature and those reported in this work. The subindices VRH refer to the Voigt-Reuss-Hill average of the modulus. All values in GPa.

| Source | C_{11} | C_{12} | C_{44} | G_{\min} | G_{\max} | G_{VRH} | E_{\min} | E_{\max} | K_{VRH} |
|----------------------------|----------|----------|----------|------------|------------|-----------|------------|------------|-----------|
| B. scattering (295 K)[59] | 9.52 | 6.87 | 0.97 | 0.97 | 1.33 | 1.1 | 2.78 | 3.77 | 7.75 |
| DFT B3LYP, reported[59] | 11.04 | 8.33 | 0.94 | 0.94 | 1.36 | 1.10 | 2.74 | 3.88 | 9.23 |
| DFT M06-2X, reported [69] | 9.95 | 8.64 | 0.79 | | | | | | 9.06 |
| MOF-FF, reported[68] | 8.54 | 6.55 | 0.62 | | | | | | |
| FF1, this work (0 K) | 11.85 | 6.69 | 2.63 | | | 2.61 | 6.93 | 7.16 | 8.36 |
| FF2, reported (258 K)[63] | | | | | | | 2.99 | | 7.24 |
| FF2, this work (0 K) | 8.16 | 6.85 | 0.67 | | | 0.66 | 1.90 | 1.90 | 7.27 |
| FF3, this work (0 K) | 9.9 | 7.74 | 0.69 | | | 0.83 | 3.09 | 3.10 | 8.42 |
| FF4, reported (298 K)[65] | | | | | | | | | 8.37 |
| FF4, this work (0 K) | 9.75 | 7.71 | 0.67 | | | 0.79 | 2.93 | 2.94 | 8.36 |
| FF5, reported (0 K)[149] | 9.33 | 6.45 | 1.37 | 1.37 | 1.44 | 1.40 | | | 7.41 |
| FF5, reported (295 K)[149] | 9.06 | 5.92 | 1.20 | 1.20 | 1.57 | 1.34 | | | 6.96 |
| FF5, this work (0 K) | 6.57 | 4.58 | 0.91 | | | 0.95 | 2.90 | 2.96 | 5.21 |

In Table 3.1 we compare the computed 0 K elastic constants and elastic moduli obtained with RASPA to the reported simulated and experimental values. Quantitatively, at zero pressure, FF2 and FF3 provide similar 0 K results and come the closest to the reported DFT and experimental values. FF1 overestimates both C_{11} and C_{12} while FF2 greatly underestimates C_{11} . FF5 provides an exceptional estimation of C_{44} and significantly underestimates C_{11} and C_{12} . Of note is the fact that the reported 0 K values for FF5 are in heavy disagreement with the ones obtained in this work. This discrepancy might be related to the difference in methodologies employed to calculate them.

3.3.4 ELASTIC CONSTANTS USING SD/CG vs. MODE-FOLLOWING MINIMIZATION

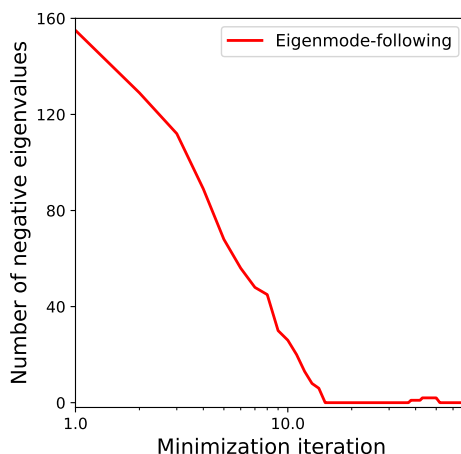


Figure 3.5: Eigenmode-following minimization of ZIF-8 using FF1, starting from a configuration previously minimized using the conjugate gradient algorithm. Initially the structure presents 170 negative eigenvalues. Notice that the number of negative eigenvalues is reduced to zero, then increases (between steps 38 and 51) before decreasing again. The increase corresponds to a structural change in the framework which the SD and CG methods are unable to induce.

To determine how the calculated elastic constants depend on the energy minimization algorithm, the SD/CG methods used in LAMMPS and eigenmode-following as implemented in RASPA were compared. For each force field, the output from the 0 K conjugate gradient LAMMPS routine was used as the input for RASPA's minimization. It was found that the former is not able to find true minimum energy configurations (Figure 3.2) due to the identification of negative eigenvalues (corresponding to first-order saddle-points). Furthermore we noted that in most cases, to find relaxed configurations resulting in zero negative eigenvalues, the CG energy minimization routine requires either a preceding NPT MD simulation at very-low temperatures or the implementation of additional iterative minimization runs of different types (such as steepest descent). This last methodology was found not to be self-consistent across force fields. The problem is that these methods have no

inherent mechanisms to systematically remove negative eigenvalues. Figure 3.5 shows how the eigenmode-following technique quickly drives the system to zero eigenvalues. Note that the number can increase again during the minimization which often signals large-scale structural changes that need to be overcome.

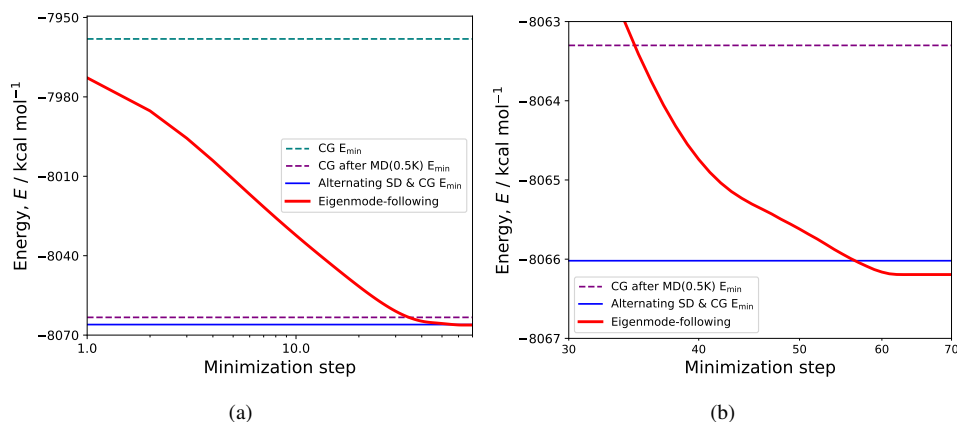


Figure 3.6: Eigenmode-following minimization of ZIF-8 using FF1, starting from a configuration previously minimized using the conjugate gradient algorithm. The convergence of system energy is presented in red. The minimum energy obtained using CG and SG iterative routines are pictured with teal and blue lines, while the one corresponding to CG minimization after a low-temperature PT simulation is presented in purple. (a) zoomed-in portion where the corresponding lattice parameter values are 16.7122Å (purple), 16.725Å (blue) and 16.711Å (red). The eigenmode-following technique relaxes both the cell shape and the atoms at the same time and produces the configuration with the lowest energy.

Figure 3.6 shows the final energies obtained from the CG-based methods compared to the iteration steps of the eigenmode following. What becomes clear is that methods based on energies or forces are not able to find (a) the lowest energy, (b) the correct structure at 0 K. We note that, even though the difference in lowest energy is small, the obtained unit cells differ in size *and* in atomic structure. When comparing the resulting energy values and unit-cell dimensions obtained using the CG-based routines with the ones obtained with eigenmode-following, it becomes clear that former are unable to efficiently relax both the framework atom's positions and the simulation box at the same time, which might produce problems when used to minimize the system after the box deformations are applied (in the elastic constants

calculation routine).

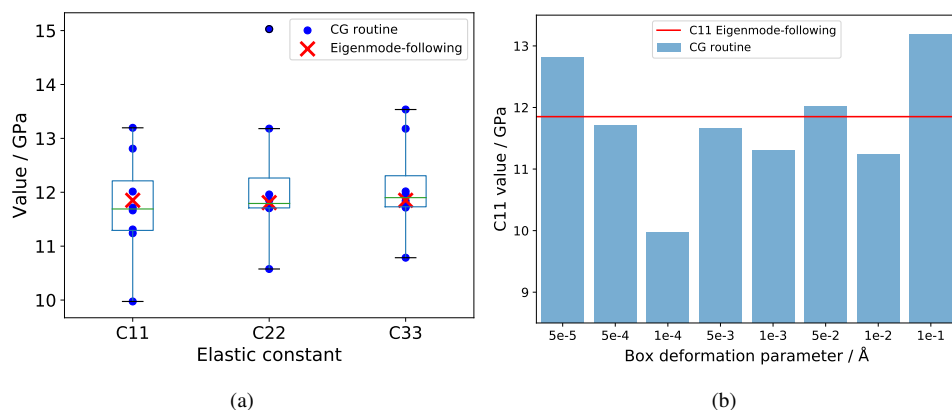


Figure 3.7: (a) Box plot of 0 K elastic constant values obtained using the CG routine for FF1. The blue dots correspond to the elastic constant values obtained using different box-deformation parameters; those outside of the whiskers are considered outliers. The red crosses represent the elastic constants obtained using the eigenmode-following technique, a self-consistent method that doesn't require user-defined parameters. (b) Bar plot of the C_{11} value obtained for each box-deformation parameter using the CG routine. The red line represents the C_{11} value obtained using eigenmode-following.

In order to compute elastic constants with LAMMPS we employed modified versions of the manual-suggested routine. These rely on user-defined deformation parameters and make use of numerical differentiation to obtain derivatives. In contrast, in RASPA, the elastic constants are computed via Eq. 3.5 using analytical derivatives of the functional forms of the potentials. Since RASPA gives zero Kelvin elastic constants basically at machine precision, we can test how sensitive the numerical procedure is to the deformation parameters. The elastic constants were re-computed using the LAMMPS CG-based routine using different box deformation parameters, with magnitudes ranging from $5e-5$ GPa (corresponding to $<0.01\%$ change in simulation box side dimensions) to 0.1 GPa (about 10%). We found that the predicted elastic constant values severely depend on the chosen parameter (Figure 3.7). Furthermore, no systematic dependency of the elastic constants estimate with respect to deformation parameter was identified in Figure 3.7(b).

3.4 CONCLUSIONS

We evaluated a set of literature classical force fields to test whether they can accurately reproduce elastic constants and thermal expansion for ZIF-8. The force fields not only gave different quantitative results, but more importantly gave different qualitative results, both when compared to each other and, in the case of elastic constants, to reported DFT-calculated values. The reason is that the majority of these force fields have been developed “bottom-up”, starting from atomic bonding parameters, parameters for bending and torsion, and next long-range interactions like Van der Waals and electrostatics. It is therefore not surprising that any reproduction of system properties is fortuitous. We find that this applies in particular when examining these properties as a function of pressure, i.e. the force fields differ significantly in the prediction of the pressure where amorphization or collapse starts to occur. Future work on force fields should therefore include this type of information in the parameterization. Although the force fields provide mostly acceptable quantitative estimations of elastic constants at very low pressures ($P < 0.1$ GPa), they are unable to reproduce the non-linear behaviour of C_{11} and C_{12} at $P > 0.2$ predicted by DFT calculations and, in the case of FF2 and FF5, unequivocally point to the correct amorphization mechanism. In this study, we used both the RASPA and LAMMPS simulation packages and compared the implementation of the literature force fields for all energy terms separately. We found that often the literature force field descriptions are defined unclear and/or ambiguously in the supporting information. Significant reverse-engineering and trial and error was required. RASPA and LAMMPS gave identical results for the unit cell volumes as a function of temperature and pressure. However, we found that zero Kelvin unit cells structures and elastic constants depend on the procedure. The conjugate gradient minimization routine implemented in LAMMPS is often unable to find the true energy minimum and 0 K structure and therefore, when employed in elastic constant calculations, provides erroneous values. The eigenmode-following minimization in RASPA is

guaranteed to find the correct zero K structure, and therefore a comparison could be made. This methodology is important in MOFs, and we showed that unit cell obtained by RASPA is the same as extrapolated from finite temperature MD data to zero Kelvin, while the minimized unit cells from conjugate gradient are often erroneous.

4

4

LINKER VACANCY DISTRIBUTION AND ITS EFFECT ON UiO-66 STABILITY

In this work, we computationally investigate the impact of the distribution of linker vacancies on the relative stability of defected UiO-66 structures. Analysis of a significant number of defected structures reveals that higher defect numbers correlate with lower stability, but variations in missing linker distribution and orientation contribute to widely differing amorphization pressures. Our results suggest that structures with more evenly distributed vacancies exhibit a positive linear relationship between amorphization pressure and bulk modulus. Furthermore, we found structures with a disproportionate number of missing linkers with the same orientation and structures where a large volume of the framework remains pristine, display outlier behavior in this respect. Evaluation of anisotropic elastic moduli uncovers directional instability in structures with a high number of vacancies with the same orientation. These findings have important implications for designing and optimizing UiO-66-based

materials, aiding in defect configuration selection for specific applications.

4.1 INTRODUCTION

Metal-organic frameworks (MOFs) have continued to receive attention from the scientific community at large ever since the first ones were synthesized more than twenty years ago [70–72]. These materials consist of metal clusters coordinated with organic ligands forming ordered crystal lattices [34, 73, 167]. Their porous structure and possibility of ligand functionalization make them an appealing alternative in applications such as catalysis [168–171], drug delivery [172] and gas storage and separation [173–176].

In the last decade, the archetypal MOF, UiO-66 [177], has received considerable attention within the field due to its high hydrothermal [178–180] and mechanical stability [92, 179], even under high-pressure conditions. The structure of UiO-66 is characterized by zirconium-based $Zr_6O_4(OH)_4$ clusters bridged to one another via 1,4-benzenedicarboxylic acid (BDC) ligands. In the pristine (defect-free) material, each inorganic cluster is 12-fold coordinated, that is, each cluster is connected to the others by 12 BDC linkers. The high structural stability of UiO-66 and its extended sibling materials (UiO-67 and UiO-68) has been attributed to the high coordination number of its inorganic clusters (12) compared to other prototypical MOFs such as ZIF-8 (4) and MOF-5 (6) [79].

The vast majority of synthesis procedures for UiO-66 result in a defected structure with missing linkers [181, 182]. Thermogravimetric analysis (TGA) measurements suggest that for the less defected UiO-66 samples, the coordination number of each zirconium cluster is 11, indicating one missing linker on average [178, 183]. This observation has been further verified via NMR [181], X-ray and neutron diffraction [184, 185], and IR/Raman spectroscopy experiments [183]. The presence

Based on  E. Acuna-Yeomans, J.J. Gutierrez-Sevillano, D. Dubbeldam and S. Calero, *A simulation study of linker vacancy distribution and its effect on UiO-66 stability*, *Microporous and Mesoporous Materials*, **2023**, 366, 1387-1811 [166].

of linker defects increases the porosity and available surface area of the material, which modifies the adsorption behavior [84, 85, 186], catalytic properties [168, 187], proton conductivity [188, 189], and thermal stability [80]. The tradeoff between enhancement in adsorption and the effect on stability when defects are introduced is an ongoing research topic, which often requires the use of computational techniques in order to analyze the relationships between specific properties and the structure of the material on a molecular scale.

In the past decade, computational simulations have been used to study the adsorption properties of both pristine and defected UiO-66, often with the focus on water and CO₂ adsorption [84–88, 95, 190]. These have provided substantial insight for industrial applications such as water harvesting and gas separation. The simulations involved in most of these works often model UiO-66 as a rigid structure, where the framework only interacts with the guest molecules via non-bonded potentials.

The computational study of structural and mechanical properties of UiO-66, especially at high pressures, requires for the framework to be modelled as flexible. Several classical force fields (FFs) have been proposed in order to gain atomistic understanding of the underlying mechanisms that control the flexible behavior of the system. In an early work, Boyd et al. [191] modelled pristine UiO-66 using both the Universal Force Field (UFF) [61] and its extension for MOFs, UFF4MOF [192], without taking into account electrostatic contributions from point charges to the potential energy. They found that they could reproduce the structural properties of the defect-free structure at ambient conditions and provide a reasonable approximation of its bulk modulus under the same conditions. Upon testing the system using three different sets of point charges (CBAC, REPEAT, Qeq), they noted that it results in unpredictable behavior with respect to the bulk modulus. In 2014, Bristow et al. [193] proposed an ab-initio derived force field for a slew of prototypical MOFs, including UiO-66, which proved capable of accurately estimating the structural parameters and the volumetric heat capacity of the material; however, it severely underestimates the bulk modulus. Said FF has seldom been used in computational studies since it was

proposed, and hence validation and comparison with experimental measurements is lacking.

The only reported classical flexible approach that is able to provide interaction parameters for defected UiO-66 structures and has been extensively validated is the one proposed by Rogge et al., in 2016 [94], which consists of constructing ab-initio derived force fields for each particular structure via the QuickFF procedure [150]. They found that for the pristine structure, applying external pressure to the system induces short-range disorder and loss of crystallinity at a pressure of 1.83 GPa. Analysis of the elastic constants at high pressure shows a breakage of the second Born stability criterion, indicating that high-pressure amorphization in the framework is caused by compression.

In their work, they constructed 8 different force fields for 8 distinct defected structures with one or two defects per UiO-66 unit cell. They estimated the pressure-versus-volume equations of state for each structure and determined that defects have a minor effect on the equilibrium volume but introduce a substantial and gradual decrease in the amorphization pressure and the bulk modulus. They found that the most profound effect on the stability of the defected system is obtained when the linker vacancies share the same orientation but lie in neighboring lattice planes.

To better understand the full impact of defects on the stability of UiO-66, it is essential to mechanically characterize a large number of defected structures. Mainly, the necessity of compensating the charge of the missing linkers in order to maintain a system with zero net charge effectively means that for every structure with a different number and distribution of defects, a distinct set of charges, and thus a distinct force field, must be used. This represents a limiting factor for the computational screening of large numbers of defected structures.

In this work, we model all defected UiO-66 structures using the same force field (UFF) without taking into account electrostatic interactions, to zero in on the effect that the number, distribution, and orientation of missing linkers has on the mechanical properties of the system. In order to validate our proposed methodology,

we reproduced the defected structures studied by Rogge et al. [94], estimated both the amorphization pressure and bulk modulus of each one, and compared them with their results. We found that although the quantitative values for them differ considerably (by a factor of ~ 2.7 for the pristine material), the trends followed by the two sets of estimations are highly correlated, indicating that although our methodology is not able to provide realistic estimations of the mechanical and structural properties, it is helpful for analyzing the stability of different defected structures relative to each other.

During the course of this project, we generated over 100 UiO-66 structures ranging from 1% defected to 18% defected, with varied missing linker spatial concentration, orientation, and order. The amorphization pressure and elastic stress tensor for all structures were computed using molecular dynamics (MD) simulations and subsequently processed, analyzed, and contrasted with each other. Our results are able to provide greater insight into how linker distribution is related to the mechanical stability of the material.

4.2 METHODOLOGY

In this study, we aim to investigate the stability of defected UiO-66. To this end, we examined two broad categories of defective structures (see Fig. 4.1). The first type involved structures with a regular arrangement of linker vacancies, which were generated by replicating a defected conventional unit cell to create a $2 \times 2 \times 2$ supercell. The second type consisted of structures with irregular linker vacancies created directly at the supercell level. To introduce these disordered vacancies, we employed various methods, such as random removal or quasirandom removal of linkers in the pristine structure. The latter approach involved selectively removing linkers in accordance with specific criteria, such as removal from specific subvolumes of the supercell or based on particular linker orientations.

To identify factors that might contribute to structural stability, we characterized

each defected structure according to five metrics: (1) the mean distance between linker vacancies, where the position of each missing linker was taken to be the geometric center of the benzene ring, (2) the mean distance from the linker vacancies to the geometric center of the $2 \times 2 \times 2$ supercell, (3) the radial distribution of linker vacancies with respect to the center of the supercell, (4) the amounts of missing linkers with a particular orientation, and (5) the amount of inorganic clusters with a particular coordination contained in the structure. Most of the metrics are included in the supporting information file, only the most useful at distinguishing mechanical behavior between structures with the same number of linker vacancies are included and referred to in the main text.

4

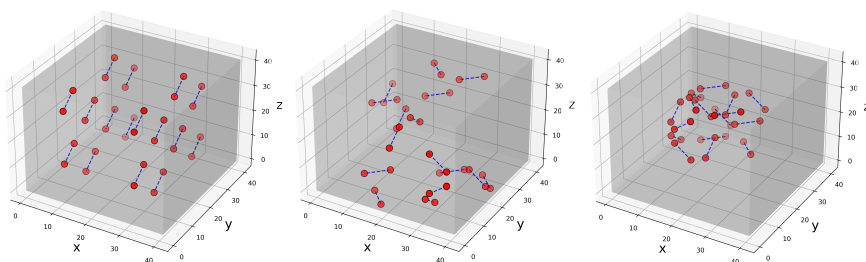


Figure 4.1: Pictorial representation of 3 different defected UiO-66 structures with an average cluster coordination of 11 at the supercell level. The linker vacancies are represented by dashed blue lines, the red end points represent the missing connection with inorganic clusters and the grey volume represents the non-defected part of the framework. Transparency of the red and blue colors is used to aid depth perception, fuller colors mean that the vacancy is located closer to the point of view of the observer, more transparent colors mean that the vacancy is located further away. The first image pictures the framework containing 16 vacancies with a regular arrangement while the second and third images are examples of structures with an irregular arrangement of vacancies, where the 16 organic linkers were removed randomly and quasi-randomly, respectively.

In this study, we decided to model the defected UiO-66 structures using the Universal Force Field (UFF) [61]. For this, we chose to exclude electrostatic contributions from the potential energy. This eliminates the need to compensate for the charge of removed organic linkers with approaches such as the redistribution of charges in the remaining structure [95] or the inclusion of ions to cap defected cluster sites [186], both of which would significantly restrict the number of defected structures that could potentially be considered in this study. Importantly, in our

experience, the inclusion of ions in the pore volume reduces the space available for the framework to "collapse into." It affects the volume change of the system during the simulations, inhibiting the methodology used in this study to determine if a collapse occurred. Additionally, although the computational cost of including short-range electrostatics would be relatively low on a per-simulation basis, the sum total for all runs using our methodology would be significant. The UFF energy equation is defined as:

$$U = U_{\text{bonded}} + U_{\text{non-bonded}} \quad (4.1)$$

where

$$\begin{aligned} U_{\text{bonded}} &= U_{\text{bonds}} + U_{\text{angles}} + U'_{\text{angles}} + U_{\text{dihedrals}} + U_{\text{impropers}} \\ &= \sum_{\text{bonds}} \frac{1}{2} K_r (r - r_0)^2 + \sum_{\text{angles}} \frac{K_\theta}{n^2} [1 - \cos(n\theta)] \\ &+ \sum_{\text{angles}} K_\theta [C_0 + C_1 \cos(\theta)] + \sum_{\text{dihedrals}} \frac{K_\varphi}{2} [1 - \cos(m\varphi_0) \cos(m\varphi)] \\ &+ \sum_{\text{improper}} K_\xi [C_0 + C_1 \cos(\xi) + C_2 \cos(2\xi)] \end{aligned} \quad (4.2)$$

$$U_{\text{non-bonded}} = \sum_{i < j} 4\epsilon_{ij} \left[\left(\frac{\sigma_{ij}}{r_{ij}} \right)^{12} - \left(\frac{\sigma_{ij}}{r_{ij}} \right)^6 \right] \quad (4.3)$$

In the bonded term, r is the bond distance while θ , φ , and ξ are the bend, dihedral and improper dihedral angles, respectively. The nonbonded part consists of the van der Waals interaction between a pair of atoms i and j separated by a distance r_{ij} where σ_{ij} and ϵ_{ij} refer to the equilibrium distance and well depth of the potential, respectively. The first angle term in the bonded potential applies to atoms in linear, trigonal-planar, square-planar, or octahedral arrangement and the second angle term can be used for the general non-linear case. In the specific case of

UiO-66, the second term is used to model the angle bending interactions inside the inorganic cluster of the types $O - Zr - O$, $H - O - Zr$, and $Zr - O - Zr$. The specific force field parameter values, their associated atom types and the definition of the angle bending and improper torsion coefficients, as used in this work, are described in the Supporting Information file.

4

In this study, we employ two complementary approaches to evaluate the stability of defective structures. The first approach, proposed by the Coudert group[194], involves assessing the anisotropy of the mechanical moduli of the structure. The uniaxial stiffness of the material in a given direction u is determined by Young's modulus $E(u)$, while the directional deformation caused by isostatic compression is measured by the linear compressibility modulus $\beta(u)$. The directional dependence of the moduli can be obtained from the inverse of the fourth-order elastic stiffness tensor \mathcal{C} (also called the compliance tensor), by applying to it a rotation mapping the x-axis onto the direction of the unit vector u , and are calculated (Einstein's notation used) as[194, 195]:

$$E(u) = \frac{1}{u_p u_q u_r u_s [\mathcal{C}^{-1}]_{pqrs}} \quad \beta(u) = u_p u_q [\mathbf{C}^{-1}]_{pqrr} \quad (4.4)$$

Where the u_x terms are the components of the rotation matrix. The anisotropy of each property is determined by calculating the ratio between its maximum and minimum values, which can range from 1 to infinity. This property reflects the flexibility of the material, where softer crystals exhibit large anisotropy factors, rigid MOFs are characterized by considerably lower values, close to unity[146].

The elastic stiffness tensor \mathcal{C} at a particular temperature can be estimated via molecular dynamics simulations via the stress-fluctuation method. In the canonical ensemble, the equations for the stress tensor σ and for the elastic stiffness tensor

reduce to [138, 196] \mathcal{C} :

$$\sigma_{\alpha\beta} = \langle \sigma_{\alpha\beta}^B \rangle - \rho k_B T \delta_{\alpha\beta} \quad (4.5)$$

$$\begin{aligned} \mathcal{C}_{\alpha\beta\mu\nu} = & \langle \mathcal{C}_{\alpha\beta\mu\nu}^B \rangle - \frac{V}{k_B T} \left[\langle \sigma_{\alpha\beta}^B \sigma_{\mu\nu}^B \rangle - \langle \sigma_{\alpha\beta}^B \rangle \langle \sigma_{\mu\nu}^B \rangle \right] \\ & + \rho k_B T (\delta_{\alpha\mu} \delta_{\beta\nu} + \delta_{\alpha\nu} \delta_{\beta\mu}) \end{aligned} \quad (4.6)$$

Where $\sigma_{\alpha\beta}^B$ and $\mathcal{C}_{\alpha\beta\mu\nu}^B$ are the Born stress tensor and the Born matrix, respectively. They are the first and second derivatives of the potential energy U with respect to strain, given by

$$\sigma_{\alpha\beta}^B = \frac{1}{V} \frac{\partial U}{\partial \epsilon_{\alpha\beta}} \quad \mathcal{C}_{\alpha\beta\mu\nu}^B = \frac{1}{V} \frac{\partial^2 U}{\partial \epsilon_{\alpha\beta} \partial \epsilon_{\mu\nu}} \quad (4.7)$$

In this work, we computed the anisotropic elastic constants tensor of all defected structures both at 0K and at finite temperatures, in order to quantify their mechanical stability at a given temperature and pressure. Calculations at finite temperatures were carried out by following the stress-fluctuation technique using the born/matrix compute [134] recently implemented in the LAMMPS [152] molecular simulation package, which allows for the computation of elastic constants for arbitrary complex potential interactions. The 0 K elastic constants were calculated using the cell deformation technique using the same simulation package.

The second approach consists of determining the pressure versus volume behavior of the structure via molecular dynamics simulations in the flexible NPT ensemble ($N, P, \sigma_{\alpha} = \mathbf{0}, T$), where the number of particles N is fixed while the internal pressure P_i , internal deviatoric stress $\sigma_{\alpha,i}$ and the internal temperature T_i are controlled. The ensemble allows for the dynamic change of both the simulation cell volume V and shape \mathbf{h}_0 and can be systematically used to estimate the pressure at which the framework amorphization takes place (P_{am}).

For each defective structure we conducted looped flexible NPT simulations starting from a sufficiently high pressure. At the start of each loop, energy minimization

of the system is conducted, and the final volume V_f is saved. The instantaneous volume V_i was monitored during the equilibration period of each simulation. Amorphization was determined to have occurred if at any point during equilibration, the value of V_i became lower than a predefined volume threshold V_t , taken to be proportional to V_f . In the scenario where amorphization was determined to have occurred, the subsequent simulation within the loop would start with a pressure value that ΔP lower than the previous one. Conversely, if it was established that amorphization had not transpired, the pressure value of the following simulation in the loop would be increased by ΔP . The final characteristic P_{am} value for the particular structure would be determined to be the final pressure value at which the structure does not collapse plus ΔP . Similar approaches have been used previously to study the stability of ZIFs and MOFs, although it has been noted that the fluctuations in instantaneous pressure inherent in MD simulations may induce phase transitions at artificially low pressures[146, 147]. In order to partially mitigate said fluctuations we employed sufficiently large simulation cells.

4

4.2.1 COMPUTATIONAL DETAILS

The defected structures were generated using an in-house program which takes the force field parameters and the pristine UiO-66 structure crystallographic information file as inputs and outputs a LAMMPS topology data file.

All pressure versus volume MD simulations reported in this work were carried out in the flexible NPT ($N, P, \sigma_\alpha = \mathbf{0}, T$) ensemble using the LAMMPS simulation package. The simulation timestep used for the Verlet integrator was 0.5 fs to ensure energy conservation. During these simulations the temperature was fixed at 300 K and controlled via a Nose-Hoover chain thermostat using a relaxation time of 50 fs. The pressure control was handled by a MTTK barostat with a relaxation time of 500 fs. The pressure was modified according to the discussed looping simulations scheme, ΔP was set at 0.005 GPa and the volume threshold V_t was set at 0.8 times the volume of the structure after energy relaxation.

For the computation of the elastic stiffness tensor, the cell parameters and atomic coordinates of each structure were first relaxed and, once a minimum was reached, the stress tensor and Born matrix were sampled in 200 ps long NVT simulations in LAMMPS, using the numerical derivative method[134] for the latter. The temperature was fixed at 300 K and controlled via a Nose-Hoover chain thermostat with a relaxation time of 100 fs. The running average of the Born matrix was sampled every timestep using the born/matrix compute[134]. For each structure, using the ELATE python module[197] with the obtained elastic constants as input, the minimal/maximal values of linear compressibility β and Young's modulus E were estimated, as well as their corresponding anisotropy values.

All simulations were performed in a supercell of the defected structure using UFF without electrostatic contributions. Periodic boundary conditions were applied in all three dimensions. As per UFF indications, for each framework atom, a "scaled 1-4" policy was taken into account; that is, non-bonded interactions (VdW) between couples of bonded atoms (1-2) or between atoms bonded to a common atom (1-3) were excluded, while the interaction between atoms separated by two others (1-4) were fully considered.

4.3 RESULTS AND DISCUSSION

To determine the viability of our proposed methodology, we constructed the 8 defected structures studied by Rogge et al.[94]: one of them (type0) corresponds to a system with one linker vacancy per unit cell and the rest (type1-7) to structures in which a different additional linker defect is introduced to the type0 parent. In order to compare our methodology with those reported by them we calculated the amorphization pressure (P_{am}) and bulk modulus K_V of each; using the flexible NPT simulation scheme and the stress fluctuation technique in the NVT ensemble, respectively. The results are provided in Table 4.1.

Table 4.1: Comparison of amorphization pressure (P_{am}) and Bulk modulus (K_V) predicted by our methodology and those reported by Rogge et al.[94], respectively. Simulations conducted at a temperature of 300 K. All values in GPa.

| Defect type | This work | | Rogge et al. | |
|-------------|-----------|-------|--------------|-------|
| | P_{am} | K_V | P_{am} | K_V |
| Pristine | 2.91 | 59.5 | 1.83 | 22.2 |
| type0 | 2.53 | 56.4 | 1.55 | 19.9 |
| type1 | 2.2 | 50.39 | 1.29 | 17.4 |
| type2 | 2.24 | 52.22 | 1.37 | 18.2 |
| type3 | 2.41 | 52.51 | 1.51 | 18.7 |
| type4 | 2.31 | 51.51 | 1.39 | 18.2 |
| type5 | 2.09 | 50.65 | 1.17 | 15.5 |
| type6 | 2.44 | 53.45 | 1.38 | 18.9 |
| type7 | 2.22 | 48.97 | 1.35 | 17.2 |

The results obtained in this study exhibit significantly greater quantitative values compared to those reported by them. Nevertheless, upon closer examination, it becomes apparent that the relative variances in properties between the two sets of results seem to be comparable. To delve deeper into this observation, we conducted an analysis of the relative trends among each set of defective structures. The outcomes of this analysis can be visualized in Fig. 4.2.

Figures 4.2A and 4.2B show that the available experimental measurements provide strong support for the accurate predictive capabilities of the Rogge force field. Our results are qualitatively similar but differ quantitatively. Despite this quantitative discrepancy, the trends observed between the values in both sets remain relatively consistent. In terms of qualitative analysis, the computed properties for the various structures indicate similar conclusions concerning the relative stability of the reference defected structures. Specifically, the type5 structure, where the removed linkers have equal orientation on two different planes, is the least stable; and type3 and type6 structures are the most stable of the structures with average cluster coordination of 11.

In order to measure the degree of similarity between the relative values of the

properties in both sets, we performed a calculation of the correlation coefficient. Figures 4.2C and 4.2D illustrate the obtained results, revealing correlation coefficient values that are close to unity. This indicates a strong positive correlation between the two sets of amorphization pressure and bulk modulus values.

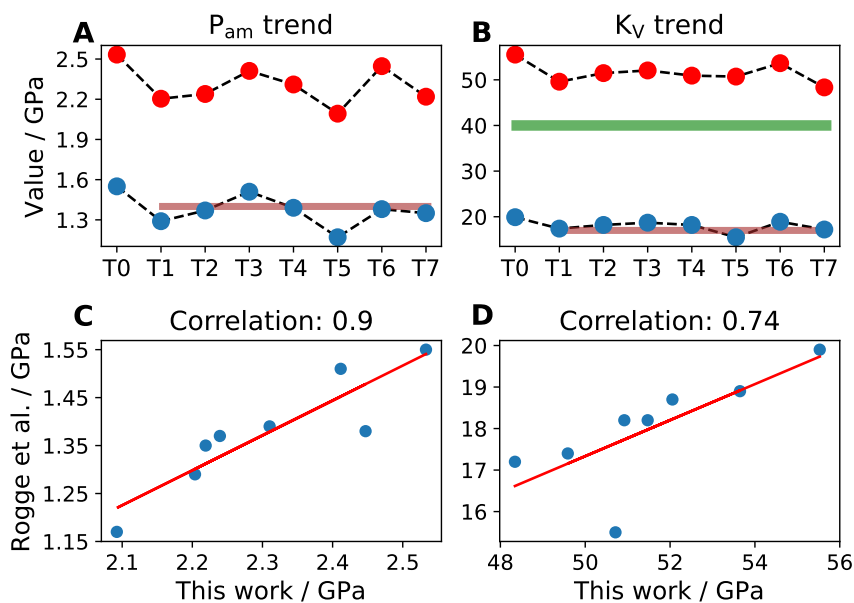


Figure 4.2: Comparison of the amorphization pressure (A) and bulk modulus (B) trends for the 8 defected structures proposed by Rogge et al.[94] using both methodologies. The trends are also compared with the reported DFT values for the pristine structure [79] (green line) and the reported experimental measurement [92] for a structure of average metal coordination of 11 (brown line). The correlation coefficient for amorphization pressures and bulk modulus between the data sets is pictured in (C) and (D), respectively. For both cases, a strong positive correlation is observed.

The preceding findings indicate that while our proposed methodology may not possess the quantitative capabilities to rival other existing schemes in terms of providing realistic values for mechanical properties, it is nonetheless well-suited for investigating the relative stability among defected structures.

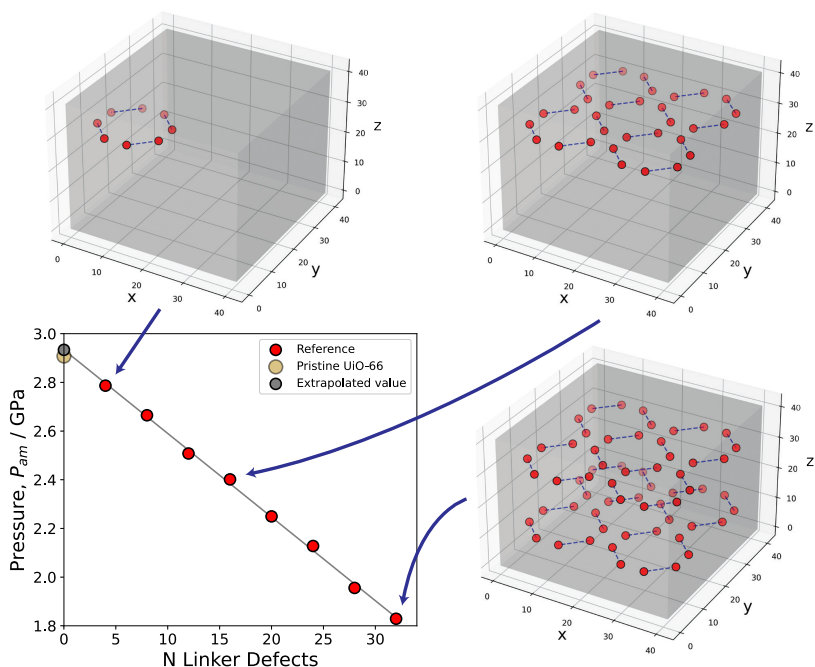


Figure 4.3: Amorphization pressure with respect to the number of linker vacancies for the reference system, where linkers were taken out in order. Included are pictorial representations of the structures with 4, 16 and 32 linker vacancies. The line represents the linear extrapolation of the P_{am} values for the reference system. The extrapolated value using the reference system data is 2.934 GPa, which is close to the value obtained by simulating the pristine structure (2.908 GPa).

Based on this conclusion regarding the suitability of our methodology for studying relative stability, we proceeded to generate a significant number of defected structures by varying the number, distribution, and orientation of linker vacancies. As a basis for future comparison we created a reference set of 8 structures with increasing number of defects (ranging from 4 to 32), where linker vacancies were introduced in an orderly fashion starting from the pristine baseline at the supercell level. As can be seen in Fig. 4.3, the pressure at which the structure collapses decreases when more defects are introduced and the obtained values are able to accurately predict the amorphization pressure simulated pristine structure, via linear extrapolation. In order to determine the degree to which the vacancy introduction process impacts the reference amorphization values, we generated an alternative

reference set in which the same vacancies are introduced randomly. As can be seen in figures S1 and S2, the difference for both individual P_{am} values and trend is minimal between the sets.

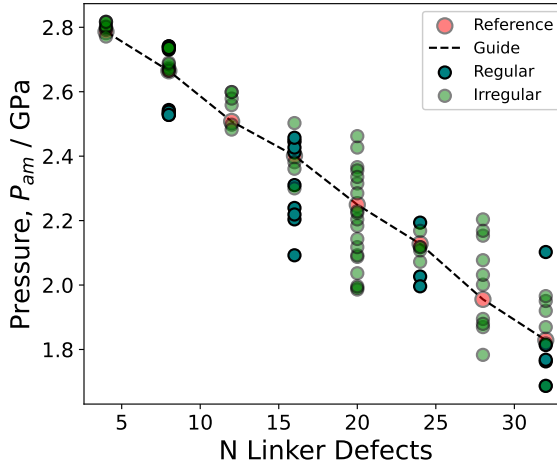


Figure 4.4: Amorphization pressure with respect to the number of linker vacancies contained for all defected structures of study. Each data point corresponds to a defected structure with different vacancy spatial concentration, orientation and order. The dotted line is a visual guide that passes through the reference data. Data points are colored according to the structure generating procedure. High amount of variance in amorphization pressure values is obtained.

Figure 4.4 depicts the amorphization pressure for all the generated defected structures. Notably, a high amount of variance in P_{am} values is observed for structures with the same number of defects but different missing linker distribution and orientation. Comparing the values obtained for $N = 8, 16, 24$ and 32 linker defects, structures with a regular arrangement of vacancies tend to present extreme amorphization values, corresponding to the least and most stable structures in terms of P_{am} , whereas structures with irregular vacancies, where missing linker positions and orientations were selected either randomly or quasi-randomly tend to fall in the middle.

Comparison of amorphization pressure values between sets of structures with different number of vacancies reveals numerous cases in which structures with

a higher number of vacancies are less prone to collapse at higher pressures than structures with fewer defects. This suggests that the number of linker vacancies alone does not solely determine the stability of the structure. Factors such as the selection method, distribution, and orientation of the defects significantly contribute to the variance in amorphization pressure, particularly for structures with a higher number of defects. As was the case for the reference system, in general, the amorphization pressure decreases as the number of defects in the structure increases.

4

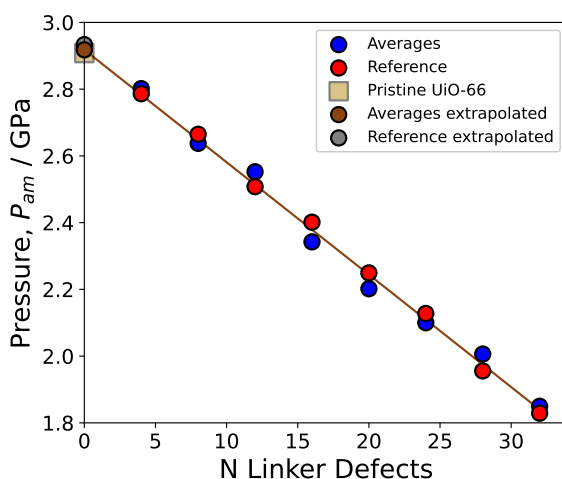


Figure 4.5: Comparison between the reference system (red circles) and the average amorphization pressure value for each set of defected structures (blue circles). The line represents the linear extrapolation of the average values. The extrapolated P_{am} estimation for a structure with 0 linker defects is 2.92 GPa, which is close to the amorphization pressure of the pristine structure obtained using MD (2.908 GPa).

Fig. 4.5 contrasts the results obtained for the reference system with the average amorphization pressure of each set of defected structures. Our results indicate that the amorphization pressure decreases linearly with increasing number of defects, where the linear trend obtained when taking into account all amorphization values is almost the same as the one obtained for the reference set.

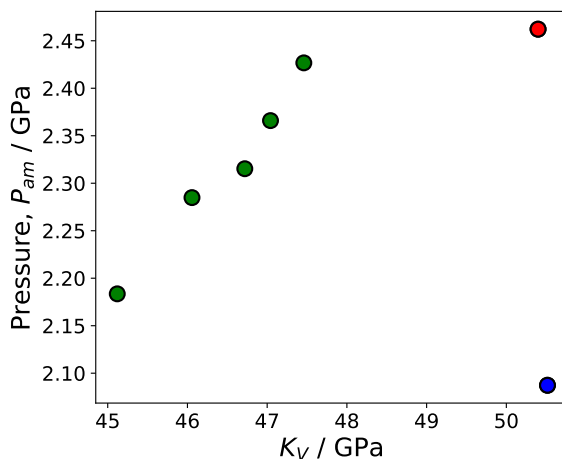


Figure 4.6: Relationship between amorphization pressure and bulk modulus for a representative subset of the structures containing 20 linker vacancies. Most of the studied defected structures follow the trend represented by the green data points where a positive linear relationship between the amorphization pressure and bulk modulus is observed. Outlier structures with high bulk modulus and contrasting P_{am} represented with red and blue circles.

As evidenced by the analysis of the structures proposed by Rogge et al.[94] amorphization pressure values do not provide a complete picture of the stability of the defected frameworks. To address this, we computed the 0 K elastic stress tensor for all structures and from them calculated the relevant elastic moduli. Comparison of amorphization pressure and bulk modulus values reveals that for structures with an irregular arrangement of defects selected randomly from the whole framework volume (which are most of the structures studied in this work) the amorphization pressure is related to the bulk modulus in a positively linear way. Furthermore, said structures tend to have a homogeneous distribution of missing linker orientations, meaning that they don't usually contain a disproportional number of missing linkers of one orientation type. Most of the structures generated quasi-randomly where defects were created in sub-volumes of the framework exhibit similar behavior. Fig. 4.6 shows the relationship between amorphization pressure and bulk modulus for a representative subset of the structures containing 20 linker vacancies. In general,

we observe that structures where the vacancies are more evenly distributed, both spatially and in orientation, follow the linear trend evidenced by the green data points in the figure. Structures where most of the missing linkers had the same orientation (blue data point) and structures with quasi-randomly distributed vacancies that leave a large part of the volume as pristine (red data point) tend to exhibit outlier behavior in this respect.

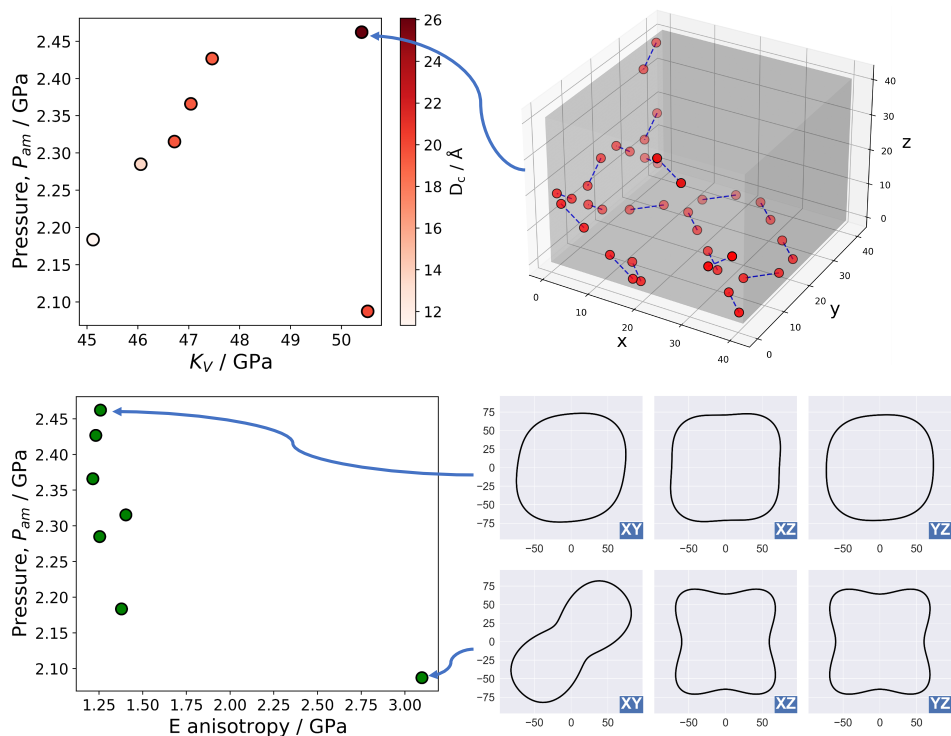


Figure 4.7: Analysis of the representative outlier structures pictured in Fig. 4.6. In plot (A), every data point is color coded according to the mean distance between the linker vacancies and the center of the $2 \times 2 \times 2$ simulation cell (in angstroms). Plot (B) shows the amorphization pressure with respect to the Young modulus' anisotropy for the same structures. The polar plots in the bottom, contrasting the Young modulus anisotropies for two of the representative structures were generated using the ELATE python module[197].

Further examination of the outlier structures reveals that cases in which the vacancies are distributed in a way that a large volume of the structure remains pristine (Fig. 4.7A) exhibit greater stability, evidenced by a large bulk modulus and

amorphization pressure value. Analysis of elastic moduli anisotropies (Fig. 4.7B) is required in order to reveal the directional instability exhibited by structures containing a large number of vacancies with the same orientation. We find that in these cases, low amorphization pressure values correspond to high elastic moduli anisotropies.

4.4 CONCLUSIONS

In this work we aimed to investigate the influence of different distributions of linker vacancies on the relative stability of defected UiO-66 structures. We employed the same force field (UFF) for modeling all defected structures without considering electrostatic interactions. While our approach may not match the quantitative accuracy of other existing schemes in predicting structural and mechanical properties, it proved suitable for examining relative stability among a large number of defected structures.

Through our investigation, we analyzed a significant number of defected structures by manipulating the number, distribution, and orientation of linker vacancies. As expected, our initial analysis revealed that structures with a higher number of defects exhibit lower stability compared to those with fewer defects. Interestingly, we observed significant variation in amorphization pressure values for structures with the same number of defects but different missing linker distributions. This suggests that the stability of a structure is not solely determined by the number of linker vacancies, but also influenced by factors such as the selection method, distribution, and orientation of the defects. Furthermore, when comparing amorphization pressure and elastic moduli values, we found that structures with more evenly distributed vacancies, both spatially and in orientation, exhibited a positive linear relationship between amorphization pressure and bulk modulus. In contrast, structures with imbalanced missing linkers of the same orientation or quasi-randomly distributed vacancies where a substantial portion of the volume remains pristine, exhibited

outlier behavior in this regard.

To gain a comprehensive understanding of the behavior of outlier defected structures, it is crucial to analyze the anisotropies of elastic moduli, particularly for structures containing a significant number of vacancies with the same orientation. Our study revealed that in such cases, structures with low amorphization pressure values exhibited high elastic moduli anisotropies, indicating directional instability. The proposed methodology can be employed to predict the stability of defected UiO-66 structures and guide the selection of optimized defect configurations for specific applications. Moreover, future studies should consider the impact of defect distribution and orientation on amorphization pressure and elastic properties to obtain a more comprehensive understanding of UiO-66-based materials' behavior.

5

5

EFFECT OF WATER LOADING ON THE STABILITY OF PRISTINE AND DEFECTED UiO-66

Materials used for water treatment purposes need to be stable for easy handling and cost-effectiveness. UiO-66 has been identified as a promising option. In this work, we investigate the impact of water loading on the structural and mechanical properties of pristine and defected UiO-66 using classical molecular simulations. We employ and compare two approaches for modeling non-bonded interactions between the framework and water molecules: direct Lorentz-Berthelot (L-B) mixing and hybrid mixing. We conducted molecular dynamics simulations to examine the spatial arrangement of water molecules within the framework, water affinity for specific framework interaction sites, and their impact on the framework's structural parameters under atmospheric conditions, high hydrostatic pressures, and increased water loading. Our results indicate both methods predict water affinity near zirconium clusters, but differ in identifying principal interaction sites and interaction strength. L-

B mixing predicts strong binding to linker oxygen atoms, restricting water movement, while hybrid mixing indicated dynamic water behavior, with site-to-site hopping and pore-to-pore movement observed at moderate and high loadings. Structural analysis at increased water loadings showed adsorption-induced expansion using L-B mixing due to linker-cluster bond stretching, contrasting with slight system contraction predicted by hybrid mixing. High-pressure NPT simulations evidence that water loading reduces amorphization pressure, although values obtained using both approaches differ significantly at moderate and high loadings.

5

5.1 INTRODUCTION

Water pollution is an escalating concern in the world, as diverse sources such as sewage, wastewater, agricultural pesticides, and industrial waste continually introduce harmful substances into natural water bodies[199–201]. This contamination poses significant threats to ecosystems, the environment, and human health. Recent research has highlighted the potential of metal-organic frameworks (MOFs) in addressing wastewater treatment challenges[93, 202–204]. MOFs have demonstrated effectiveness in eliminating a variety of pollutants, including phosphates[205, 206], fluorides[207, 208], heavy metals[209, 210], pharmaceuticals[211, 212], and chemical warfare agents[213, 214]. The limitations of traditional water harvesting methods, such as their reliance on high humidity and energy inputs, further underscore the need for innovative and efficient approaches like MOFs[215–217].

For industrial applications, it is crucial that materials used in water treatment exhibit structural stability in moist conditions to ensure ease of handling and cost-effectiveness. Despite the development of numerous MOFs, only a select few are chemically stable enough for such applications[91, 218–220]. Among these, UiO-66, a Zr-based MOF, is particularly noteworthy for its exceptional water stabil-

Based on  E. Acuna-Yeomans, P.J. Goosen, J.J. Gutierrez-Sevillano, D. Dubbeldam and S. Calero, *Effect of water loading on the stability of pristine and defective UiO-66*, Journal of Materials Chemistry A, **2024**, 37, 2050-7496 [198].

ity, which is attributed to the robustness of the Zr-O bond and a unique geometry that minimizes water inclusion and reduces hydrolysis reactions[89, 90, 90, 91, 210]. UiO-66 features zirconium-based $Zr_6O_4(OH)_4$ clusters interconnected by 1,4-benzenedicarboxylic acid (BDC) ligands. In its pristine, defect-free state, each inorganic cluster is 12-fold coordinated, contributing to its remarkable structural stability under high pressure conditions[177–180, 185, 186]. Functionalized derivatives of UiO-66, developed to tune hydrophobicity, also exhibit impressive stability, further underscoring the potential of Zr-based MOFs in advanced water treatment applications[92, 93, 214, 221–223]. Most synthesis procedures for UiO-66 result in a defected structure with missing linkers, typically reducing the coordination number of each zirconium cluster to 11, indicating one missing linker per unit cell on average[168, 178, 181–183]. Defects increase the porosity and surface area, enhancing adsorption behavior[79, 84, 85, 186], catalytic properties[168, 187], and proton conductivity[188, 189]. However, defects also reduce structural stability, creating a trade-off between improved adsorption and mechanical integrity[84, 94, 181].

Molecular simulations provide a reliable means to analyze the relationships between material structure and specific properties, particularly when adsorbates or defects are present. Over the past decade, computational studies have extensively examined the adsorption properties of pristine and defected UiO-66, focusing primarily on water and CO_2 adsorption[87, 88, 95, 190, 224]. These simulations have offered valuable insights for industrial applications such as water harvesting and gas separation, often modeling UiO-66 as a rigid structure interacting with guest molecules solely via non-bonded potentials.

To accurately study the structural and mechanical properties of UiO-66, a flexible model of the framework is essential. Flexible models, such as the Rogge et al. force fields developed in 2016[94], have been extensively validated for predicting the properties of unloaded UiO-66. These models employ ab-initio derived parameters tailored to each specific structure, constructed through the QuickFF procedure[150, 225] developed by the same group. However, these force fields

were primarily validated by reproducing the structural and mechanical properties of evacuated systems, where interactions with adsorbate molecules were not considered. Recent studies[226, 227] have demonstrated that when adsorbates such as acetone and isopropyl alcohol are introduced, the Rogge potential inadequately captures adsorbate-framework interactions, particularly hydrogen bonding with the inorganic clusters. This limitation underscores the need for modifications to the force field to accurately model the interaction between Zr clusters and adsorbates in loaded UiO-66 systems. The primary objective of this work is to determine how water loading affects the structural and mechanical properties of flexible UiO-66. Given the established reliability of the Rogge force fields in accurately predicting these properties, we prioritized maintaining their original parameters for simulating water-loaded frameworks. Instead of altering these parameters, we assessed and compared two approaches for modeling the interaction between the framework and water molecules: direct Lorentz-Berthelot (L-B) mixing and hybrid mixing. The hybrid mixing method has been previously employed to study the pore filling process and water diffusion within UiO-66[228], using separate water force fields to model water-water interactions (MB-pol[229]), intra-framework interactions and water-framework interactions (TIP4P2005[230]). In our study, the hybrid mixing method utilizes the Rogge force field for interactions between framework atoms and a combination of the Generalized amber force field (GAFF)[60] and Universal force field (UFF)[61] for interactions between the framework and water molecules. By systematically evaluating these approaches, we aim to provide a deeper understanding of how water impacts the stability and performance of UiO-66, with significant implications for its use in industrial water treatment applications.

5.2 METHODOLOGY

Along with the pristine structure, we considered the eight defected structures (and corresponding force fields) proposed by Rogge et al.[94], each containing linker defects: one of them (type 0) corresponds to a system with one linker vacancy per unit cell, while the rest (types 1-7) represent structures in which an additional, distinct linker defect is introduced to the type 0 parent structure (Fig. C.1). Further details on the force fields and the construction of the structures are provided in the first portion of Appendix C. Before the production simulations, these structures were loaded with different amounts of water molecules, from 10 molecules per unit cell of the framework (corresponding to a relative humidity of 5%) to 120 molecules per unit cell (80% RH), near the water saturation point at room temperature. As was done in recent published work[88, 228, 231], the quantity of water molecules within the MOF structure at various relative humidity levels was determined using the experimental water adsorption isotherm for UiO-66[95, 232].

5

5.2.1 FORCE FIELDS AND MODELS

We model the pristine and defected frameworks using the group of force fields proposed by Rogge et al.[94] which have proven to provide an accurate prediction of the structural and mechanical properties of the unloaded systems. The functional form for the interactions between framework atoms, regardless of the inclusion of linker vacancies, is the following:

$$U = U_{\text{bonded}} + U_{\text{non-bonded}} \quad (5.1)$$

where the covalent interactions between neighboring atoms are mediated through harmonic and Fourier-style potentials

$$U_{\text{bonds}} = \sum_{N=1}^{N_{\text{bonds}}} \frac{1}{2} K_{r,n} (r_n - r_{n,0})^2 \quad (5.2)$$

$$U_{\text{bends}} = \sum_{N=1}^{N_{\text{bends}}} \frac{1}{2} K_{\theta,n} (\theta_n - \theta_{n,0})^2 \quad (5.3)$$

$$U_{\text{dihedrals}} = \sum_{N=1}^{N_{\text{dihed}}} \frac{1}{2} K_{\phi,n} (1 - \cos(m\phi - \phi_0)) \quad (5.4)$$

$$U_{\text{oopd}} = \sum_{N=1}^{N_{\text{oopd}}} \frac{1}{2} K_{d,n} (d_n - d_{n,0})^2 \quad (5.5)$$

5

Two terms contribute to the non-bonded portion of the potential energy function. The electrostatics are described by the Coulomb interaction between spherical Gaussian densities with distinct radii d_i and d_j containing charges q_i and q_j , respectively. The potential energy term for particles separated by a distance r_{ij} is:

$$U_{\text{Electrostatic}} = \frac{1}{2} \sum_{i < j} \frac{q_i q_j}{4\pi\epsilon_0 r_{ij}} \operatorname{erf} \left(\frac{r_{ij}}{\sqrt{d_i^2 + d_j^2}} \right) \quad (5.6)$$

The second term models the van der Waals interactions between two atoms i and j separated by a distance r_{ij} using the two-parameter Molecular Mechanics (MM3)[233, 234] Buckingham potential:

$$U_{\text{vdw}} = \sum_{i < j} \epsilon_{ij} \left[1.84 \times 10^5 \exp \left(-12 \frac{r_{ij}}{\sigma_{ij}} \right) - 2.25 \left(\frac{\sigma_{ij}}{r_{ij}} \right) \right] \quad (5.7)$$

For bonded atoms, different scaling and exclusion rules are applied for each contribution to the non-bonded part of the potential energy. As defined by the MM3 force field, 1-2 and 1-3 exclusion rules for bonded pairs are applied to VdW interactions, with no scaling applied to atoms separated by two or more atoms (1-4). For framework atoms of different species, the equilibrium distance (σ_{ij}) and well depth (ϵ_{ij})

parameters are determined via the empirical Lorentz-Berthelot mixing rules:

$$\sigma_{ij} = \frac{1}{2}(\sigma_i + \sigma_j) \quad \epsilon_{ij} = \sqrt{\epsilon_i \epsilon_j} \quad (5.8)$$

The interaction parameters of the energy equation depend on the particular structure to be modelled, that is, each of the 9 structures simulated (pristine, type 0 defected and type 1-7 defected) have distinct associated sets of parameters, and they are provided in the original publication of the force field[94].

The water molecules were modeled using the extended SPC model[235, 236] , although the Tip4P2005[230] force field was initially implemented and considered as well. The SPC/E model was selected primarily due to its lower computational cost, as it involves taking into account fewer interactions, and because early results showed that both models influenced the framework similarly. The non-bonded parameters for the description of water-water interactions were derived using Lorentz-Berthelot mixing rules as well.

Two distinct methods for modeling the interaction between water molecules and the framework atoms were employed, in both cases the VdW interactions are modelled using the Lennard-Jones potential and the electrostatics are modelled using the canonical Coulomb potential for point charges. In the first method, the Lennard-Jones parameters for the description of the water - framework interaction were derived by applying Lorentz-Berthelot (L-B) mixing rules directly. In here, it should be noted that although the empirical combination of L-J parameters from popular rigid water models and generic force fields have been used extensively in published work to study this and similar systems, this is not the case for the combination of SPC/E and MM3 parameters. This first mixing methodology is thus implemented as an intuitive point of reference, reflective of the usual default choice in the simulation community. In the second method, the Lennard-Jones contribution of the water - framework interaction was modified by employing GAFF[60] and UFF[61] ϵ and σ parameters for the framework atoms instead of the MM3 force

field (MM3)[233, 234] parameters used for intra-framework non-bonded interactions, therefore making use of two framework force fields in a hybrid manner.

5.2.2 SIMULATION DETAILS

The pressure-volume behavior of UiO-66 structures was determined using molecular dynamics (MD) simulations in the flexible NPT ensemble ($N, P, \sigma_\alpha = 0, T$). This ensemble allows dynamic changes in both simulation cell volume and shape, enabling the estimation of the amorphization pressure (P_{am}) of the framework. For each system, flexible NPT simulations were conducted starting from a high pressure. The unloaded structures were first energy minimized and equilibrated at atmospheric conditions to record the reference volume (V_r). After loading with water molecules, the structures were equilibrated at high pressure, monitoring the instantaneous volume (V_i). Amorphization was deemed to occur if V_i dropped below a predefined threshold (V_t), proportional to V_r . The pressure was adjusted in subsequent simulations based on whether amorphization occurred, using a step size (ΔP) of 0.005 GPa. The final P_{am} was determined as the highest pressure at which the structure remained stable. Large simulation cells were used to mitigate fluctuations in instantaneous pressure, which can induce phase transitions at artificially low pressures, particularly in flexible MOFs[146, 147].

All simulations were performed using the LAMMPS package[152]. The Verlet integrator with a timestep of 1 fs ensured energy conservation, while independent thermostats optimized equilibration times by grouping atoms of the framework and water. A Nose-Hoover thermostat (300 K, 100 fs relaxation time) and an MTTK barostat (1000 fs relaxation time) controlled temperature and pressure, respectively. Radial distribution functions (RDFs) and 3D water density distribution maps[237] were averaged from 500 ps NVT ensemble runs after equilibration. Simulations used a $2 \times 2 \times 2$ supercell with non-bonded interactions truncated at 14.0 Å and long-range electrostatics calculated via Ewald summation. Periodic boundary conditions were applied in all dimensions, with specific scaling of 1-2, 1-3, 1-4 non-bonded

interactions as per the force field requirements.

5.3 RESULTS AND DISCUSSION

5.3.1 EFFECT OF WATER LOADING ON THE PRISTINE STRUCTURES

In order to evaluate the performance of each parameter mixing method, we start by analyzing the spatial arrangement of water molecules inside the undefected framework at different water loadings. The Radial Distribution Function (RDF) describes how the average density varies as a function of distance from a chosen reference particle. By selecting framework atoms as references, they can be used to identify preferential adsorption sites within its surface and characterize the interaction environment in the vicinity of the metal clusters and organic ligands.

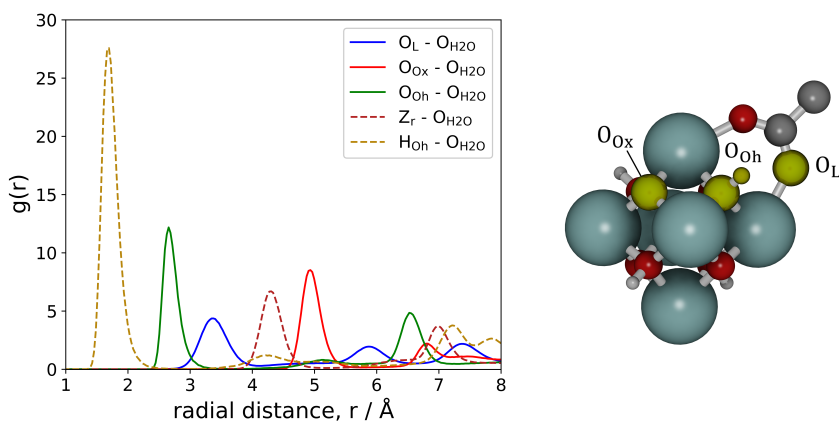


Figure 5.1: Left: RDF calculated using hybrid mixing between water molecules and framework interaction sites near the zirconium (Zr) cluster. Obtained at a temperature and pressure of 300 K and 1 atm, respectively, with a water loading of 10 molecules per unit cell. Right: The identified interaction sites in the inorganic cluster are the linker oxygen O_L , hydroxyl group O_{Oh} and the dehydroxylated group O_{Ox} within the cluster.

Regarding the initial interaction sites, at low loadings both models predict water molecules tend to agglomerate around the metal clusters while keeping away from the central portion of the organic ligands, in line with previously published research[88, 224, 228]. However, each model suggests different species near the

metal cluster as the primary interaction site for water. L-B mixing predicts that the oxygen atoms connecting the Zr atoms with the linkers are the main interaction site, whereas hybrid mixing points to the hydroxyl groups within the inorganic cluster.

For the L-B mixing simulations at low loadings, the RDF describing the spatial correlation between O_{H_2O} and O_L peaks at a radial distance of 1.9 Å, contrasting with a clear separation from O_{Ox} and O_{Oh} sites (Fig. C.2a). This behavior is not consistent with previous computational studies indicating that water preferentially binds to the hydroxyl hydrogens in the zirconium clusters. Recently published computational studies of water diffusion and pore filling process in UiO-66 predicts an interaction site affinity order of $O_{Oh} > O_L > O_{Ox}$ [228]. Furthermore, the peak distance indicates heavy perturbation of the Zr – O_L bond electronic environment. While the interaction site water affinity order predicted by hybrid mixing (Fig 5.1) is qualitatively congruent with said findings and the radial distance to O_{Oh} is the same (≈ 2.8 Å) the density of water molecules near the preferential site at low loadings is underestimated by 36%. The RDFs between water oxygen atoms (O_{H_2O}) and potential bonding sites were analyzed at higher loadings of 40 and 100 water molecules per unit cell using both mixing methods (Fig. C.2). Hybrid mixing predicts a broadening of RDF peaks with increasing water content, indicating a more dispersed distribution of water molecules. As loading increases, more water molecules shift away from the zirconium clusters toward the pore centers, forming one-dimensional water chains and clusters (Fig. C.3). In contrast, L-B mixing shows a slight decrease in water presence around zirconium clusters, with less pronounced occupancy within the pore volume.

A series of 3 ns simulations in the NVT ensemble were conducted at increasing loadings to monitor water molecule positions and analyze their trajectories. Figure C.4 in Appendix C compares the mean square displacement (MSD) of water molecules for the two interaction methods at a moderate loading of 40 water molecules per unit cell. As shown in Figure 5.2, L-B mixing results in water molecules remaining highly localized near the linker oxygen, with minimal dimer

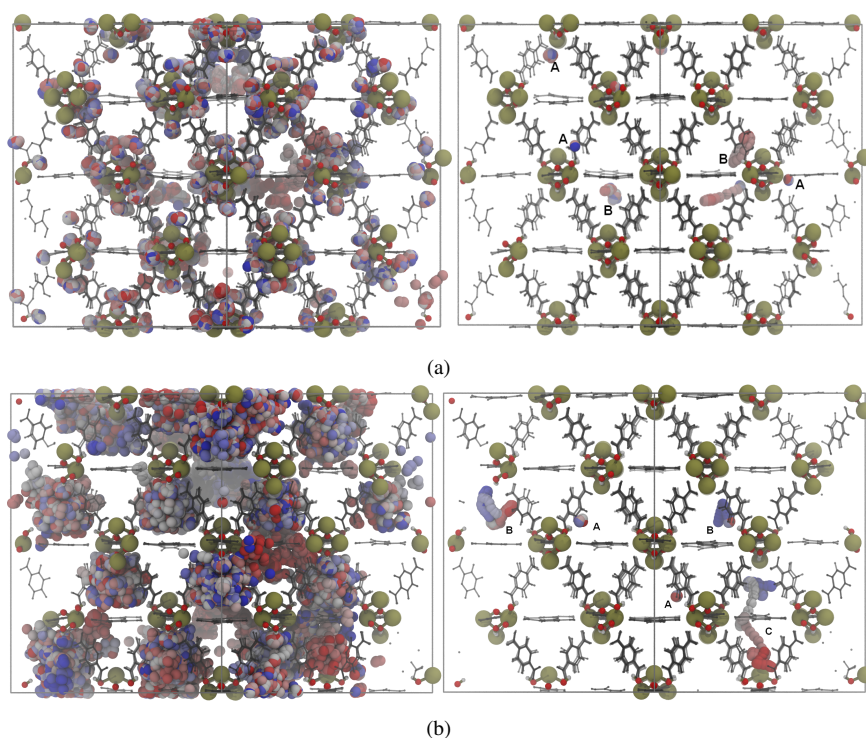


Figure 5.2: Trajectories described by water molecules inside the framework over a simulation period of 500 picoseconds at moderate loading (40 molecules / uc) using (a) L-B and (b) hybrid mixing at atmospheric conditions. On the left side, the cumulative trajectories of all O(H₂O) atoms are pictured. On the right side a subset of trajectories is presented, representative of 3 types of observed behavior: A) molecules bounded to an interaction site, B) molecules orbiting already occupied sites, C) molecules of the previous type hopping from one interaction site to another within the same pore. Trajectories are colored based on a gradient from red (start of trajectory) to blue (end of trajectory).

formation. In contrast, hybrid mixing simulations exhibit diffusive behavior around the predicted adsorption sites, with occasional formation of water dimers.

To assess how differences in predicted adsorption sites affect the framework structure, NPT simulations were performed at atmospheric conditions with increased water loadings. System volume and bond distances between inner-cluster atoms were monitored and averaged. As shown in Figure 5.3, L-B mixing predicts a significant increase in the unit cell lattice parameter with loading, reaching a 7% volume increase at 80 molecules per unit cell compared to the unloaded structure. In

contrast, hybrid mixing simulations indicate a slight decrease in lattice parameter, suggesting water-induced framework contraction.

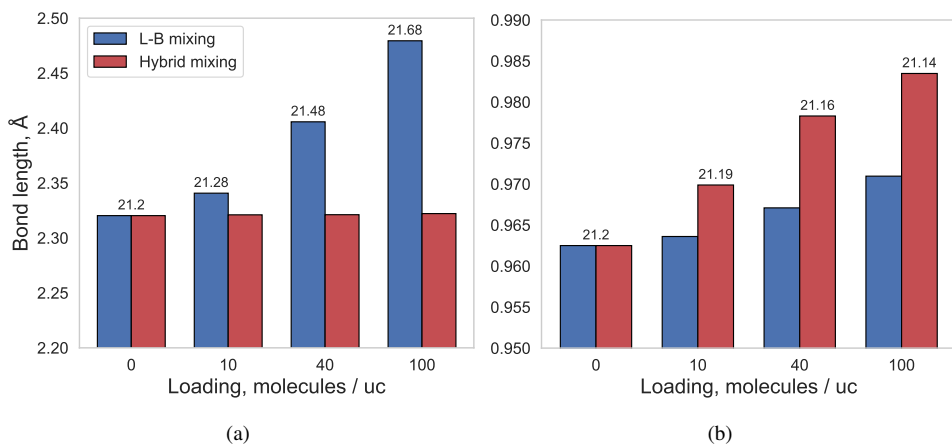


Figure 5.3: Average bond lengths between (a) Zr and O_L , and (b) O_{Oh} and its bonded hydrogen. The unit cell lattice parameter is indicated above each bar. The data for (a) and (b) at a given loading are from the same four simulation sets.

The expansion correlates with stretching of Zr – O_L bonds. In L-B mixing, increased water presence near O_L results in noticeable elongation of Zr – O_L bonds, while hybrid simulations show a more pronounced effect on O_{Oh} – H bonds. Non-preferential site bonds, such as Zr-Ox and Zr-Oh, experience minimal changes in L-B mixing (Fig. C.5). The observed weakening of framework bonds, particularly Zr – O_L , suggests a reduction in cluster-linker coordination and a decrease in mechanical stability upon water loading.

The UiO-66 crystal structure is known for its stability under high pressure, remaining intact up to approximately 1.4 GPa [92]. To assess the impact of water loading on structural stability, NPT simulations were conducted under varying hydrostatic pressures and water loadings. Figure 5.4 shows that the amorphization pressure (P_{am}) decreases with increasing water loading. At low loadings (10-20 H_2O molecules per unit cell), P_{am} values are similar for both models. However, at intermediate loadings (30-40 H_2O molecules), significant differences emerge, due

to the hybrid model predicting water dimer and cluster formation at lower water concentrations than the L-B model. The water groupings tend to occupy space closer to the middle of the pores and away from the metal clusters, thus contributing less to cluster-linker weakening. L-B mixing likely predicts unrealistically low P_{am} values, and the use of hybrid mixing is suggested at moderate and low loadings.

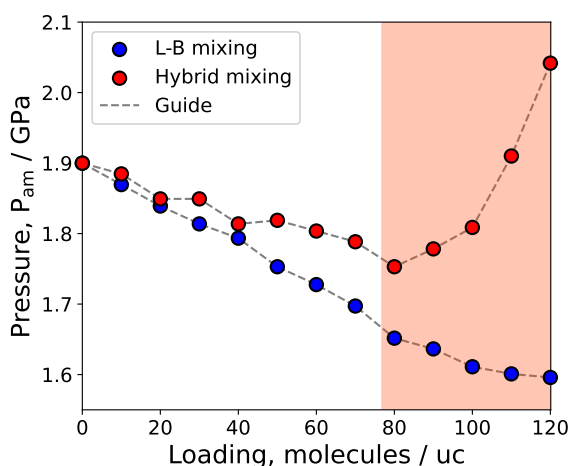


Figure 5.4: Amorphization pressure (P_{am}) with increased water loading at 300 K. Both models show similar P_{am} values at low loadings but diverge at higher loadings. Hybrid mixing predicts a higher P_{am} at high loadings, reflecting methodological limitations.

At high loadings (> 80 molecules per u.c.), simulations using hybrid mixing exhibit a noticeable increase in P_{am} values, a behavior absent in L-B mixing simulations. This difference stems from the water distribution within the crystal and highlights a limitation in our framework collapse detection methodology, in which a framework collapse is defined by a system volume drop below a threshold during equilibration. At high particle loadings, the collapse may be impeded or masked, preventing detection by our criteria.

Our findings indicate that in a system as complex as UiO-66 and water, the selection of guest-host interaction parameters significantly influences the distribution of the former within the available pore volume. When comparing the employed methodologies, hybrid mixing predicts water molecule behavior more in line with

5

previous published simulation studies on the diffusion and pore-filling process of different adsorbates in UiO-66 and analogous structures [88, 226–228]. The results obtained when employing direct Lorentz-Berthelot mixing rules predicts an unusually strong coordination between the water molecules and the framework oxygen atoms connecting the organic linkers with the zirconium cluster, heavily restricting the movement of individual water molecules and inhibiting the formation of water clusters at moderate loadings. Moreover, in both cases, the results indicate that the particular spatial arrangement of the water molecules at different loadings influences both inner-cluster and framework structural parameters. This is more evident when employing L-B mixing, as water coordination causes a stretching of the linker-cluster bonds and subsequent increase in system volume. This mechanical response to loading also impacts loss of crystallinity pressures and is uncharacteristic of a MOF as rigid as UiO-66, and it might be evidence of poor cross-interaction parameter selection.

5.3.2 EFFECT OF WATER LOADING ON DEFECTED STRUCTURES

Previous simulation studies show that although the inclusion of defects correspond to a negligible decrease in equilibrium volume at a particular temperature, they introduce substantial decrease in both amorphization pressure and bulk moduli [94, 238]. The effect of water loading at high pressure was investigated for structures containing one and two linker defects per unit cell. NPT simulations were conducted at 300 K, systematically varying the water loading from 10 molecules per unit cell to 80. The resulting P_{am} data obtained using both methods are visually presented in figure 5.5.

A decrease in amorphization pressure is predicted upon increasing water inclusion for all defected structures, using both parameter mixing methods. In terms of discerning the relative stability of 11-fold coordination structures under increasing water loading, both methodologies predict that inclusion of type 3 vacancies yield the most stable configuration, while type 5 defects exhibit the least stability to high

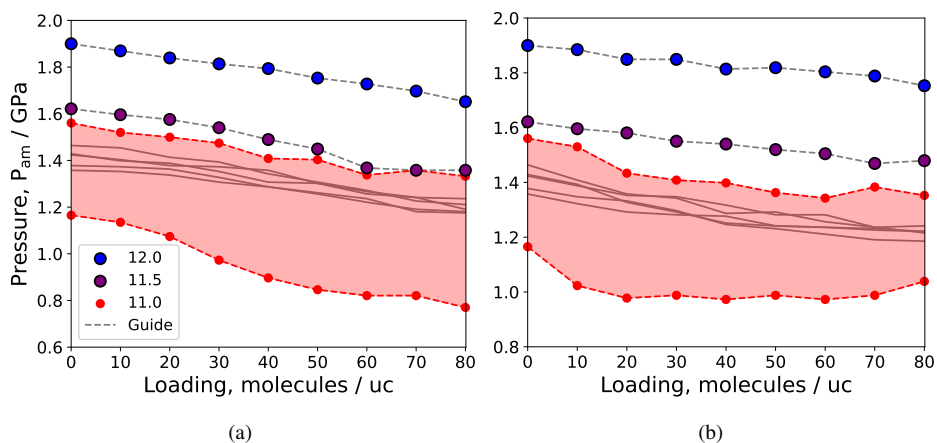


Figure 5.5: Amorphization pressure predicted with increased water loading for structures containing linker defects using (a) L-B mixing and (b) hybrid mixing. The color of the curve indicates the average linker - cluster coordination per unit cell. The area in red indicates the P_{am} range of values obtained for structures with an average cluster coordination of 11.0, where the limiting upper and lower red curves indicate the most (type 3) and least stable (type 5) structures. Results for the pristine structures (blue) included for comparison.

hydrostatic pressure. A close inspection of the results obtained for the structure with 1 missing linker per unit cell (Fig. C.6a) reveals a similar comparative behavior to the pristine structures, where the amorphization values predicted at low loadings using both models are almost identical, followed by deviations at middle and high loadings. Interestingly, a different trend is observed for the 11-fold coordinated structures (Figs. C.6b-d), where the hybrid mixing simulations predict a sharper decrease in P_{am} values at low loadings when compared to the L-B mixing results. Furthermore, unlike with the less-defected structures, both methods predict comparable high-loading values for all structures with two linker vacancies per unit cell.

Figure 5.6 depicts the RDF of water molecules with respect to the metal sites in a structure containing type 3 defects at low loading. For this structure as well as all others containing two linker vacancies per unit cell, when hybrid mixing is employed, water molecules preferentially interact with open Zr atoms and thus tend to agglomerate around them, evidencing strong $O_{H_2O} - Z_r$ interactions between them.

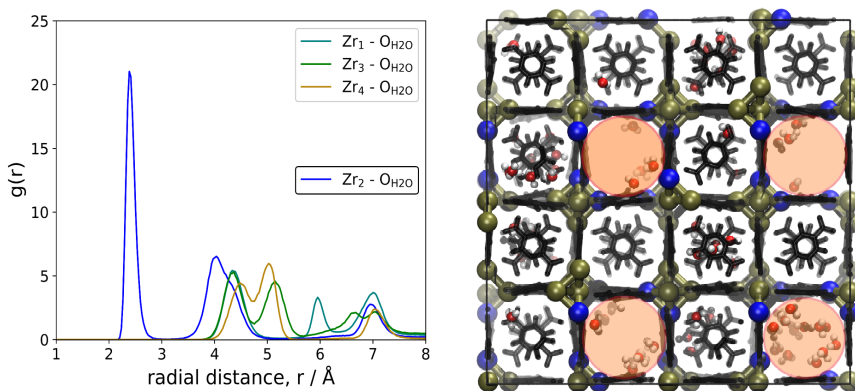


Figure 5.6: Left: RDF between water molecules and the zirconium atoms for the structure containing type 3 defects. The blue curve depicts the RDF between H_2O and open Zr_2 sites, where all other show the average density of water with respect to fully coordinated Zr sites. Right: Representative snapshot along the XY plane of the structure containing type 3 defects. Open metal sites pictured in blue. 1D channels created by linker vacancies highlighted in orange. Similar water molecule behavior observed in simulations with other defected structures at low loading, using hybrid mixing (Figs. C.7-C.12).

5

Furthermore, water molecules bonded to the open metal sites exhibit reduced translational and rotational movement, similarly to water molecules near the O_L atoms when using L-B mixing in the pristine structures. Water molecules near defected inorganic clusters, but not directly bonded to Zr, frequently change hydrogen-bond partners and exhibit higher orientational mobility. As loading increases water begins to occupy the pore regions, with molecules near the center displaying less restricted movement compared to those near interaction sites.

As was done for the pristine framework, the structural properties of the defected systems at atmospheric conditions, using both mixing methods were also analyzed. Figure 5.7a illustrates the change in unit cell volume for pristine, type 0 defected, and type 3 defected structures when using hybrid mixing. Although all three systems generally contract upon loading, the defected structures show a slight expansion at low loadings. This predicted volume expansion is more noticeable in structures with more linker vacancies, as seen when comparing the results for type 0 and type 3. The type 3 defected structure, representative of other structures with two linker defects

per unit cell, exhibits a linear increase in system volume followed by contraction once a loading of 20 molecules per unit cell is reached. Comparing the trends for the type 0 and type 3 structures with the pristine one, the initial increase in system volume is likely related to the number of open metal sites available after linker vacancies are introduced. When employing hybrid mixing, water molecules bound to open metal sites contribute to the stretching of linker-cluster bonds, and once these sites are occupied, the general trend of volume contraction resumes.

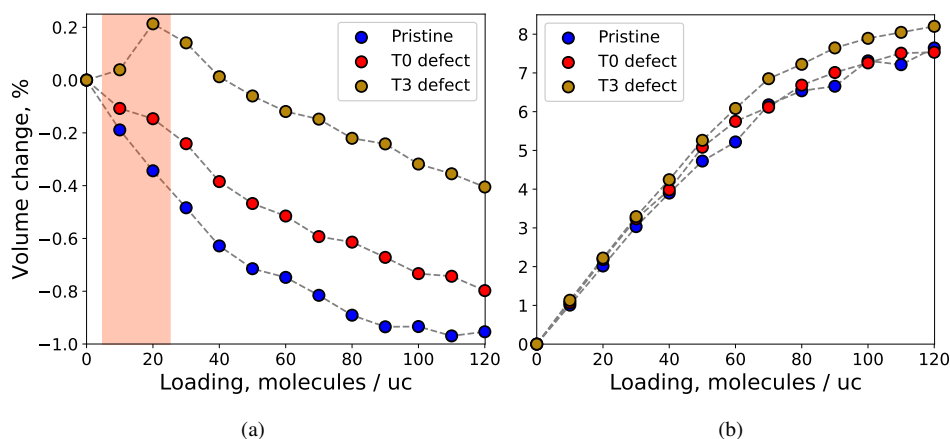


Figure 5.7: System volume change upon water loading at atmospheric conditions, using (a) hybrid mixing and (b) L-B mixing. Results for the pristine, type 0 (1 defect / uc) and type 3 (2 defects / uc) structures presented. Unlike pristine behavior upon water loading, slight increase in framework volume is observed at low loadings for defected structures when using hybrid mixing (highlighted in orange).

For all three structures and over the loading range, the simulations employing hybrid mixing predict an overall gradual reduction in volume, eventually plateauing for loading values close to saturation. As was the case for the pristine structure, direct Lorentz-Berthelot mixing predicts a significant volume expansion (a 7% to 8% increase over the loading range) of framework volume upon water loading for defected systems (Figure 5.7b). Although the results obtained using hybrid mixing are more in line with the expected behavior of UiO-66 and its employment over direct L-B mixing is recommended (comparisons in Figs. 13-15), further force field refinement might be necessary to more accurately capture the interactions between

water molecules and open metal sites in the defected structures.

5.4 CONCLUSIONS

This work investigated the effect of water loading on the stability of pristine and defected UiO-66 via molecular simulations. We used two methodologies for modeling non-bonded interactions: direct Lorentz-Berthelot (L-B) mixing and hybrid mixing. L-B mixing combines Lennard-Jones parameters for framework-framework and water-water interactions, while hybrid mixing employs GAFF and UFF parameters for the framework. We examined water distribution within the framework at atmospheric conditions. Both methodologies predicted water clustering around zirconium clusters, but RDF analysis showed differences in interaction sites and strengths. L-B mixing suggests strong binding of water to linker oxygen atoms (O_L), restricting movement and diffusion. Hybrid mixing, however, shows interactions with the hydroxyl groups of the inorganic cluster (O_{Oh}), resulting in dimer formation, site-to-site hopping at low loadings, and pore-to-pore diffusion at higher loadings, which aligns with recent studies on water diffusion in UiO-66.

NPT simulations at atmospheric conditions demonstrated that interaction strength significantly influences structural parameters. At high water loadings, hybrid mixing predicted slight contraction of the system, whereas L-B mixing indicated over a 7 percent expansion due to stretching of linker-cluster bonds. This suggests that L-B mixing inadequately models the rigidity of UiO-66. High-pressure NPT simulations showed that water loading decreases amorphization pressure for both methodologies compared to the unloaded structure. L-B mixing consistently predicted lower amorphization pressures, with notable deviations at middle and high loadings, consistent with previous studies where water agglomeration reduces linker-cluster bond weakening. Similar trends were observed for structures with one missing linker per unit cell. For 11-fold coordinated structures, hybrid mixing predicted a sharper decrease in amorphization pressure at low loadings compared to L-B mixing, though both

methods converged at high loadings for structures with two linker vacancies per unit cell.

For structures with two linker vacancies, hybrid mixing simulations showed water molecules preferentially interacting with open Zr atoms, leading to agglomeration and strong $\text{O}_{\text{H}_2\text{O}} - \text{Zr}$ interactions. These water molecules exhibited reduced movement, similar to those near O_{L} atoms in L-B mixing. Initial volume expansion was observed at low loadings due to interactions with open metal sites, which then resumed contraction once these sites were filled. This indicates a need for refining force field parameters to better model interactions with open Zr sites in defected UiO-66. Overall, our findings emphasize the significant impact of water loading on UiO-66's structural stability and the importance of selecting appropriate interaction parameters for accurate simulations. The differences between L-B and hybrid mixing highlight the need for careful parameter selection and further development of force fields for defected frameworks.

6

INFLUENCE OF ADSORBATE POLARITY ON THE STRUCTURAL STABILITY OF UiO-66

6

This study investigates the structural stability of UiO-66 under varying loadings of methane, methanol, water, dimethylformamide (DMF), and chloroform using molecular dynamics simulations. The interplay between adsorbate properties—such as polarity, molecular size, and hydrogen-bonding capacity—and framework interactions reveal trends affecting amorphization pressure and structural deformation. Polar adsorbates exhibited stronger framework interactions, while non-polar and larger molecules displayed distinct packing behaviors. These results provide insights into the relationship between adsorbate characteristics and framework stability, offering guidance for optimizing UiO-66 for applications in gas storage and separation.

Based on  E. Acuna-Yeomans, J.J. Gutierrez-Sevillano, D. Dubbeldam and S. Calero, *Influence of adsorbate properties on the structural stability of UiO-66*(in preparation).

6.1 INTRODUCTION

The performance of UiO-66 under real-world conditions depends on its structural response to external stimuli, such as mechanical stresses, the presence of defects, and the loading of guest molecules. Adsorption in UiO-66 material may occur with a preference for interactions with the metal-oxide zirconium clusters or more favorable interactions with aromatic linker rings, depending on the chemical nature of the adsorbate molecule[239, 240]. Among the diverse adsorbates studied in UiO-66, methane has been extensively investigated for its potential as a clean-burning fuel, as well as for its storage and separation applications. Previous studies have shown that methane adsorption in UiO-66 is primarily driven by van der Waals interactions with the framework linkers[241–243]. Methanol, on the other hand, exhibits a more complex adsorption behavior due to its higher dipole moment and hydrogen bonding capabilities, which facilitate interactions with the hydroxylated zirconium clusters in UiO-66[244, 245]. The polar nature of methanol enhances adsorption selectivity and provides insights into framework-adsorbate interactions involving polar solvents.

Water adsorption in UiO-66 has also been extensively studied, not only for its role in adsorption and separation applications, but also for understanding the framework's stability under humid conditions[246, 247]. The robust Zr-O bonds in UiO-66 confer significant water stability, although structural defects can alter the hydrophilicity of the framework and influence adsorption behavior[239, 247]. Studies have shown that water preferentially interacts with hydroxyl groups on the zirconium clusters, forming hydrogen-bonded networks that impact both adsorption and framework stability[248, 249].

Unlike methane, methanol, and water, dimethylformamide (DMF) and chloroform have received comparatively less attention as adsorbates in UiO-66. Research on these compounds has primarily focused on their roles in the preparation and synthesis of UiO-66, where they act as solvents or activation agents[250–252]. In this study, DMF and chloroform were selected as adsorbates due to their contrasting

dipole moments and molecular sizes relative to methane, methanol, and water, as well as their link to UiO-66 synthesis. DMF, with a relatively high dipole moment, is expected to exhibit notable interactions with polar sites in the framework, while chloroform, with a lower dipole moment and larger molecular size, may demonstrate distinct adsorption and packing behavior.

This study builds upon our previous work, where we investigated the effect of water loading on the structural stability of pristine and defective UiO-66 frameworks using classical molecular simulations[166]. In that work, we employed two distinct methodologies—direct Lorentz-Berthelot (L-B) mixing and hybrid mixing—to model framework-adsorbate interactions, with hybrid mixing demonstrating superior accuracy in capturing the dynamic behavior of water within UiO-66. The results highlighted the critical influence of water loading on amorphization pressure, structural expansion or contraction, and water clustering around specific interaction sites such as zirconium clusters and linker oxygen atoms. Building on this methodology, the present study extends its application to a broader range of guest molecules, including methane, methanol, dimethylformamide (DMF), and chloroform. By systematically investigating these adsorbates, which vary in molecular size, polarity, and hydrogen-bonding capability, this work aims to elucidate the interplay of adsorbate properties and framework-adsorbate interactions in determining adsorption behavior and structural stability. Through this comparative approach, the study seeks to validate the effectiveness of hybrid mixing across diverse adsorbates, expand our knowledge of adsorption mechanisms in UiO-66, and provide insights into its practical applications.

6.2 METHODOLOGY

In systems as complex as flexible UiO-66 loaded with guest molecules, selecting appropriate guest-host interaction parameters is critical for predicting the spatial distribution of adsorbates within the pore network, their coordination with framework interaction sites, and the structural stability of the loaded framework. The direct application of Lorentz-Berthelot (L-B) rules to mix canonical adsorbate force field (FF) parameters with the non-bonded parameters from the Rogge et al. [94] FF has been shown to yield unrealistic interaction predictions for adsorbates such as water. To address this limitation, hybrid mixing has been employed to improve the accuracy of framework-adsorbate interactions [166]. It involves using two distinct sets of non-bonded interaction parameters for the framework: one set for intra-framework interactions in order to accurately reproduce the flexible behavior of the framework, and a second set from a generic force field previously used to model adsorption in rigid MOFs, specifically for adsorbate-framework interactions. This approach addresses the issue of unrealistic adsorbate behavior observed when the same parameters are applied uniformly to all interactions, thereby improving the accuracy of framework-adsorbate predictions. In this study, hybrid mixing is employed to investigate the structural response of pristine UiO-66 under varying loading levels of methane, methanol, chloroform, and dimethylformamide (DMF). By systematically analyzing the effects of these adsorbates on the stability and structural integrity of the framework, this work aims to contribute to better understanding of adsorbate-induced structural behavior in UiO-66.

6

6.2.1 FORCE FIELDS AND MODELS

We model the pristine UiO-66 framework using the force field developed by Rogge et al.[94], which has been shown to accurately predict the structural and mechanical properties of the crystal. This force field provides a higher degree of accuracy when compared to ad-hoc modified flexible force fields based on UFF[61],

UFF4MOF[253, 254], and Dreiding[255]. The functional form for the interactions between framework atoms is:

$$U = U_{\text{bonded}} + U_{\text{non-bonded}} \quad (6.1)$$

where the covalent interactions between neighboring atoms are mediated through harmonic and Fourier-style potentials

$$U_{\text{bonds}} = \sum_{N=1}^{N_{\text{bonds}}} \frac{1}{2} K_{r,n} (r_n - r_{n,0})^2 \quad (6.2)$$

$$U_{\text{bends}} = \sum_{N=1}^{N_{\text{bends}}} \frac{1}{2} K_{\theta,n} (\theta_n - \theta_{n,0})^2 \quad (6.3)$$

$$U_{\text{dihedrals}} = \sum_{N=1}^{N_{\text{dihed}}} \frac{1}{2} K_{\phi,n} (1 - \cos(m\phi - \phi_0)) \quad (6.4)$$

$$U_{\text{oopd}} = \sum_{N=1}^{N_{\text{oopd}}} \frac{1}{2} K_{d,n} (d_n - d_{n,0})^2 \quad (6.5)$$

Two terms contribute to the non-bonded portion of the potential energy function. The electrostatics are described by the Coulomb interaction between spherical Gaussian densities with distinct radii d_i and d_j containing charges q_i and q_j , respectively. The potential energy term for particles separated by a distance r_{ij} is:

$$U_{\text{Electrostatic}} = \frac{1}{2} \sum_{i < j} \frac{q_i q_j}{4\pi\epsilon_0 r_{ij}} \operatorname{erf} \left(\frac{r_{ij}}{\sqrt{d_i^2 + d_j^2}} \right) \quad (6.6)$$

The second term models the van der Waals interactions between two atoms i and j separated by a distance r_{ij} using the two-parameter Molecular Mechanics (MM3)[233, 234] Buckingham potential:

$$U_{\text{vdw}} = \sum_{i < j} \epsilon_{ij} \left[1.84 \times 10^5 \exp(-12 \frac{r_{ij}}{\sigma_{ij}}) - 2.25 \left(\frac{\sigma_{ij}}{r_{ij}} \right) \right] \quad (6.7)$$

For bonded atoms, different scaling and exclusion rules are applied for each contribution to the non-bonded part of the potential energy. As defined by the MM3 force field, 1-2 and 1-3 exclusion rules for bonded pairs are applied to VdW interactions, with no scaling applied to atoms separated by two or more atoms (1-4). Unlike when employing generic force fields, the Coulombic portion requires all interactions between all pairs of atoms to be included without scaling. For framework atoms of different species, the size (σ_{ij}) and interaction strength (ϵ_{ij}) parameters are determined via the empirical Lorentz-Berthelot mixing rules:

$$\sigma_{ij} = \frac{1}{2}(\sigma_i + \sigma_j) \quad \epsilon_{ij} = \sqrt{\epsilon_i \epsilon_j} \quad (6.8)$$

The interaction parameters of the energy equation are provided in the original publication of the force field[94].

All adsorbates were modeled as rigid molecules, allowing us to focus on framework deformation and adsorbate-framework interactions without the added computational cost of considering intra-molecular interactions. The models for each adsorbate are:

- **Methane** was implemented using the TraPPE (Transferable Potentials for Phase Equilibria) united atom model [256], where each CH₄ molecule is represented as a single interaction site. This model has been used extensively to study adsorption in numerous different MOFs[257–260], including UiO-66[261].
- **Methanol** was implemented by using the OPLS/2016 three-site model [262], which treats the CH₃ group as a united atom. Improves over the standard OPLS-UA[263] model in single-component simulations.
- **Chloroform** was simulated using the five-site model developed by Fox et al.[264, 265].

- **DMF** (dimethylformamide) was modeled with the OPLS-UA[263] five-site model, where the CH and CH₃ groups are treated as united atoms.

The non-bonded parameters of each adsorbate were implemented according to its specific model, and hybrid mixing was employed to model interactions with the UiO-66 framework. In this method, van der Waals (VdW) interactions are described by the Lennard-Jones (LJ) potential, while electrostatic interactions are handled using the canonical Coulomb potential for point charges. The Lennard-Jones parameters for framework-adsorbate interactions were derived by employing ϵ and σ coefficients from the Generalized Amber Force Field (GAFF)[60] and (UFF)[61] for the framework atoms in the parameter mixing, rather than using the MM3 parameters[233, 234] that model intra-framework VdW interactions in the Rogge et al. FF[94]. This approach thus combines two different force fields to model the framework: Rogge et al. for internal framework interactions and the GAFF[60] and UFF[61] parameters (“GAFF/UFF”) specifically for framework-adsorbate interactions. To evaluate the effect of using different interaction parameters, the GAFF/UFF results were systematically compared to those obtained using a uniform set of UFF parameters (“All UFF”). The primary results are presented in the main text, while additional comparisons are provided in Appendix D for completeness.

6.2.2 SIMULATION DETAILS

To systematically investigate adsorbate behavior, we varied the adsorbate loading from zero molecules per unit cell up to near saturation of the UiO-66 framework. Fractional loading is a dimensionless parameter that quantifies the degree of pore occupancy by the adsorbate within the framework. It is calculated as:

$$\text{Fractional Loading} = \frac{\text{Current Loading}}{\text{Maximum Loading}} \quad (6.9)$$

where *Current Loading* refers to the number of adsorbate molecules present in

the simulation cell, and *Maximum Loading* represents the theoretical maximum capacity of the framework. The maximum loading was estimated based on the available pore volume of the UiO-66 structure and the liquid-phase density of the adsorbate. This estimation was performed for both atmospheric and high-pressure conditions to account for variations in unloaded framework pore volume under different conditions. To generate each system, adsorbates were randomly inserted into a previously equilibrated, unloaded UiO-66 structure. By representing loading in terms of fractional occupancy, we established a normalized measure that allows for direct comparisons between adsorbates with differing molecular sizes and densities. This approach provides a consistent basis for analyzing adsorption behavior and its influence on the structural stability of UiO-66. Additionally, fractional loading highlights the relative efficiency of pore filling for different adsorbates, enabling systematic comparisons of methane, methanol, water, DMF, and chloroform within the framework. Each adsorbate was modeled as an independent rigid body, with the total force and torque acting on each molecule computed by summing the forces and torques on its constituent pseudoatoms. This approach ensured that each rigid body, including all atoms within each molecule, moved and rotated as a single entity. For the smallest multi-site adsorbate, methanol, we employed the SHAKE algorithm to constrain the internal angle, allowing for simulation timesteps of 0.5 and 1 fs. For the larger adsorbates, chloroform and DMF, we applied the LAMMPS simulation package[152] `fix rigid` command to enforce rigidity, which required a smaller timestep of 0.2 fs to maintain numerical stability.

The pressure-volume behavior of the structure was determined through molecular dynamics simulations in the NPT ensemble ($N, P, \sigma_\alpha = 0, T$), where the number of particles (N) is fixed while internal pressure (P_i), internal deviatoric stress ($\sigma_{\alpha,i}$), and internal temperature (T_i) are controlled. This ensemble allows for dynamic changes in both the simulation cell volume (V) and shape (h_0), and it is systematically used to estimate the pressure at which framework amorphization occurs (P_{am}). For each system, looped flexible NPT simulations were conducted, starting from the same

configuration, at sufficiently high pressure. At the start of each loop, an equilibration process at high pressure was conducted, during which the instantaneous volume (V_i) was monitored. Amorphization was considered to have occurred if, at any point during equilibration, V_i dropped below a predefined volume threshold (V_t). If amorphization occurred, the subsequent simulation in the loop started with a pressure value reduced by ΔP . The final characteristic P_{am} value for each structure was determined as the highest pressure at which the structure remained intact, plus ΔP . This approach has been previously applied to study the stability of ZIFs and MOFs[148, 166, 266], although it is noted that fluctuations in instantaneous pressure inherent in MD simulations may induce phase transitions at artificially low pressures, especially in more flexible MOFs[146, 147]. To partially mitigate these fluctuations, large $2 \times 2 \times 2$ simulation cells were employed.

All pressure versus volume MD simulations reported in this work were carried out in the NPT ensemble using the LAMMPS simulation package. The simulation timestep for the Verlet integrator was set according to the requirements needed to ensure adsorbate rigidity. In all simulations involving both the framework and adsorbates, their respective atoms were grouped and thermostatted independently, optimizing system equilibration times. This approach was particularly important in the looped simulations, where collapse was determined during system equilibration. This independent thermostating is commonly applied when a system contains two different species, such as a solid and a fluid. During these simulations, the temperature was fixed at 300 K and controlled via Nose-Hoover chain thermostats using a relaxation time of 100 times the timestep value. The pressure control was handled by an MTTK barostat with a relaxation time of 1000 times the timestep value. In the looped simulations, pressure was modified according to the discussed loop scheme, with ΔP set to 0.005 GPa and the volume threshold V_t set to 0.85 times the volume of the unloaded structure at high pressure. Radial distribution functions (RDFs) were averaged from independent trajectories taken from 500 ps runs in the NVT ensemble after equilibration. All simulations were performed in a

$2 \times 2 \times 2$ supercell of the structure using the specified force fields, with non-bonded interactions truncated at 14.0 \AA) and long-range electrostatics calculated via Ewald summation. Periodic boundary conditions were applied in all three dimensions, with 1-2, 1-3, and 1-4 non-bonded interactions included, excluded, or scaled according to the force field requirements.

6.3 RESULTS AND DISCUSSION

The stability of the UiO-66 framework under varying adsorbate loadings is a critical parameter for understanding its potential applications. In this study, we begin by analyzing the results for methane, the only non-polar molecule considered. Methane serves as a useful starting point as its interactions with the framework are modeled without considering electrostatics, relying solely on van der Waals forces. This simplifies the analysis and highlights the role of dispersion interactions in influencing the mechanical response of the framework.

The variation of amorphization pressure (P_{am}) with fractional loading of methane reveals a non-linear relationship (Figure 6.1a). At low loadings, P_{am} slightly decreases with increasing fractional loading, followed by a plateau at medium loadings before reaching a minimum at approximately 0.6. This behavior suggests that adsorbate-framework interactions dominate at lower loadings, causing a relatively small decrease in amorphization pressure compared to the unloaded structure. Beyond this minimum point, P_{am} increases sharply as loading continues to rise. This stabilization at higher fractional loadings can be attributed to adsorbate-adsorbate interactions and packing behavior, which become more significant within the confined pore spaces. Notably, beyond a fractional loading of 0.6, the amorphization pressure surpasses that of the unloaded structure. This result indicates an enhancement in the stability of the framework due to the packing of methane molecules, which counteracts the destabilizing effects of the applied hydrostatic pressure. The amorphization pressure trends therefore reflect the balance between destabilizing

framework interactions at lower loadings and the stabilizing effects of adsorbate clustering as the pores approach saturation.

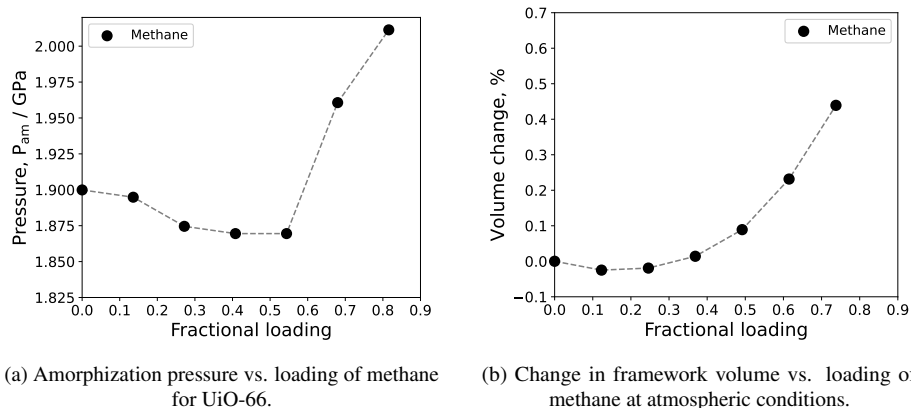


Figure 6.1: Effect of methane loading on the mechanical response of the UiO-66 framework.

Changes in framework volume at atmospheric pressure provide additional insight into the structural response to methane loading (Fig. 6.1b). At low loadings, the framework volume remains roughly unchanged, suggesting that the low strength of van der Waals interactions has a negligible effect on the structural integrity of the framework. This behavior is expected given methane's non-polar nature and the absence of electrostatic interactions. At higher fractional loadings, however, significant volume expansion is observed. This can be attributed to the packing behavior of methane molecules within the confined pore spaces, where adsorbate-adsorbate interactions exert outward stress on the framework. These observations further demonstrate how the mechanical response of UiO-66 evolves with increasing adsorbate loading, transitioning from a framework-dominated regime at low loadings to a packing-dominated regime at higher loadings.

To better understand the molecular mechanisms underlying these observations, the radial distribution functions (RDFs) of methane were analyzed with respect to framework atoms in the inorganic cluster and the organic linker at low loadings (Appendix Fig. D.1A). The RDFs exhibit broadly distributed peaks, indicating the

absence of strong preferential interaction sites for methane. This result aligns with methane's non-polar nature, where weak van der Waals interactions dominate its behavior. Consequently, the stabilization observed at higher loadings is likely a collective effect of adsorbate-adsorbate interactions rather than specific binding to the framework. Together, these results provide a cohesive picture of the structural dynamics of UiO-66 under methane loading. The framework's response reflects a balance between destabilizing adsorbate-framework interactions at lower loadings and stabilizing adsorbate-adsorbate interactions and packing behavior as the system approaches higher fractional loadings. The simplified nature of methane's non-polar interactions highlights the importance of van der Waals forces and their contribution to the mechanical response of the framework, providing a baseline for comparison with polar adsorbates.

6

The effects of methanol loading on P_{am} are presented in Figure 6.2a, with red points representing methanol and black points representing methane for comparison. Both adsorbates exhibit a non-linear relationship with fractional loading, where P_{am} decreases initially, reaches a minimum, and then increases at higher loadings. However, distinct differences emerge in the intermediate loading range. In contrast to methane, methanol exhibits a sharper decrease in P_{am} before reaching its minimum at a fractional loading of approximately 0.6. The pressure values for methanol are consistently lower than for methane, reflecting the stronger framework-adsorbate interactions induced by methanol's polar nature. These stronger interactions weaken the framework structure to a greater extent compared to methane, resulting in a more significant reduction in amorphization pressure.

Figure 6.2b shows the change in framework volume as a function of methanol fractional loading at atmospheric pressure. In contrast to methane, methanol causes a significant contraction in the framework volume at low and intermediate fractional loadings, with a minimum volume change observed near 0.6 fractional loading. This behavior can be attributed to methanol's polar nature, which allows it to interact strongly with the framework, particularly at low loadings. The stronger hydrogen

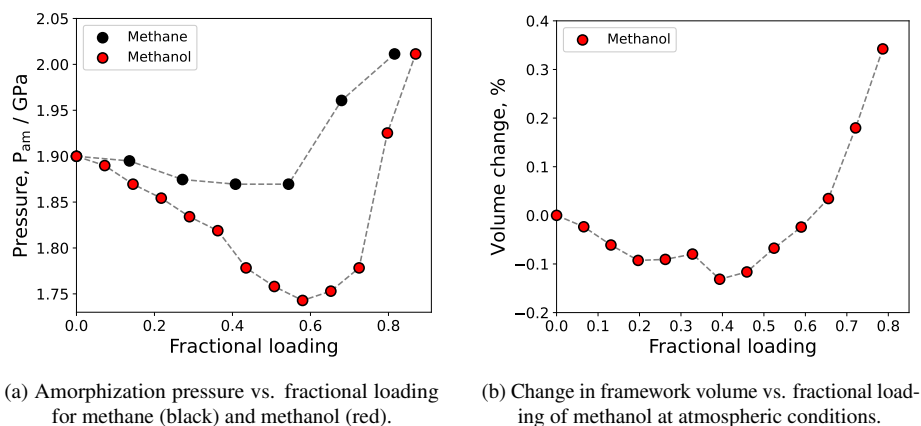


Figure 6.2: Effect of methanol loading on the mechanical response of the UiO-66 framework.

bonding between methanol and the hydroxylated oxygen sites pulls the framework inward, inducing the observed contraction. As the fractional loading increases further, the contraction plateaus, and slight volume recovery occurs due to adsorbate-adsorbate interactions, which become increasingly significant as the pores approach saturation. These packing effects are less pronounced compared to methane, where non-polar van der Waals interactions dominate and do not cause the same degree of framework contraction.

To gain molecular-level insights into methanol-framework interactions, the radial distribution functions (RDFs) of methanol oxygen atoms with respect to framework atoms were analyzed (Figure 6.3). The RDFs exhibit distinct, sharp peaks corresponding to the hydroxylated oxygen sites (H_{oh} and O_{oh}) of the framework. This strong affinity reflects the role of hydrogen bonding in destabilizing methanol-framework interactions at low loadings. The peaks at shorter radial distances further highlight the localized and directional nature of these interactions, which are absent in the RDFs for methane.

The observed differences between methane and methanol can be attributed to the dipole moment of methanol. While methane and methanol are similar in molecular size, the polar nature of methanol introduces significant differences in framework-

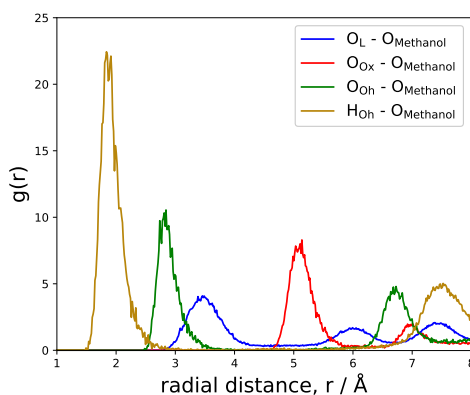


Figure 6.3: Radial distribution function for methanol oxygen with respect to framework atoms in the inorganic cluster.

adsorbate interactions. Methanol's dipole moment enables it to form hydrogen bonds with polar framework sites, particularly the hydroxylated oxygen atoms in the inorganic cluster. These strong framework-adsorbate interactions contribute to greater structural destabilization and framework contraction compared to methane, where the non-polar nature limits interactions to weaker van der Waals forces.

The interplay between framework-adsorbate and adsorbate-adsorbate interactions also differs between the two adsorbates. For methanol, the strong hydrogen bonding observed at low loadings drives framework contraction, while at higher loadings, adsorbate-adsorbate interactions counterbalance this effect, leading to slight volume recovery. In contrast, methane's behavior is dominated by adsorbate-adsorbate interactions through the entire loading range, resulting in an increase in framework volume due to packing effects. These findings highlight the critical role of adsorbate polarity in determining the structural response of UiO-66 under loading. Methanol's strong interactions with the framework destabilize the structure at lower loadings, leading to more pronounced reductions in amorphization pressure and framework volume compared to methane. By contrast, methane's non-polar nature limits its impact on the framework, underscoring the relative importance of hydrogen bonding and polar interactions in driving structural changes in flexible MOFs.

The variation of amorphization pressure (P_{am}) with fractional loading for water (blue points) and methanol (red points) is shown in Figure 6.4. Both adsorbates exhibit a non-linear relationship, characterized by an initial decrease in P_{am} , reaching a minimum before increasing at higher loadings. However, significant differences arise in the position and magnitude of the minimum. For water, the minimum occurs at a lower fractional loading (~ 0.5) compared to methanol (~ 0.6), indicating that framework destabilization sets in earlier for water. This behavior reflects the interplay between the strong hydrogen bonding of water with hydroxylated framework sites and its more pronounced water-water interactions, which dominate within the confined pore spaces as the fractional loading increases.

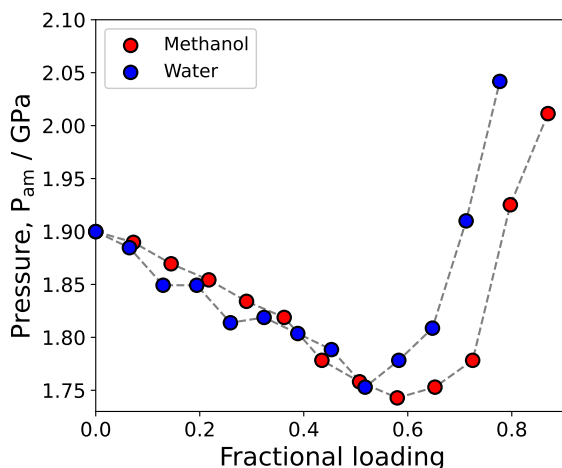


Figure 6.4: Comparison of amorphization pressure vs. fractional loading for methanol (red) and water (blue).

The stronger polarity of water enhances its hydrogen bonding with framework hydroxylated oxygen atoms, leading to earlier destabilization of the framework compared to methanol. However, as loading increases, water-water interactions become significant and contribute to clustering, which partially counteracts further framework destabilization. In contrast, methanol, while also polar, has weaker methanol-methanol interactions. This allows the destabilizing effect of framework-

adsorbate interactions to persist over a broader range of fractional loadings before adsorbate-adsorbate interactions begin to dominate.

To better understand these observations, Figure 6.5 compares the radial distribution functions (RDFs) of water and methanol oxygen atoms with respect to framework atoms in the inorganic cluster. The RDF for water oxygen (left) shows a sharp and intense peak at approximately 2 \AA , corresponding to strong hydrogen bonding between water and the hydroxylated oxygen sites of the framework. This peak is notably sharper and more intense than the equivalent peak observed for methanol (right), reflecting the stronger affinity of water for these framework sites. The peaks corresponding to O_{oh} and H_{oh} interactions for water are also more pronounced, emphasizing the localized nature of water-framework hydrogen bonding.

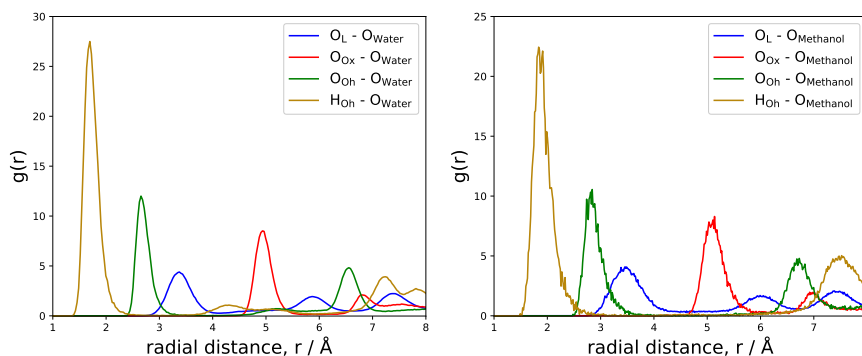
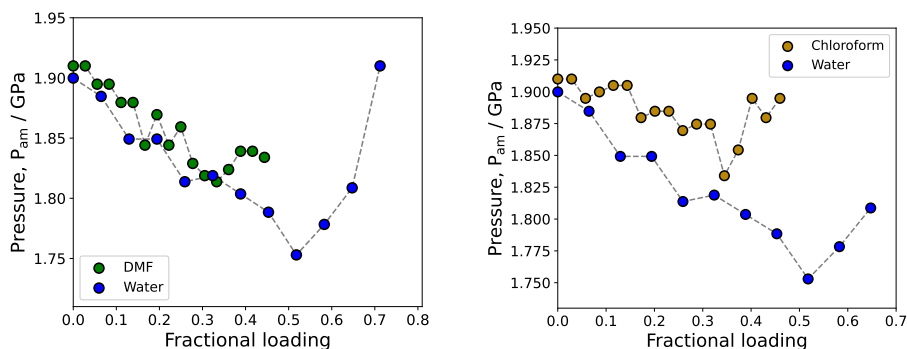


Figure 6.5: Radial distribution functions for water oxygen (left) and methanol oxygen (right) with respect to framework atoms in the inorganic cluster.

Water's smaller molecular size and higher polarity enable it to form stronger and more localized hydrogen bonds with the framework. However, these same properties also promote stronger water-water interactions at higher fractional loadings, leading to clustering and limiting further decrease of the framework's amorphization pressure. In comparison, methanol's weaker self-interactions allow framework-adsorbate interactions to dominate over a broader range of loadings, delaying the onset of stabilization observed for water.

The analysis of amorphization pressure (P_{am}) for dimethylformamide (DMF)

and chloroform reveals more complex trends compared to the smaller adsorbates discussed earlier. As shown in Figures 6.6a and 6.6b, both DMF (green points) and chloroform (brown points) exhibit a stepped decrease in P_{am} with increasing fractional loading, in contrast to the smoother trends observed for methane, methanol, and water. For DMF, P_{am} decreases linearly at low loadings but follows a stepped pattern as fractional loading increases. A minimum P_{am} is observed at a fractional loading of approximately 0.35, which is significantly lower than the minima observed for methane, methanol, and water (all near 0.5–0.6). Furthermore, the continued decrease at higher loadings suggests that the general amorphization pressure minimum may not yet have been reached.



(a) Amorphization pressure vs. fractional loading for DMF (green) and water (blue).

(b) Amorphization pressure vs. fractional loading for Chloroform (yellow) and water (blue).

Figure 6.6: Amorphization pressure results of DMF and Chloroform. Water included for comparison.

For chloroform, a similar stepped decrease in P_{am} is observed, but the minimum occurs at a slightly higher fractional loading of approximately 0.45. While DMF exhibits a gradual and less-defined minimum, chloroform shows a more pronounced transition at its minimum P_{am} . In terms of absolute values, P_{am} for DMF at low to medium loadings is comparable to those of water and methanol. This can be attributed to the strong affinity between DMF's CH sites and the hydroxylated oxygen atoms in the inorganic clusters. Such interactions are evident in the RDF analysis for DMF (Appendix Fig. D.4), where a distinct short-range peak between the

CH_{DMF} sites and the H_{oh} atoms highlights a preferential interaction. In contrast, the P_{am} values for chloroform are closer to those of methane. The RDFs for chloroform (Appendix Fig. D.6) display broadly distributed peaks, indicating weaker and less specific interactions with the framework and higher density of molecules towards the pore centers.

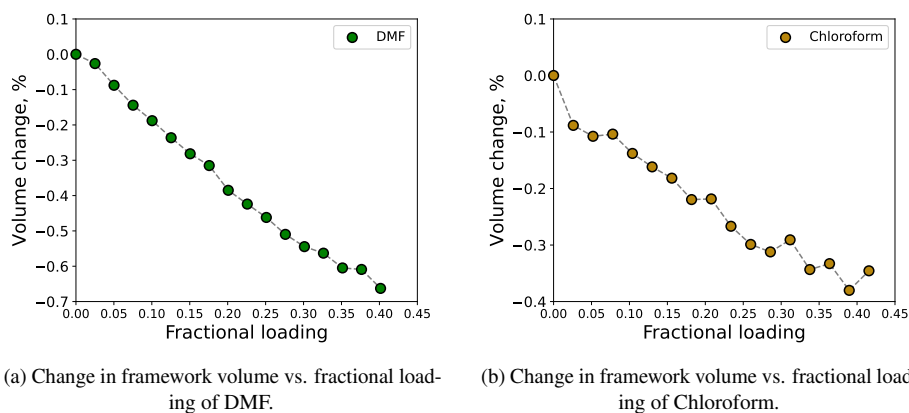


Figure 6.7: Framework volume change at atmospheric conditions for DMF and Chloroform.

The trends in framework volume changes at atmospheric conditions further emphasize the contrasting roles of molecular size and interaction strength for DMF and chloroform. As shown in Figure 6.7a, DMF induces a steady, nearly linear decrease in framework volume with increasing fractional loading. This behavior suggests a uniform and more efficient packing of DMF molecules within the framework, facilitated by their relatively smaller size. In contrast, the volume trend for chloroform (Fig. 6.7b) is distinctly non-linear, with notable inflection points. This irregular behavior indicates more complex packing dynamics, likely driven by steric effects due to the larger molecular size of chloroform, which disrupts uniform distribution within the framework.

The results for DMF and chloroform also highlight certain limitations in the modeling of these larger adsorbates. For example, treating the molecules as rigid may have restricted the flexibility needed to achieve more realistic packing behav-

ior. Additionally, the larger molecular size of DMF and chloroform constrained the number of molecules that could be inserted into the framework pores. As a result, it was not possible to approach the estimated theoretical saturation limits for these adsorbates, potentially limiting the completeness of the observed trends. These observations suggest that further refinement of adsorbate models, such as incorporating molecular flexibility, could enhance the accuracy of predictions for large adsorbates interacting with flexible frameworks.

6.4 CONCLUSIONS

This study highlights the critical role of adsorbate properties—polarity, molecular size, and self-interaction strength—in governing the structural stability and mechanical response of the UiO-66 framework under varying fractional loadings. By systematically analyzing the behavior of methane, methanol, water, dimethylformamide (DMF), and chloroform, we elucidate the interplay between adsorbate-framework interactions, adsorbate-adsorbate interactions, and packing dynamics, as reflected in amorphization pressures (P_{am}) and framework volume changes.

Methane, as the only non-polar molecule studied, provided a baseline for understanding the effects of weak van der Waals interactions. P_{am} showed a non-linear trend, with a slight decrease at low loadings, a plateau at intermediate loadings, and stabilization beyond a fractional loading of ~ 0.6 . This behavior reflects the transition from framework-dominated destabilization to stabilizing adsorbate-adsorbate interactions and packing effects at higher loadings. Framework volume remained nearly unchanged at low loadings, with significant expansion observed at higher loadings due to methane's packing behavior. In contrast, methanol and water, both polar molecules, demonstrated much stronger framework-adsorbate interactions driven by hydrogen bonding. Methanol exhibited a sharper decrease in P_{am} , reaching a minimum at ~ 0.6 , while water's minimum occurred earlier at ~ 0.5 . The earlier destabilization for water can be attributed to its stronger hydrogen bonding capacity

combined with significant water-water interactions at higher loadings, which partially offset the destabilizing effects of framework interactions. Framework volume changes mirrored these trends, with methanol and water inducing significant contraction at low loadings due to strong framework interactions, followed by distinct volume recovery as fractional loading increased.

The results for DMF and chloroform revealed additional complexities due to their larger molecular size and distinct polarity. DMF exhibited a linear decrease in P_{am} at low loadings, followed by a stepped pattern and a less defined minimum at approximately 0.35. Strong framework interactions, particularly between DMF's CH sites and hydroxylated framework oxygens, contributed to its intermediate destabilization behavior. However, DMF's relatively weaker hydrogen bonding compared to water and methanol resulted in higher P_{am} values. Chloroform, on the other hand, displayed a clearer minimum in P_{am} at ~ 0.45 , but its broadly distributed RDF peaks reflected weaker and less specific framework interactions. The larger molecular size of chloroform contributed to more irregular packing dynamics, as evidenced by the non-linear framework volume changes and distinct inflection points observed with increasing fractional loading.

6

The trends in volume changes at atmospheric conditions further reinforced the interplay between molecular size, polarity, and packing behavior. Methane exhibited the smallest volume changes, reflecting its weaker framework interactions. Methanol and water caused significant volume contraction at low loadings, driven by strong framework hydrogen bonding, followed by stabilization or slight recovery at higher loadings. DMF exhibited a steady, nearly linear volume decrease indicative of uniform packing, whereas chloroform showed irregular, non-linear trends consistent with steric effects imposed by its larger size.

These findings collectively emphasize the critical influence of both adsorbate polarity and molecular size on framework stability. Polar adsorbates like water and methanol destabilize the framework through strong hydrogen bonding, while non-polar methane relies solely on van der Waals interactions, resulting in weaker

structural effects. Larger adsorbates such as DMF and chloroform highlight the role of packing dynamics, where molecular size disrupts uniform packing and influences destabilization behavior. The differences observed between DMF and chloroform further underscore the interplay between polarity and steric effects, with DMF's smaller size facilitating efficient packing and chloroform's larger size driving irregular structural changes.

Overall, this study provides insights into the molecular mechanisms that govern the structural response of UiO-66 under varying adsorbate loadings. The results demonstrate that fractional loading, as a normalized measure, is a powerful tool for comparing adsorbate behavior across systems, enabling a basis for analyzing framework stability. The findings underscore the importance of tailoring adsorbate selection based on polarity, molecular size, and packing efficiency to optimize the performance of flexible metal-organic frameworks (MOFs) for applications such as gas storage, separation, and adsorption-driven processes. Future work should consider refinements in the modeling of larger adsorbates, including the incorporation of molecular flexibility, to achieve more accurate predictions of framework-adsorbate behavior at higher loadings.

The findings demonstrate that adsorbate polarity, molecular size, and self-interactions must be carefully considered when selecting adsorbates for MOF applications. Polar molecules such as water and methanol can enhance framework stability through hydrogen bonding, particularly at higher fractional loadings, although competing self-interactions may alter their stabilizing effects. Non-polar or weakly polar molecules such as methane and chloroform rely on van der Waals interactions, which are less effective in stabilizing the framework. The differences between DMF and chloroform further emphasize the importance of understanding the trade-offs between packing efficiency and interaction strength.

Overall, this study demonstrates the influence of adsorbate properties on the stability and structural integrity of the UiO-66 framework under varying loadings. The findings emphasize the importance of tailoring adsorbate selection based on

polarity, molecular size, and self-interaction strength to optimize the performance of MOFs in gas storage, separation, and other applications. The results also highlight the utility of fractional loading as a dimensionless metric for comparing the behavior of different adsorbates within the same framework, providing a normalized measure of pore occupancy and adsorbate-framework interactions.

7

CONCLUSIONS AND OUTLOOK

The primary aim of this thesis was to investigate the structural and mechanical stability of metal-organic frameworks (MOFs), with a particular focus on zeolitic imidazolate frameworks (ZIFs) and zirconium-based frameworks such as the UiO-66 family. Through a series of computational studies, we have gained significant insights into the behavior of these materials under various external conditions, including temperature, pressure, defect inclusion, and adsorbate loading.

In **Chapter 3**, we explored the mechanical stability of the prototypical ZIF-8 framework by evaluating a set of classical flexible force fields, commonly employed to simulate the physical properties of MOFs. Our work revealed that the force fields produced not only different quantitative results but also diverging qualitative predictions, particularly in the context of elastic constants and structural changes under pressure. This variability is attributed to the fact that the force fields were developed using a "bottom-up" approach, wherein atomic bonding, bending, torsion, and long-range interactions are parameterized independently, often without full consideration of their collective effect on macroscopic properties such as amorphization pressure. The discrepancies observed in elastic constant predictions across different

pressure regimes suggest that the mechanical collapse of ZIF-8, as pressure increases, is highly sensitive to the specific force field chosen. We also compared results from two molecular simulation platforms, RASPA and LAMMPS, and found that while both provided consistent predictions of unit cell volume as a function of temperature and pressure, there were significant differences in zero Kelvin structures and elastic constants. The conjugate gradient minimization algorithm in LAMMPS often failed to identify the true minimum energy structure, leading to erroneous elastic constant values. In contrast, the eigenmode-following minimization method in RASPA provided more reliable results. These findings suggest that future development of force fields for MOFs should include pressure-dependent properties and employ advanced minimization techniques to ensure accurate modeling of mechanical stability, particularly under high-pressure conditions.

In **Chapter 4**, we investigated the impact of linker vacancies on the stability of defected UiO-66 structures. By analyzing a wide variety of defected structures with varying numbers and distributions of vacancies, we demonstrated that the overall number of defects is not the sole determinant of a framework's stability. Instead, the spatial distribution and orientation of the missing linkers play a critical role in determining the amorphization pressure and elastic behavior of the material. Our results showed that structures with more evenly distributed vacancies tend to exhibit a positive linear correlation between amorphization pressure and bulk modulus, indicating a degree of mechanical robustness. On the other hand, structures with a disproportionate number of vacancies oriented in the same direction or with large, intact regions of the framework showed anomalous mechanical behavior, with significantly reduced amorphization pressures and heightened elastic moduli anisotropies. This suggests that directional instability can occur when defects are clustered or aligned, leading to localized structural weaknesses. The analysis of anisotropic elastic moduli further confirmed this behavior, revealing that vacancy orientation significantly affects mechanical stability in specific directions. These findings have important implications for the design and optimization of UiO-66-

based materials, particularly in applications where mechanical integrity is paramount, such as in gas storage or mechanical reinforcement. By carefully controlling the distribution and orientation of defects, it is possible to fine-tune the mechanical properties of the material to meet the requirements of specific applications.

In **Chapter 5**, we expanded the study to investigate the effects of water loading on both pristine and defected UiO-66 frameworks, employing two different methodologies for modeling non-bonded interactions between the framework and water: Lorentz-Berthelot (L-B) mixing and hybrid mixing. Water plays a crucial role in many MOF applications, influencing both the structural stability and the functionality of the material. Our simulations revealed that both L-B and hybrid mixing methodologies predict strong water clustering around the zirconium clusters of UiO-66, but they differ significantly in their predictions of interaction sites and strengths. The L-B approach, which combines Lennard-Jones parameters for framework-water and water-water interactions, predicted strong binding of water molecules to the oxygen atoms of the linkers, leading to restricted water mobility. This resulted in significant expansion of the framework at high water loadings, due to the stretching of linker-cluster bonds. In contrast, the hybrid mixing approach, which uses Universal Force Field (UFF) parameters for framework interactions, predicted a more dynamic water behavior, with water molecules exhibiting site-to-site hopping and pore-to-pore diffusion at higher loadings. This approach suggested that water molecules are more likely to interact with the hydroxyl groups of the inorganic cluster, leading to dimer formation and a slight contraction of the framework at high water loadings. These contrasting behaviors highlight the importance of selecting appropriate force field parameters when modeling MOF-water interactions, as the choice of method can significantly influence the predicted structural response to water loading.

High-pressure NPT simulations further demonstrated the effect of water on the amorphization pressure of UiO-66. Both L-B and hybrid mixing showed that water loading decreases the amorphization pressure relative to the unloaded structure, but

the magnitude of this effect differed between the two methods. The L-B mixing consistently predicted lower amorphization pressures, particularly at moderate and high water loadings, where water clustering around the zirconium clusters leads to weakening of the linker-cluster bonds. In contrast, the hybrid mixing approach predicted a sharper decrease in amorphization pressure at low water loadings, followed by convergence with the L-B results at higher loadings. Similar trends were observed in defected UiO-66 structures, where the presence of missing linkers influenced the interaction of water with the framework. In particular, structures with open zirconium sites exhibited strong water agglomeration and reduced water mobility, similar to the behavior observed near linker oxygen atoms in L-B mixing. These results emphasize the critical role that water plays in determining the mechanical stability of UiO-66 and highlight the need for accurate parameterization of framework-water interactions in molecular simulations.

7 In **Chapter 6**, we analyzed the effects of adsorbate properties—including polarity, molecular size, and self-interaction strength—on the structural stability of UiO-66. By studying methane, methanol, water, dimethylformamide (DMF), and chloroform, we demonstrated that adsorbate-framework and adsorbate-adsorbate interactions play a pivotal role in determining amorphization pressures and framework volume changes. Methane, the only non-polar molecule, exhibited weaker framework-adsorbate interactions, with framework stabilization dominated by packing effects at higher loadings. In contrast, methanol and water destabilized the framework through strong hydrogen bonding, with water exhibiting earlier destabilization due to its higher polarity and stronger water-water interactions. Larger adsorbates like DMF and chloroform introduced additional complexities, where molecular size influenced packing dynamics and structural destabilization. These findings highlight the critical interplay of adsorbate properties in governing the mechanical response of flexible MOFs.

In summary, this thesis has provided a detailed investigation into the structural and mechanical properties of ZIF-8 and UiO-66 frameworks, under varying condi-

tions of pressure, defects, and water loading. By leveraging molecular simulations, we have identified the limitations of existing force fields in accurately capturing mechanical stability, particularly under high-pressure and defect-laden conditions. Our work on linker vacancies and water interactions in UiO-66 provides insights for the design and optimization of MOFs, offering strategies for enhancing mechanical stability and guiding the development of future computational models. The findings presented in this thesis have implications for the practical application of MOFs in areas such as gas adsorption, catalysis, and materials design, where mechanical integrity and stability are of paramount importance.

One critical area for future lines of research is the improvement of adsorbate-framework interaction parameters, especially in the context of flexible frameworks. The results from **Chapters 5** and **6** demonstrate that non-bonded interaction parametrization using generic force fields can have a very large influence on the predicted mechanical response of highly rigid MOFs such as UiO-66, particularly at high loadings. The findings underscore the need for more accurate and refined force fields or an alternative methodology that can account for the complex and dynamic nature of large flexible MOFs when interacting with adsorbates. Developing a more comprehensive force field that captures the interplay between framework flexibility and adsorbate-induced deformations would greatly enhance the predictive accuracy of molecular simulations for practical applications, including gas storage and separation.

Another promising direction is the study of how functional groups incorporated into the organic linkers of MOFs influence both the flexibility of the framework and its adsorption properties. As discussed, the inclusion of functional groups, such as hydroxyl, amino, or carboxyl groups, can significantly alter the hydrophobicity, pore environment, and even the mechanical response of the material. Investigating the effects of functional group incorporation on MOF flexibility could provide valuable insights into how these modifications enhance or reduce mechanical stability under different conditions. Furthermore, these modifications can influence adsorption

properties, particularly with respect to selective adsorption of guest molecules like water, gases, or organic vapors. For example, functional groups that increase the hydrophilicity of the framework may improve water uptake, but may also reduce mechanical stability due to increased interactions with the framework, as we observed in **Chapter 5**. Systematically studying the relationship between functional group chemistry, framework flexibility, and adsorption properties will offer crucial guidance for the design of MOFs tailored for specific applications, such as water harvesting, gas separation, or catalysis. Moreover, extending these studies to include the effects of defects and disorder on functionalized frameworks would provide a more comprehensive understanding of how real-world imperfections in MOFs affect their mechanical and adsorption behaviors. Investigating how defects influence the distribution and interaction of adsorbates in frameworks modified with functional groups could shed light on optimizing defect engineering strategies for improved performance.

7 A further area of interest is the influence of external stimuli, such as mechanical strain or electric fields, on the behavior of functionalized MOFs. Exploring how these factors impact both the structural flexibility and adsorption performance of MOFs could reveal new ways to dynamically control MOF properties. For example, applying mechanical strain could lead to tunable pore sizes, while electric fields could potentially influence the orientation of polar functional groups, enabling selective adsorption of polar molecules. Incorporating these external stimuli into molecular simulations would help to develop MOFs with adaptive or switchable functionalities, broadening their potential applications.

Additionally, experimental validation of the computational predictions remains an essential aspect of future work. The insights gained from simulations must be tested and refined through detailed experimental studies, which would allow for improved accuracy in force field development and validation of proposed modifications, such as functional group inclusion and defect engineering. Collaborations between computational and experimental researchers are crucial in ensuring that the proposed

models align with actual material behavior under relevant operational conditions. In conclusion, future research should focus on refining adsorbate-framework interaction methodologies, investigating the role of functional group modifications, further exploring the effect of defects, and considering external stimuli on MOF flexibility and adsorption properties. These avenues will not only deepen the understanding of MOF behavior but also contribute to the design of more robust, versatile, and application-specific materials for industrial and environmental applications.

A

APPENDIX 1

A.1 DESCRIPTION OF THE FORCE FIELDS

This section contains the description of functional forms and corresponding parameter sets of the five ZIF-8 force fields used in this study, taken from the literature, as well as notes regarding their implementation in both RASPA and LAMMPS.

As is the case in Chapter 3, for organizational and convenience purposes the following nomenclature will be used:

- **FF1** : B. Zheng et al. (2012) [62]
- **FF2** : J. Jiang et al. (2012) [63]
- **FF3** : L. Zhang et al. (2013) [64]
- **FF4** : X. Wu et al. (2014) [65]
- **FF5** : T. Weng and J. R. Schmidt (2019) [149]

A.1.1 FUNCTIONAL FORMS

The starting point of development for all force fields used in this study is the General AMBER Force Field (GAFF) [60]. This force field was proposed for the modelling of biomolecules, and therefore is able to describe the organic linker of ZIF-8 well. The connection of the linker with the metal is what needs custom parameterization and it represents the biggest difference between these force fields.

In FF1, the bonded and non-bonded interactions between framework atoms are modelled according to the following terms:

$$U_{\text{bonded}} = \sum_{\text{bonds}} \frac{1}{2} K_r (r - r_0)^2 + \sum_{\text{angles}} \frac{1}{2} K_\theta (\theta - \theta_0)^2 \quad (\text{A.1})$$

$$+ \sum_{\text{dihedrals}} K_\phi [1 + \cos(m\phi - \phi_0)] + \sum_{\text{improper}} \frac{1}{2} K_\xi (\xi - \xi_0)^2$$

$$U_{\text{non-bonded}} = \sum_{i < j} 4\epsilon_{ij} \left[\left(\frac{\sigma_{ij}}{r_{ij}} \right)^{12} - \left(\frac{\sigma_{ij}}{r_{ij}} \right)^6 \right] + \sum_{i < j} \frac{q_i q_j}{4\pi\epsilon_0 r_{ij}} \quad (\text{A.2})$$

For the bonded contribution r , θ , ϕ , ξ are the bond lengths and angles, proper and improper dihedrals, respectively, K_r , K_θ , K_ϕ , K_ξ are the force constants, and r_0 , θ_0 , ϕ_0 , ξ_0 are the equilibrium values. Canonically, GAFF handles the improper torsions through the same formulation as the dihedral torsions, using a fourier-like potential. FF1, instead, opts to use a harmonic potential. The non-bonded contribution includes the Lennard-Jones and Coulombic potentials, where σ_{ij} is the collision diameter, ϵ_{ij} is the well depth, q_i and q_j are the atomic charges and ϵ_0 is the vacuum permittivity. The FF1 paper reports using a L-J interaction cutoff radius of 14 Å, although it doesn't specify whether the potential was shifted to 0 after truncation or if tail corrections were considered. Electrostatic interactions were reported as treated with the particle mesh Ewald method, with no cutoff specified to distinguish between

direct and reciprocal-space calculations. For each framework atom, a “scaled 1-4” policy was applied, that is, both the VdW and electrostatic interactions between couples of bonded atoms (1-2) or between atoms bonded to a common atom (1-3) are excluded, and for the interaction between atoms separated by two other atoms (1-4) a scaling of 0.5 and 0.8333 is applied, respectively (Figure A.1).

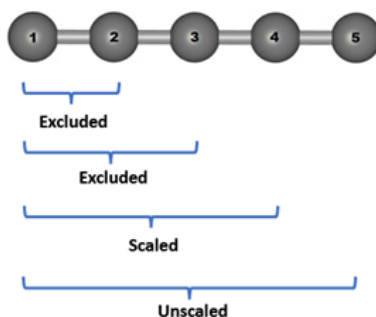


Figure A.1: Pictorial representation of the 1-4 scaling policy for non-bonded interactions.

FF2, FF3 and FF4 all use the same functional form for the energy equation, the unmodified GAFF, where the improper torsions are handled using a fourier-like potential. The bonded and non-bonded interactions between framework atoms are modelled according to the following terms:

$$\begin{aligned}
 U_{\text{bonded}} = & \sum_{\text{bonds}} \frac{1}{2} K_r (r - r_0)^2 + \sum_{\text{angles}} \frac{1}{2} K_\theta (\theta - \theta_0)^2 \\
 & + \sum_{\text{dihedrals}} K_\phi [1 + \cos(m\phi - \phi_0)] + \sum_{\text{improper}} K_\xi [1 + \cos(m\xi - \xi_0)]
 \end{aligned} \tag{A.3}$$

$$U_{\text{non-bonded}} = \sum_{i < j} 4\epsilon_{ij} \left[\left(\frac{\sigma_{ij}}{r_{ij}} \right)^{12} - \left(\frac{\sigma_{ij}}{r_{ij}} \right)^6 \right] + \sum_{i < j} \frac{q_i q_j}{4\pi\epsilon_0 r_{ij}} \tag{A.4}$$

The FF2 paper reports using a L-J interaction cutoff radius of 14 Å, although it doesn't specify whether the potential was shifted to 0 after truncation or if tail

A

corrections were considered. Electrostatic interactions were reported as treated with the particle mesh Ewald method with a grid spacing of 1.2 Å and a fourth-order interpolation, however no cutoff was specified to distinguish between direct and reciprocal-space calculations. The use of a 1-4 non-bonded interaction policy for closely bonded atoms is not mentioned.

The FF3 paper, written by the same authors as FF2, does not provide information regarding non-bonded interaction cutoffs, long-range treatment or 1-4 non-bonded interaction policy.

The FF4 paper reports using a L-J interaction cutoff radius of 14 Å, although it doesn't specify whether the potential was shifted to 0 after truncation or if tail corrections were considered. Electrostatic interactions were reported as treated via the particle mesh Ewald method, with no cutoff specified to distinguish between direct and reciprocal-space calculations. A scaled 1-4 interaction policy was used in which 1-2 and 1-3 interactions are excluded and scaling values of 0.5 for both the 1-4 coulombic and VdW interactions are considered.

FF5 makes use of the same functional forms, but includes an Urey-Bradley term as part of the 3-body angular potential. The bonded and non-bonded interactions between framework atoms are modelled according to the following terms:

$$U_{\text{bonded}} = \sum_{\text{bonds}} \frac{1}{2} K_r (r - r_0)^2 + \sum_{\text{angles}} \frac{1}{2} K_\theta (\theta - \theta_0)^2 + \sum_{\text{U-B}} \frac{1}{2} K_u (u - u_0)^2 \quad (\text{A.5})$$

$$+ \sum_{\text{dihedrals}} K_\phi [1 + \cos(m\phi - \phi_0)] + \sum_{\text{improper}} K_\xi [1 + \cos(m\xi - \xi_0)]$$

$$U_{\text{non-bonded}} = \sum_{i < j} 4\epsilon_{ij} \left[\left(\frac{\sigma_{ij}}{r_{ij}} \right)^{12} - \left(\frac{\sigma_{ij}}{r_{ij}} \right)^6 \right] + \sum_{i < j} \frac{q_i q_j}{4\pi\epsilon_0 r_{ij}} \quad (\text{A.6})$$

The paper reports using a L-J interaction cutoff radius of 13 Å with long-range tail corrections considered. Electrostatic interactions were reported as treated via the

particle-particle particle-mesh (PPPM) method, with a cutoff radius of 13 Å. A 1-4 scaling 0.6874 factor for coulombic interactions was reported. The 1-4 scaling factor for VdW interactions was not explicitly reported in the paper, however, in the files provided as part of the supporting information the conventional choice for GAFF (0.5) is used. As was the case for other force fields, as part of the 1-4 scaling policy, 1-2 and 1-3 non-bonded interactions are excluded.

A.1.2 PARAMETER SETS

The tables included in this subsection contain the interaction parameters used in this work for the previously described force fields. The atom types referenced in the text and tables are labeled in a standardized manner according to the pictured nomenclature (Figure A.2).

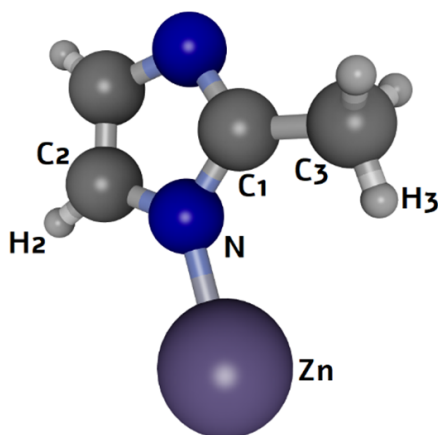


Figure A.2: Atom nomenclature used in this work.

The parameters for FF1 contained in the tables were taken directly from the original paper, including the changes published by the authors in a subsequent erratum concerning the VdW σ parameter for H3 and the partial charge for C3. According to the paper, the parameters for the organic linker not included in the “parm10.dat” AMBER database were obtained via the parmcal program of the Antechamber package[267]. The bond-length and bond-angle parameters involved

A

in interactions of tetrahedral ZnN_4 were taken and adapted from a couple of quantum-chemical studies describing Zn-containing biomolecules for AMBER[268, 269]. The VdW parameters for Zn were taken from the work of Mertz et al.[270], which some of the AMBER parameter databases include. The partial charges were obtained via density functional theory calculations on finite clusters previously published by the same research group[271]. In the parametrization presented by the paper the torsion terms N-Zn-N-C1, N-Zn-N-C2 and N-C1-C3-H3 were neglected, to ensure higher mobility of the organic linkers with respect to each other and to allow free rotation of the methyl group in the linker, respectively. As far as we can tell, the Zn-containing torsion terms Zn-N-C2-H2, Zn-N-C2-C2, C3-C1-N-Zn and N-C1-N-Zn were considered and modelled the same way as the purely organic torsions, via the X-CR-NB-X, X-CC-CV-X and X-CR-NA-X (where X denotes generic entries, any atom) interaction parameters located in the “parm10.dat” database. The parameters for the improper torsions used are missing in the database, therefore it can be assumed they were calculated using the parmcal program.

The parameters for FF2 contained in the tables were taken directly from the original paper, including the changes published by the authors in a subsequent erratum concerning the correct equilibrium bond lengths r_0 of C2-H2 and C3-H1. According to the paper, the equilibrium bond lengths and angles for all bonded interactions were set to the experimentally measured average values. The force constants for the organic linkers were adopted from the AMBER force field (no specific database mentioned), while those involving Zn atoms were derived by fitting to experimental lattice constants. The non-bonded Lennard-Jones parameters for all atoms were taken from the AMBER force field (no specific database file mentioned). The atomic charges were obtained via DFT calculations using a fragmental cluster model, previously published by the same research group[272]. It is worth noting that the charge values presented in the FF2 paper and those from the referenced paper differ slightly, and no reason was given to justify said change. In this work we used the ones published with the proposed FF[63].

Table A.1: Non-bonded interaction parameters. ϵ in $kcal/mol$, σ in \AA , q in e .

| | | FF1 | FF2 | FF3 | FF4 | FF5 |
|-----------|------------|------------|------------|------------|----------------|------------|
| N | ϵ | 0.17 | 0.17 | 0.0373 | 0.0438 | 0.17 |
| | σ | 3.25 | 3.25 | 3.261 | 3.261 | 3.25 |
| | q | -0.3008 | -0.5 | -0.28 | -0.3879 | -0.4203 |
| C1 | ϵ | 0.086 | 0.086 | 0.0567 | 0.0667 | 0.086 |
| | σ | 3.4 | 3.4 | 3.431 | 3.431 | 3.4 |
| | q | 0.4339 | 0.5 | 0.4184 | 0.4291 | 0.4375 |
| C2 | ϵ | 0.086 | 0.086 | 0.0567 | 0.0667 | 0.086 |
| | σ | 3.4 | 3.4 | 3.431 | 3.431 | 3.4 |
| | q | -0.1924 | -0.1 | -0.191 | -0.0839 | -0.0662 |
| C3 | ϵ | 0.1094 | 0.1094 | 0.0567 | 0.0667 | 0.086 |
| | σ | 3.4 | 3.4 | 3.431 | 3.431 | 3.4 |
| | q | -0.6042 | -0.3 | -0.5726 | -0.4526 | -0.4606 |
| H2 | ϵ | 0.015 | 0.015 | 0.0238 | 0.0279 | 0.015 |
| | σ | 2.511 | 2.421 | 2.571 | 2.571 | 2.51 |
| | q | 0.1585 | 0.1 | 0.1536 | 0.1128 | 0.1141 |
| H3 | ϵ | 0.0157 | 0.0157 | 0.0238 | 0.0279 | 0.0157 |
| | σ | 2.471 | 2.65 | 2.571 | 2.571 | 2.471 |
| | q | 0.1572 | 0.1 | 0.1481 | 0.1325, 0.1306 | 0.1381 |
| Zn | ϵ | 0.0125 | 0.0125 | 0.067 | 0.0787 | 0.0125 |
| | σ | 1.96 | 1.96 | 2.462 | 2.462 | 1.96 |
| | q | 0.7362 | 1.0 | 0.6894 | 0.6918 | 0.7072 |

Table A.2: Bond stretching interaction parameters. K_r in $kcal \cdot mol^{-1} \cdot \text{\AA}^{-2}$, r_0 in \AA .

| | | FF1 | FF2 | FF3 | FF4 | FF5 |
|--------------|-------|------------|------------|------------|------------|------------|
| C1-C3 | K_r | 693.086 | 634 | 634 | 634 | 451.26 |
| | r_0 | 1.49 | 1.493 | 1.492 | 1.492 | 1.498 |
| C1-N | K_r | 976 | 976 | 976 | 976 | 674.52 |
| | r_0 | 1.335 | 1.34 | 1.339 | 1.339 | 1.355 |
| C2-N | K_r | 880.42 | 820 | 820 | 820 | 579.3 |
| | r_0 | 1.37 | 1.371 | 1.371 | 1.3711 | 1.386 |
| C2-H2 | K_r | 734 | 734 | 734 | 734 | 739.5 |
| | r_0 | 1.08 | 0.929 | 0.929 | 0.929 | 1.088 |
| C2-C2 | K_r | 1080.50 | 1036 | 1036 | 1036 | 804.64 |
| | r_0 | 1.35 | 1.346 | 1.346 | 1.346 | 1.377 |
| C3-H3 | K_r | 680 | 680 | 680 | 680 | 643.54 |
| | r_0 | 1.09 | 0.96 | 0.959 | 0.959 | 1.102 |
| Zn-N | K_r | 157 | 167.304 | 172 | 172 | 149 |
| | r_0 | 2.011 | 1.987 | 1.987 | 1.987 | 2.024 |

It's worth mentioning that although the LJ parameters for both FF1 and FF2 were taken from AMBER databases, their values are not the same for all atoms, as can be seen in Table A.1. This is due to the atom model selection each paper employs. For example, FF1 models H2 as an aromatic hydrogen bonded to a carbon atom with 1 electron-withdrawing group (denoted as H4 in AMBER databases) while FF2 models H2 as an aromatic hydrogen bonded to a carbon atom with 2 electron-withdrawing groups (denoted as H5 in AMBER databases), hence there's a difference in the σ LJ parameter. The previous observation applies for all discussed force fields, meaning that if the parameters from different were said to be taken from the GAFF force field and when comparing between them they are not exactly the same; it's usually due to decisions relating to atom model selection.

Table A.3: Angle bending interaction parameters. K_θ in $kcal \cdot mol^{-1} \cdot rad^{-2}$, θ_0 in deg .

| | | FF1 | FF2 | FF3 | FF4 | FF5 |
|----------|------------|---------|--------|---------|--------|---------|
| N-C1-N | K_θ | 150.968 | 140 | 140 | 140 | 64.68 |
| | θ_0 | 112.16 | 112.17 | 112.17 | 112.17 | 111.169 |
| N-C1-C3 | K_θ | 132.03 | 140 | 140 | 140 | 78.14 |
| | θ_0 | 123.92 | 123.89 | 1123.89 | 123.89 | 124.197 |
| C2-C2-N | K_θ | 147.5 | 140 | 140 | 140 | 67.16 |
| | θ_0 | 108.65 | 108.67 | 108.67 | 108.67 | 107.995 |
| C2-C2-H2 | K_θ | 98.902 | 100 | 100 | 100 | 38.78 |
| | θ_0 | 125.67 | 125.67 | 125.67 | 125.67 | 130.034 |
| N-C2-H2 | K_θ | 99.908 | 100 | 100 | 100 | 63.16 |
| | θ_0 | 125.68 | 125.66 | 125.66 | 125.66 | 121.317 |
| C1-N-C2 | K_θ | 142.508 | 140 | 140 | 140 | 92.66 |
| | θ_0 | 105.27 | 105.24 | 105.24 | 105.24 | 106.252 |
| C1-C3-H3 | K_θ | 96.176 | 100 | 100 | 100 | 72.62 |
| | θ_0 | 109.32 | 109.44 | 109.44 | 109.44 | 110.963 |
| H3-C3-H3 | K_θ | 70 | 70 | 70 | 70 | 54.36 |
| | θ_0 | 109.5 | 109.5 | 109.5 | 109.5 | 107.741 |
| C1-N-Zn | K_θ | 97.36 | 40.631 | 100 | 100 | 28.86 |
| | θ_0 | 128.33 | 128.35 | 127.5 | 127.5 | 126.85 |
| C2-N-Zn | K_θ | 64.954 | 43.021 | 70 | 70 | 22.72 |
| | θ_0 | 126.4 | 126.4 | 128 | 128 | 126.95 |
| N-Zn-N | K_θ | 70.48 | 23.9 | 21 | 21 | 22.18 |
| | θ_0 | 109.48 | 109.47 | 109.47 | 109.47 | 109.42 |

The parameters for FF3 contained in the tables were taken directly from the

original paper. According to it, the equilibrium bond lengths and angles for all bonded interactions were set to the experimentally measured average values. The force constants of the bonded interactions for the organic linkers were adopted from the AMBER force field (no specific database file mentioned). Regarding the ZnN_4 tetrahedra, the force constant for the N-Zn bond was adopted from a parameter-optimization study intended for the Molecular Mechanics (MM2) force field[273] and the force constants for C1-N-Zn and C2-N-Zn were taken from the work of Lin and Wang[269]. For N-Zn-N bending and the torsional terms Zn-N-C1-N, Zn-N-C1-C3 and Zn-N-C2-C2 the force constants were adopted from FF2. Unlike the previous two force fields, FF3 was specifically tuned to study the structural transition of ZIF-8 upon N_2 loading. The N-Zn-N-C1 and N-Zn-N-C2 force constants were fitted to experimental data of the N_2 sorption isotherm[47]. The LJ parameters were adopted from the universal force field[61] with the well depth parameters ϵ rescaled by a factor of 0.54, in order to better reproduce the adsorption isotherm of N_2 . The atomic charges were adopted from previously published plane-wave DFT calculations on a periodic structure[271].

The parameters for FF4 contained in the tables were taken directly from the original paper. According to it, the equilibrium bond lengths and angles for all bonded interactions were set to the experimentally measured average values. The force constants of the bonded interactions for the organic linkers were adopted from the AMBER force field (no specific database file mentioned). All bonded interaction parameters involving Zn were taken from FF3. This force field was tuned to study diffusion and adsorption of N_2 , CH_2 , CO_2 and CH_4 and as was the case with the previous force field, the LJ parameters were adopted from the universal force field[61] but with the well depth ϵ rescaled by a factor of 0.635. The partial charges were computed by using the density-derived electrostatic and chemical charge method (DDEC). The paper provides 2 values for the charge of H3 atoms and does not specify which value or combination of values was used for their simulations. We found that in order to obtain a charge-neutral framework, two of

Table A.4: Urey-Bradley interaction parameters. K_u in $kcal \cdot mol^{-1} \cdot \text{\AA}^{-2}$, u_0 in \AA .

| | | FF5 |
|-----------------|-------|------------|
| N-C1-N | K_u | 214.74 |
| | u_0 | 2.236 |
| N-C1-C3 | K_u | 61.22 |
| | u_0 | 2.522 |
| C2-C2-N | K_u | 198.1 |
| | u_0 | 2.235 |
| C2-C2-H2 | K_u | 29.56 |
| | u_0 | 2.236 |
| N-C2-H2 | K_u | 40.86 |
| | u_0 | 2.16 |
| C1-N-C2 | K_u | 223.3 |
| | u_0 | 2.193 |
| C1-C3-H3 | K_u | 38.32 |
| | u_0 | 2.153 |
| H3-C3-H3 | K_u | 37.34 |
| | u_0 | 1.779 |
| C1-N-Zn | K_u | 0 |
| | u_0 | 0 |
| C2-N-Zn | K_u | 0 |
| | u_0 | 0 |
| N-Zn-N | K_u | 0 |
| | u_0 | 0 |

the H3 hydrogens in the methyl group must have a charge of 0.1306e (first value in Table A.1) and the other H3 hydrogen must have a charge of 0.1306 (second value in Table A.1).

Table A.5: Improper torsion interaction parameters. ^a in $kcal/mol$, ^b in $kcal \cdot mol^{-1} \cdot rad^{-2}$, ξ_0 in deg, 2nd atom is the central one.

| | | FF2 | FF3 | FF4 | FF5 | | FF1 | |
|-------------------|-----------|------------|------------|------------|------------|-------------------|-------------------|-----------|
| N-C1-N-C3 | K_ξ^a | 1.1 | 1.1 | 1.1 | 3.5 | N-C1-N-C3 | K_ξ^b | 4 |
| | m | 2 | 2 | 2 | 2 | | ξ_0 | 180 |
| | ξ_0 | 180 | 180 | 180 | 180 | | N-C2-C2-H2 | K_ξ^b |
| N-C2-C2-H2 | K_ξ^a | 1.1 | 1.1 | 1.1 | 0 | ξ_0 | | 180 |
| | m | 2 | 2 | 2 | 2 | Zn-N-C1-C2 | | K_ξ^b |
| | ξ_0 | 180 | 180 | 180 | 180 | | ξ_0 | 180 |
| Zn-N-C1-C2 | K_ξ^a | 0.0956 | — | — | 0.056 | | Zn-N-C1-C2 | K_ξ^b |
| | m | 2 | — | — | 2 | ξ_0 | | 180 |
| | ξ_0 | 180 | — | — | 180 | | | |

The parameters for FF5 contained in the tables were taken directly from the original paper. The parameters of the bonded interactions for the organic linkers were adopted from the work of Gabrieli et al.[274] who optimized the GAFF originals on the basis of force matching. All bonded interaction parameters involving Zn were re-optimized by the authors against DFT-calculated properties using a genetic algorithm. The LJ parameters were taken directly from GAFF while the partial charges were computed using DDEC.

Table A.6: Dihedral torsion interaction parameters. K_ϕ in *kcal/mol*, ϕ_0 in *deg*.

| | | FF1 | FF2 | FF3 | FF4 | FF5 |
|--------------------|----------|------------|------------|------------|------------|------------|
| C1-N-C2-H2 | K_ϕ | 2.325 | 4.8 | 4.8 | 4.8 | 3.65 |
| | m | 2 | 2 | 2 | 2 | 2 |
| | ϕ_0 | 180 | 180 | 180 | 180 | 180 |
| C1-N-C2-C2 | K_ϕ | 2.325 | 4.8 | 4.8 | 4.8 | 6.64 |
| | m | 2 | 2 | 2 | 2 | 2 |
| | ϕ_0 | 180 | 180 | 180 | 180 | 180 |
| N-C2-C2-H2 | K_ϕ | 5.15 | 4 | 4 | 4 | 3.55 |
| | m | 2 | 2 | 2 | 2 | 2 |
| | ϕ_0 | 180 | 180 | 180 | 180 | 180 |
| N-C2-C2-N | K_ϕ | 5.15 | 4 | 4 | 4 | 15.33 |
| | m | 2 | 2 | 2 | 2 | 2 |
| | ϕ_0 | 180 | 180 | 180 | 180 | 180 |
| H2-C2-C2-H2 | K_ϕ | 5.15 | 4 | 4 | 4 | 0.34 |
| | m | 2 | 2 | 2 | 2 | 2 |
| | ϕ_0 | 180 | 180 | 180 | 180 | 180 |
| C3-C1-N-C2 | K_ϕ | 5 | 4.8 | 4.15 | 4.15 | 3.64 |
| | m | 2 | 2 | 2 | 2 | 2 |
| | ϕ_0 | 180 | 180 | 180 | 180 | 180 |
| N-C1-N-C2 | K_ϕ | 5 | 4.8 | 4.8 | 4.8 | 10.77 |
| | m | 2 | 2 | 2 | 2 | 2 |
| | ϕ_0 | 180 | 180 | 180 | 180 | 180 |
| N-C1-C3-H3 | K_ϕ | — | — | — | — | 0.27 |
| | m | — | — | — | — | 2 |
| | ϕ_0 | — | — | — | — | 180 |

A.1.3 ADDITIONAL DETAILS

The force fields were implemented as close as stated by the original papers as possible, however, as mentioned in section 1.2 some of them do not include crucial

Table A.7: Dihedral torsion interaction parameters involving Zn. K_ϕ in kcal/mol, ϕ_0 in deg.

| | | FF1 | FF2 | FF3 | FF4 | FF5 |
|-------------------|----------|------------|------------|------------|------------|------------|
| Zn-N-C2-H2 | K_ϕ | 2.325 | 0.12 | — | — | 1.056 |
| | m | 2 | 2 | — | — | 2 |
| | ϕ_0 | 180 | 180 | — | — | 180 |
| Zn-N-C2-C2 | K_ϕ | 2.325 | 0.12 | 0.1 | 0.1 | 1.416 |
| | m | 2 | 2 | 2 | 2 | 2 |
| | ϕ_0 | 180 | 180 | 180 | 180 | 180 |
| C3-C1-N-Zn | K_ϕ | 5 | 0.12 | 0.1 | 0.1 | 0.227 |
| | m | 2 | 2 | 2 | 2 | 2 |
| | ϕ_0 | 180 | 180 | 180 | 180 | 180 |
| N-C1-N-Zn | K_ϕ | 5 | 0.12 | 0.1 | 0.1 | 0.614 |
| | m | 2 | 2 | 2 | 2 | 2 |
| | ϕ_0 | 180 | 180 | 180 | 180 | 180 |
| N-Zn-N-C1 | K_ϕ | — | — | 0.174 | 0.174 | 0.026 |
| | m | — | — | 3 | 3 | 3 |
| | ϕ_0 | — | — | 0 | 0 | 0 |
| N-Zn-N-C2 | K_ϕ | — | — | 0.174 | 0.174 | 0.021 |
| | m | — | — | 3 | 3 | 3 |
| | ϕ_0 | — | — | 0 | 0 | 180 |

information. For example, if not stated explicitly by the article, the cutoff for direct electrostatic calculations in our simulations was set to 12.0 Å. A summary of the cutoffs and 1-4 scaling parameters used in this work is provided in Table A.8. In order to determine the 1-4 non-bonded interaction scaling parameters for FF2, a series of NPT MD simulations were run using a variety of classical FF scaling policies, specifically, those of AMBER (0.5 for VdW, 0.8333 for electrostatic), Dreiding (both unscaled) CHARMM (0 for both) and OPLS/AA (0.5 for both). The average lattice parameters of the unit cell were subsequently computed and compared to those reported by the authors. We found that a 1-4 scaling policy of 0.5 for both VdW and electrostatic interactions provided the reported average lattice parameter value of ≈ 17.0 Å.

For FF3, a VdW interaction cutoff of 14.0 Å and 1-4 scaling policy of 0.5 for both VdW and electrostatic interactions were tested and found to reproduce the geometric properties of the unit cell reported by the paper. Said values were selected for analysis based on the fact that FF3 was created by the same group that

Table A.8: Interaction cutoff values and 1-4 scaling parameters. r_{cut} in Å.

| | VdW r_{cut} | Elec. r_{cut} | VdW 1-4 scaling | Elec. 1-4 scaling |
|------------|----------------------|------------------------|-----------------|-------------------|
| FF1 | 14.0 | 12.0 | 0.50 | 0.8333 |
| FF2 | 14.0 | 12.0 | 0.50 | 0.50 |
| FF3 | 14.0 | 12.0 | 0.50 | 0.50 |
| FF4 | 14.0 | 12.0 | 0.50 | 0.50 |
| FF5 | 13.0 | 13.0 | 0.50 | 0.6875 |

proposed FF2. As previously stated, FF5 does not explicitly report on the 1-4 scaling parameter for VdW interactions, however, the simulation files provided as supporting documentation use a value of 0.5 and therefore we do too.

A.2 FORCE FIELD IMPLEMENTATION

A.2.1 POTENTIAL FUNCTIONS

The potential terms defined in the original papers are available in both the RASPA and LAMMPS simulation packages, thus one can produce a faithful adaptation without the need to resort to any approximate functions. Care must be taken when writing-in the FF parameters, as the default input energy units for each code is different. The bond stretching term is provided as the “harmonic” `bond_style` in LAMMPS and the “HARMONIC_BOND” potential in RASPA. The usual 1/2 factor is included in the force constant in the former while it’s not in the latter. The harmonic angle bending term is provided as the “harmonic” `angle_style` in LAMMPS and the “HARMONIC_BEND” potential in RASPA. As is the case with the previous potential type, the usual 1/2 factor is included in the force constant in LAMMPS while it is not in RASPA. For FF5, where the bending potential includes both a harmonic and Urey-Bradley contribution, LAMMPS provides the “charmm” `angle_style` which encompasses both. RASPA requires the separate inclusion of the U-B term “HARMONIC_UREYBRADLEY” in addition to the canonical harmonic bend. The Fourier-style dihedral torsion is provided as the “charmm” `dihedral_style` in LAMMPS (with a ‘weighing factor’ of 0.0) and the “CVFF_DIHEDRAL” po-

tential in RASPA. The harmonic improper torsion is provided as the “harmonic” improper_style in LAMMPS and the “HARMONIC_IMPROPER_DIHEDRAL” potential in RASPA. The usual 1/2 factor is included in the force constant in LAMMPS while it is not in RASPA. The Fourier-style improper torsion is provided as “cvff” in LAMMPS and as “CVFF_IMPROPER_DIHEDRAL” in RASPA.

A.2.2 SIMULATION CODE CONGRUENCY VERIFICATION

In order to employ the two-code approach for the analysis and comparison of structural and mechanical properties, it is necessary to first verify that the FF implementations provide congruent results between the codes. For this, the term-by-term contributions to the energy were calculated with both codes, for the same atomic configuration.

A system consisting of $8 \times 2 \times 2$ unit cells of ZIF-8 was employed in the RASPA simulations, using the unit cell crystallographic information file (CIF) constructed by D. Dubbeldam based on previously reported experimental measurements by K. S. Park, et al.[36]. The input topologies for LAMMPS were created using an in-house script using the atomic positions from the same CIF and the framework atom connectivity information inferred from each force field. The reason for using CIF instead of the more ubiquitous PDB file is that the latter only allows for the representation of a maximum of 3 decimal numbers.

Table A.9: Initial configuration energy contributions comparison of RASPA (R) vs LAMMPS (L). Units of $\text{kcal} \cdot \text{mol}^{-1}$.

| | | Bond | Bend | Torsion | Improper | VdW | Coulomb |
|------------------|---|-------------|-------------|----------------|-----------------|--------------|----------------|
| FF1 [62] | L | 6546.2087 | 0.58568845 | 17.604775 | 1.2026054 | -1297.5469 | -6623.2763 |
| | R | 6546.208735 | 0.585688452 | 17.60477513 | 1.202605444 | -1297.54688 | -6623.114704 |
| FF2 [63] | L | 0.38769074 | 0.17431773 | 12.203572 | 0.79748426 | -1269.003 | 1793.179 |
| | R | 0.387690631 | 0.174320676 | 12.21174146 | 0.797485075 | -1269.02699 | 1793.198783 |
| FF3 [64] | L | 0.32090403 | 14.967566 | 417.93868 | 0.76345557 | -840.44983 | 3181.5197 |
| | R | 0.320904031 | 14.96756588 | 417.9386731 | 0.763455565 | -840.4498429 | 3181.594673 |
| FF4 [65] | L | 0.32090403 | 14.967566 | 417.93868 | 0.95044739 | -987.47822 | 1379.6331 |
| | R | 0.320904031 | 14.96756588 | 417.9386777 | 0.950447386 | -987.4782257 | 1379.68962 |
| FF5 [149] | L | 7500.0047 | 1243.3146 | 326.53627 | 2.4490301 | -1243.3647 | -6434.1725 |
| | R | 7500.004681 | 1243.314574 | 326.5362699 | 2.449030136 | -1243.364629 | -6434.159446 |

As can be seen in Table A.9 the energy terms of each contribution match up to at least the fourth decimal in the case of bonded and VdW interactions and up to the second decimal in the case of electrostatic interactions. The differences in the latter might be due to either different implementations of the Ewald summation in the codes or the finite precision of the specified atom positions.

A.3 ADDITIONAL RESULTS: TEMPERATURE AND PRESSURE DEPENDENCE OF THE UNIT CELL

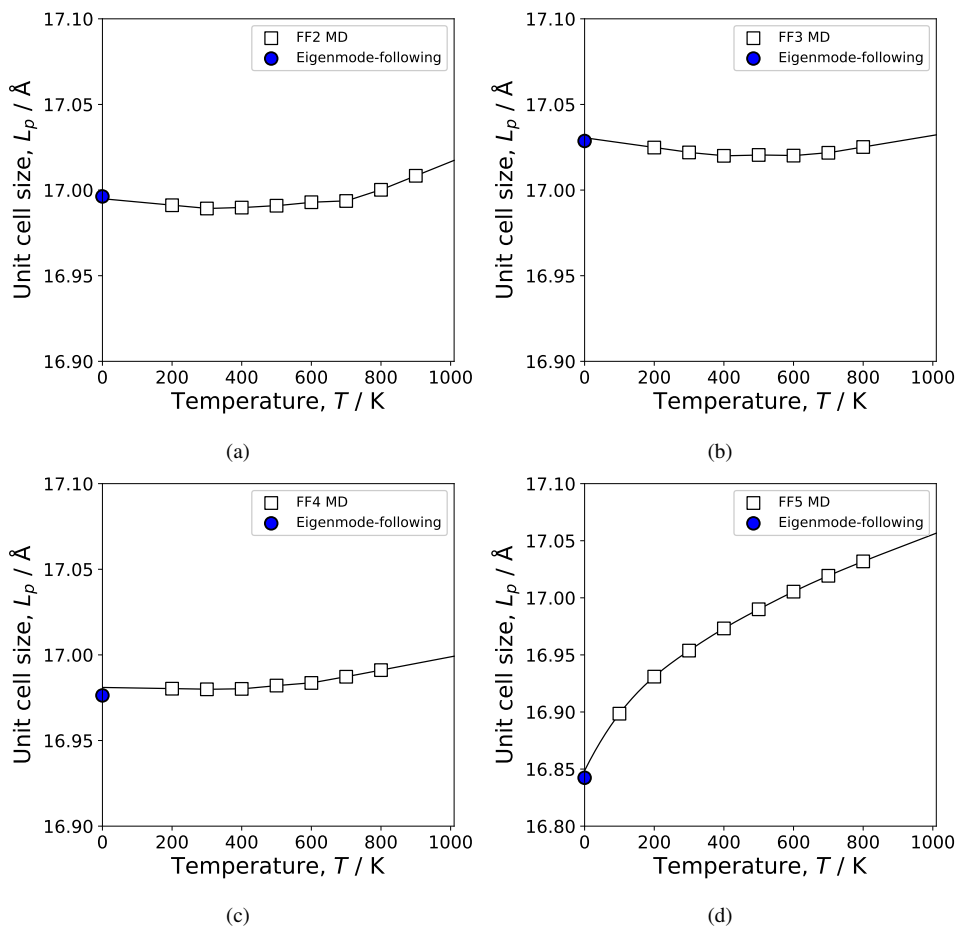


Figure A.3: Size of the unit cell of ZIF-8 predicted by FF2-FF4. MD data obtained at a pressure of 1 atm and represented with open squares. Extrapolated values at 0 K are compared with the unit cell size obtained using Eigenmode-following minimization technique.

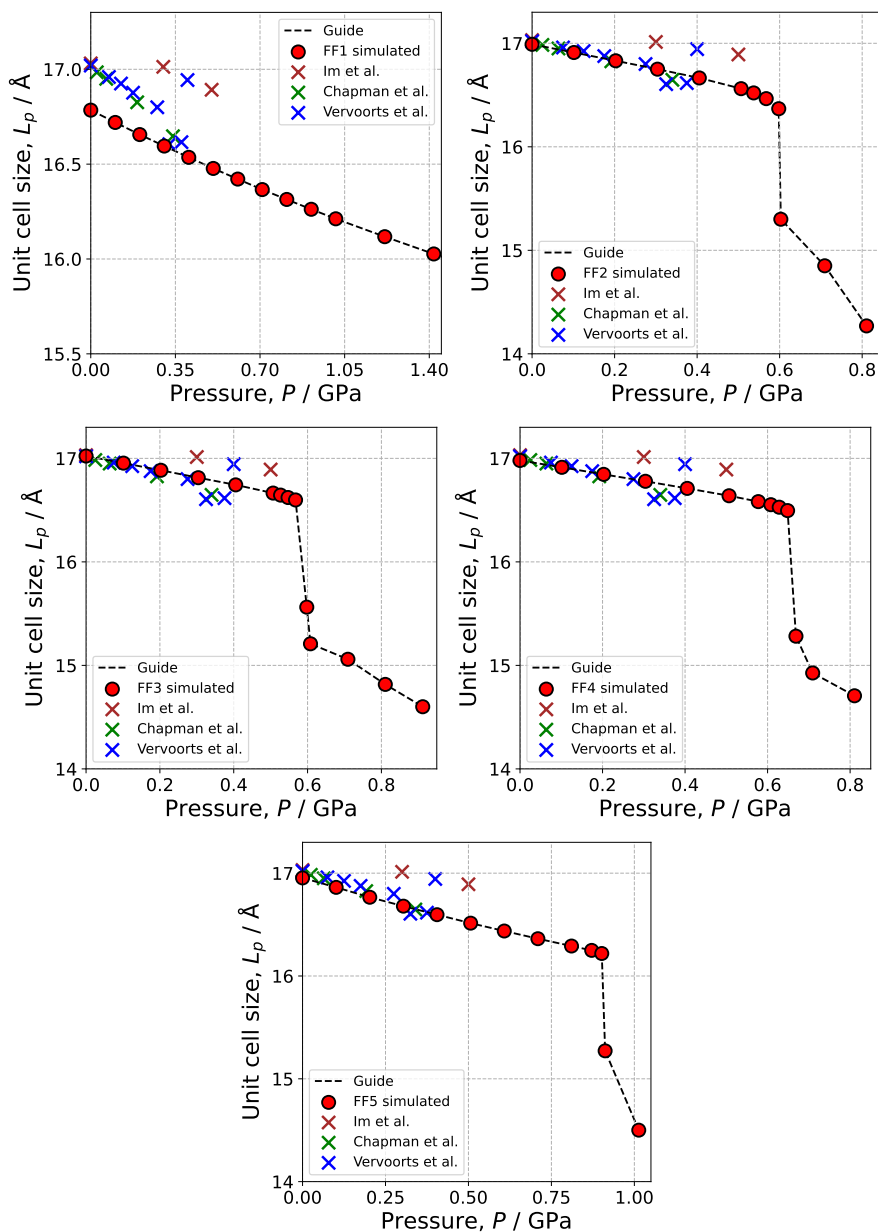


Figure A.4: Pressure dependence isotherms ($T = 300$ K) of the unit cell lattice parameter for the implemented force fields. Reported experimental measurements represented as crosses.[54, 165, 275]

B

APPENDIX 2

B.0.1 ATOM NOMENCLATURE AND FORCE FIELD PARAMETERS

The tables included in this subsection contain the interaction parameters for each term of the Universal Force Field[61], as used in this work. The atom types referenced in the text and tables are labeled according to the pictured nomenclature (Fig. B.1).

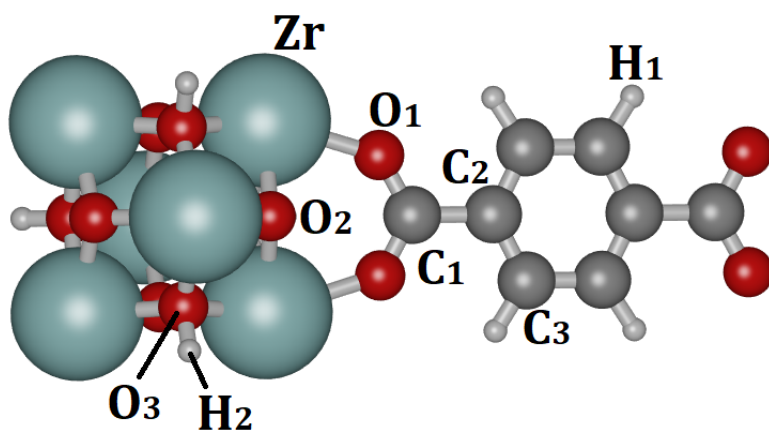


Figure B.1: Atom nomenclature used in this work

The parameters were initially obtained using the ‘LAMMPS interface’ python module created by P. Boyd, M. Moosavi and M. Witman for the publication by Boyd et al.[191]. The module takes a crystallographic information file (CIF) as input to generate the parameter sets. In this work, we used the pristine UiO-66 CIF constructed by D. Dubbeldam included in the RASPA2 simulation package[151] based on previously reported experimental measurements by J.S. Cavka et al.[177]. The derivation of the outputted parameters were verified according to the UFF recipes, reformatted according to our atom nomenclature and used in the creation of the LAMMPS input files. The force field parameters are organized term by term and provided in tables B.1 to B.3.

Table B.1: Parameters for the bond stretching potential energy contribution of the force field (left). Non-bonded interaction (right).

| $U_{\text{bonds}} = \frac{1}{2}K_r(r - r_0)^2$ | | |
|--|--------------------------------------|-----------|
| Bond | K_r [kcal/(mol · Å ²)] | r_0 [Å] |
| C3-C3 | 925.31 | 1.379 |
| C3-C2 | 925.31 | 1.379 |
| C3-H1 | 714.88 | 1.081 |
| C1-O1 | 1293.36 | 1.312 |
| C1-C2 | 783.34 | 1.458 |
| O3-H2 | 1119.99 | 0.990 |
| O1-Zr | 582.00 | 2.127 |
| O3-Zr | 598.89 | 2.107 |
| O2-Zr | 618.00 | 2.085 |

| $U_{\text{LJ}} = 4\epsilon \left[\left(\frac{\sigma}{r_{ij}} \right)^{12} - \left(\frac{\sigma}{r_{ij}} \right)^6 \right]$ | | |
|---|-----------------------|--------------|
| Atoms | ϵ [kcal/mol] | σ [Å] |
| Zr - Zr | 0.069 | 2.783 |
| O1 - O1 | 0.060 | 3.118 |
| O2 - O2 | 0.060 | 3.118 |
| O3 - O3 | 0.060 | 3.118 |
| C1 - C1 | 0.105 | 3.431 |
| C2 - C2 | 0.105 | 3.431 |
| C3 - C3 | 0.105 | 3.431 |
| H1 - H1 | 0.044 | 2.571 |
| H2 - H2 | 0.044 | 2.571 |

Table B.2: Parameters for the angle bending contributions of the force field. The coefficients C_0 , C_1 and C_2 are derived according to the recipe provided in the original article[61] given an equilibrium angle. The specific coefficients used in this work were obtained using the equilibrium angle generated by the ‘LAMMPS interface’ python module.

| $U_{\text{angles}} = \frac{K_{\theta}}{n^2} [1 - \cos(n\theta)]$ | | | $U'_{\text{angles}} = K_{\theta} [C_0 + C_1 \cos(\theta) + C_2 \cos(2\theta)]$ | | | | |
|--|-------------------------|---|--|-------------------------|-------|-------|-------|
| Bend | K_{θ} [kcal/mol] | n | Bend | K_{θ} [kcal/mol] | c_0 | c_1 | C_2 |
| C3-C3-C2 | 111.30 | 3 | Zr-O3-Zr | 331.86 | 0.300 | 0.267 | 0.267 |
| C3-C2-C3 | 111.30 | 3 | H2-O3-Zr | 122.14 | 0.300 | 0.267 | 0.267 |
| C3-C3-H1 | 57.29 | 3 | O3-Zr-O2 | 116.83 | 0.344 | 0.375 | 0.281 |
| C2-C3-H1 | 57.29 | 3 | O1-Zr-O2 | 115.14 | 0.344 | 0.375 | 0.281 |
| O1-C1-O1 | 187.14 | 3 | O1-Zr-O2 | 115.14 | 0.344 | 0.375 | 0.281 |
| C2-C1-O1 | 131.76 | 3 | O1-Zr-O3 | 113.38 | 0.344 | 0.375 | 0.281 |
| C3-C2-C1 | 102.18 | 3 | O1-Zr-O3 | 113.38 | 0.344 | 0.375 | 0.281 |
| C1-O1-Zr | 124.83 | 3 | O1-Zr-O1 | 111.77 | 0.344 | 0.375 | 0.281 |
| Zr-O2-Zr | 118.51 | 3 | O1-Zr-O1 | 111.77 | 0.344 | 0.375 | 0.281 |
| | | | O2-Zr-O2 | 118.69 | 0.344 | 0.375 | 0.281 |
| | | | O3-Zr-O3 | 115.02 | 0.344 | 0.375 | 0.281 |

| $U_{\text{dihedrals}} = \frac{K_{\phi}}{2} [1 - \cos(m\phi_0) \cos(m\phi)]$ | | | $U_{\text{impropers}} = K_{\xi} [C_0 + C_1 \cos(\xi) + C_2 \cos(2\xi)]$ | | | | |
|---|-----------------------|---|---|----------------------|-------|-------|-------|
| Dihedral | K_{ϕ} [kcal/mol] | m | Improper | K_{ξ} [kcal/mol] | C_0 | C_1 | C_2 |
| H1-C3-C2-C1 | 6.74 | 2 | C3-C3-C2-H1 | 2 | 1 | -1 | 0 |
| H1-C3-C2-C3 | 6.74 | 2 | C3-H1-C3-C2 | 2 | 1 | -1 | 0 |
| H1-C3-C3-H1 | 6.74 | 2 | C3-C2-H1-C3 | 2 | 1 | -1 | 0 |
| H1-C3-C3-C2 | 6.74 | 2 | C1-C2-O1-O1 | 2 | 1 | -1 | 0 |
| C3-C3-C2-C3 | 6.74 | 2 | C1-O1-C2-O1 | 2 | 1 | -1 | 0 |
| C3-C3-C2-C1 | 6.74 | 2 | C1-O1-O1-C2 | 2 | 1 | -1 | 0 |
| C2-C3-C3-C2 | 6.74 | 2 | C2-C3-C3-C1 | 2 | 1 | -1 | 0 |
| C2-C1-O1-Zr | 13.47 | 2 | C2-C1-C3-C3 | 2 | 1 | -1 | 0 |
| O1-C1-O1-Zr | 13.47 | 2 | C2-C3-C1-C3 | 2 | 1 | -1 | 0 |
| O1-C1-C2-C3 | 2.50 | 2 | O2-Zr-Zr-Zr | 2 | 1 | -1 | 0 |

Table B.3: Left: Parameters for the dihedral torsion potential (left). UFF stipulates there should be no dihedrals defined for metal ions in the two middle positions. Angle ϕ_0 for the defined dihedrals is either 0 or π . Parameters for the improper dihedral term of the force field (right).

B.0.2 ALTERNATIVE REFERENCE SET COMPARISON

In Chapter 4 a comparison with a reference set of 8 structures is presented. Said structures were created sequentially by introducing linker vacancies in an orderly fashion to the pristine UiO-66 structure (see Fig. 4.3). In order to determine the degree to which the vacancy introduction process impacts the result, we generated an alternative reference set in which the same vacancies are introduced randomly.

As can be seen in Figure B.2 and B.3, the amorphization pressures for every pair of structures with N vacancies is similar. The extrapolated values for 0 linker vacancies are quite similar as well.

B

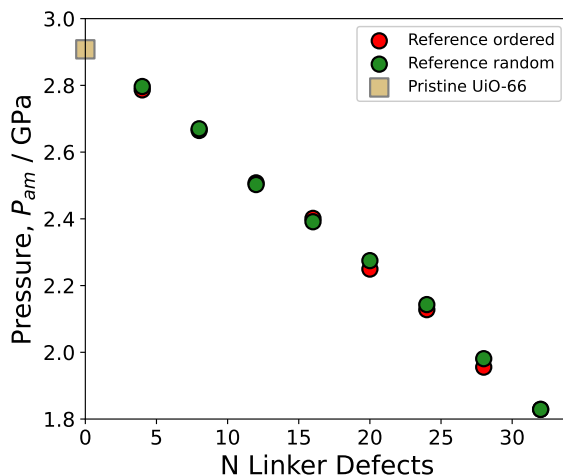


Figure B.2: Amorphization pressure with respect to the number of linker vacancies for the reference systems. The red data points correspond to structures in which the vacancies were introduced in order and the green data points correspond to structures where the same defects were introduced randomly.

B.0.3 AMORPHIZATION PRESSURE WITH RESPECT TO NUMBER OF LINKER VACANCIES

As mentioned in Chapter 4, for each defective structure certain distance-based metrics were calculated. Figures S4 and S5 are P_{am} v.s N plots where the data for each structure is coloured according to the mean distance between vacancies and the mean distance with respect to the geometric centre of the supercell, respectively.

B.0.4 RESULTS DATA TABLES

In this section, we present tables (B.4-B.13) comparing amorphization pressure (P_{am}), mean distance between vacancies (D_V), mean distance from linker vacancies to the geometric center of the supercell (D_C), bulk modulus (K_V), and anisotropies (E_{ani})

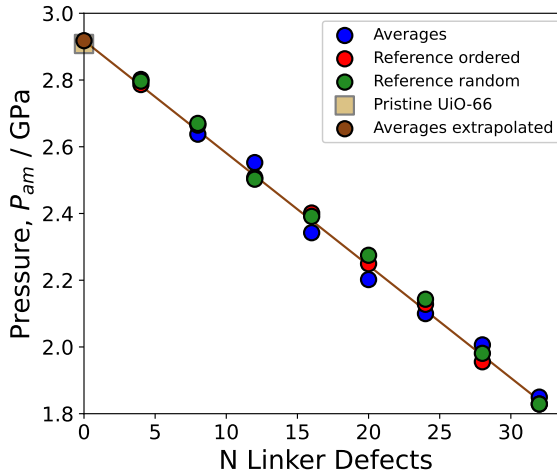


Figure B.3: Comparison between the reference systems (red and green) and the average amorphization pressure value for each set of defected structures (blue circles). The line represents the linear extrapolation of the average values. The extrapolated P_{am} estimation for a structure with 0 linker defects is 2.92 GPa which is close to the amorphization pressure of the pristine structure obtained using MD (2.908 GPa).

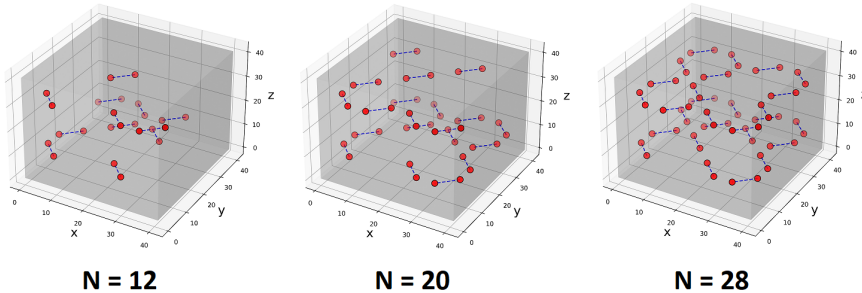


Figure B.4: Pictorial representation of the structures with 12, 20 and 28 randomly introduced linker vacancies. The vacancies are the same ones as those previously introduced in an orderly fashion and used as a reference in Chapter 4 therefore the $N = 32$ structure is the same for both sets.

and β_{ani}) for the structures analyzed in this study. Each table provides information for structures with the same number of linker vacancies and includes details about the orientation-specific distribution of these vacancies. That is, each defected structure is characterized by the number of missing linkers with particular orientations. In UiO-66, there are six distinct BDC linker orientations, and the nomenclature used

B

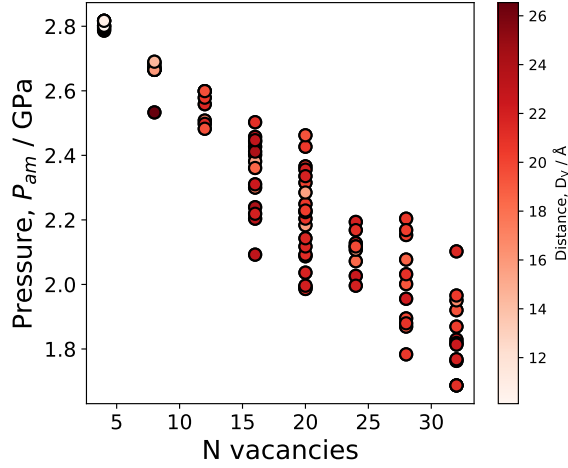


Figure B.5: Amorphization pressure with respect to the number of linker vacancies contained for all defected structures of study. Each data point corresponds to a defected structure with different vacancy spatial concentration, orientation and order. The data points are colored according to the mean distance between linker vacancies (in Å). As can be seen in the picture, this metric ceases to be a good differentiator of structures with more than a few linker vacancies.

for these orientations is illustrated in Fig. B.7.

| Structures with 4 defects in the 2X2X2 supercell | | | | | | | | | | | |
|--|-----------|-----------|------|------|------|------|------|------|-------------|-----------------|---------------------|
| P_{am} [GPa] | D_V [Å] | D_C [Å] | #OT1 | #OT2 | #OT3 | #OT4 | #OT5 | #OT6 | K_V [GPa] | E_{ani} [GPa] | β_{ani} [GPa] |
| 2.792 | 18.12 | 12.59 | 0 | 1 | 0 | 1 | 1 | 1 | 57.80 | 1.18 | 1.10 |
| 2.797 | 19.28 | 16.67 | 0 | 2 | 0 | 0 | 2 | 0 | 57.76 | 1.22 | 1.22 |
| 2.802 | 22.31 | 15.69 | 0 | 0 | 1 | 0 | 2 | 1 | 57.73 | 1.19 | 1.14 |
| 2.802 | 10.12 | 7.32 | 1 | 1 | 1 | 1 | 0 | 0 | 58.00 | 1.17 | 1.09 |
| 2.817 | 20.92 | 25.05 | 0 | 0 | 2 | 0 | 0 | 2 | 57.92 | 1.22 | 1.21 |
| 2.817 | 16.79 | 11.34 | 1 | 0 | 0 | 1 | 1 | 1 | 57.91 | 1.18 | 1.11 |
| 2.817 | 10.83 | 19.16 | 2 | 0 | 1 | 1 | 0 | 0 | 58.38 | 1.18 | 1.11 |

Table B.4: Results comparison for the structures containing 4 linker vacancies. Columns denoted with #OT refer to the number of linker vacancies with a given orientation type. Data is sorted according to amorphization pressure, in ascending order.

| Structures with 8 defects in the 2X2X2 supercell | | | | | | | | | | | |
|--|-----------|-----------|------|------|------|------|------|------|-------------|-----------------|---------------------|
| P_{am} [GPa] | D_V [Å] | D_C [Å] | #OT1 | #OT2 | #OT3 | #OT4 | #OT5 | #OT6 | K_V [GPa] | E_{ani} [GPa] | β_{ani} [GPa] |
| 2.533 | 26.54 | 18.92 | 0 | 0 | 0 | 8 | 0 | 0 | 55.53 | 1.54 | 1.739 |
| 2.665 | 22.07 | 22.57 | 8 | 0 | 0 | 0 | 0 | 0 | 55.38 | 1.561 | 1.7608 |
| 2.665 | 15.95 | 19.59 | 2 | 1 | 1 | 1 | 2 | 1 | 54.80 | 1.185 | 1.0923 |
| 2.670 | 22.75 | 21.39 | 0 | 0 | 8 | 0 | 0 | 0 | 55.20 | 1.614 | 1.8661 |
| 2.675 | 22.60 | 19.28 | 0 | 8 | 0 | 0 | 0 | 0 | 55.57 | 1.554 | 1.7465 |
| 2.685 | 22.48 | 17.71 | 2 | 4 | 0 | 2 | 0 | 0 | 55.34 | 1.234 | 1.2955 |
| 2.690 | 14.53 | 23.90 | 0 | 1 | 2 | 3 | 0 | 2 | 56.29 | 1.216 | 1.2055 |

Table B.5: Results comparison for the structures containing 8 linker vacancies.

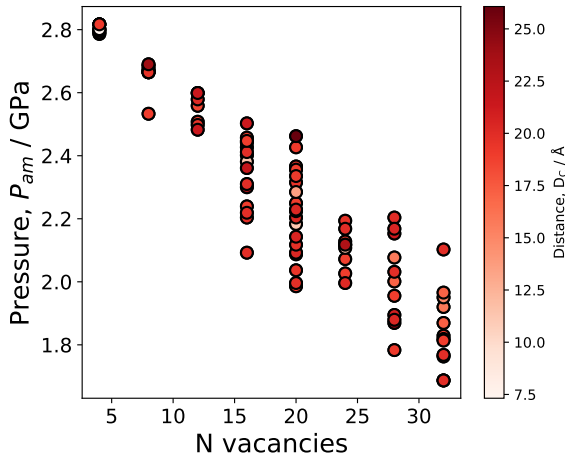


Figure B.6: Analogous to Figure B.5. The data points are colored according to the mean distance from linker vacancies to the geometric center of the supercell (in Å).

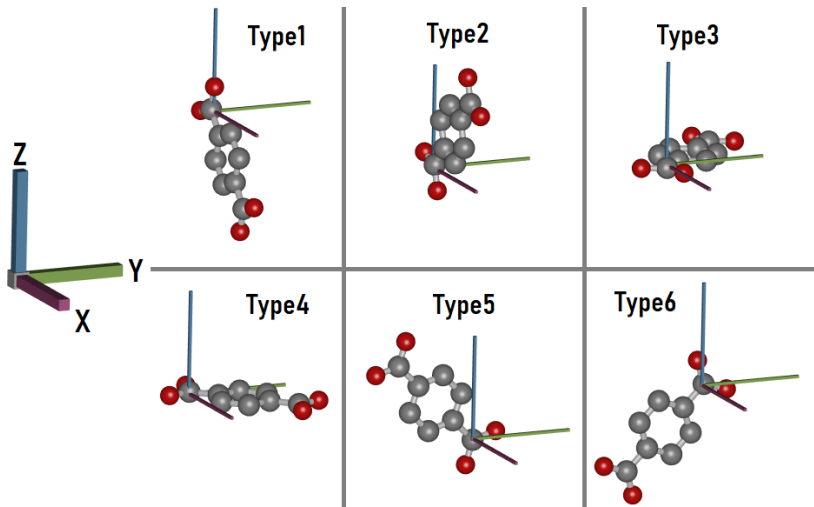


Figure B.7: BDC linker orientation nomenclature used in this work. Orientation type (OT) is categorized according to their position with respect to cartesian coordinate axes.

| Structures with 12 defects in the 2X2X2 supercell | | | | | | | | | | | |
|---|-----------|-----------|------|------|------|------|------|------|-------------|-----------------|---------------------|
| P_{am} [GPa] | D_V [Å] | D_C [Å] | #OT1 | #OT2 | #OT3 | #OT4 | #OT5 | #OT6 | K_V [GPa] | E_{ani} [GPa] | β_{ani} [GPa] |
| 2.482 | 19.46 | 21.39 | 3 | 2 | 2 | 3 | 1 | 1 | 51.74 | 1.20 | 1.19 |
| 2.498 | 21.52 | 19.55 | 0 | 12 | 0 | 0 | 0 | 0 | 53.40 | 1.99 | 2.61 |
| 2.558 | 21.54 | 18.46 | 12 | 0 | 0 | 0 | 0 | 0 | 53.84 | 1.85 | 2.27 |
| 2.579 | 20.48 | 20.11 | 1 | 2 | 4 | 2 | 1 | 2 | 51.97 | 1.23 | 1.28 |
| 2.599 | 20.79 | 19.24 | 1 | 3 | 2 | 2 | 2 | 2 | 52.59 | 1.22 | 1.21 |
| 2.599 | 19.54 | 21.44 | 1 | 3 | 2 | 2 | 0 | 4 | 52.47 | 1.30 | 1.33 |

Table B.6: Results comparison for the structures containing 12 linker vacancies.

B

| Structures with 16 defects in the 2X2X2 supercell | | | | | | | | | | | |
|---|-----------|-----------|------|------|------|------|------|------|-------------|-----------------|---------------------|
| P_{am} [GPa] | D_V [Å] | D_C [Å] | #OT1 | #OT2 | #OT3 | #OT4 | #OT5 | #OT6 | K_V [GPa] | E_{ani} [GPa] | β_{ani} [GPa] |
| 2.092 | 23.05 | 19.89 | 0 | 0 | 0 | 16 | 0 | 0 | 50.71 | 3.02 | 7.21 |
| 2.204 | 23.51 | 19.89 | 0 | 8 | 0 | 8 | 0 | 0 | 49.59 | 1.73 | 2.65 |
| 2.219 | 21.95 | 19.89 | 0 | 0 | 8 | 8 | 0 | 0 | 48.34 | 1.36 | 2.17 |
| 2.239 | 24.08 | 18.92 | 0 | 0 | 8 | 8 | 0 | 0 | 51.47 | 1.50 | 2.02 |
| 2.300 | 17.60 | 23.75 | 2 | 4 | 1 | 3 | 3 | 3 | 46.73 | 1.26 | 1.19 |
| 2.310 | 22.48 | 19.89 | 8 | 0 | 0 | 8 | 0 | 0 | 50.92 | 1.62 | 2.08 |
| 2.361 | 18.46 | 21.87 | 2 | 2 | 0 | 3 | 5 | 4 | 48.36 | 1.36 | 1.52 |
| 2.381 | 15.45 | 11.34 | 4 | 1 | 2 | 4 | 2 | 3 | 49.26 | 1.27 | 1.39 |
| 2.412 | 24.08 | 19.89 | 0 | 0 | 8 | 8 | 0 | 0 | 52.05 | 1.43 | 1.62 |
| 2.427 | 24.08 | 19.89 | 0 | 0 | 0 | 0 | 8 | 8 | 52.05 | 1.43 | 1.62 |
| 2.442 | 20.22 | 22.30 | 2 | 1 | 4 | 2 | 2 | 5 | 48.92 | 1.27 | 1.33 |
| 2.447 | 23.05 | 18.92 | 0 | 0 | 0 | 16 | 0 | 0 | 53.65 | 1.85 | 2.22 |
| 2.457 | 23.05 | 18.92 | 0 | 0 | 0 | 0 | 0 | 16 | 53.65 | 1.85 | 2.22 |
| 2.503 | 21.08 | 21.27 | 1 | 1 | 2 | 4 | 3 | 5 | 50.45 | 1.26 | 1.26 |

Table B.7: Results comparison for the structures containing 16 linker vacancies.

| Structures with 24 defects in the 2X2X2 supercell | | | | | | | | | | | |
|---|-----------|-----------|------|------|------|------|------|------|-------------|-----------------|---------------------|
| P_{am} [GPa] | D_V [Å] | D_C [Å] | #OT1 | #OT2 | #OT3 | #OT4 | #OT5 | #OT6 | K_V [GPa] | E_{ani} [GPa] | β_{ani} [GPa] |
| 1.996 | 21.94 | 20.22 | 16 | 0 | 8 | 0 | 0 | 0 | 46.17 | 3.11 | 7.32 |
| 2.027 | 22.39 | 18.92 | 8 | 8 | 0 | 8 | 0 | 0 | 46.50 | 1.68 | 2.48 |
| 2.072 | 18.37 | 18.76 | 7 | 1 | 4 | 6 | 2 | 4 | 43.67 | 1.55 | 1.92 |
| 2.108 | 16.23 | 11.82 | 3 | 5 | 4 | 5 | 3 | 4 | 42.80 | 1.21 | 1.29 |
| 2.118 | 18.90 | 22.79 | 5 | 4 | 2 | 7 | 3 | 3 | 44.73 | 1.30 | 1.48 |
| 2.118 | 19.68 | 23.06 | 4 | 5 | 4 | 5 | 3 | 3 | 42.39 | 1.25 | 1.27 |
| 2.168 | 21.00 | 19.99 | 3 | 1 | 6 | 5 | 7 | 2 | 43.72 | 1.41 | 1.68 |
| 2.194 | 21.93 | 19.57 | 0 | 8 | 8 | 8 | 0 | 0 | 48.23 | 1.56 | 1.85 |

Table B.8: Results comparison for the structures containing 24 linker vacancies.

| Structures with 28 defects in the 2X2X2 supercell | | | | | | | | | | | |
|---|-----------|-----------|------|------|------|------|------|------|-------------|-----------------|---------------------|
| P_{am} [GPa] | D_V [Å] | D_C [Å] | #OT1 | #OT2 | #OT3 | #OT4 | #OT5 | #OT6 | K_V [GPa] | E_{ani} [GPa] | β_{ani} [GPa] |
| 1.783 | 20.55 | 19.14 | 0 | 0 | 0 | 14 | 0 | 14 | 44.12 | 2.72 | 8.28 |
| 1.869 | 19.11 | 24.75 | 6 | 5 | 5 | 8 | 1 | 3 | 41.69 | 1.67 | 1.80 |
| 1.880 | 20.87 | 20.43 | 14 | 0 | 0 | 0 | 14 | 0 | 44.79 | 2.60 | 6.33 |
| 1.895 | 19.83 | 20.89 | 3 | 5 | 9 | 1 | 1 | 9 | 41.67 | 1.84 | 2.97 |
| 2.001 | 19.24 | 17.06 | 6 | 4 | 5 | 4 | 4 | 5 | 39.28 | 1.38 | 1.56 |
| 2.032 | 20.98 | 19.88 | 0 | 0 | 0 | 0 | 14 | 14 | 45.91 | 2.37 | 6.11 |
| 2.077 | 18.65 | 15.79 | 4 | 4 | 7 | 5 | 4 | 4 | 40.99 | 1.20 | 1.19 |
| 2.153 | 20.18 | 21.36 | 3 | 3 | 7 | 6 | 3 | 6 | 42.91 | 1.24 | 1.37 |
| 2.168 | 20.26 | 20.50 | 3 | 5 | 5 | 5 | 5 | 5 | 41.99 | 1.28 | 1.16 |
| 2.204 | 20.63 | 20.01 | 6 | 4 | 3 | 5 | 6 | 4 | 42.67 | 1.26 | 1.28 |

Table B.9: Results comparison for the structures containing 28 linker vacancies.

| Structures with 32 defects in the 2X2X2 supercell | | | | | | | | | | | |
|---|-----------|-----------|------|------|------|------|------|------|-------------|-----------------|---------------------|
| P_{am} [GPa] | D_V [Å] | D_C [Å] | #OT1 | #OT2 | #OT3 | #OT4 | #OT5 | #OT6 | K_V [GPa] | E_{ani} [GPa] | β_{ani} [GPa] |
| 1.687 | 21.01 | 19.89 | 0 | 8 | 0 | 8 | 8 | 8 | 40.17 | 1.76 | 2.43 |
| 1.687 | 20.25 | 20.49 | 6 | 6 | 5 | 3 | 8 | 4 | 37.71 | 1.42 | 1.75 |
| 1.763 | 20.89 | 19.89 | 8 | 8 | 8 | 8 | 0 | 0 | 38.15 | 1.69 | 1.93 |
| 1.768 | 21.92 | 19.89 | 8 | 8 | 8 | 8 | 0 | 0 | 42.35 | 1.70 | 2.01 |
| 1.814 | 22.47 | 18.92 | 16 | 16 | 0 | 0 | 0 | 0 | 50.50 | 1.81 | 3.59 |
| 1.819 | 20.46 | 19.32 | 2 | 7 | 9 | 3 | 6 | 5 | 40.16 | 1.52 | 1.66 |
| 1.869 | 20.26 | 17.20 | 6 | 7 | 5 | 2 | 8 | 4 | 40.76 | 1.44 | 1.64 |
| 1.920 | 19.29 | 15.89 | 2 | 4 | 7 | 6 | 5 | 8 | 40.12 | 1.36 | 1.51 |
| 1.951 | 16.77 | 15.06 | 4 | 7 | 4 | 8 | 3 | 6 | 40.34 | 1.28 | 1.40 |
| 1.966 | 20.48 | 17.03 | 3 | 2 | 8 | 8 | 9 | 2 | 41.55 | 1.46 | 1.74 |
| 2.102 | 21.44 | 19.89 | 0 | 0 | 16 | 16 | 0 | 0 | 46.79 | 1.50 | 2.29 |

Table B.10: Results comparison for the structures containing 32 linker vacancies.

| Reference structures (ordered deletion) | | | | | | | | | | | | |
|---|----------------|-----------|-----------|------|------|------|------|------|------|-------------|-----------------|---------------------|
| N | P_{am} [GPa] | D_V [Å] | D_C [Å] | #OT1 | #OT2 | #OT3 | #OT4 | #OT5 | #OT6 | K_V [GPa] | E_{ani} [GPa] | β_{ani} [GPa] |
| 32 | 1.829 | 22.47 | 18.92 | 0 | 0 | 16 | 16 | 0 | 0 | 50.50 | 1.81 | 3.59 |
| 28 | 1.956 | 22.30 | 18.92 | 0 | 0 | 14 | 14 | 0 | 0 | 50.75 | 1.73 | 3.02 |
| 24 | 2.128 | 21.70 | 18.92 | 0 | 0 | 12 | 12 | 0 | 0 | 51.98 | 1.60 | 2.42 |
| 20 | 2.249 | 20.58 | 18.92 | 0 | 0 | 10 | 10 | 0 | 0 | 53.17 | 1.47 | 2.00 |
| 16 | 2.401 | 17.55 | 18.92 | 0 | 0 | 8 | 8 | 0 | 0 | 55.66 | 1.28 | 1.55 |
| 12 | 2.508 | 17.02 | 18.92 | 0 | 0 | 6 | 6 | 0 | 0 | 55.93 | 1.24 | 1.42 |
| 8 | 2.665 | 14.88 | 18.92 | 0 | 0 | 4 | 4 | 0 | 0 | 57.14 | 1.19 | 1.28 |
| 4 | 2.786 | 11.78 | 18.92 | 0 | 0 | 2 | 2 | 0 | 0 | 58.34 | 1.16 | 1.15 |

Table B.11: Results comparison for the reference set of 8 structures where the vacancies were introduced in an orderly fashion. The first column refers to the number of linker defects in the structure. Columns denoted with #OT refer to the number of linker vacancies with a given orientation type. Data is sorted according to number of defects, in descending order.

| Reference structures (random deletion) | | | | | | | | | | | | |
|--|----------------|-----------|-----------|------|------|------|------|------|------|-------------|-----------------|---------------------|
| N | P_{am} [GPa] | D_V [Å] | D_C [Å] | #OT1 | #OT2 | #OT3 | #OT4 | #OT5 | #OT6 | K_V [GPa] | E_{ani} [GPa] | β_{ani} [GPa] |
| 32 | 1.829 | 22.47 | 18.92 | 0 | 0 | 16 | 16 | 0 | 0 | 50.50 | 1.81 | 3.59 |
| 28 | 1.981 | 22.44 | 19.57 | 0 | 0 | 15 | 13 | 0 | 0 | 50.71 | 1.75 | 3.01 |
| 24 | 2.143 | 22.32 | 19.89 | 0 | 0 | 12 | 12 | 0 | 0 | 51.21 | 1.57 | 2.33 |
| 20 | 2.275 | 22.26 | 20.08 | 0 | 0 | 8 | 12 | 0 | 0 | 52.07 | 1.55 | 2.15 |
| 16 | 2.391 | 22.29 | 19.95 | 0 | 0 | 7 | 9 | 0 | 0 | 52.87 | 1.40 | 1.76 |
| 12 | 2.503 | 22.42 | 19.33 | 0 | 0 | 6 | 6 | 0 | 0 | 53.93 | 1.29 | 1.53 |
| 8 | 2.670 | 22.39 | 18.08 | 0 | 0 | 3 | 5 | 0 | 0 | 55.81 | 1.22 | 1.35 |
| 4 | 2.797 | 19.55 | 14.35 | 0 | 0 | 1 | 3 | 0 | 0 | 58.21 | 1.19 | 1.19 |

Table B.12: Results comparison for the reference set of 8 structures where the vacancies were introduced randomly.

| Structures with 20 defects in the 2X2X2 supercell | | | | | | | | | | | | |
|---|-----------|-----------|------|------|------|------|------|------|-------------|-----------------|---------------------|--|
| P_{am} [GPa] | D_V [Å] | D_C [Å] | #OT1 | #OT2 | #OT3 | #OT4 | #OT5 | #OT6 | K_V [GPa] | E_{ani} [GPa] | β_{ani} [GPa] | |
| 1.986 | 21.43 | 18.90 | 20 | 0 | 0 | 0 | 0 | 0 | 50.22 | 3.36 | 9.99 | |
| 1.991 | 21.46 | 19.05 | 0 | 0 | 0 | 0 | 20 | 0 | 50.21 | 3.38 | 10.34 | |
| 1.996 | 22.07 | 19.80 | 0 | 0 | 2 | 16 | 0 | 2 | 48.04 | 3.02 | 7.98 | |
| 2.037 | 21.80 | 19.45 | 2 | 1 | 0 | 16 | 1 | 0 | 47.56 | 3.04 | 6.22 | |
| 2.087 | 21.21 | 19.98 | 0 | 0 | 20 | 0 | 0 | 0 | 50.52 | 3.10 | 7.17 | |
| 2.092 | 21.27 | 20.32 | 0 | 20 | 0 | 0 | 0 | 0 | 50.30 | 3.26 | 8.79 | |
| 2.118 | 21.58 | 19.70 | 0 | 0 | 0 | 20 | 0 | 0 | 50.12 | 3.26 | 8.70 | |
| 2.143 | 21.54 | 20.51 | 0 | 0 | 0 | 0 | 0 | 20 | 50.45 | 3.06 | 6.78 | |
| 2.184 | 15.70 | 11.34 | 5 | 4 | 3 | 2 | 5 | 1 | 45.12 | 1.38 | 1.65 | |
| 2.204 | 20.74 | 20.37 | 10 | 0 | 10 | 0 | 0 | 0 | 47.80 | 1.94 | 3.42 | |
| 2.224 | 20.84 | 19.93 | 0 | 0 | 0 | 10 | 0 | 10 | 48.03 | 1.92 | 3.28 | |
| 2.229 | 20.37 | 20.39 | 5 | 0 | 5 | 5 | 0 | 5 | 46.10 | 1.49 | 1.76 | |
| 2.285 | 15.58 | 13.60 | 4 | 4 | 4 | 2 | 3 | 3 | 46.06 | 1.25 | 1.24 | |
| 2.315 | 20.09 | 19.49 | 3 | 2 | 2 | 7 | 3 | 3 | 46.72 | 1.40 | 1.53 | |
| 2.336 | 21.91 | 19.06 | 0 | 2 | 1 | 0 | 0 | 17 | 50.66 | 2.04 | 2.72 | |
| 2.356 | 21.85 | 18.87 | 0 | 1 | 1 | 1 | 1 | 16 | 50.60 | 1.79 | 2.11 | |
| 2.366 | 20.76 | 19.35 | 3 | 2 | 4 | 3 | 4 | 4 | 47.04 | 1.21 | 1.13 | |
| 2.427 | 20.58 | 19.18 | 3 | 3 | 3 | 3 | 4 | 4 | 47.46 | 1.23 | 1.11 | |
| 2.462 | 19.31 | 26.07 | 3 | 1 | 6 | 3 | 4 | 3 | 50.40 | 1.26 | 1.21 | |

Table B.13: Results comparison for the structures containing 20 linker vacancies. Columns denoted with #OT refer to the number of linker vacancies with a given orientation type. Data is sorted according to amorphization pressure, in ascending order.

B

The relationship between amorphization pressure and both the bulk modulus and elastic anisotropies are represented for the structures with 20 linker vacancies in Figs. B.8-B.10. The data points are colored according to the following: (1) green circles correspond to structures where the vacancies were selected randomly from the whole volume, (2) teal circles to structures where the vacancies were selected quasi-randomly from an outer sub-volume, (3) blue circles to structures where all missing linkers had the same orientation, (4) yellow circles to structures where 16 of the 20 missing linkers had OT4 orientation and the rest were selected randomly, (5) gold circles to structures where 16 of the 20 missing linkers had OT6 orientation and the rest were selected randomly, (6) red circles correspond to structures where 10 missing linkers had one type of orientation and 10 missing linkers had another.

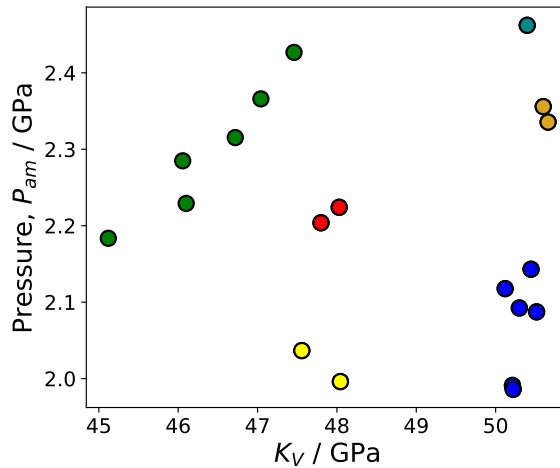


Figure B.8: Amorphization pressure v.s bulk modulus plot for the structures containing 20 linker vacancies.

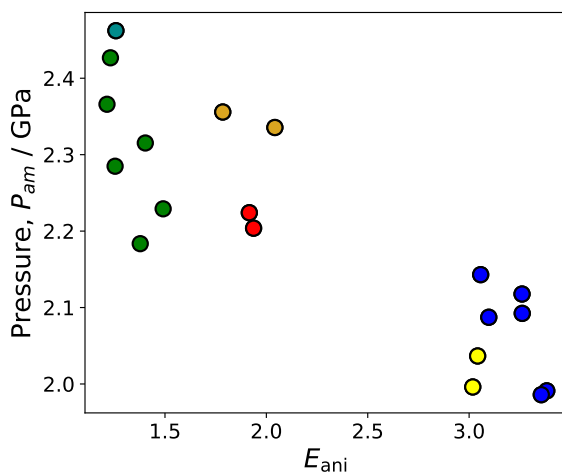


Figure B.9: Amorphization pressure v.s young modulus anisotropy plot for the structures containing 20 linker vacancies. The data points are colored as indicated in Fig. B.8.

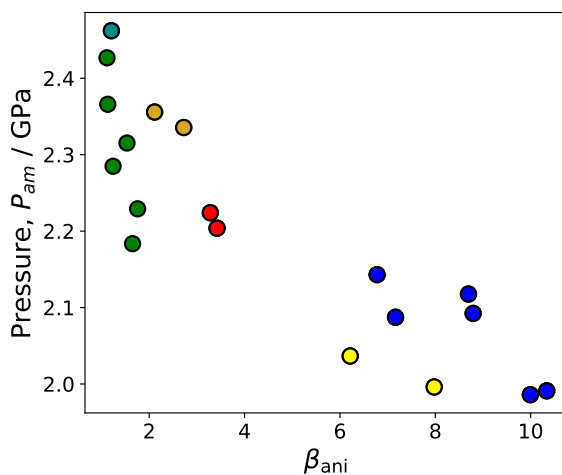


Figure B.10: Amorphization pressure v.s anisotropy of linear compressibility modulus plot for the 19 structures containing 20 linker vacancies. The data points are colored as indicated in Fig. B.8.

C

C

APPENDIX 3

C.1 FRAMEWORK FORCE FIELDS AND STRUCTURES

In this study, the pristine and defected UiO-66 frameworks were modeled using the family of periodic force fields developed by Rogge et al.[94] These force fields are designed to accurately represent both covalent and noncovalent interactions within the framework, ensuring reliable predictions of the structural and mechanical properties of the frameworks. The construction of these force fields follows the QuickFF procedure. The force fields are composed of two main contributions:

- **Covalent Terms:** These terms model the chemical bonds within the framework using internal coordinates such as bond lengths, bend angles, dihedral angles, torsions, and out-of-plane distances. These terms are fitted to first-principles data derived from representative cluster model systems.
- **Noncovalent Terms:** These model the long-range interactions between non-bonded atoms, consisting of electrostatic interactions (EI) and van der Waals (vdW) forces. The electrostatic interactions are described by Coulomb inter-

actions between spherical Gaussian densities, with charges derived from the DFT electron density of each cluster model. The van der Waals interactions are modeled using a two-parameter MM3 Buckingham potential.

C

To generate these force fields, the isolated cluster models were first extracted from DFT-optimized periodic structures. These isolated models were then optimized using DFT with the B3LYP functional, and the geometry, Hessian, and electron density were used as input to the QuickFF procedure to estimate the force field parameters. For each of the pristine and defected UiO-66 structures, a separate periodic force field was constructed by combining the parameters derived from the relevant isolated cluster models.

The force fields developed by Rogge et al. were employed to model both the pristine and defected UiO-66 structures in this study. The structures themselves were generated using the unit cell crystallographic information file (CIF) constructed by D. Dubbeldam (included as part of the RASPA[151] simulation package), which was based on previously reported experimental measurements by J. S. Cavka et al.[177] To prepare the input topologies for LAMMPS, 2x2x2 representations of the periodic unit cells were created using an in-house script. This script utilized the atomic positions from the same CIF file and the framework atom connectivity information inferred from each specific force field. Figure C.1 visually depicts these structures, with the missing linkers clearly indicated to facilitate understanding of the defect sites.

- **Type 0 structure:** Two of the four inorganic clusters are 11-fold coordinated. Average coordination number of 11.5.
- **Type 1 structure:** Two of the four inorganic clusters are 11-fold coordinated, one is 10-fold coordinated, and one is 12-fold coordinated. Average coordination number of 11.

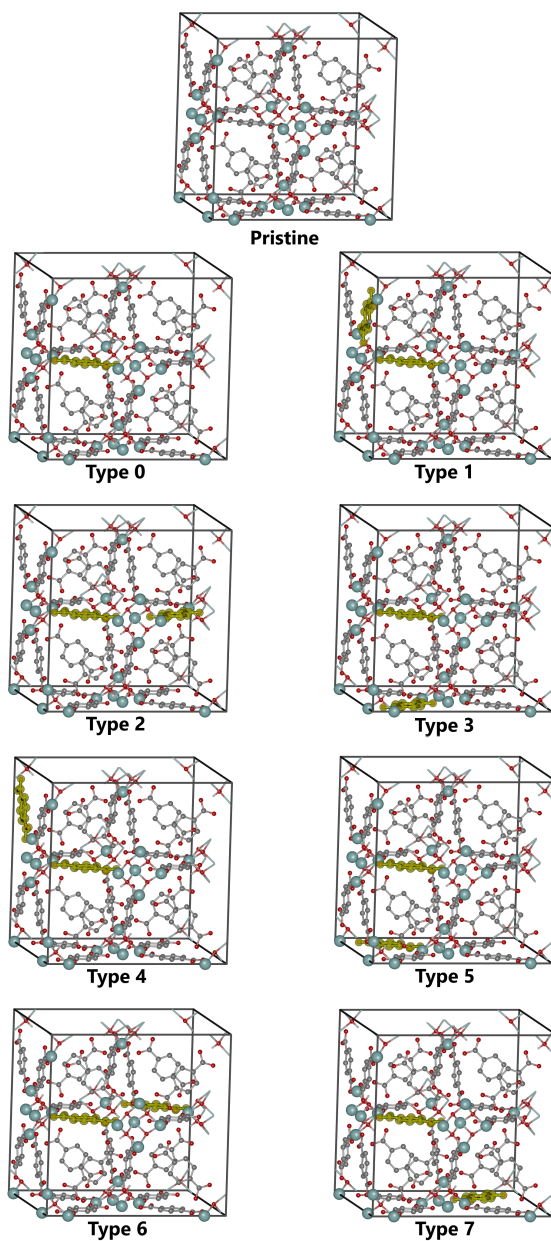


Figure C.1: Periodic unit cell representations of the structures considered in this work. Highlighted in yellow are the missing BDC organic in each structure. In the pictures, the linker hydrogen atoms and linker-cluster bonds were removed for clarity. All type 1-7 defected structures share one of the removed linker from the type 0 parent.

- **Type 2 structure:** Two of the four inorganic clusters are 10-fold coordinated. Average coordination number of 11.
- **Type 3 structure:** All four inorganic clusters are 11-fold coordinated. Average coordination number of 11.
- **Type 4 structure:** Two of the four inorganic clusters are 11-fold coordinated, one is 10-fold coordinated, and one is 12-fold coordinated. Average coordination number of 11.
- **Type 5 structure:** All four inorganic clusters are 11-fold coordinated. Average coordination number of 11.
- **Type 6 structure:** Two of the four inorganic clusters are 10-fold coordinated. Average coordination number of 11.
- **Type 7 structure:** All four inorganic clusters are 11-fold coordinated. Average coordination number of 11.

C.2 WATER LOADING ON THE PRISTINE STRUCTURE

This section provides additional figures and plots that complement the first part of the results section of Chapter 5. The radial distribution functions (RDFs) between water oxygen atoms ($\text{O}_{\text{H}_2\text{O}}$) and potential bonding sites in the pristine framework at higher water loadings of 40 and 100 water molecules per unit cell are shown in Figure C.2. Figure C.3 presents volumetric density maps illustrating that hybrid mixing captures the formation of one-dimensional water chains and clusters, which emerge as the loading increases, causing more water molecules to shift from the zirconium clusters toward the central regions of the pores. Figure C.4 compares the mean square displacement (MSD) of water molecules for the two interaction methods at a moderate loading of 40 water molecules per unit cell. The differences in MSD between the two methods highlight the impact of the mixing approach on

water mobility within the pores of UiO-66. Finally, Figure C.5 includes additional plots showing the average bond length changes for non-preferential adsorption sites, Zr-O_x and Zr-O_h, upon water loading.

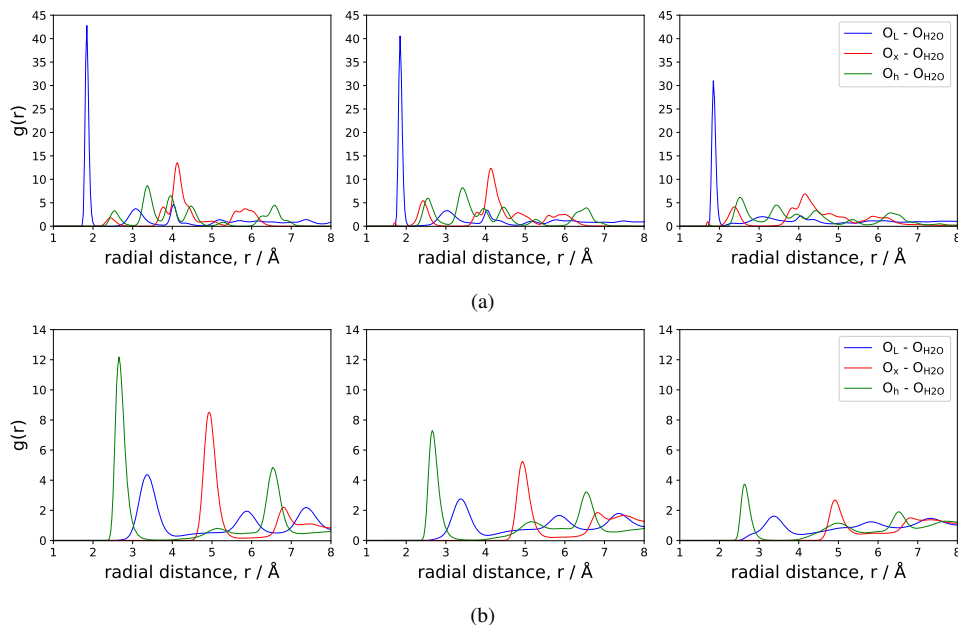


Figure C.2: RDFs between water oxygens and potential interaction sites around the inorganic cluster at loadings of 10, 40 and 100 molecules per unit cell (from left to right), using (a) L-B mixing (b) hybrid mixing. Computed at a temperature and pressure of 300 K and 1 atm, respectively.

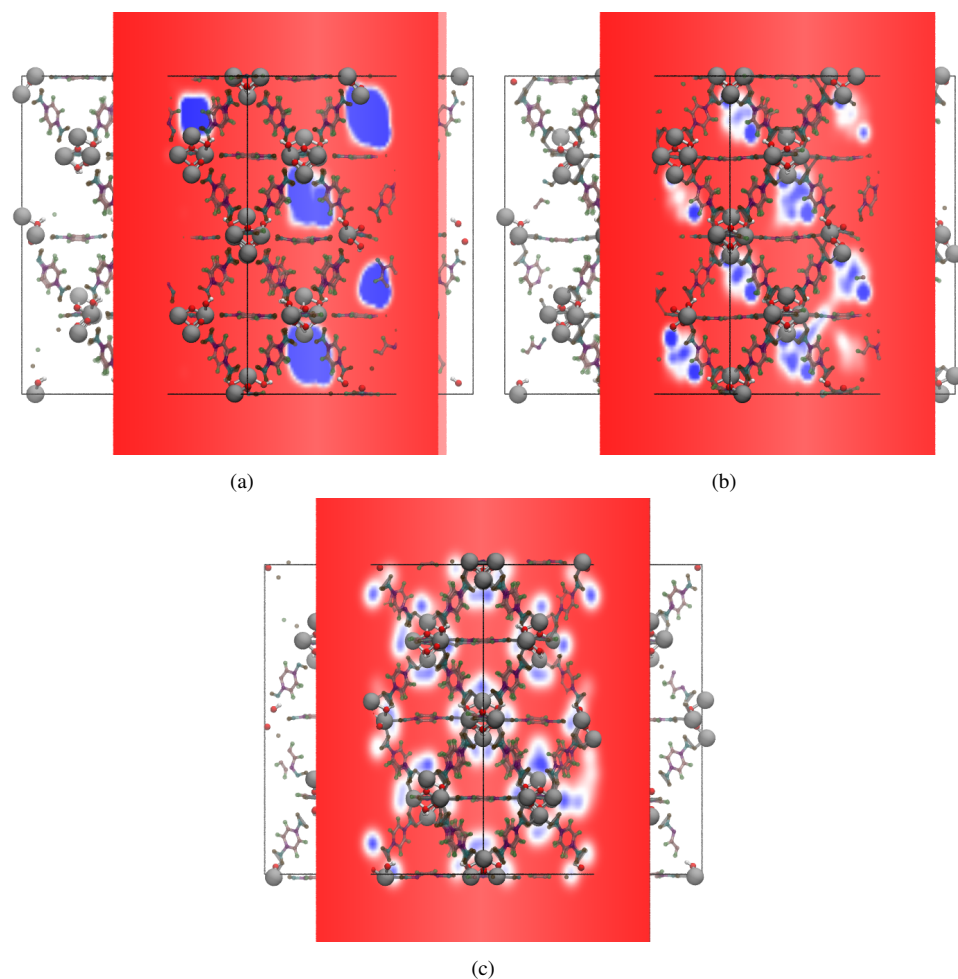


Figure C.3: Volumetric density maps of water over a trajectory of 500 ps for a loading of (a) 10 and (b) 40 molecules per unit cell using hybrid mixing. Higher density of water molecules presented in blue and lower density in red. Using hybrid mixing, at low loadings the molecules occupy pore space near the main interaction sites and hopping from one to another within the same pore is observed. Movement between pores observed at moderate and higher loadings. (c) shows a volumetric density map of water at a loading of 10 molecules per unit cell using L-B mixing.

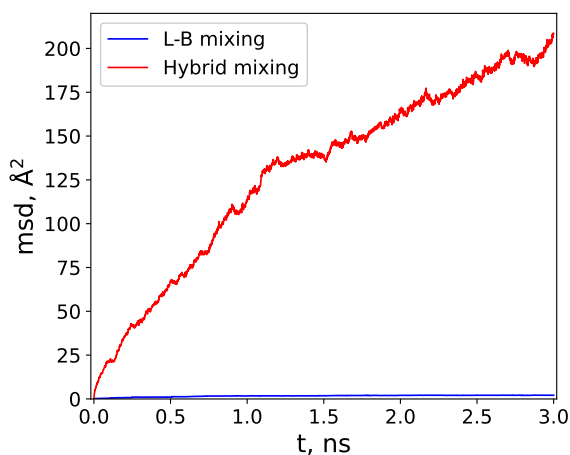


Figure C.4: MSD of water molecules over a simulation period of 3 nanoseconds at a loading of 40 molecules per unit cell at atmospheric conditions. L-B mixing simulations (blue curve) predicts minimal increase in MSD, indicative of heavily restricted molecular mobility within the framework. In contrast, hybrid mixing simulations (red curve) predict a more realistic diffusive behavior.

C

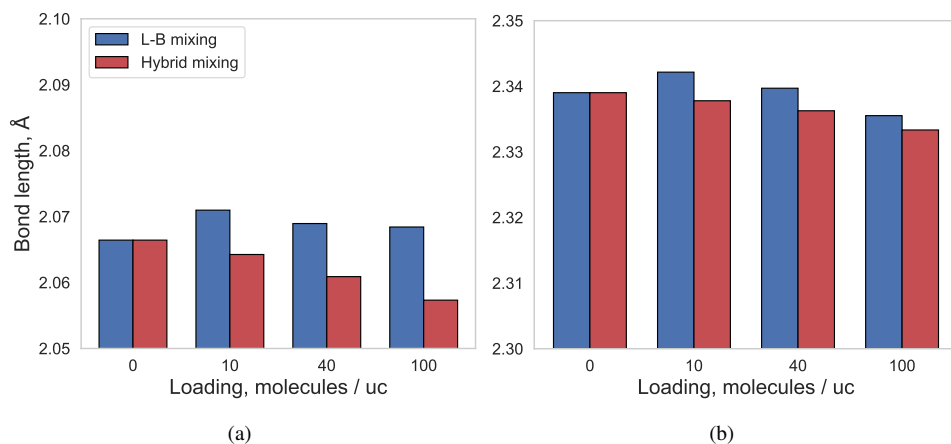


Figure C.5: Average bond length between (a) Zr and O_{Ox} and between (b) Zr and O_{Oh} . The pictured bars in (a) and (b) at a particular loading value are the result of the same four sets of simulations pictured in Fig. 5.3.

C.3 WATER LOADING ON THE DEFECTED STRUCTURES

This section provides additional figures and plots that complement the second part of the results section of Chapter 5. Predicted amorphization pressure for all defected structures are presented in Figure C.6. RDFs between water molecules and the zirconium atoms for the structure containing linker vacancies (and containing uncoordinated Zr atoms) are provided in Figures C.7-C.12. Direct mixing methodology comparison of system volume changes upon water loading are presented in Figures C.13-C.15, where the results for representative pristine, 1-missing linker and 2-missing linker structures are shown.

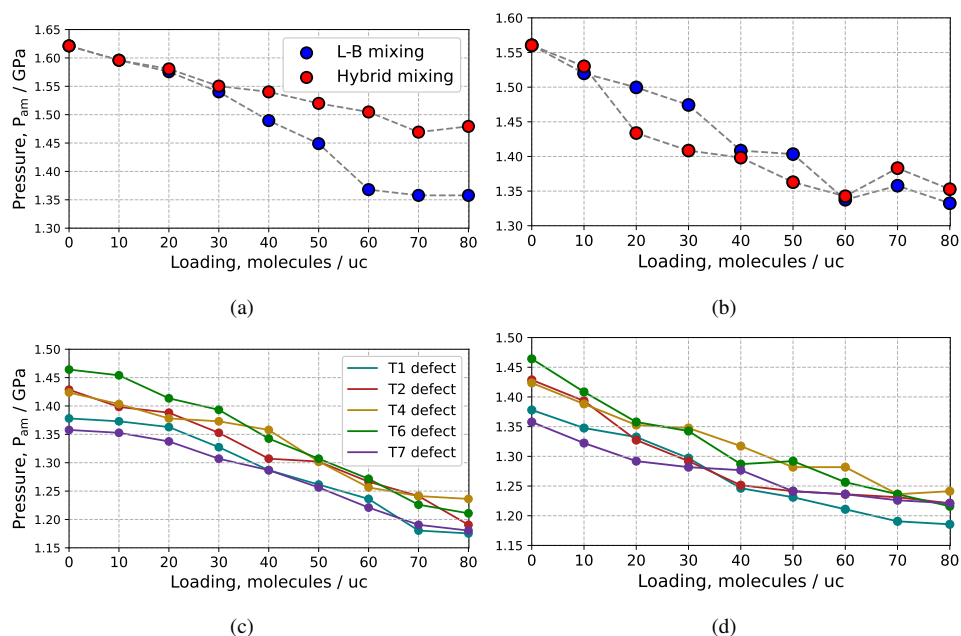


Figure C.6: A closer look at the P_{am} trends predicted using both mixing models. (a) Comparison for the structure with average inorganic cluster coordination of 11.5. (b) Comparison for the most stable 11-coordinated structure (type 3). (c) and (d) present a breakdown of the remaining structures with 11.0 cluster coordination for the L-B and hybrid method, respectively. Hybrid mixing simulations predict a sharper decrease in P_{am} values at low loadings when compared to the L-B mixing results. Both methods predict comparable high-loading values for all structures with two linker vacancies per unit cell.

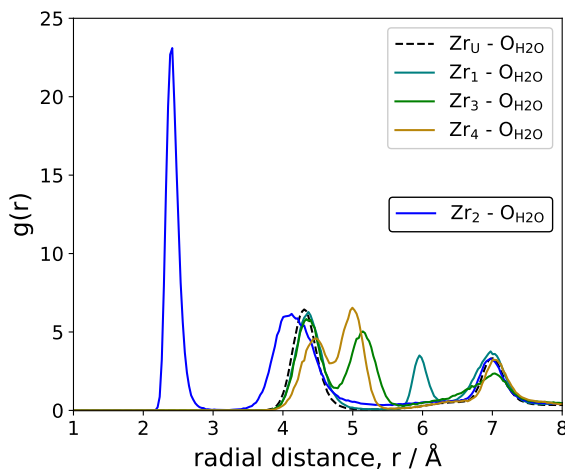


Figure C.7: RDF between water molecules and the zirconium atoms for the defected type 0 structure. Grey legend indicates fully coordinated (8) zirconium atoms and black legend indicates Zr atoms with lower coordination. The blue curve depicts the RDF between H₂O and the 7-coordinated Zr₂ site.

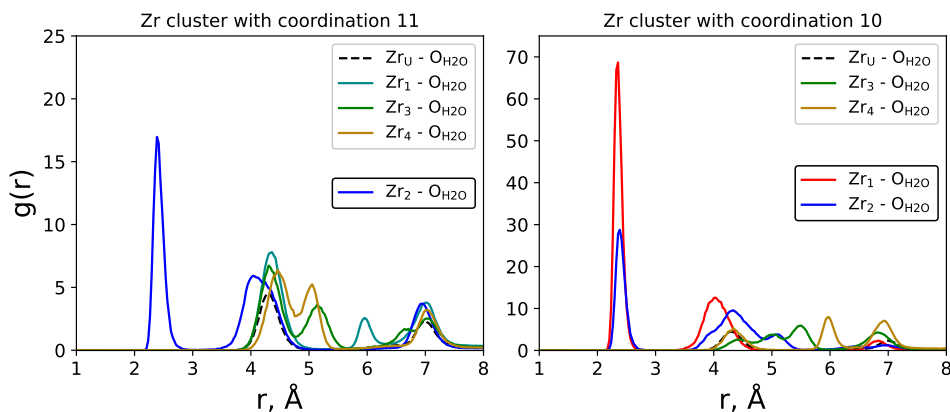


Figure C.8: RDF between water molecules and the zirconium atoms for the defected type 1 structure. Grey legend indicates fully coordinated (8) zirconium atoms and black legend indicates Zr atoms with lower coordination. The blue curves depict the RDF between H₂O and 7-coordinated Zr₂ sites. The red curve depicts the RDF between H₂O and the 6-coordinated Zr₁ site.

C

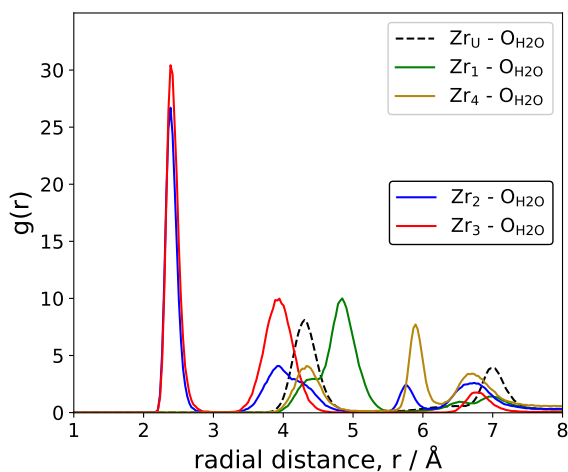


Figure C.9: RDF between water molecules and the zirconium atoms for the defected type 2 structure. Grey legend indicates fully coordinated (8) zirconium atoms and black legend indicates Zr atoms with lower coordination. The blue curve depicts the RDF between H_2O and the 7-coordinated Zr_2 site. The red curve depicts the RDF between H_2O and the 6-coordinated Zr_3 site.

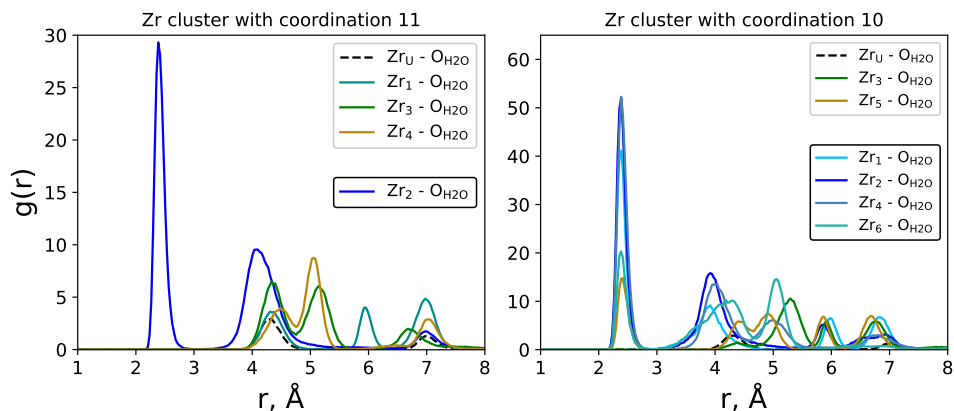


Figure C.10: RDF between water molecules and the zirconium atoms for the defected type 4 structure. Grey legend indicates fully coordinated (8) zirconium atoms and black legend indicates Zr atoms with lower coordination. The blue-colored curves depict the RDF between H_2O and 7-coordinated sites.

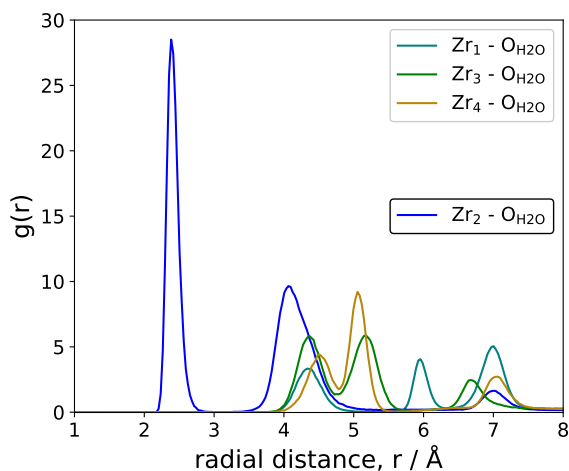


Figure C.11: RDF between water molecules and the zirconium atoms for the defected type 5 structure. Grey legend indicates fully coordinated (8) zirconium atoms and black legend indicates Zr atoms with lower coordination. The blue curve depicts the RDF between H₂O and the 7-coordinated Zr₂ site.

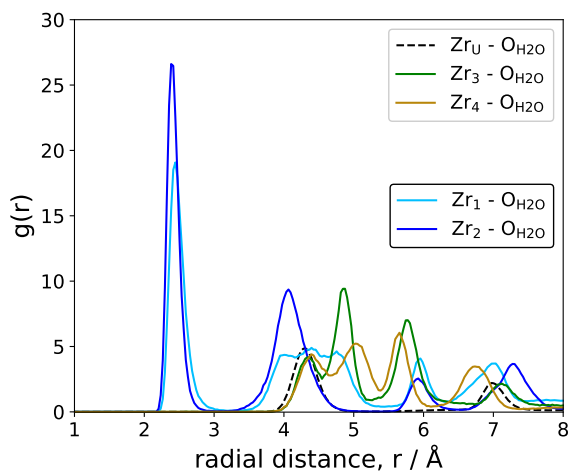


Figure C.12: RDF between water molecules and the zirconium atoms for the defected type 2 structure. Grey legend indicates fully coordinated (8) zirconium atoms and black legend indicates Zr atoms with lower coordination. The blue-colored curves depict the RDF between H₂O and 7-coordinated sites.

C

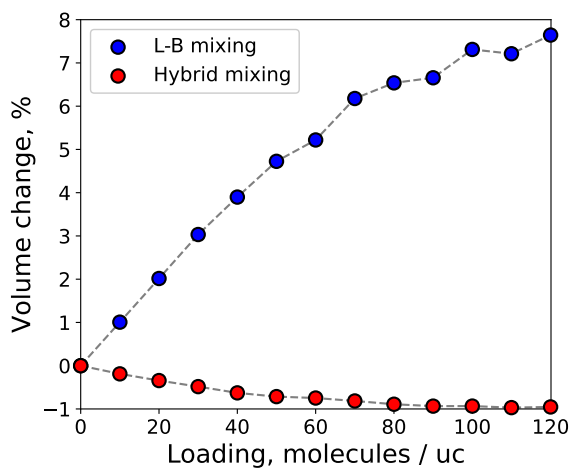


Figure C.13: Comparison of percentage volume change as a function of loading at atmospheric conditions for the pristine structure.

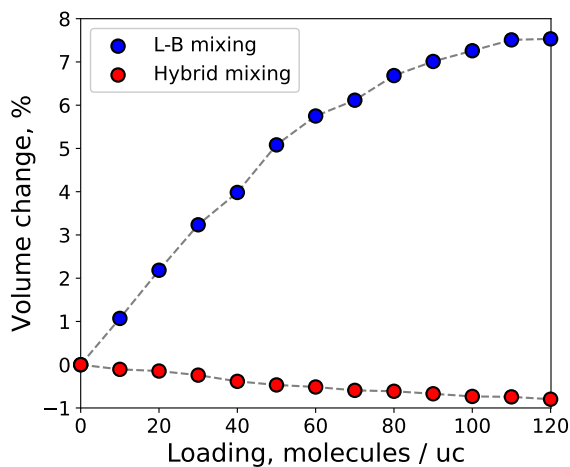


Figure C.14: Comparison of percentage volume change as a function of loading at atmospheric conditions for the structure with one linker vacancy per unit cell (type 0 structure).

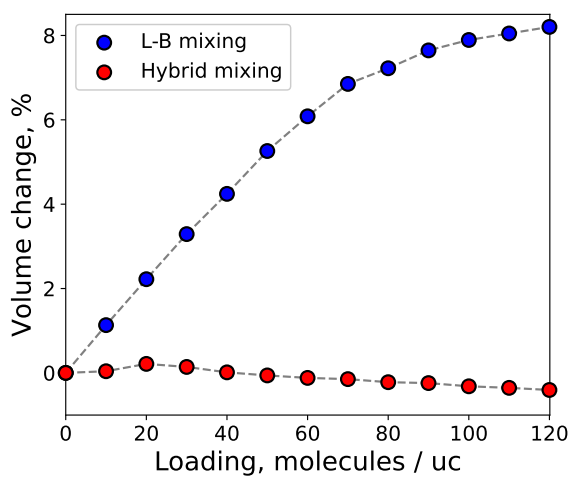


Figure C.15: Comparison of percentage volume change as a function of loading at atmospheric conditions for a structure with two linker vacancies per unit cell (type 3 structure).

C.4 FRAMEWORK COLLAPSE

Regarding the mechanism of collapse, although the implemented force fields are classical and do not allow for bond creation or breaking, a well tuned FF can help in characterizing the elasticity of the material, identifying the nature of instability at high pressures as well as characterizing the movement of certain regions prior to collapse. Regardless of the mixing model used, the intra-framework force field predicts collapse due to spatially alternated rotations of the zirconium clusters and a corresponding loss of planarity of organic linkers, as can be seen in Fig. C.16.

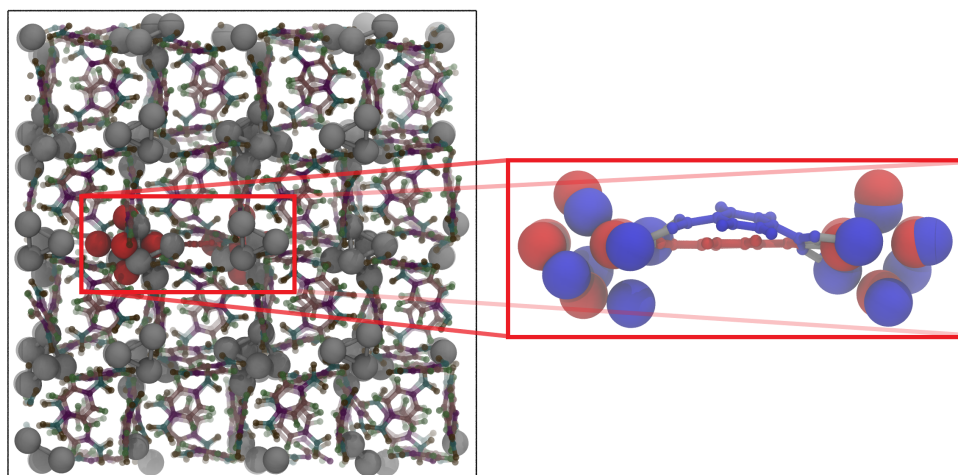


Figure C.16: XY snapshot of the pristine framework atoms after amorphization has occurred. The positions of two zirconium clusters and their connecting linker are highlighted and colored according to average atomic positions before (red) and after (blue) amorphization.

D

D

APPENDIX 4

D.1 GAFF/UFF AND ALL UFF PARAMETRIZATIONS

This appendix explores the influence of different framework parametrizations on the simulation results, comparing “All UFF”, where all non-bonded interactions between the adsorbates and the framework are described using the Universal Force Field (UFF), to “GAFF/UFF”, where the Generalized Amber Force Field (GAFF) is used for all interactions except for the zirconium atoms, for which UFF is retained. Results presented in Chapter 6 reflect only the latter, as specified in the methodology. The basis of comparison includes radial distribution functions (RDFs), amorphization pressures, and framework volume changes for all adsorbates considered.

D.1.1 RADIAL DISTRIBUTION FUNCTIONS

The figures in this section compare the obtained RDFs for methane, methanol, DMF, and chloroform, with respect to inorganic cluster framework atoms using the GAFF/UFF and All UFF parametrizations. These RDFs provide insight into the na-

ture and strength of adsorbate-framework interactions under the two parametrization schemes and help identify differences in interaction sites within the inorganic cluster.

The results for methane using both parametrizations are similar (Fig. D.1), both exhibit widely distributed peaks indicating the absence of strong preferential interaction sites. GAFF/UFF predicts slightly larger distribution of molecules close to the interaction sites within the inorganic cluster when compared to All UFF. For methanol, the results show distinct differences between the GAFF/UFF and All UFF parametrizations. In the GAFF/UFF case (Fig. D.2), the radial distribution functions (RDFs) exhibit more pronounced and sharper peaks compared to those obtained with All UFF (Fig. D.3). This is particularly noticeable for interactions involving hydroxylated oxygen sites O_{oh} , where the peaks occur at shorter radial distances, indicating a greater localization of methanol molecules around these sites. The sharper peaks in the GAFF/UFF RDFs suggest enhanced specificity and stronger directionality in the adsorbate-framework interactions, leading to a higher density of methanol molecules near the inorganic cluster. The GAFF/UFF parametrization most likely predicts hydrogen bonding between the hydroxylated oxygen sites and methanol oxygen atoms, further supporting the observed differences in molecular distribution and interaction strength.

For DMF, the comparison between the GAFF/UFF and All UFF parametrizations reveals notable differences in the radial distribution functions (RDFs). In the GAFF/UFF results (Fig. D.4), the CH_{DMF} site exhibits a sharp peak at shorter radial distances with the hydroxylated oxygen sites (O_{oh}) and hydrogen sites (H_{oh}) of the framework. This peak indicates a strong and localized interaction between the CH_{DMF} group and the inorganic cluster atoms, suggesting a more specific binding interaction. In contrast, the All UFF parametrization (Fig. D.5) shows broader and less pronounced peaks, indicating weaker directionality and lower specificity in adsorbate-framework interactions. The N_{DMF} site also displays more structured peaks in GAFF/UFF, which is due to the intramolecular distance between the N_{DMF} and CH_{DMF} sites. Overall, the sharper peaks and closer distances observed with

GAFF/UFF reflect enhanced adsorbate-framework interactions and a stronger localization of DMF molecules around the framework's cluster sites. For chloroform, the differences between the GAFF/UFF and All UFF parametrizations are less pronounced. Both models display broadly distributed peaks in the RDFs, suggesting weaker and less specific interactions between chloroform and the framework atoms. However, the GAFF/UFF parametrization (Fig. D.6) shows slightly enhanced peaks for the hydrogen interactions with hydroxylated sites ($H_{\text{Chloroform}}$ to O_{oh}), compared to the All UFF results (Fig. D.7). This indicates a marginal improvement in capturing the polar interactions between the chloroform hydrogen atoms and the hydroxylated oxygen sites of the framework. Overall, the interactions remain relatively diffuse, reflecting weaker adsorbate-framework specificity for chloroform.

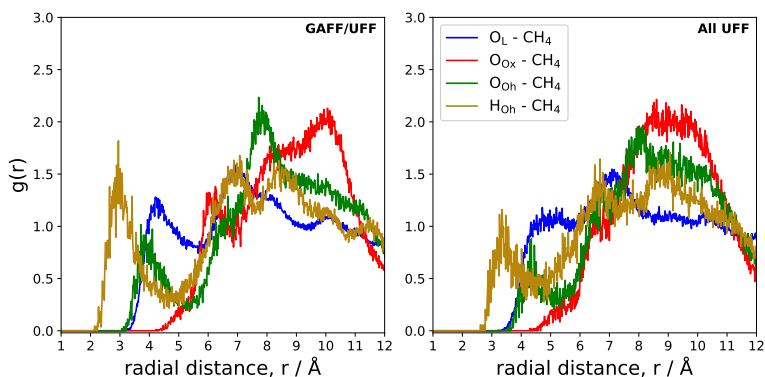


Figure D.1: RDF comparison for methane atoms with cluster framework atoms using GAFF/UFF and All UFF.

D.1.2 FRAMEWORK VOLUME CHANGES

The volume change of the framework as a function of fractional loading under atmospheric conditions for methane, methanol, water, DMF, and chloroform reveals distinct trends across the two parametrizations (GAFF/UFF and All UFF). The percentage change in framework volume is calculated relative to the average volume of the unloaded framework. For methane the results are similar (Fig. D.8),

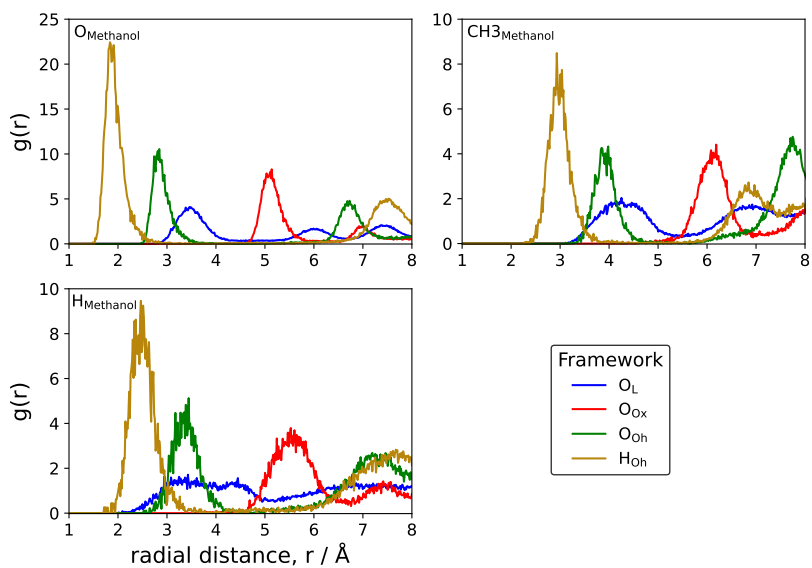


Figure D.2: Radial distribution functions for methanol atoms with framework atoms using GAFF/UFF.

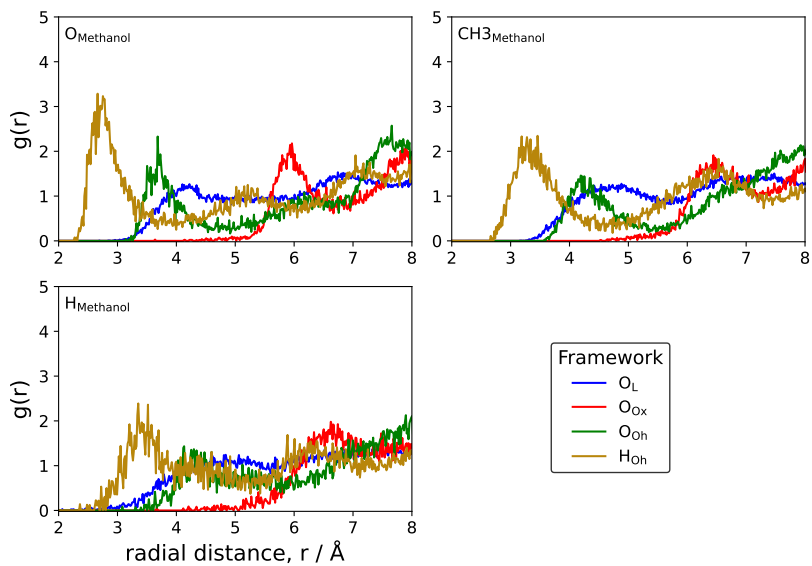


Figure D.3: Radial distribution functions for methanol atoms with framework atoms using All UFF.

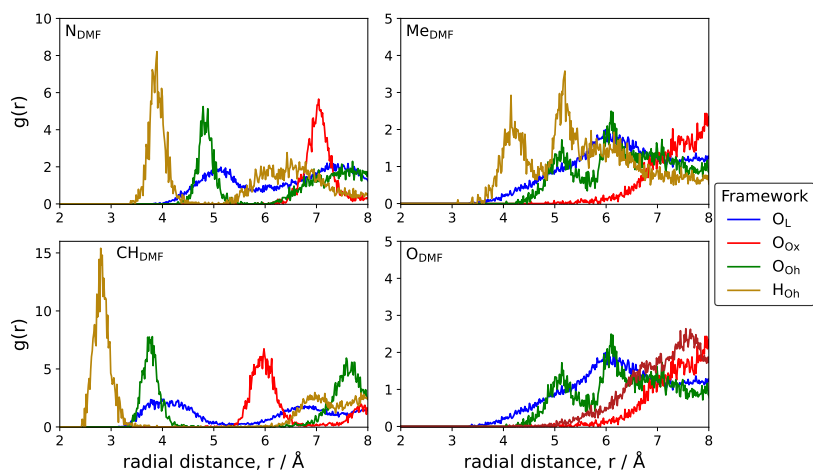


Figure D.4: Radial distribution functions for DMF atoms with framework atoms using GAFF/UFF.

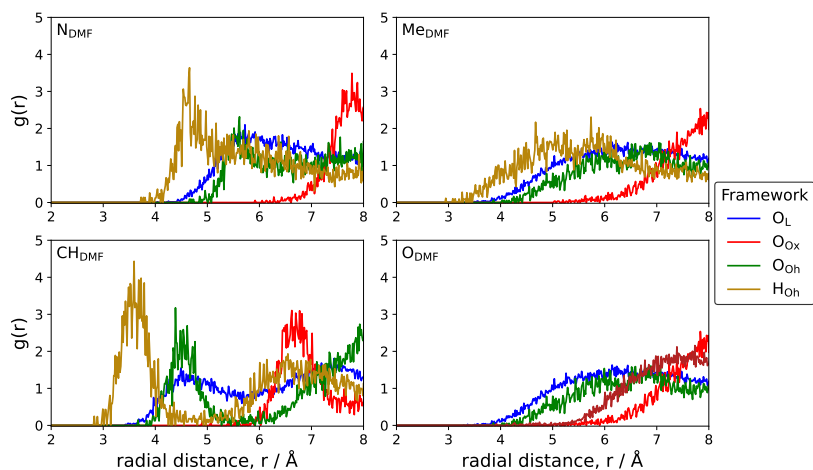


Figure D.5: Radial distribution functions for DMF atoms with framework atoms using All UFF.

both parametrizations show a consistent volume increase with increasing fractional loading. However, the GAFF/UFF parametrization predicts a slightly smaller volume change compared to All UFF, especially at higher loadings.

For methanol (Fig. D.9), the GAFF/UFF parametrization exhibits a more pronounced volume contraction at lower loadings compared to All UFF. This behavior

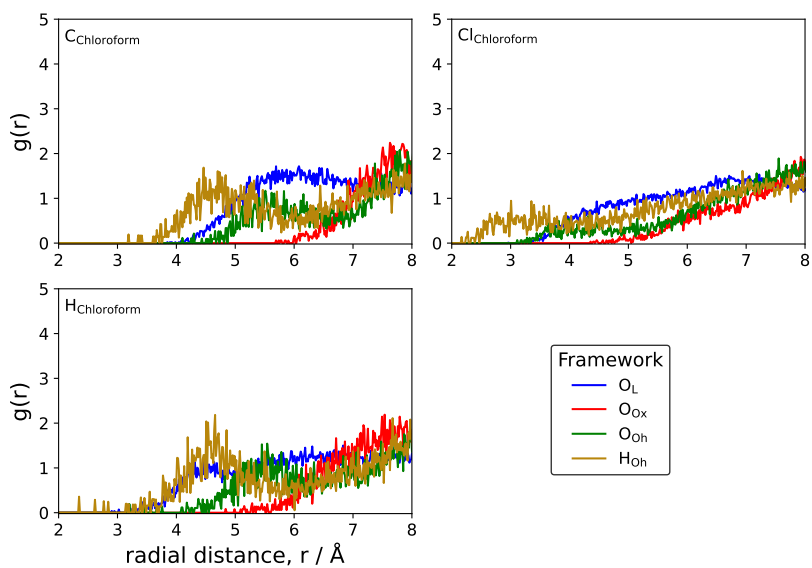


Figure D.6: Radial distribution functions for chloroform atoms with framework atoms using GAFF/UFF.

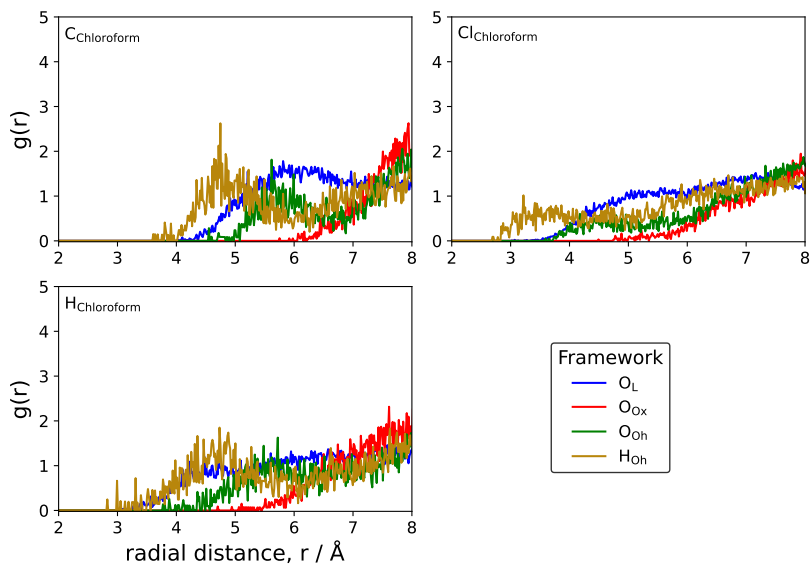


Figure D.7: Radial distribution functions for chloroform atoms with framework atoms using All UFF.

can be attributed to the stronger and more localized interactions observed in the RDFs (Fig. D.2), particularly between methanol's oxygen and the hydroxylated oxygen sites (O_{oh}). In contrast, the broader RDF peaks in All UFF suggest weaker interactions, resulting in a smaller volume contraction. At higher fractional loadings, the differences between the two parametrizations diminish, likely due to saturation effects. For water, a similar trend is observed, with GAFF/UFF predicting a significantly larger volume contraction compared to All UFF. This difference is consistent with the stronger and more specific polar interactions seen in the RDFs under GAFF/UFF, particularly with the hydroxylated sites (H_{oh} and O_{oh}). The enhanced hydrogen bonding captured by GAFF/UFF leads to greater framework deformation as the fractional loading increases.

In the case of DMF, both parametrizations show a continuous volume decrease with increasing fractional loading, but the contraction is more pronounced for GAFF/UFF. This result correlates with the sharper peaks observed in the RDFs for CH_{DMF} and N_{DMF} interactions under GAFF/UFF (Fig. D.4), reflecting stronger framework-adsorbate interactions. These localized interactions contribute to a more significant framework deformation. For chloroform, the volume change trends are less distinct, with both parametrizations predicting a gradual volume contraction. The GAFF/UFF results show a slightly smaller contraction compared to All UFF at higher loadings. This behavior aligns with the RDF analysis (Fig. D.6), which indicates weaker and less specific interactions for chloroform. The broadly distributed peaks and absence of strong binding sites result in minimal framework deformation for both parametrizations.

Overall, the GAFF/UFF parametrization consistently predicts stronger and more localized adsorbate-framework interactions, particularly for methanol, water, and DMF. These stronger interactions lead to greater framework volume contractions at lower fractional loadings compared to All UFF. In contrast, for nonpolar molecules like methane and chloroform, where interactions are weaker and less specific, the differences between the two parametrizations are less pronounced, and the volume

changes remain relatively small.

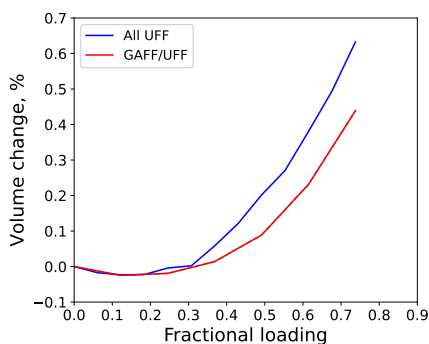


Figure D.8: Comparison of framework volume changes for methane using All UFF (blue) and GAFF/UFF (red).

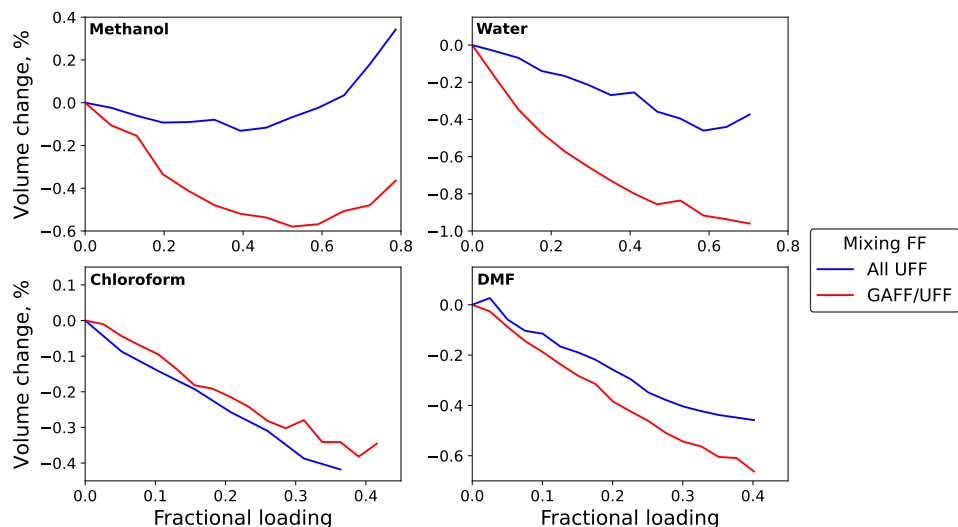


Figure D.9: Comparison of framework volume changes for methanol, water, DMF, and chloroform using All UFF (blue) and GAFF/UFF (red).

D.1.3 AMORPHIZATION PRESSURE AS A FUNCTION OF FRACTIONAL LOADING

The amorphization pressure (P_{am}), defined as the pressure at which the framework collapses (indicating a significant reduction in volume), is analyzed as a function of

fractional loading for methane, methanol, water, DMF, and chloroform. The results for both GAFF/UFF and All UFF parametrizations are discussed below.

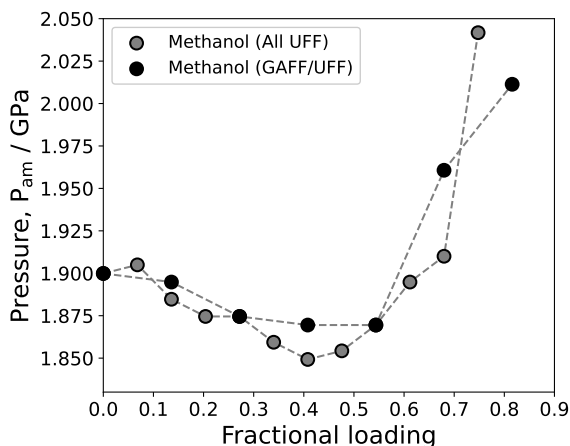


Figure D.10: Amorphization pressure for methane as a function of fractional loading under GAFF/UFF and All UFF parametrizations.

For methane (Fig. D.10), both parametrizations show a relatively stable amorphization pressure at low loadings, followed by a gradual decrease as loading increases. The similarity in trends reflects the absence of strong preferential binding sites, as observed in the RDF results (Fig. D.1). The broadly distributed RDF peaks confirm weaker interactions with the framework, contributing to the structural stability of the framework even at higher fractional loadings.

In the case of methanol (Fig. D.11), P_{am} decreases significantly with increasing fractional loading for both parametrizations. The GAFF/UFF results predict slightly lower amorphization pressures compared to All UFF, particularly at intermediate loadings. This behavior is consistent with the RDF analysis (Fig. D.2), which showed stronger and more localized interactions between methanol's oxygen atoms and the hydroxylated framework sites (O_{oh}). These strong interactions lead to earlier structural instability and framework collapse under GAFF/UFF.

For water (Fig. D.12), there is a pronounced decrease in P_{am} with increasing fractional loading. The GAFF/UFF parametrization consistently predicts lower

D

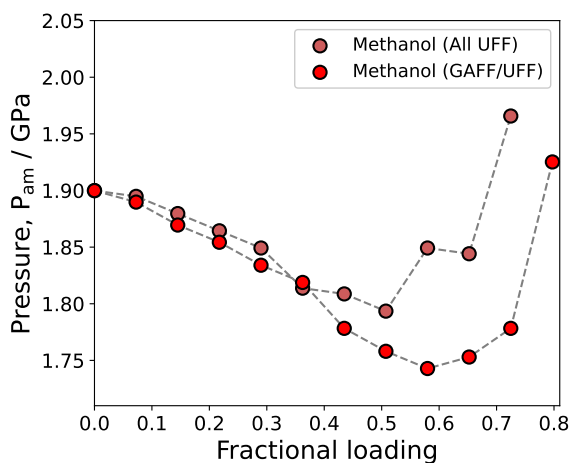


Figure D.11: Amorphization pressure for methanol as a function of fractional loading under GAFF/UFF and All UFF parametrizations.

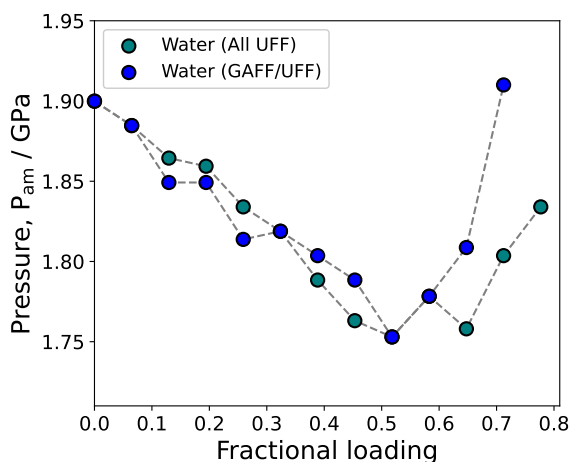


Figure D.12: Amorphization pressure for water as a function of fractional loading under GAFF/UFF and All UFF parametrizations.

amorphization pressures than All UFF. This trend aligns with the RDF results, where water exhibited strong hydrogen bonding with hydroxylated framework sites (H_{oh} and O_{oh}) under GAFF/UFF. These stronger interactions induce greater framework deformation and contribute to earlier collapse.

For DMF, as can be seen in Fig. D.13, P_{am} decreases with increasing fractional

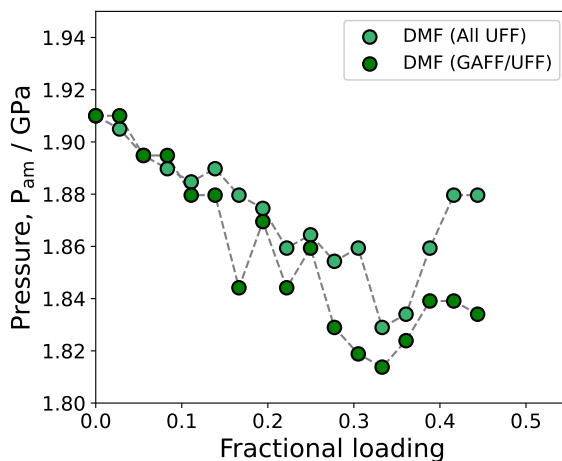


Figure D.13: Amorphization pressure for DMF as a function of fractional loading under GAFF/UFF and All UFF parametrizations.

D

loading, and the GAFF/UFF parametrization predicts consistently lower values than All UFF. The RDF analysis (Fig. D.4) revealed sharper peaks for CH_{DMF} and N_{DMF} interactions under GAFF/UFF, indicating stronger framework-adsorbate interactions. These localized interactions are likely responsible for the earlier structural collapse observed in the GAFF/UFF results.

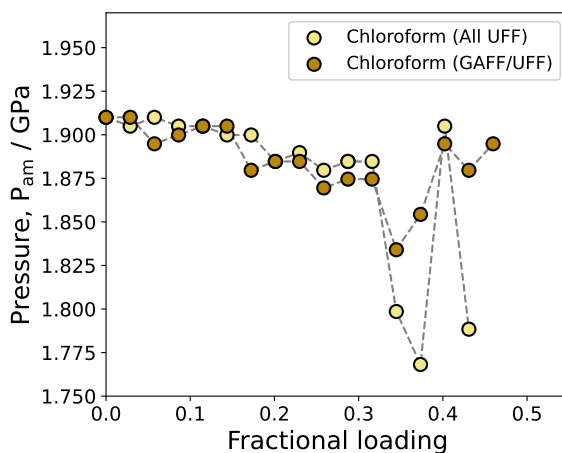


Figure D.14: Amorphization pressure for chloroform as a function of fractional loading under GAFF/UFF and All UFF parametrizations.

For chloroform (Fig. D.14), the amorphization pressure remains relatively stable at lower loadings but decreases sharply at intermediate loadings for both parametrizations. While GAFF/UFF predicts slightly lower P_{am} values compared to All UFF, the differences are minimal. This result corresponds to the RDF conclusions (Fig. D.6), where the interactions were observed to be weaker and less specific. The broadly distributed RDF peaks explain the relative stability of P_{am} at low fractional loadings.

Overall, the amorphization pressure trends highlight the role of adsorbate-framework interactions in determining the structural stability of the framework. The GAFF/UFF parametrization, which predicts stronger and more localized interactions (particularly for polar adsorbates like methanol, water, and DMF), leads to lower P_{am} values and earlier framework collapse. In contrast, for nonpolar adsorbates such as methane and chloroform, where interactions are weaker, the differences between the two parametrizations are less pronounced, and the framework remains more stable.

Summary

My doctoral research focuses on the development and application of advanced molecular simulation techniques to evaluate the structural and mechanical stability of multifunctional nanoporous materials, particularly Metal-Organic Frameworks (MOFs). These materials hold immense potential for applications such as gas separation and storage, water treatment, and adsorption-driven processes, where stability is essential for performance and longevity. By employing computational methods, this research uncovers relationships between MOF stability and their intrinsic properties, aiming to understand their elastic and mechanical behavior under various conditions, such as pressure, defect presence, and adsorbate presence, and to optimize their design for specific applications.

Chapter 3 examines the mechanical properties of the canonical MOF, ZIF-8, under varying conditions using classical molecular simulation techniques. Multiple force fields were evaluated for their performance in reproducing structural and mechanical properties, such as unit cell sizes and elastic constants, across different temperatures and pressures. The analysis revealed critical discrepancies between force fields, emphasizing the importance of eigenmode-following approaches for accurate energy minimization in stability assessments.

In Chapter 4, the investigation focuses on the effect of linker vacancies on the structural stability of UiO-66. Computational analysis demonstrated that the distribution and orientation of missing linkers significantly influence amorphization pressures. Evenly distributed vacancies positively correlate with bulk modulus and stability, while directional instability arises in structures with aligned vacancies. These findings provide insights into tailoring defect configurations to optimize MOF stability for specific applications.

Chapter 5 explores the impact of water loading on both pristine and defective

UiO-66 frameworks. By comparing direct Lorentz-Berthelot (L-B) mixing and hybrid mixing for modeling non-bonded interactions, differences were observed in water interaction sites, binding strengths, and dynamics. L-B mixing predicted restricted water movement and stronger binding, while hybrid mixing captured dynamic behavior such as site-to-site hopping. Increasing water loading led to contrasting effects on framework expansion, contraction, and amorphization pressures, highlighting the critical role of water-MOF interactions in determining stability.

The final chapter (Chapter 6) extends the analysis to a range of adsorbates, including methane, methanol, dimethylformamide (DMF), and chloroform, to evaluate how polarity, molecular size, and hydrogen-bonding capabilities affect framework stability. Methane, as a non-polar molecule, exhibited weaker interactions with the framework, with amorphization pressures stabilizing at higher loadings due to packing effects. In contrast, polar molecules such as methanol and water destabilized the framework through strong hydrogen bonding at low loadings, followed by stabilization at higher fractional loadings due to adsorbate-adsorbate interactions. Larger adsorbates, DMF and chloroform, introduced steric effects that disrupted uniform packing, resulting in distinct trends in framework destabilization and volume changes.

This research advances the understanding of MOF stability under varying conditions and provides computational guidelines for assessing their structural and mechanical properties. The findings contribute to the design of more robust and efficient MOFs for applications in gas storage, separation, and water treatment, emphasizing the importance of tailoring adsorbate selection and defect engineering to enhance material performance.

Curriculum Vitae

Esteban Acuna Yeomans was born on the 30th of December 1991 in Hermosillo, Sonora, Mexico. After completing high school in 2010, he earned a bachelor's degree in Physics from the University of Sonora (UNISON), where he focused on General Relativity, Computational Physics, and Analytical Mechanics. In 2015, he moved to London to conduct research at Imperial College London, successfully defending his thesis, "Global and regional emissions of radiocarbon from nuclear power plants." Between 2018 and 2019, he pursued an MSc in Molecular Simulations at the Universidad Internacional de Andalucía (UNIA), graduating with a master's degree after completing a project titled "Prediction of the behaviour of clathrates using molecular simulations." In early 2021, he joined the Materials Simulation & Modelling group at the Eindhoven University of Technology as a PhD candidate. For the next four years, he investigated the structural and mechanical stability of Metal-Organic Frameworks using classical molecular simulations. The results of his doctoral research are presented in this thesis.

List of Publications

1. [E. Acuna-Yeomans](#), J.J. Gutierrez-Sevillano, S. Calero and D. Dubbeldam: Evaluation of ZIF-8 flexible force fields for structural and mechanical properties, *Microporous and Mesoporous Materials*, **2022**, 348, 1387-1811 [148].
2. [E. Acuna-Yeomans](#), J.J. Gutierrez-Sevillano, D. Dubbeldam and S. Calero: A simulation study of linker vacancy distribution and its effect on UiO-66 stability, *Microporous and Mesoporous Materials*, **2023**, 366, 1387-1811 [166].
3. [E. Acuna-Yeomans](#), P.J. Goosen, J.J. Gutierrez-Sevillano, D. Dubbeldam and S. Calero: Effect of water loading on the stability of pristine and defective UiO-66, *Journal of Materials Chemistry A*, **2024**, 37, 2050-7496 [198].
4. [E. Acuna-Yeomans](#), J.J. Gutierrez-Sevillano, D. Dubbeldam and S. Calero: Influence of adsorbate properties on the structural stability of UiO-66 (in preparation).

List of Presentations

1. “Molecular simulation of flexible Zn and Zr-based MOFs”, Computational Methods in Nanothermodynamics workshop, Trondheim, Norway (2022).
2. “Comprehensive characterization of ZIF-8 flexible force fields according to their mechanical and structural properties”, Fundamentals of Adsorption 14th International Conference, Colorado, USA (2022).
3. “Understanding the mechanical stability of MOFs using molecular simulations”, CCER seminars, Eindhoven, Netherlands (2024).
4. “Effect of water loading on the stability of pristine and defected UiO-66. A simulation study”, XLIII Iberian Adsorption Meeting, Porto, Portugal (2024).

Acknowledgements

I would like to begin by expressing my gratitude to everyone I had positive contact with during the past four years. The journey of a PhD is shaped by countless interactions, big and small, and to name everyone who has contributed in one way or another would be an impossible task. I will keep this section as concise as possible, but I sincerely appreciate all those who have shared their time, knowledge, and kindness with me throughout this journey.

I am deeply grateful to my supervisors, Sofia, David, and Juanjo, for their invaluable guidance and support. Sofia, thank you for giving me the opportunity to take on this project and be part of the group from its early stages. It has been a truly rewarding experience, and I appreciate your ideas and guidance throughout the development of my work. David, your openness to discussions about science and your unwavering support during the hardest parts of the project were instrumental in helping me move forward. Your crucial insights helped me break the inertia that could have led me down a more difficult path, and your kindness made the time and effort invested even more meaningful. Juanjo, thank you for your open communication and support from a distance. Your awareness of the project and constant reminders kept me focused and on track. I would also like to extend my gratitude to the other members of my doctoral committee for their feedback and time.

A heartfelt thank you to all past and present members of our research group. The most important part of any scientific structure is its people, and I have been fortunate to work alongside so many brilliant and interesting individuals. Mike, Haibo, Sofia, and Viktor, thank you for embracing my company when I first started, helping me overcome my initial reservations, and for all the great conversations—both mundane and serious. Your example of how to conduct a research project and be part of a

scientific community in the Netherlands has been truly inspiring. To my fellow PhD candidates and colleagues, you have been the main source of daily community and fraternal interaction within the group, especially during lunch breaks and the occasional outings. A special thanks to Koen, Viren, Konrad, Susanne, Marko, Tijin, Zijin, and everyone else, including the MSc and bachelor students conducting their projects. I am also grateful to my BEP students, Luc, Pieter, and Lorens, for their dedication and effort. Supervising your projects was a valuable learning experience for me, providing a true yardstick for my personal growth as an academic. To the colleagues with whom I share an academic class and those with whom I shared an office at various points in time, Dominika, Botagoz, Xiucheng, and Diego, for the communication, being great colleagues, and contributing to a positive work environment. I also acknowledge Vicent for being so positive, eager to help, and providing everyone else in the group with resources day in and out.

Mis más especial agradecimiento a mi familia y amigos de la vida. Especialmente a mi eterna compañía, Eduardo, Emilio y Yasel. Emilio, no paras de sorprenderme por tu visión particular, proactividad e individualidad; eres un verdadero ejemplo a emular y tu presencia ha sido invaluable. Eduardo, por tu apoyo holístico, tanto técnico como personal, por permitirme rebotar ideas y brindarme claridad mental con nuestras pláticas. A mis padres, Laura y Heriberto, por proveerme apoyo incondicional, sabiduría y compañía a la distancia. Yasel, mi compañera, por estar presente todos los días, sin importar las circunstancias, y proveer los componentes más esenciales que me permitieron concluir esta etapa. Es un verdadero honor poder seguir construyendo un proyecto de vida contigo. Te todo.

BIBLIOGRAPHY

- [1] Hailian Li, Mohamed Eddaoudi, M O’Keeffe, and O M Yaghi. Design and synthesis of an exceptionally stable and highly porous metal-organic framework. *Nature*, 402(6759):276–279, November 1999.
- [2] Carine Livage, Nathalie Guillou, Jérôme Marrot, and Gérard Férey. Construction of two- and three-dimensional coordination polymers from cobalt trimesate. *Chem. Mater.*, 13(11):4387–4392, November 2001.
- [3] Susumu Kitagawa, Ryo Kitaura, and Shin-Ichiro Noro. Functional porous coordination polymers. *Angew. Chem. Int. Ed Engl.*, 43(18):2334–2375, April 2004.
- [4] Qi Wang and Didier Astruc. State of the art and prospects in metal-organic framework (MOF)-based and MOF-derived nanocatalysis. *Chem. Rev.*, 120(2):1438–1511, January 2020.
- [5] Vadia Foziya Yusuf, Naved I Malek, and Suresh Kumar Kailasa. Review on metal-organic framework classification, synthetic approaches, and influencing factors: Applications in energy, drug delivery, and wastewater treatment. *ACS Omega*, 7(49):44507–44531, December 2022.
- [6] Mohadeseh Safaei, Mohammad Mehdi Foroughi, Nasser Ebrahimpoor, Shohreh Jahani, Ali Omidi, and Mehrdad Khatami. A review on metal-organic frameworks: Synthesis and applications. *Trends Analyt. Chem.*, 118:401–425, September 2019.
- [7] Christopher A Trickett, Aasif Helal, Bassem A Al-Maythalony, Zain H Yamani, Kyle E Cordova, and Omar M Yaghi. The chemistry of metal-organic frameworks for CO₂ capture, regeneration and conversion. *Nat. Rev. Mater.*, 2(8):17045, July 2017.
- [8] Tyler G Grissom, Darren M Driscoll, Diego Troya, Nicholas S Sapienza, Pavel M Usov, Amanda J Morris, and John R Morris. Molecular-level insight into CO₂ adsorption on the zirconium-based metal-organic framework, UiO-66: A combined spectroscopic and computational approach. *J. Phys. Chem. C Nanomater. Interfaces*, 123(22):13731–13738, June 2019.
- [9] Camille Petit. Present and future of MOF research in the field of adsorption and molecular separation. *Curr. Opin. Chem. Eng.*, 20:132–142, June 2018.
- [10] Jian-Rong Li, Ryan J Kuppler, and Hong-Cai Zhou. Selective gas adsorption and separation in metal-organic frameworks. *Chem. Soc. Rev.*, 38(5):1477–1504, May 2009.

- [11] Patricia Horcajada, Ruxandra Gref, Tarek Baati, Phoebe K Allan, Guillaume Maurin, Patrick Couvreur, Gérard Férey, Russell E Morris, and Christian Serre. Metal-organic frameworks in biomedicine. *Chem. Rev.*, 112(2):1232–1268, February 2012.
- [12] Frederik Vermoortele, Bart Bueken, Gaëlle Le Bars, Ben Van de Voorde, Matthias Vandichel, Kristof Houthoofd, Alexandre Vimont, Marco Daturi, Michel Waroquier, Veronique Van Speybroeck, Christine Kirschhock, and Dirk E De Vos. Synthesis modulation as a tool to increase the catalytic activity of metal-organic frameworks: the unique case of UiO-66(Zr). *J. Am. Chem. Soc.*, 135(31):11465–11468, August 2013.
- [13] Jorge Gascon, María D Hernández-Alonso, Ana Rita Almeida, Gerard P M van Klink, Freek Kapteijn, and Guido Mul. Isorecticular MOFs as efficient photocatalysts with tunable band gap: an operando FTIR study of the photoinduced oxidation of propylene. *ChemSusChem*, 1(12):981–983, 2008.
- [14] Anil H Valekar, Kyung-Ho Cho, Sachin K Chitale, Do-Young Hong, Ga-Young Cha, U-Hwang Lee, Dong Won Hwang, Christian Serre, Jong-San Chang, and Young Kyu Hwang. Catalytic transfer hydrogenation of ethyl levulinate to γ -valerolactone over zirconium-based metal-organic frameworks. *Green Chem.*, 18(16):4542–4552, 2016.
- [15] Víctor L Rechac, Francisco G Cirujano, Avelino Corma, and Francesc X Llabrés i Xamena. Diastereoselective synthesis of pyranoquinolines on zirconium-containing UiO-66 metal-organic frameworks. *Eur. J. Inorg. Chem.*, 2016(27):4512–4516, September 2016.
- [16] C Volkringer, C Falaise, P Devaux, R Giovine, V Stevenson, F Pourpoint, O Lafon, M Osmond, C Jeanjacques, B Marcillaud, J C Sabroux, and T Loiseau. Stability of metal-organic frameworks under gamma irradiation. *Chem. Commun. (Camb.)*, 52(84):12502–12505, 2016.
- [17] Tianjiao Wu, Lingjuan Shen, Matthew Luebbers, Chunhua Hu, Qingmei Chen, Zheng Ni, and Richard I Masel. Enhancing the stability of metal-organic frameworks in humid air by incorporating water repellent functional groups. *Chem. Commun. (Camb.)*, 46(33):6120–6122, September 2010.
- [18] Yao Cai, Wei Xie, Yin Ting Teng, P C Harikesh, Biplab Ghosh, Patrick Huck, Kristin A Persson, Nripan Mathews, Subodh G Mhaisalkar, Matthew Sherburne, and Mark Asta. High-throughput computational study of halide double perovskite inorganic compounds. *Chem. Mater.*, 31(15):5392–5401, August 2019.
- [19] Zhe-Ning Chen, Gang Fu, Igor Ying Zhang, and Xin Xu. Understanding the non-planarity in aromatic metallabenzenes: A σ -control mechanism. *Inorg. Chem.*, 57(15):9205–9214, August 2018.
- [20] N I Abu-Elsaad, A S Nawara, and S A Mazen. Synthesis, structural characterization, and magnetic properties of Ni-Zn nanoferrites substituted with different metal ions (mn²⁺, co²⁺, and cu²⁺). *J. Phys. Chem. Solids*, 146(109620):109620, November 2020.
- [21] Xiao-Min Liu, Lin-Hua Xie, and Yufeng Wu. Recent advances in the shaping of metal-organic frameworks. *Inorg. Chem. Front.*, 7(15):2840–2866, 2020.

-
- [22] Jaewoo Park, Nour F Attia, Minji Jung, Kiyoun Lee, and Hyunchul Oh. Biobased derived nanoporous carbon for hydrogen isotope separation. *Microporous Mesoporous Mater.*, 304(109291):109291, September 2020.
- [23] Seunghun Lee, Haihang Wang, Priya Gopal, Jongmoon Shin, H M Iftekhar Jaim, Xiaohang Zhang, Se-Young Jeong, Demet Usanmaz, Stefano Curtarolo, Marco Fornari, Marco Buongiorno Nardelli, and Ichiro Takeuchi. Systematic band gap tuning of BaSnO_3 via chemical substitutions: The role of clustering in mixed-valence perovskites. *Chem. Mater.*, 29(21):9378–9385, November 2017.
- [24] Xiulin Fan, Long Chen, Xiao Ji, Tao Deng, Singyuk Hou, Ji Chen, Jing Zheng, Fei Wang, Jianjun Jiang, Kang Xu, and Chunsheng Wang. Highly fluorinated interphases enable high-voltage li-metal batteries. *Chem*, 4(1):174–185, January 2018.
- [25] Dongbo Wang, Jingjuan Liu, and Zhiliang Liu. A chemically stable europium metal-organic framework for bifunctional chemical sensor and recyclable on–off–on vapor response. *J. Solid State Chem.*, 251:243–247, July 2017.
- [26] Anthony Stone. *The theory of intermolecular forces*. Oxford University Press, London, England, 2 edition, February 2013.
- [27] Jasmina Hafizovic, Morten Bjørgen, Unni Olsbye, Pascal D C Dietzel, Silvia Bordiga, Carmelo Prestipino, Carlo Lamberti, and Karl Petter Lillerud. The inconsistency in adsorption properties and powder XRD data of MOF-5 is rationalized by framework interpenetration and the presence of organic and inorganic species in the nanocavities. *J. Am. Chem. Soc.*, 129(12):3612–3620, March 2007.
- [28] Thibault De Villenoisy, Naomi Ho, Sherry Chen, Xiaoran Zheng, Charles C Sorrell, Yingjie Zhang, and Pramod Koshy. Elucidating the role of synthesis conditions on Zr-MOF properties and yield. *Mater. Chem. Phys.*, 309(128448):128448, November 2023.
- [29] Arni Sturluson, Melanie T Huynh, Alec R Kaija, Caleb Laird, Sunghyun Yoon, Feier Hou, Zhenxing Feng, Christopher E Wilmer, Yamil J Colón, Yongchul G Chung, Daniel W Siderius, and Cory M Simon. The role of molecular modelling and simulation in the discovery and deployment of metal-organic frameworks for gas storage and separation. *Mol. Simul.*, 45(14-15):1082–1121, 2019.
- [30] Hakan Demir, Hilal Daglar, Hasan Can Gulbalkan, Gokhan Onder Aksu, and Seda Keskin. Recent advances in computational modeling of MOFs: From molecular simulations to machine learning. *Coord. Chem. Rev.*, 484(215112):215112, June 2023.
- [31] Satoshi Horike, Satoru Shimomura, and Susumu Kitagawa. Soft porous crystals. *Nature Chemistry*, 1(9):695–704, November 2009.
- [32] Gérard Férey. Hybrid porous solids: past, present, future. *Chem. Soc. Rev.*, 37(1):191–214, 2008.
- [33] Omar K. Farha and Joseph T. Hupp. Rational design, synthesis, purification, and activation of metal-organic framework materials. *Accounts of Chemical Research*, 43(8):1166–1175, July 2010.

- [34] Hiroyasu Furukawa, Kyle E. Cordova, Michael O’Keeffe, and Omar M. Yaghi. The chemistry and applications of metal-organic frameworks. *Science*, 341(6149), August 2013.
- [35] Yun-Qi Tian, Yu-Ming Zhao, Zhen-Xia Chen, Guang-Ning Zhang, Lin-Hong Weng, and Dong-Yuan Zhao. Design and generation of extended zeolitic metal-organic frameworks (ZMOFs): Synthesis and crystal structures of zinc(II) imidazolate polymers with zeolitic topologies. *Chemistry - A European Journal*, 13(15):4146–4154, May 2007.
- [36] Kyo Sung Park, Zheng Ni, Adrien P. Côté, Jae Yong Choi, Rudan Huang, Fernando J. Uribe-Romo, Hee K. Chae, Michael O’Keeffe, and Omar M. Yaghi. Exceptional chemical and thermal stability of zeolitic imidazolate frameworks. *Proceedings of the National Academy of Sciences*, 103(27):10186–10191, July 2006.
- [37] Xiao-Chun Huang, Yan-Yong Lin, Jie-Peng Zhang, and Xiao-Ming Chen. Ligand-directed strategy for zeolite-type metal-organic frameworks: Zinc(II) imidazolates with unusual zeolitic topologies. *Angewandte Chemie International Edition*, 45(10):1557–1559, February 2006.
- [38] Jie-Peng Zhang, Ai-Xin Zhu, Rui-Biao Lin, Xiao-Lin Qi, and Xiao-Ming Chen. Pore surface tailored SOD-type metal-organic zeolites. *Advanced Materials*, 23(10):1268–1271, January 2011.
- [39] Jie-Peng Zhang, Yue-Biao Zhang, Jian-Bin Lin, and Xiao-Ming Chen. Metal azolate frameworks: From crystal engineering to functional materials. *Chemical Reviews*, 112(2):1001–1033, September 2011.
- [40] A. Schneemann, V. Bon, I. Schwedler, I. Senkowska, S. Kaskel, and R. A. Fischer. Flexible metal-organic frameworks. *Chem. Soc. Rev.*, 43(16):6062–6096, May 2014.
- [41] Thomas D. Bennett, Alain H. Fuchs, Anthony K. Cheetham, and François-Xavier Coudert. Flexibility and disorder in metal-organic frameworks. *Dalton Transactions*, 45(10):4058–4059, 2016.
- [42] Wei Zhang, Jefferson Maul, Diana Vulpe, Peyman Z. Moghadam, David Fairen-Jimenez, Daniel M. Mittleman, J. Axel Zeitler, Alessandro Erba, and Michael T. Ruggiero. Probing the mechanochemistry of metal-organic frameworks with low-frequency vibrational spectroscopy. *The Journal of Physical Chemistry C*, 122(48):27442–27450, November 2018.
- [43] Claire L. Hobday, Christopher H. Woodall, Matthew J. Lennox, Mungo Frost, Konstantin Kamenev, Tina Düren, Carole A. Morrison, and Stephen A. Moggach. Understanding the adsorption process in ZIF-8 using high pressure crystallography and computational modelling. *Nature Communications*, 9(1), April 2018.
- [44] Kátilla Monique Costa Santos, Tamires dos Reis Menezes, Cesar Costapinto Santana, Alexander Junges, Juliana Faccin de Conto, Gustavo Rodrigues Borges, Cláudio Dariva, Silvia Maria Egues, and Elton Franceschi. Study of CO₂ and n₂ sorption into ZIF-8 at high pressure and different temperatures. *Journal of Solid State Chemistry*, 314:123370, October 2022.

-
- [45] Qiang Ma, Hua Jin, and Yanshuo Li. Tuning the adsorption selectivity of ZIF-8 by amorphization. *Chemistry – A European Journal*, 26(58):13137–13141, September 2020.
- [46] M. E. Casco, Y. Q. Cheng, L. L. Daemen, D. Fairen-Jimenez, E. V. Ramos-Fernández, A. J. Ramirez-Cuesta, and J. Silvestre-Albero. Gate-opening effect in ZIF-8: the first experimental proof using inelastic neutron scattering. *Chemical Communications*, 52(18):3639–3642, 2016.
- [47] D. Fairen-Jimenez, S. A. Moggach, M. T. Wharmby, P. A. Wright, S. Parsons, and T. Düren. Opening the gate: Framework flexibility in ZIF-8 explored by experiments and simulations. *Journal of the American Chemical Society*, 133(23):8900–8902, May 2011.
- [48] David Fairen-Jimenez, Raimondas Galvelis, Antonio Torrisi, Alistair D. Gellan, Michael T. Wharmby, Paul A. Wright, Caroline Mellot-Draznieks, and Tina Düren. Flexibility and swing effect on the adsorption of energy-related gases on ZIF-8: combined experimental and simulation study. *Dalton Transactions*, 41(35):10752, 2012.
- [49] Chen Zhang, Ryan P. Lively, Ke Zhang, Justin R. Johnson, Oguz Karvan, and William J. Koros. Unexpected molecular sieving properties of zeolitic imidazolate framework-8. *The Journal of Physical Chemistry Letters*, 3(16):2130–2134, July 2012.
- [50] Helge Bux, Fangyi Liang, Yanshuo Li, Janosch Cravillon, Michael Wiebcke, and Jürgen Caro. Zeolitic imidazolate framework membrane with molecular sieving properties by microwave-assisted solvothermal synthesis. *Journal of the American Chemical Society*, 131(44):16000–16001, October 2009.
- [51] Helge Bux, Christian Chmelik, Jasper M. van Baten, Rajamani Krishna, and Jürgen Caro. Novel MOF-membrane for molecular sieving predicted by IR-diffusion studies and molecular modeling. *Advanced Materials*, 22(42):4741–4743, September 2010.
- [52] Helge Bux, Christian Chmelik, Rajamani Krishna, and Juergen Caro. Ethene/ethane separation by the MOF membrane ZIF-8: Molecular correlation of permeation, adsorption, diffusion. *Journal of Membrane Science*, 369(1-2):284–289, March 2011.
- [53] Helge Bux, Armin Feldhoff, Janosch Cravillon, Michael Wiebcke, Yan-Shuo Li, and Juergen Caro. Oriented zeolitic imidazolate framework-8 membrane with sharp h_2/c_3h_2 molecular sieve separation. *Chemistry of Materials*, 23(8):2262–2269, March 2011.
- [54] Karena W. Chapman, Gregory J. Halder, and Peter J. Chupas. Pressure-induced amorphization and porosity modification in a metal-organic framework. *Journal of the American Chemical Society*, 131(48):17546–17547, November 2009.
- [55] Stephen A. Moggach, Thomas D. Bennett, and Anthony K. Cheetham. The effect of pressure on ZIF-8: Increasing pore size with pressure and the formation of a high-pressure phase at 1.47 GPa. *Angewandte Chemie International Edition*, 48(38):7087–7089, September 2009.

- [56] Aurélie U. Ortiz, Anne Boutin, Alain H. Fuchs, and François-Xavier Coudert. Investigating the pressure-induced amorphization of zeolitic imidazolate framework ZIF-8: Mechanical instability due to shear mode softening. *The Journal of Physical Chemistry Letters*, 4(11):1861–1865, May 2013.
- [57] Ben Van de Voorde, Ivo Stassen, Bart Bueken, Frederik Vermoortele, Dirk De Vos, Rob Ameloot, Jin-Chong Tan, and Thomas D. Bennett. Improving the mechanical stability of zirconium-based metal–organic frameworks by incorporation of acidic modulators. *Journal of Materials Chemistry A*, 3(4):1737–1742, 2015.
- [58] Thomas D. Bennett, Paul J. Saines, David A. Keen, Jin-Chong Tan, and Anthony K. Cheetham. Ball-milling-induced amorphization of zeolitic imidazolate frameworks (ZIFs) for the irreversible trapping of iodine. *Chemistry - A European Journal*, 19(22):7049–7055, April 2013.
- [59] Jin-Chong Tan, Bartolomeo Civalieri, Chung-Cherng Lin, Loredana Valenzano, Raimondas Galvelis, Po-Fei Chen, Thomas D. Bennett, Caroline Mellot-Draznieks, Claudio M. Zicovich-Wilson, and Anthony K. Cheetham. Exceptionally low shear modulus in a prototypical imidazole-based metal-organic framework. *Physical Review Letters*, 108(9), February 2012.
- [60] Junmei Wang, Romain M. Wolf, James W. Caldwell, Peter A. Kollman, and David A. Case. Development and testing of a general amber force field. *Journal of Computational Chemistry*, 25(9):1157–1174, 2004.
- [61] A. K. Rappe, C. J. Casewit, K. S. Colwell, W. A. Goddard, and W. M. Skiff. UFF, a full periodic table force field for molecular mechanics and molecular dynamics simulations. *Journal of the American Chemical Society*, 114(25):10024–10035, December 1992.
- [62] Bin Zheng, Marco Sant, Pierfranco Demontis, and Giuseppe B. Suffritti. Force field for molecular dynamics computations in flexible ZIF-8 framework. *The Journal of Physical Chemistry C*, 116(1):933–938, January 2012.
- [63] Zhongqiao Hu, Liling Zhang, and Jianwen Jiang. Development of a force field for zeolitic imidazolate framework-8 with structural flexibility. *The Journal of Chemical Physics*, 136(24):244703, June 2012.
- [64] Liling Zhang, Zhongqiao Hu, and Jianwen Jiang. Sorption-induced structural transition of zeolitic imidazolate framework-8: A hybrid molecular simulation study. *Journal of the American Chemical Society*, 135(9):3722–3728, February 2013.
- [65] Xuanjun Wu, Jin Huang, Weiquan Cai, and Mietek Jaroniec. Force field for ZIF-8 flexible frameworks: atomistic simulation of adsorption, diffusion of pure gases as CH₄, H₂, CO₂ and N₂. *RSC Adv.*, 4(32):16503–16511, 2014.
- [66] Panagiotis Krokidas, Marcelo Castier, Salvador Moncho, Edward Brothers, and Ioannis G. Economou. Molecular simulation studies of the diffusion of methane, ethane, propane, and propylene in ZIF-8. *The Journal of Physical Chemistry C*, 119(48):27028–27037, November 2015.

-
- [67] Jurn Heinen and David Dubbeldam. On flexible force fields for metal–organic frameworks: Recent developments and future prospects. *WIREs Computational Molecular Science*, 8(4), March 2018.
- [68] Johannes P. Dürholt, Guillaume Fraux, François-Xavier Coudert, and Rochus Schmid. Ab initio derived force fields for zeolitic imidazolate frameworks: MOF-FF for ZIFs. *Journal of Chemical Theory and Computation*, 15(4):2420–2432, March 2019.
- [69] Jefferson Maul, Matthew R. Ryder, Michael T. Ruggiero, and Alessandro Erba. Pressure-driven mechanical anisotropy and destabilization in zeolitic imidazolate frameworks. *Physical Review B*, 99(1), January 2019.
- [70] Hailian Li, Mohamed Eddaoudi, M O’Keeffe, and O M Yaghi. Design and synthesis of an exceptionally stable and highly porous metal-organic framework. *Nature*, 402(6759):276–279, November 1999.
- [71] Carine Livage, Nathalie Guillou, Jérôme Marrot, and Gérard Férey. Construction of two- and three-dimensional coordination polymers from cobalt trimesate. *Chem. Mater.*, 13(11):4387–4392, November 2001.
- [72] Susumu Kitagawa, Ryo Kitaura, and Shin-Ichiro Noro. Functional porous coordination polymers. *Angew. Chem. Int. Ed Engl.*, 43(18):2334–2375, April 2004.
- [73] Hong-Cai Zhou, Jeffrey R Long, and Omar M Yaghi. Introduction to metal-organic frameworks. *Chem. Rev.*, 112(2):673–674, February 2012.
- [74] Jasmina Hafizovic Cavka, Søren Jakobsen, Unni Olsbye, Nathalie Guillou, Carlo Lamberti, Silvia Bordiga, and Karl Petter Lillerud. A new zirconium inorganic building brick forming metal organic frameworks with exceptional stability. *Journal of the American Chemical Society*, 130(42):13850–13851, September 2008.
- [75] Loredana Valenzano, Bartolomeo Civalieri, Sachin Chavan, Silvia Bordiga, Merete H Nilsen, Søren Jakobsen, Karl Petter Lillerud, and Carlo Lamberti. Disclosing the complex structure of UiO-66 metal organic framework: A synergic combination of experiment and theory. *Chem. Mater.*, 23(7):1700–1718, April 2011.
- [76] Jared B. DeCoste, Gregory W. Peterson, Himanshu Jasuja, T. Grant Glover, You-gui Huang, and Krista S. Walton. Stability and degradation mechanisms of metal–organic frameworks containing the $\text{zr}_6\text{o}_4(\text{oh})_4$ secondary building unit. *Journal of Materials Chemistry A*, 1(18):5642, 2013.
- [77] Karen Leus, Thomas Bogaerts, Jeroen De Decker, Hannes Depauw, Kevin Hendrickx, Henk Vrielinck, Veronique Van Speybroeck, and Pascal Van Der Voort. Systematic study of the chemical and hydrothermal stability of selected “stable” metal organic frameworks. *Microporous Mesoporous Mater.*, 226:110–116, May 2016.
- [78] Pascal. G. Yot, Ke Yang, Florence Ragon, Vladimir Dmitriev, Thomas Devic, Patricia Horcajada, Christian Serre, and Guillaume Maurin. Exploration of the mechanical behavior of metal organic frameworks uio-66(zr) and mil-125(ti) and their nh2functionalized versions. *Dalton Transactions*, 45(10):4283–4288, 2016.

- [79] Hui Wu, Taner Yildirim, and Wei Zhou. Exceptional mechanical stability of highly porous zirconium metal-organic framework UiO-66 and its important implications. *J. Phys. Chem. Lett.*, 4(6):925–930, March 2013.
- [80] Matthew J Cliffe, Joshua A Hill, Claire A Murray, François-Xavier Coudert, and Andrew L Goodwin. Defect-dependent colossal negative thermal expansion in UiO-66(Hf) metal-organic framework. *Phys. Chem. Chem. Phys.*, 17(17):11586–11592, May 2015.
- [81] Stefano Dissegna, Pia Vervoorts, Claire L Hobday, Tina Düren, Dominik Daisenberger, Andrew J Smith, Roland A Fischer, and Gregor Kieslich. Tuning the mechanical response of metal-organic frameworks by defect engineering. *J. Am. Chem. Soc.*, 140(37):11581–11584, September 2018.
- [82] Zhi Su, Yu-Run Miao, Guanghui Zhang, Jeffrey T Miller, and Kenneth S Suslick. Bond breakage under pressure in a metal organic framework. *Chem. Sci.*, 8(12):8004–8011, December 2017.
- [83] Yueting Sun, Sven M. J. Rogge, Aran Lamaire, Steven Vandenbrande, Jelle Wieme, Clive R. Siviour, Veronique Van Speybroeck, and Jin-Chong Tan. High-rate nanofluidic energy absorption in porous zeolitic frameworks. *Nature Materials*, 20(7):1015–1023, April 2021.
- [84] Pritha Ghosh, Yamil J Colón, and Randall Q Snurr. Water adsorption in UiO-66: the importance of defects. *Chem. Commun. (Camb.)*, 50(77):11329–11331, October 2014.
- [85] Weibin Liang, Campbell J Coghlan, Florence Ragon, Marta Rubio-Martinez, Deanna M D'Alessandro, and Ravichandar Babarao. Defect engineering of UiO-66 for CO₂ and H₂O uptake - a combined experimental and simulation study. *Dalton Trans.*, 45(11):4496–4500, March 2016.
- [86] Mohammad I Hossain, Jackson D Cunningham, Tim M Becker, Bogna E Grabicka, Krista S Walton, Brooks D Rabideau, and T Grant Glover. Impact of MOF defects on the binary adsorption of CO₂ and water in UiO-66. *Chem. Eng. Sci.*, 203:346–357, August 2019.
- [87] Arnaud Planchais, Sabine Devautour-Vinot, Fabrice Salles, Florence Ragon, Thomas Devic, Christian Serre, and Guillaume Maurin. A joint experimental/computational exploration of the dynamics of confined water/zr-based MOFs systems. *J. Phys. Chem. C Nanomater. Interfaces*, 118(26):14441–14448, July 2014.
- [88] Shanshan Wang, Guobing Zhou, Yunhao Sun, and Liangliang Huang. A computational study of water in UiO-66 Zr-MOFs : Diffusion, hydrogen bonding network, and confinement effect. *AIChE J.*, 67(3), March 2021.
- [89] Jared B. DeCoste, Gregory W. Peterson, Bryan J. Schindler, Kato L. Killops, Matthew A. Browe, and John J. Mahle. The effect of water adsorption on the structure of the carboxylate containing metal-organic frameworks cu-btc, mg-mof-74, and uio-66. *Journal of Materials Chemistry A*, 1(38):11922, 2013.
- [90] D Zou and D Liu. Understanding the modifications and applications of highly stable porous frameworks via UiO-66. *Mater. Today Chem.*, 12:139–165, June 2019.

- [91] Asmaa Jrad, Patrick Damacet, Zahraa Yaghi, Mohammad Ahmad, and Mohamad Hmadeh. Zr-based metal–organic framework nanocrystals for water remediation. *ACS Appl. Nano Mater.*, 5(8):10795–10808, August 2022.
- [92] Pascal G Yot, Ke Yang, Florence Ragon, Vladimir Dmitriev, Thomas Devic, Patricia Horcajada, Christian Serre, and Guillaume Maurin. Exploration of the mechanical behavior of metal organic frameworks UiO-66(Zr) and MIL-125(Ti) and their NH₂ functionalized versions. *Dalton Trans.*, 45(10):4283–4288, March 2016.
- [93] Chen Zhao, Yang Li, Hongyu Chu, Xi Pan, Li Ling, Peng Wang, Huifen Fu, Chong-Chen Wang, and Zhihua Wang. Construction of direct z-scheme Bi₅O₇I/UiO-66-NH₂ heterojunction photocatalysts for enhanced degradation of ciprofloxacin: Mechanism insight, pathway analysis and toxicity evaluation. *J. Hazard. Mater.*, 419(126466):126466, October 2021.
- [94] Sven M J Rogge, Jelle Wieme, Louis Vanduyfhuys, Steven Vandenbrande, Guillaume Maurin, Toon Verstraelen, Michel Waroquier, and Veronique Van Speybroeck. Thermodynamic insight in the high-pressure behavior of UiO-66: Effect of linker defects and linker expansion. *Chem. Mater.*, 28(16):5721–5732, August 2016.
- [95] Gabriela Jajko, Juan José Gutiérrez-Sevillano, Andrzej Sławek, Monika Szuffa, Paweł Kozyra, Dariusz Matoga, Waław Makowski, and Sofia Calero. Water adsorption in ideal and defective UiO-66 structures. *Microporous Mesoporous Mater.*, 330(111555):111555, January 2022.
- [96] Luca Monticelli and D. Peter Tieleman. *Force Fields for Classical Molecular Dynamics*, page 197–213. Humana Press, August 2012.
- [97] Martin J Field. Molecular mechanics. In *A Practical Introduction to the Simulation of Molecular Systems*, pages 81–109. Cambridge University Press, Cambridge, July 2007.
- [98] Rodney J Bartlett and John F Stanton. Applications of post-Hartree-Fock methods: A tutorial. In *Reviews in Computational Chemistry*, Reviews in Computational Chemistry, pages 65–169. John Wiley & Sons, Inc., Hoboken, NJ, USA, January 2007.
- [99] Christopher J Cramer. *Essentials of computational chemistry*. John Wiley & Sons, Chichester, England, 2 edition, September 2004.
- [100] T Daniel Crawford and Henry F Schaefer, III. An introduction to coupled cluster theory for computational chemists. In *Reviews in Computational Chemistry*, Reviews in Computational Chemistry, pages 33–136. John Wiley & Sons, Inc., Hoboken, NJ, USA, January 2007.
- [101] Frank Jensen. *Introduction to computational chemistry*. John Wiley & Sons, Nashville, TN, 3 edition, February 2017.
- [102] Richard M Martin. Preface. In *Electronic Structure*, pages xvii–xix. Cambridge University Press, Cambridge, April 2004.
- [103] Priscilla G Watkins, editor. *Molecular Mechanics & Modeling*. Nova Science, Hauppauge, NY, September 2015.

-
- [104] Katsunosuke Machida. *Principles of molecular mechanics*. John Wiley & Sons, Nashville, TN, August 1999.
- [105] Michael Patrick Allen and Dominic J Tildesley. *Computer simulation of liquids*. Oxford University Press, London, England, 2 edition, May 2017.
- [106] Daan Frenkel and Berend Smit. *Understanding molecular simulation*. Computational science series. Academic Press, San Diego, CA, 2 edition, October 2001.
- [107] David J Wales. *Cambridge molecular science: Energy landscapes: Applications to clusters, biomolecules and glasses*. Cambridge University Press, Cambridge, England, October 2013.
- [108] Julian D Gale and Andrew L Rohl. The general utility lattice program (GULP). *Mol. Simul.*, 29(5):291–341, May 2003.
- [109] Uri Dinur and Arnold T Hagler. New approaches to empirical force fields. In *Reviews in Computational Chemistry*, Reviews in Computational Chemistry, pages 99–164. John Wiley & Sons, Inc., Hoboken, NJ, USA, January 2007.
- [110] Jacob N Israelachvili. *Intermolecular and Surface Forces*. Academic Press, San Diego, CA, 3 edition, December 2010.
- [111] Jörg-Rüdiger Hill, Clive M Freeman, and Lalitha Subramanian. Use of force fields in materials modeling. In *Reviews in Computational Chemistry*, Reviews in Computational Chemistry, pages 141–216. John Wiley & Sons, Inc., Hoboken, NJ, USA, January 2007.
- [112] Michael R Shirts, David L Mobley, John D Chodera, and Vijay S Pande. Accurate and efficient corrections for missing dispersion interactions in molecular simulations. *J. Phys. Chem. B*, 111(45):13052–13063, November 2007.
- [113] Kun Zhou and Bo Liu. *Molecular dynamics simulation*. Elsevier Science Publishing, Philadelphia, PA, February 2022.
- [114] William H. Press, B P Flannery, S A Teukolsky, and W T Vetterling. *Numerical Recipes in C*. Cambridge University Press, Cambridge, England, February 1988.
- [115] Jon Baker. An algorithm for the location of transition states. *J. Comput. Chem.*, 7(4):385–395, August 1986.
- [116] Ajit Banerjee, Noah Adams, Jack Simons, and Ron Shepard. Search for stationary points on surfaces. *J. Phys. Chem.*, 89(1):52–57, January 1985.
- [117] J A Nelder and R Mead. A simplex method for function minimization. *Comput. J.*, 7(4):308–313, January 1965.
- [118] J A Snyder. A new and dynamic method for unconstrained minimization. *Appl. Math. Model.*, 6(6):449–462, December 1982.
- [119] J A Snyder. An improved version of the original leap-frog dynamic method for unconstrained minimization: LFOP1(b). *Appl. Math. Model.*, 7(3):216–218, June 1983.

-
- [120] Mark E Tuckerman. *Statistical mechanics: Theory and molecular simulation*, August 2023.
- [121] D C Rapaport. *The art of molecular dynamics simulation*. Cambridge University Press, Cambridge, England, 2 edition, February 2011.
- [122] I. P. Omelyan, I. M. Mryglod, and R. Folk. Optimized verlet-like algorithms for molecular dynamics simulations. *Physical Review E*, 65(5), May 2002.
- [123] R.W Hockney and J.W Eastwood. *Computer Simulation Using Particles*. CRC Press, March 2021.
- [124] M Parrinello and A Rahman. Polymorphic transitions in single crystals: A new molecular dynamics method. *J. Appl. Phys.*, 52(12):7182–7190, December 1981.
- [125] Glenn J Martyna, Douglas J Tobias, and Michael L Klein. Constant pressure molecular dynamics algorithms. *J. Chem. Phys.*, 101(5):4177–4189, September 1994.
- [126] Andreas Dullweber, Benedict Leimkuhler, and Robert McLachlan. Symplectic splitting methods for rigid body molecular dynamics. *J. Chem. Phys.*, 107(15):5840–5851, October 1997.
- [127] M Parrinello and A Rahman. Crystal structure and pair potentials: A molecular-dynamics study. *Phys. Rev. Lett.*, 45(14):1196–1199, October 1980.
- [128] M Parrinello and A Rahman. Polymorphic transitions in single crystals: A new molecular dynamics method. *J. Appl. Phys.*, 52(12):7182–7190, December 1981.
- [129] Reza Najafabadi and Sidney Yip. Observation of finite-temperature bain transformation (f.c.c. \rightarrow b.c.c.) in monte carlo simulation of iron. *Scr. Metall.*, 17(10):1199–1204, October 1983.
- [130] M Parrinello and A Rahman. Strain fluctuations and elastic constants. *J. Chem. Phys.*, 76(5):2662–2666, March 1982.
- [131] L D Landau, L P Pitaevskii, E M Lifshitz, and A M Kosevich. *Theory of elasticity*. Butterworth-Heinemann, Oxford, England, 3 edition, January 1984.
- [132] C R A Catlow and W C Mackrodt, editors. *Computer Simulation of Solids*. Lecture notes in physics. Springer, Berlin, Germany, October 1982.
- [133] Vladimir S Bystrov, editor. *Simulation and modeling of nanomaterials*. MDPI, July 2022.
- [134] Germain Clavier and Aidan P Thompson. Computation of the thermal elastic constants for arbitrary manybody potentials in LAMMPS using the stress-fluctuation formalism. *Comput. Phys. Commun.*, 286(108674):108674, May 2023.
- [135] Eduardo W V Chaves. *Notes on Continuum Mechanics*. Lecture notes on numerical methods in engineering and sciences. Springer, Dordrecht, Netherlands, 2013 edition, March 2013.
- [136] Ted Belytschko, Kam Liu, and Brian Moran. *Nonlinear finite elements for continua and structures*. John Wiley & Sons, Chichester, England, August 2000.

- [137] Pisidhi Karasudhi. *Foundations of solid mechanics*. Solid mechanics and its applications. Springer, Dordrecht, Netherlands, September 2012.
- [138] J F Lutsko. Stress and elastic constants in anisotropic solids: Molecular dynamics techniques. *J. Appl. Phys.*, 64(3):1152–1154, August 1988.
- [139] D J Quesnel, D S Rimai, and L P DeMejo. Elastic compliances and stiffnesses of the fcc Lennard-Jones solid. *Phys. Rev. B Condens. Matter*, 48(10):6795–6807, September 1993.
- [140] J F Lutsko. Generalized expressions for the calculation of elastic constants by computer simulation. *J. Appl. Phys.*, 65(8):2991–2997, April 1989.
- [141] Shuichi Nosé. A unified formulation of the constant temperature molecular dynamics methods. *J. Chem. Phys.*, 81(1):511–519, July 1984.
- [142] D R Squire, A C Holt, and W G Hoover. Isothermal elastic constants for argon. theory and monte carlo calculations. *Physica*, 42(3):388–397, May 1969.
- [143] Kevin Van Workum, Kenji Yoshimoto, Juan J de Pablo, and Jack F Douglas. Isothermal stress and elasticity tensors for ions and point dipoles using ewald summations. *Phys. Rev. E Stat. Nonlin. Soft Matter Phys.*, 71(6 Pt 1):061102, June 2005.
- [144] Max Born. On the stability of crystal lattices. I. *Math. Proc. Camb. Philos. Soc.*, 36(2):160–172, April 1940.
- [145] Félix Mouhat and François-Xavier Coudert. Necessary and sufficient elastic stability conditions in various crystal systems. *Phys. Rev. B Condens. Matter Mater. Phys.*, 90(22), December 2014.
- [146] Sven M J Rogge, Michel Waroquier, and Veronique Van Speybroeck. Reliably modeling the mechanical stability of rigid and flexible metal–organic frameworks. *Acc. Chem. Res.*, 51(1):138–148, January 2018.
- [147] S M J Rogge, L Vanduyfhuys, A Ghysels, M Waroquier, T Verstraelen, G Maurin, and V Van Speybroeck. A comparison of barostats for the mechanical characterization of metal-organic frameworks. *J. Chem. Theory Comput.*, 11(12):5583–5597, December 2015.
- [148] E. Acuna-Yeomans, J.J. Gutierrez-Sevillano, S. Calero, and D. Dubbeldam. Evaluation of zif-8 flexible force fields for structural and mechanical properties. *Microporous and Mesoporous Materials*, 348:112406, January 2023.
- [149] Tingting Weng and J. R. Schmidt. Flexible and transferable ab initio force field for zeolitic imidazolate frameworks: ZIF-FF. *The Journal of Physical Chemistry A*, 123(13):3000–3012, March 2019.
- [150] Louis Vanduyfhuys, Steven Vandenbrande, Toon Verstraelen, Rochus Schmid, Michel Waroquier, and Veronique Van Speybroeck. QuickFF: A program for a quick and easy derivation of force fields for metal-organic frameworks from *ab initio* input. *Journal of Computational Chemistry*, 36(13):1015–1027, March 2015.

-
- [151] D. Dubbeldam, S. Calero, D. E. Ellis, and R. Q. Snurr. RASPA: Molecular simulation software for adsorption and diffusion in flexible nanoporous materials. *Mol. Simulat.*, 42(2):81, 2016.
- [152] A. P. Thompson, H. M. Aktulga, R. Berger, D. S. Bolintineanu, W. M. Brown, P. S. Crozier, P. J. in 't Veld, A. Kohlmeyer, S. G. Moore, T. D. Nguyen, R. Shan, M. J. Stevens, J. Tranchida, C. Trott, and S. J. Plimpton. LAMMPS - a flexible simulation tool for particle-based materials modeling at the atomic, meso, and continuum scales. *Comp. Phys. Comm.*, 271:10817, 2022.
- [153] A. Banerjee, N. Adams, J. Simons, and R. Shepard. Search for stationary-points on surface. *J. Phys. Chem.*, 89(1):52–57, 1985.
- [154] J. Baker. An algorithm for the location of transition-states. *J. Comp. Chem.*, 7(4):385–395, 1986.
- [155] J. Wang, R. M. Wolf, J. W. Caldwell, P. A. Kollman, and D. A. Case. Development and testing of a general amber force field. *J. Comput. Chem.*, 25:1157, 2004.
- [156] D.C. Wallace. *Thermodynamics of Crystals*. John Wiley, New York, 1972.
- [157] J. F. Nye. *Physical Properties of Crystals: Their Representation by Tensors and Matrices*. Oxford University Press, London, 1957.
- [158] J.F. Lutsko. Generalized expressions for the calculation of elastic constants by computer simulation. *J. Appl. Phys.*, 65(8):2991–2997, 1989.
- [159] M. Born and K. Huang. *Dynamical Theory of Crystal Lattices*. Clarendon Press, Oxford, 1957.
- [160] G. Grimvall, B. Magyari-Köpe, V. Ozoli, and K.A. Persson. Lattice instabilities in metallic elements. *Rev. Mod. Phys.*, 84(2):945, 2012.
- [161] J. Wang, J. Li, S. Yip, S. Phillpot, and D. Wolf. Mechanical instabilities of homogeneous crystals. *Phys. Rev. B*, 52(17):12627, 1995.
- [162] Wei Zhou, Hui Wu, Terrence J. Udovic, John J. Rush, and Taner Yildirim. Quasi-free methyl rotation in zeolitic imidazolate framework-8. *The Journal of Physical Chemistry A*, 112(49):12602–12606, November 2008.
- [163] B.T. Polyak. The conjugate gradient method in extremal problems. *USSR Computational Mathematics and Mathematical Physics*, 9(4):94–112, January 1969.
- [164] Boris T. Polyak. *Introduction to Optimization (Translations Series in Mathematics and Engineering)*. Optimization Software, 1987.
- [165] Pia Vervoorts, Stefan Burger, Karina Hemmer, and Gregor Kieslich. Revisiting the high-pressure properties of the metal-organic frameworks ZIF-8 and ZIF-67. October 2020.
- [166] Esteban Acuna-Yeomans, J.J. Gutiérrez-Sevillano, David Dubbeldam, and Sofia Calero. A simulation study of linker vacancy distribution and its effect on uio-66 stability. *Microporous and Mesoporous Materials*, 366:112922, February 2024.

- [167] Hong-Cai Joe Zhou and Susumu Kitagawa. Metal-organic frameworks (MOFs). *Chem. Soc. Rev.*, 43(16):5415–5418, August 2014.
- [168] Frederik Vermoortele, Bart Bueken, Gaëlle Le Bars, Ben Van de Voorde, Matthias Vandichel, Kristof Houthoofd, Alexandre Vimont, Marco Daturi, Michel Waroquier, Veronique Van Speybroeck, Christine Kirschhock, and Dirk E De Vos. Synthesis modulation as a tool to increase the catalytic activity of metal-organic frameworks: the unique case of UiO-66(Zr). *J. Am. Chem. Soc.*, 135(31):11465–11468, August 2013.
- [169] Jorge Gascon, María D Hernández-Alonso, Ana Rita Almeida, Gerard P M van Klink, Freek Kapteijn, and Guido Mul. Isorecticular MOFs as efficient photocatalysts with tunable band gap: an operando FTIR study of the photoinduced oxidation of propylene. *ChemSusChem*, 1(12):981–983, 2008.
- [170] Anil H Valekar, Kyung-Ho Cho, Sachin K Chitale, Do-Young Hong, Ga-Young Cha, U-Hwang Lee, Dong Won Hwang, Christian Serre, Jong-San Chang, and Young Kyu Hwang. Catalytic transfer hydrogenation of ethyl levulinate to γ -valerolactone over zirconium-based metal-organic frameworks. *Green Chem.*, 18(16):4542–4552, 2016.
- [171] Víctor L Rechac, Francisco G Cirujano, Avelino Corma, and Francesc X Llabrés i Xamena. Diastereoselective synthesis of pyranoquinolines on zirconium-containing UiO-66 metal-organic frameworks. *Eur. J. Inorg. Chem.*, 2016(27):4512–4516, September 2016.
- [172] Patricia Horcajada, Ruxandra Gref, Tarek Baati, Phoebe K Allan, Guillaume Maurin, Patrick Couvreur, Gérard Férey, Russell E Morris, and Christian Serre. Metal-organic frameworks in biomedicine. *Chem. Rev.*, 112(2):1232–1268, February 2012.
- [173] Christopher A Trickett, Aasif Helal, Bassem A Al-Maythaly, Zain H Yamani, Kyle E Cordova, and Omar M Yaghi. The chemistry of metal-organic frameworks for CO₂ capture, regeneration and conversion. *Nat. Rev. Mater.*, 2(8):17045, July 2017.
- [174] Tyler G Grissom, Darren M Driscoll, Diego Troya, Nicholas S Sapienza, Pavel M Usov, Amanda J Morris, and John R Morris. Molecular-level insight into CO₂ adsorption on the zirconium-based metal-organic framework, UiO-66: A combined spectroscopic and computational approach. *J. Phys. Chem. C Nanomater. Interfaces*, 123(22):13731–13738, June 2019.
- [175] Camille Petit. Present and future of MOF research in the field of adsorption and molecular separation. *Curr. Opin. Chem. Eng.*, 20:132–142, June 2018.
- [176] Jian-Rong Li, Ryan J Kuppler, and Hong-Cai Zhou. Selective gas adsorption and separation in metal-organic frameworks. *Chem. Soc. Rev.*, 38(5):1477–1504, May 2009.
- [177] Jasmina Hafizovic Cavka, Søren Jakobsen, Unni Olsbye, Nathalie Guillou, Carlo Lamberti, Silvia Bordiga, and Karl Petter Lillerud. A new zirconium inorganic building brick forming metal organic frameworks with exceptional stability. *J. Am. Chem. Soc.*, 130(42):13850–13851, October 2008.

- [178] Loredana Valenzano, Bartolomeo Civalleri, Sachin Chavan, Silvia Bordiga, Merete H Nilsen, Søren Jakobsen, Karl Petter Lillerud, and Carlo Lamberti. Disclosing the complex structure of UiO-66 metal organic framework: A synergetic combination of experiment and theory. *Chem. Mater.*, 23(7):1700–1718, April 2011.
- [179] Jared B DeCoste, Gregory W Peterson, Himanshu Jasuja, T Grant Glover, You-Gui Huang, and Krista S Walton. Stability and degradation mechanisms of metal–organic frameworks containing the $Zr_6O_4(OH)_4$ secondary building unit. *J. Mater. Chem. A Mater. Energy Sustain.*, 1(18):5642, 2013.
- [180] Karen Leus, Thomas Bogaerts, Jeroen De Decker, Hannes Depauw, Kevin Hendrickx, Henk Vrielinck, Veronique Van Speybroeck, and Pascal Van Der Voort. Systematic study of the chemical and hydrothermal stability of selected “stable” metal organic frameworks. *Microporous Mesoporous Mater.*, 226:110–116, May 2016.
- [181] Greig C Shearer, Sachin Chavan, Silvia Bordiga, Stian Svelle, Unni Olsbye, and Karl Petter Lillerud. Defect engineering: Tuning the porosity and composition of the metal–organic framework UiO-66 via modulated synthesis. *Chem. Mater.*, 28(11):3749–3761, June 2016.
- [182] Lingmei Liu, Zhijie Chen, Jianjian Wang, Daliang Zhang, Yihan Zhu, Sanliang Ling, Kuo-Wei Huang, Youssef Belmabkhout, Karim Adil, Yuxin Zhang, Ben Slater, Mohamed Eddaoudi, and Yu Han. Imaging defects and their evolution in a metal-organic framework at sub-unit-cell resolution. *Nat. Chem.*, 11(7):622–628, July 2019.
- [183] Greig C Shearer, Sachin Chavan, Jayashree Ethiraj, Jenny G Vitillo, Stian Svelle, Unni Olsbye, Carlo Lamberti, Silvia Bordiga, and Karl Petter Lillerud. Tuned to perfection: Ironing out the defects in metal–organic framework UiO-66. *Chem. Mater.*, 26(14):4068–4071, July 2014.
- [184] Matthew J Cliffe, Wei Wan, Xiaodong Zou, Philip A Chater, Annette K Kleppe, Matthew G Tucker, Heribert Wilhelm, Nicholas P Funnell, François-Xavier Coudert, and Andrew L Goodwin. Correlated defect nanoregions in a metal-organic framework. *Nat. Commun.*, 5(1):4176, June 2014.
- [185] Hui Wu, Yong Shen Chua, Vaiva Krungleviciute, Madhusudan Tyagi, Ping Chen, Taner Yildirim, and Wei Zhou. Unusual and highly tunable missing-linker defects in zirconium metal-organic framework UiO-66 and their important effects on gas adsorption. *J. Am. Chem. Soc.*, 135(28):10525–10532, July 2013.
- [186] A W Thornton, R Babarao, A Jain, F Trousselet, and F-X Coudert. Defects in metal-organic frameworks: a compromise between adsorption and stability? *Dalton Trans.*, 45(10):4352–4359, March 2016.
- [187] J Canivet, M Vandichel, and D Farrusseng. Origin of highly active metal-organic framework catalysts: defects? defects! *Dalton Trans.*, 45(10):4090–4099, March 2016.
- [188] Jared M Taylor, Shun Dekura, Ryuichi Ikeda, and Hiroshi Kitagawa. Defect control to enhance proton conductivity in a metal–organic framework. *Chem. Mater.*, 27(7):2286–2289, April 2015.

- [189] Jared M Taylor, Tokutaro Komatsu, Shun Dekura, Kazuya Otsubo, Masaki Takata, and Hiroshi Kitagawa. The role of a three dimensionally ordered defect sublattice on the acidity of a sulfonated metal-organic framework. *J. Am. Chem. Soc.*, 137(35):11498–11506, September 2015.
- [190] Qingyuan Yang, Vincent Guillermin, Florence Ragon, Andrew D Wiersum, Philip L Llewellyn, Chongli Zhong, Thomas Devic, Christian Serre, and Guillaume Maurin. CH₄ storage and CO₂ capture in highly porous zirconium oxide based metal-organic frameworks. *Chem. Commun. (Camb.)*, 48(79):9831–9833, October 2012.
- [191] Peter G Boyd, Seyed Mohamad Moosavi, Matthew Witman, and Berend Smit. Force-field prediction of materials properties in metal-organic frameworks. *J. Phys. Chem. Lett.*, 8(2):357–363, January 2017.
- [192] Damien E Coupry, Matthew A Addicoat, and Thomas Heine. Extension of the universal force field for metal-organic frameworks. *J. Chem. Theory Comput.*, 12(10):5215–5225, October 2016.
- [193] Jessica K Bristow, Davide Tiana, and Aron Walsh. Transferable force field for metal-organic frameworks from first-principles: BTW-FF. *J. Chem. Theory Comput.*, 10(10):4644–4652, October 2014.
- [194] Aurélie U Ortiz, Anne Boutin, Alain H Fuchs, and François-Xavier Coudert. Anisotropic elastic properties of flexible metal-organic frameworks: how soft are soft porous crystals? *Phys. Rev. Lett.*, 109(19):195502, November 2012.
- [195] Arnaud Marmier, Zoe A D Lethbridge, Richard I Walton, Christopher W Smith, Stephen C Parker, and Kenneth E Evans. ELAM: A computer program for the analysis and representation of anisotropic elastic properties. *Comput. Phys. Commun.*, 181(12):2102–2115, December 2010.
- [196] Kevin Van Workum, Guangtu Gao, J David Schall, and Judith A Harrison. Expressions for the stress and elasticity tensors for angle-dependent potentials. *J. Chem. Phys.*, 125(14):144506, October 2006.
- [197] Romain Gaillac, Pluton Pullumbi, and François-Xavier Coudert. ELATE: an open-source online application for analysis and visualization of elastic tensors. *J. Phys. Condens. Matter*, 28(27):275201, July 2016.
- [198] E. Acuna-Yeomans, P. J. Goosen, J. J. Gutiérrez-Sevillano, D. Dubbeldam, and S. Calero. Effect of water loading on the stability of pristine and defective uio-66. *Journal of Materials Chemistry A*, 12(37):25233–25243, 2024.
- [199] Walter M Warren-Vega, Armando Campos-Rodríguez, Ana I Zárata-Guzmán, and Luis A Romero-Cano. A current review of water pollutants in american continent: Trends and perspectives in detection, health risks, and treatment technologies. *Int. J. Environ. Res. Public Health*, 20(5), March 2023.
- [200] Xiaocang Xu, Haoran Yang, and Chang Li. Theoretical model and actual characteristics of air pollution affecting health cost: A review. *Int. J. Environ. Res. Public Health*, 19(6):3532, March 2022.

-
- [201] Li Lin, Haoran Yang, and Xiaocang Xu. Effects of water pollution on human health and disease heterogeneity: A review. *Front. Environ. Sci.*, 10, June 2022.
- [202] Jafar Abdi, Manouchehr Vossoughi, Niyaz Mohammad Mahmoodi, and Iran Alemzadeh. Synthesis of metal-organic framework hybrid nanocomposites based on GO and CNT with high adsorption capacity for dye removal. *Chem. Eng. J.*, 326:1145–1158, October 2017.
- [203] Milad Raeiszadeh, Alireza Hakimian, Akbar Shojaei, and Hossein Molavi. Nanodiamond-filled chitosan as an efficient adsorbent for anionic dye removal from aqueous solutions. *J. Environ. Chem. Eng.*, 6(2):3283–3294, April 2018.
- [204] Ke Yue, Xiaodong Zhang, Shuntong Jiang, Jinfeng Chen, Yang Yang, Fukun Bi, and Yuxin Wang. Recent advances in strategies to modify MIL-125 (ti) and its environmental applications. *J. Mol. Liq.*, 335(116108):116108, August 2021.
- [205] Xiaojie Fang, Di Zhang, Zhenfeng Chang, Ruoyan Li, and Shuangshuang Meng. Phosphorus removal from water by the metal-organic frameworks (MOFs)-based adsorbents: A review for structure, mechanism, and current progress. *Environ. Res.*, 243(117816):117816, February 2024.
- [206] Qiyang Xie, Yan Li, Zhaoling Lv, Hang Zhou, Xiangjun Yang, Jing Chen, and Hong Guo. Effective adsorption and removal of phosphate from aqueous solutions and eutrophic water by Fe-based MOFs of MIL-101. *Sci. Rep.*, 7(1):3316, June 2017.
- [207] Lili Zhang, Decheng Mao, Yining Qu, Xiaohong Chen, Jindi Zhang, Mengyang Huang, and Jiaqiang Wang. Facile synthesis of Ce-MOF for the removal of phosphate, fluoride, and arsenic. *Nanomaterials (Basel)*, 13(23), November 2023.
- [208] Athanasia K Tolkou and Anastasios I Zouboulis. Fluoride removal from water sources by adsorption on MOFs. *Separations*, 10(9):467, August 2023.
- [209] S Essalmi, S Lotfi, A BaQais, M Saadi, M Arab, and H Ait Ahsaine. Design and application of metal organic frameworks for heavy metals adsorption in water: a review. *RSC Adv.*, 14(13):9365–9390, March 2024.
- [210] Ping Chen, Yalan Wang, Xiaoqin Zhuang, Haijin Liu, Guoguang Liu, and Wenyang Lv. Selective removal of heavy metals by Zr-based MOFs in wastewater: New acid and amino functionalization strategy. *J. Environ. Sci. (China)*, 124:268–280, February 2023.
- [211] Erik Svensson Grape, Antonio J Chacón-García, Sara Rojas, Yolanda Pérez, Aleksander Jaworski, Mathias Nero, Michelle Åhlén, Eva Martínez-Ahumada, Athina E Galetsa Feindt, Mathieu Pepillo, Mayumi Narongin-Fujikawa, Ilich A Ibarra, Ocean Cheung, Christian Baresel, Tom Willhammar, Patricia Horcajada, and A Ken Inge. Removal of pharmaceutical pollutants from effluent by a plant-based metal-organic framework. *Nat Water*, 1(5):433–442, May 2023.
- [212] Lijin Huang, Rujia Shen, and Qin Shuai. Adsorptive removal of pharmaceuticals from water using metal-organic frameworks: A review. *J. Environ. Manage.*, 277(111389):111389, January 2021.

- [213] Y Kalinovsky, N J Cooper, M J Main, S J Holder, and B A Blight. Microwave-assisted activation and modulator removal in zirconium MOFs for buffer-free CWA hydrolysis. *Dalton Trans.*, 46(45):15704–15709, 2017.
- [214] Gregory W Peterson, Annie X Lu, and Thomas H Epps, III. Tuning the morphology and activity of electrospun polystyrene/Uio-66-NH₂ metal–organic framework composites to enhance chemical warfare agent removal. *ACS Appl. Mater. Interfaces*, 9(37):32248–32254, September 2017.
- [215] Anna Lee, Myoung-Woon Moon, Hyuneui Lim, Wan-Doo Kim, and Ho-Young Kim. Water harvest via dewing. *Langmuir*, 28(27):10183–10191, July 2012.
- [216] Mussie Fessehaye, Sabah A Abdul-Wahab, Michael J Savage, Thomas Kohler, Tsegai Gherezghiher, and Hans Hurni. Fog-water collection for community use. *Renew. Sustain. Energy Rev.*, 29:52–62, January 2014.
- [217] Musaddaq Azeem, Muhammad Tayyab Noman, Jakub Wiener, Michal Petru, and Petr Louda. Structural design of efficient fog collectors: A review. *Environ. Technol. Innov.*, 20(101169):101169, November 2020.
- [218] Xiaoge Liu, Yuying Shan, Songtao Zhang, Qingquan Kong, and Huan Pang. Application of metal organic framework in wastewater treatment. *Green Energy Environ.*, 8(3):698–721, June 2023.
- [219] Farhad Ahmadijokani, Hossein Molavi, Mashallah Rezakazemi, Shima Tajahmadi, Addie Bahi, Frank Ko, Tejraj M Aminabhavi, Jian-Rong Li, and Mohammad Arjmand. UiO-66 metal–organic frameworks in water treatment: A critical review. *Prog. Mater. Sci.*, 125(100904):100904, April 2022.
- [220] Nicholas C Burtch, Himanshu Jasuja, and Krista S Walton. Water stability and adsorption in metal-organic frameworks. *Chem. Rev.*, 114(20):10575–10612, October 2014.
- [221] Mostakim Sk, Salini Kar, Jayant K Dewangan, and Mithun Chowdhury. Engineering linker defects in functionalized UiO-66 MOF nanoparticles for oil-in-water pickering emulsion stabilization. *Dalton Trans.*, 52(34):11886–11896, August 2023.
- [222] Yuting Huang, Weiping Qin, Zhong Li, and Yingwei Li. Enhanced stability and CO₂ affinity of a UiO-66 type metal-organic framework decorated with dimethyl groups. *Dalton Trans.*, 41(31):9283–9285, August 2012.
- [223] Huong Giang T Nguyen, Neil M Schweitzer, Chih-Yi Chang, Tasha L Drake, Monica C So, Peter C Stair, Omar K Farha, Joseph T Hupp, and Sonbinh T Nguyen. Vanadium-node-functionalized UiO-66: A thermally stable MOF-supported catalyst for the gas-phase oxidative dehydrogenation of cyclohexene. *ACS Catal.*, 4(8):2496–2500, August 2014.
- [224] Mohammad I Hossain and T Grant Glover. Kinetics of water adsorption in UiO-66 MOF. *Ind. Eng. Chem. Res.*, 58(24):10550–10558, June 2019.
- [225] Louis Vanduyfhuys, Steven Vandenbrande, Jelle Wieme, Michel Waroquier, Toon Verstraelen, and Veronique Van Speybroeck. Extension of the QuickFF force field

- protocol for an improved accuracy of structural, vibrational, mechanical and thermal properties of metal-organic frameworks. *J. Comput. Chem.*, 39(16):999–1011, June 2018.
- [226] Jacob J Wardzala, Jonathan P Ruffley, Isabella Goodenough, Allie M Schmidt, Priyanka B Shukla, Xin Wei, Abhishek Bagusetty, Mattheus De Souza, Prasennjit Das, Dorian J Thompson, Christopher J Karwacki, Christopher E Wilmer, Eric Borguet, Nathaniel L Rosi, and J Karl Johnson. Modeling of diffusion of acetone in UiO-66. *J. Phys. Chem. C Nanomater. Interfaces*, 124(52):28469–28478, December 2020.
- [227] Chinmay V. Mhatre, Jacob J. Wardzala, Priyanka B. Shukla, Mayank Agrawal, and J. Karl Johnson. Calculation of self, corrected, and transport diffusivities of isopropyl alcohol in uiO-66. *Nanomaterials*, 13(11):1793, June 2023.
- [228] Jierui Zhang, Francesco Paesani, and Martina Lessio. Computational insights into the interaction of water with the uiO-66 metal-organic framework and its functionalized derivatives. *Journal of Materials Chemistry C*, 11(30):10247–10258, 2023.
- [229] Xuanyu Zhu, Marc Riera, Ethan F Bull-Vulpe, and Francesco Paesani. MB-pol(2023): Sub-chemical accuracy for water simulations from the gas to the liquid phase. *J. Chem. Theory Comput.*, 19(12):3551–3566, June 2023.
- [230] J L F Abascal and C Vega. A general purpose model for the condensed phases of water: TIP4P/2005. *J. Chem. Phys.*, 123(23):234505, December 2005.
- [231] Hilliary O Frank and Francesco Paesani. Molecular driving forces for water adsorption in MOF-808: A comparative analysis with UiO-66. *J. Chem. Phys.*, 160(9), March 2024.
- [232] Hiroyasu Furukawa, Felipe Gándara, Yue-Biao Zhang, Juncong Jiang, Wendy L. Queen, Matthew R. Hudson, and Omar M. Yaghi. Water adsorption in porous metal-organic frameworks and related materials. *Journal of the American Chemical Society*, 136(11):4369–4381, March 2014.
- [233] Norman L. Allinger, Young H. Yuh, and Jenn Huei Lii. Molecular mechanics. the mm3 force field for hydrocarbons. 1. *Journal of the American Chemical Society*, 111(23):8551–8566, November 1989.
- [234] Norman L. Allinger, Xuefeng Zhou, and John Bergsma. Molecular mechanics parameters. *Journal of Molecular Structure: THEOCHEM*, 312(1):69–83, January 1994.
- [235] H J C Berendsen, J R Grigera, and T P Straatsma. The missing term in effective pair potentials. *J. Phys. Chem.*, 91(24):6269–6271, November 1987.
- [236] Swaroop Chatterjee, Pablo G Debenedetti, Frank H Stillinger, and Ruth M Lynden-Bell. A computational investigation of thermodynamics, structure, dynamics and solvation behavior in modified water models. *J. Chem. Phys.*, 128(12):124511, March 2008.
- [237] W Humphrey, A Dalke, and K Schulten. VMD: visual molecular dynamics. *J. Mol. Graph.*, 14(1):33–8, 27–8, February 1996.

- [238] Thomas D Bennett, Tanya K Todorova, Emma F Baxter, David G Reid, Christel Gervais, Bart Bueken, B Van de Voorde, Dirk De Vos, David A Keen, and Caroline Mellot-Draznieks. Connecting defects and amorphization in UiO-66 and MIL-140 metal–organic frameworks: a combined experimental and computational study. *Phys. Chem. Chem. Phys.*, 18(3):2192–2201, January 2016.
- [239] Gabriela Jajko, Sofia Calero, Paweł Kozyra, Waław Makowski, Andrzej Sławek, Barbara Gil, and Juan José Gutiérrez-Sevillano. Defect-induced tuning of polarity-dependent adsorption in hydrophobic-hydrophilic UiO-66. *Commun. Chem.*, 5(1):120, October 2022.
- [240] Andrzej Sławek, Gabriela Jajko, Karolina Ogorzały, David Dubbeldam, Thijs J H Vlugt, and Waław Makowski. The influence of UiO-66 metal-organic framework structural defects on adsorption and separation of hexane isomers. *Chemistry*, 28(29):e202200030, May 2022.
- [241] K Vasanth Kumar, G Charalambopoulou, M Kainourgiakis, A Stubos, and Th Steriotis. Insights on the physical adsorption of hydrogen and methane in UiO series of MOFs using molecular simulations. *Comput. Theor. Chem.*, 1061:36–45, June 2015.
- [242] João M M Maia, Rui P P L Ribeiro, and José P B Mota. Prediction of carbon dioxide and methane adsorption on UiO-66 metal–organic framework via molecular simulation. *Crystals (Basel)*, 13(10):1523, October 2023.
- [243] Katherine A Forrest, Gaurav Verma, Yingxiang Ye, Junyu Ren, Shengqian Ma, Tony Pham, and Brian Space. Methane storage in flexible and dynamical metal–organic frameworks. *Chem. Phys. Rev.*, 3(2):021308, June 2022.
- [244] Chiara Caratelli, Julianna Hajek, Sven M J Rogge, Steven Vandenbrande, Evert Jan Meijer, Michel Waroquier, and Veronique Van Speybroeck. Influence of a confined methanol solvent on the reactivity of active sites in UiO-66. *Chemphyschem*, 19(4):420–429, February 2018.
- [245] Gabriela Jajko, Paweł Kozyra, Juan José Gutiérrez-Sevillano, Waław Makowski, and Sofia Calero. Carbon dioxide capture enhanced by pre-adsorption of water and methanol in UiO-66. *Chemistry*, 27(59):14653–14659, October 2021.
- [246] Himanshu Jasuja and Krista S Walton. Experimental study of CO₂, CH₄, and water vapor adsorption on a dimethyl-functionalized UiO-66 framework. *J. Phys. Chem. C Nanomater. Interfaces*, 117(14):7062–7068, April 2013.
- [247] Farhad Ahmadijokani, Rahman Mohammadkhani, Salman Ahmadipouya, Atefeh Shokrgozar, Mashallah Rezakazemi, Hossein Molavi, Tejraj M Aminabhavi, and Mohammad Arjmand. Superior chemical stability of UiO-66 metal-organic frameworks (MOFs) for selective dye adsorption. *Chem. Eng. J.*, 399(125346):125346, November 2020.
- [248] Priyanka B Shukla and J Karl Johnson. Impact of loading-dependent intrinsic framework flexibility on adsorption in UiO-66. *J. Phys. Chem. C Nanomater. Interfaces*, 126(41):17699–17711, October 2022.

- [249] Haoyuan Chen and Randall Q Snurr. Understanding the loading dependence of adsorbate diffusivities in hierarchical metal-organic frameworks. *Langmuir*, 36(5):1372–1378, February 2020.
- [250] Farhad Ahmadijokani, Salman Ahmadipouya, Hossein Molavi, Mashallah Reza-kazemi, Tejraj M Aminabhavi, and Mohammad Arjmand. Impact of scale, activation solvents, and aged conditions on gas adsorption properties of UiO-66. *J. Environ. Manage.*, 274(111155):111155, November 2020.
- [251] Sheng Feng, Runbai Wang, Shanshan Feng, Zihui Zhang, and Shuguang Liu. Synthesis of UiO-66 based on benzoic acid and chloroform with highly efficient adsorption of congo red dye. *Desalination Water Treat.*, 126:350–360, September 2018.
- [252] Florian Venel, Christophe Volkringer, Olivier Lafon, and Frédérique Pourpoint. Probing adsorption of water and DMF in UiO-66(Zr) using solid-state NMR. *Solid State Nucl. Magn. Reson.*, 120(101797):101797, August 2022.
- [253] Matthew A Addicoat, Nina Vankova, Ismot Farjana Akter, and Thomas Heine. Extension of the universal force field to metal-organic frameworks. *J. Chem. Theory Comput.*, 10(2):880–891, February 2014.
- [254] Damien E Coupry, Matthew A Addicoat, and Thomas Heine. Extension of the universal force field for metal-organic frameworks. *J. Chem. Theory Comput.*, 12(10):5215–5225, October 2016.
- [255] Stephen L Mayo, Barry D Olafson, and William A Goddard. DREIDING: a generic force field for molecular simulations. *J. Phys. Chem.*, 94(26):8897–8909, December 1990.
- [256] Marcus G. Martin and J. Ilja Siepmann. Transferable potentials for phase equilibria. 1. united-atom description of n-alkanes. *The Journal of Physical Chemistry B*, 102(14):2569–2577, March 1998.
- [257] M. Yiannourakou, P. Ungerer, B. Leblanc, X. Rozanska, P. Saxe, S. Vidal-Gilbert, F. Gouth, and F. Montel. Molecular simulation of adsorption in microporous materials. *Oil amp; Gas Science and Technology – Revue d’IFP Energies nouvelles*, 68(6):977–994, November 2013.
- [258] Yuanyuan Tian, Changhui Yan, and Zhehui Jin. Characterization of methane excess and absolute adsorption in various clay nanopores from molecular simulation. *Scientific Reports*, 7(1), September 2017.
- [259] Steven Vandenbrande, Toon Verstraelen, Juan José Gutiérrez-Sevillano, Michel Waroquier, and Veronique Van Speybroeck. Methane adsorption in zr-based mofs: Comparison and critical evaluation of force fields. *The Journal of Physical Chemistry C*, 121(45):25309–25322, November 2017.
- [260] Gregory S. Larsen, Ping Lin, Flor R. Siperstein, and Coray M. Colina. Methane adsorption in pim-1. *Adsorption*, 17(1):21–26, October 2010.
- [261] João M. M. Maia, Rui P. P. L. Ribeiro, and José P. B. Mota. Prediction of carbon dioxide and methane adsorption on uio-66 metal-organic framework via molecular simulation. *Crystals*, 13(10):1523, October 2023.

- [262] D. Gonzalez-Salgado and C. Vega. A new intermolecular potential for simulations of methanol: The opl/2016 model. *The Journal of Chemical Physics*, 145(3), July 2016.
- [263] William L. Jorgensen. Optimized intermolecular potential functions for liquid alcohols. *The Journal of Physical Chemistry*, 90(7):1276–1284, March 1986.
- [264] Thomas Fox, Thomas, Margaret McCarrick, and Peter A. Kollman. Application of free energy perturbation calculations to the “tennis ball” dimer: Why is cf₄ not encapsulated by this host? *The Journal of Physical Chemistry*, 100(25):10779–10783, January 1996.
- [265] Thomas Fox and Peter A. Kollman. Application of the resp methodology in the parametrization of organic solvents. *The Journal of Physical Chemistry B*, 102(41):8070–8079, September 1998.
- [266] Mustafa Erkartal and Murat Durandurdu. Pressure-induced amorphization of MOF-5: A first principles study. *ChemistrySelect*, 3(28):8056–8063, July 2018.
- [267] Junmei Wang, Wei Wang, Peter A. Kollman, and David A. Case. Automatic atom type and bond type perception in molecular mechanical calculations. *Journal of Molecular Graphics and Modelling*, 25(2):247–260, October 2006.
- [268] Martin B. Peters, Yue Yang, Bing Wang, László Füsti-Molnár, Michael N. Weaver, and Kenneth M. Merz. Structural survey of zinc-containing proteins and development of the zinc AMBER force field (ZAFF). *Journal of Chemical Theory and Computation*, 6(9):2935–2947, August 2010.
- [269] Fu Lin and Renxiao Wang. Systematic derivation of AMBER force field parameters applicable to zinc-containing systems. *Journal of Chemical Theory and Computation*, 6(6):1852–1870, May 2010.
- [270] Stephen C. Hoops, Kenneth W. Anderson, and Kenneth M. Merz. Force field design for metalloproteins. *Journal of the American Chemical Society*, 113(22):8262–8270, October 1991.
- [271] Malay Kumar Rana, Federico Giovanni Pazzona, Giuseppe Baldovino Suffritti, Pierfranco Demontis, and Marco Masia. Estimation of partial charges in small zeolite imidazolate frameworks from density functional theory calculations. *Journal of Chemical Theory and Computation*, 7(6):1575–1582, May 2011.
- [272] Zhongqiao Hu, Yifei Chen, and Jianwen Jiang. Zeolitic imidazolate framework-8 as a reverse osmosis membrane for water desalination: Insight from molecular simulation. *The Journal of Chemical Physics*, 134(13):134705, April 2011.
- [273] Helder M. Marques and Ignacy Cukrowski. Molecular mechanics parameters for the modelling of four-coordinate zn(ii) porphyrins. *Phys. Chem. Chem. Phys.*, 5(24):5499–5506, 2003.
- [274] Andrea Gabrieli, Marco Sant, Pierfranco Demontis, and Giuseppe B. Suffritti. Fast and efficient optimization of molecular dynamics force fields for microporous materials: Bonded interactions via force matching. *Microporous and Mesoporous Materials*, 197:339–347, October 2014.

- [275] Junhyuck Im, Narae Yim, Jaheon Kim, Thomas Vogt, and Yongjae Lee. High-pressure chemistry of a zeolitic imidazolate framework compound in the presence of different fluids. *Journal of the American Chemical Society*, 138(36):11477–11480, September 2016.